UNIVERSITA' DEGLI STUDI DI PADOVA

Scuola di Dottorato di Ricerca in Fisica

XXV Ciclo

Design and Fabrication of Nanostructures for Plasmonic Focusing

Direttore della Scuola: Ch.mo Prof. Andrea Vitturi

Supervisore: Ch.mo Prof. Filippo Romanato

Dottorando: Tommaso Ongarello

To My Family

Abstract

Plasmonic structures have known an increasing interest in the realization of miniaturized devices for light manipulation at subwavelenght scales. New plasmonic phenomena like extraordinary transmission of light and adiabatic nanofocusing opened up to a wide range of promising applications, from biosensing to spectroscopy and imaging. This work is aimed to the design and fabrication of plasmonic nanostructures for plasmon concentration. Two main configurations are proposed, both of them proved to support Surface Plasmon Polaritons (SPP) resonances and allowing light concentration. 1D metallic gratings allow the extraordinary transmission of light and SPP concentration inside subwavelenght slits, while tapered metallic waveguides, thanks to the adiabatic compression of a travelling SPP wave, allow the formation of high intense electromagnetic field hot spots in nanometric volumes (well below the diffraction limit) on the tip of the waveguide. A complete study of the problem, based on a chain process consisting of simulation-nanofabrication-characterization provides an exhaustive investigation into the physics of surface plasmon confinement and its innovative and original applications for Raman spectroscopy, biosensing and subwavelength energy confinement. Different optical setups are proposed and investigated both theoretically and experimentally, from far field measures to near field detection schemes, even with the use of novel input sources, like light possessing orbital angular momentum.

Abstract

Le strutture plasmoniche hanno conosciuto di recente un aumento di interesse per quanto riguarda la realizzazione di dispositivi per la manipolazione della luce su scale di dimensioni inferiori alla lunghezza d'onda. Una nuova serie di fenomeni plasmonici, come la trasmissione straordinaria della luce o il nanofocusing adiabatico ha dato il via allo sviluppo di una vasta serie di applicazioni promettenti, dal biosensing alla spettroscopia e all'imaging. Lo scopo di questo lavoro è il design e fabbricazione di nanostrutture plasmoniche per la concentrazione plasmonica. In particolare sono proposte due principali configurazioni, le quali entrambe hanno dimostrato di supportare risonanze plasmoniche e consentire la concentrazione della luce. Reticoli metallici 1D danno luogo al fenomeno della trasmissione straordinaria della luce e la conseguente concentrazione della radiazione elettromagnetica dentro fenditure di dimensioni inferiori alla lunghezza d'onda, mentre guide d'onda appuntite, grazie alla compressione adiabatica di un'onda plasmonica propagante, consentono la formazione di hot-spots di campo elettromagnetico in regioni nanometriche (ben al di sotto del limite di diffrazione). Uno studio completo del problema presentato in questo lavoro, basato su un processo a catena simulazione-fabbricazione-caratterizzazione, fornisce una esaustiva investigazione della fisica del confinamento plasmonico e consente originali applicazioni nella spettroscpia Raman, biosensing e confinamento energetico in dimensioni inferiori alla lunghezza d'onda. Diversi setup ottici sono proposti e investigati sia dal punto di vista teorico che sperimentale come misure far-field e sistemi di rivelazione near-field, anche con l'uso di innovative sorgenti di luce, come la luce dotata di momento angolare orbitale.

Summary

Preface

The advent and fast development of modern nano-fabrication techniques in the last decades has made it possible to explore new properties of light/matter interaction at nanoscale regions, even in sub-wavelength regime. The importance of delivering light and electromagnetic energy to the nanoscale is a crucial issue, and the advantages that such a possibility offers can be exploited in different technological fields, ranging from microelectronics and biosensing to near-field medical imaging and photovoltaic. The advantages of light-based technology strictly depend on the possibility to concentrate electromagnetic radiation (and thus energy) in the smallest volume possible. However, contrary to electronic devices, where the miniaturization process has reached very high standards, standard photonic devices are size-limited by the diffraction limit, making thus hard to combine the two different technologies in order to take the advantages from both of them. Surface Plasmon Polaritons (SPP) can provide one solution to this problem, because due to their nature of electromagnetic waves confined to a metal/dielectric interfaces, they possess a very strong electromagnetic field which can be localized in very small areas.

Plasmonics is part of the field concerning nanophotonics or nano-optics, which studies how electromagnetic fields can be confined to sizes much smaller than wavelength in vacuum. Light concentration by means of SPP has gathered a great interest in the scientific community after the discovery of exotic optical phenomena related to SPP excitation and propagation on metallic structures, like the extraordinary transmission of light observed by Ebbesen in 1998 and the nanofocusing effect predicted by Stockman in 2003. These effects demonstrate that under proper conditions, SPP and thus electromagnetic radiation energy can be confined in subwavelenght regions leading to the formation of hot-spots. Plasmonic devices which exploit these effects are used in a variety of promising applications, like sensing, near field imaging, photovoltaic, optics and wave guiding and all of these applications can be brought to sub-wavelength dimensions, thus overcoming the problem of diffraction limit which affects standard photonic devices. The realization of a plasmonic device requires a multi-disciplinary know-how, with different scientific backgrounds, comprising physics, engineering as well as biology, chemistry and science materials, thus making plasmonics a cross-disciplinary research field. Two main problems must be addressed when dealing with plasmonic phenomena: the first concerns the physical understanding of the different optical and electrical mechanisms which are at the base of a plasmonic device. The second affects the actual realization and characterization of the plasmonic device itself. Although SPP are known since the beginning of XX century, only in the last decade the scientific community has turned its attention to plasmonics and in this sense, there is a lot of room left for basic scientific study. Moreover, due to the high

sensitivity to geometrical conditions, the technological issue of employing a high fidelity nanofabrication process must be addressed and overcome.

The main topic of this thesis is the design and fabrication of plasmonic nanostructures for plasmon concentration. Several geometries and setups are proposed, all of them proved to support SPP resonances and allow light concentration. One of the main findings is the demonstration that plasmonic light concentration can be achieved with different structures but also with different experimental conditions, ranging from far field measures to near field detection schemes, even with the use of novel input sources, like for instance the case of light possessing orbital angular momentum.

Two main structures are analyzed in this work: plasmonic gratings and tapered metallic waveguides. 1D metallic gratings allow the extraordinary transmission of light and SPP concentration inside subwavelenght slits, which can be used to create intense electromagnetic field hot-spots in nanometric volumes as well as boost by several orders of magnitude the far-field transmittance, when compared with standard dielectric subwavelength apertures. Tapered metallic waveguides instead, thanks to the adiabatic compression of a travelling SPP wave, allow the formation of high intense electromagnetic field hot spots in nanometric volumes (well below the diffraction limit) on the tip of the waveguide, giving rise to the nanofocusing effect. Although these geometries have been the object of different studies in the last years, some questions still remain open. For instance the correlation between far-field transmission resonances and near field electromagnetic field profiles for 1D metallic grating needs further investigation, especially on experimental level. Also the way in which different geometrical parameters can be tuned in order to maximize a certain optical response is a non-trivial question when the actual fabrication of real samples must be taken into account. Regarding the nanofocusing effect, more investigations on other structures different from the conical shape proposed by Stockman are certainly needed, with different materials and illumination sources, in order to find geometries which improve the field enhancement but also allow a relatively ease of near-field detection. More in general, the integration of plasmonics with other opto-electrical structures for different technological applications is a problem that requires to be addressed.

In order to answer some of the questions, this thesis presents a detailed numerical and experimental description of the plasmonic resonances and phenomena occurring in such structures. Regarding 1D metallic gratings, two original devices exploiting the above-mentioned resonances are presented and tested, proving the capabilities of plasmonic devices as high sensitive detectors. The first structure consists of a subwavelength gold metallic grating on a glass substrate; by the optimization of the geometrical parameters it is possible to enhance the Raman signal from an active molecule placed in the

sits, thus creating a Surface Enhanced Raman Spectroscopy (SERS) device. The strength of choosing a simple geometry is highlighted by the possibility of making a direct comparison between the simulated and experimental data for the enhancement factor in $|E|^4$ approximation. In the second structure, the high sensitivity of plasmonic resonances to variations of the local refractive index due to functionalization in a V-shaped gold grating is coupled with a highly sensitive and scalable photo-detection scheme inspired by high electron mobility transistors (HEMTs). In this way a novel integrated platform can be tested for biosensoristic applications.

Regarding nanofocusing on tapered waveguides, the first geometry considered is a 3D metal conical waveguide. If the proper radial bound SPP mode is excited, a great electric field enhancement in the order of 10^3 is observed at the very end of the waveguide, at the tip's position. This effect is studied in detail with the help of the adiabatic theory, showing that the total enhancement depends on the materials and geometries used. The theoretical results are then used for the fabrication and near field-characterization of a focusing plasmonic device. Also the illumination of the conical waveguide with an unconventional illumination source, i.e. light possessing Orbital Angular Momentum (OAM) is investigated, in order to boost even more the total field enhancement and overcome the experimental technical difficulties arising with a radial polarized beam. The second geometry studied refers to a metallic planar tapered waveguide placed on a substrate. The possibility to obtain an adiabatic compression even on planar configuration is studied through a detailed modal analysis showing that an efficient nanofocusing effect is possible if the proper symmetry of the SPP mode is chosen accordingly to the dielectric environment. Again, the possibility of illuminating a planar nanofocusing device with light possessing OAM is addressed, allowing a further degree of control on the charge distribution in nanometric volumes and opening to new promising application.

The problems have been analyzed from different points of view and with a multidisciplinary approach, from a theoretical and numerical analysis to experimental activities regarding nanofabrication and characterization of the nanostructures, resulting in a three years interdisciplinary work on plasmonics and nanoscience. Great effort has been put in developing and supporting a chain process consisting of simulation-fabrication-characterization steps. This is a sort of modern view of the Galilean scientific approach, which moves from hypothesis generation and verification to the comparison of experimental data with the formulated theory, which will eventually result either reinforced or corrected. The strength of this approach is shown in this thesis, where in each of the different plasmonic structures which have been studied, the chain process has been applied in its entirety, leading in most of the cases to the realization of a plasmonic device whose working principle has been theoretical predicted, optimized and

experimentally investigated. This was possible thanks to the opportunity of working in a new but yet developing modern laboratory (LaNN Laboratory in Padova, Italy) which has made different numerical and experimental tools available in a unique facility. This sets a difference and also a novelty to other previous works in plasmonic field where only some parts of the problem were addressed, but little attention has been given to the interaction and coordination between the different steps required in order to get to a practical result.

Theoretical studies and modeling are required in order to fully understand the physical mechanisms underlying the working principle of each proposed structure and to perform optimization studies. These are mainly performed in this thesis with the help of the finite element method, a powerful numerical tool which allows to fully simulate the electro and optical response of a given physical system. A great part of this thesis consists also in the developing of processes for the fabrication and characterization of the plasmonic structures for light concentration. Due to the high sensitivity of plasmonic structures with respect to geometrical parameters, the related nanofabrication process must ensure very high resolution and pattern fidelity capabilities. In this perspective, nanofabrication by means of Electron Beam Lithography (EBL) represents the state of art in terms of high-resolution process. All the different steps of an EBL fabrication process are investigated, developed and optimized in this thesis work, including the correction of the proximity effect, which is the major cause of loss of resolution in a lithographic process. Alongside EBL, other nanofabrication techniques are also exploited, in order to develop a complete multi-step and multi-technique fabrication process for each of the proposed device. The characterization of the final samples is then performed by using both near- and far-field detection schemes, consisting mainly of ellipsometry and Scaning Near-field Optical Microscope (SNOM), but also spectroscopy and electronic measures are included in order to test the response of some of the devices proposed to an external functionalization event.

In summary, the content of this thesis work is organized as follows:

Chapter 1: Plasmonics. In this section the reader is introduced to the basics on plasmonics, starting from the diffraction limit and dispersion relation on the simplest geometry sustaining SPP propagation (a dielectric/metal interface) and up to multi-layers geometries. Details on calculations can be found in Appendix A at the end of the thesis. The basic properties of plasmon propagation, like propagation and decay lengths are discussed, along with the most common configurations for SPP excitation. Finally, a brief introduction on Plasmonic Vortexes (PV) generated by means of a Plasmonic Vortex Lens is provided (PVL), in order to give the basic background for the illumination source used in chapters 4 and 5.

Chapter 2: Experimental and Numerical Methods. This chapter is dedicated to the description of the different techniques, processes and tools used for modeling, fabrication and characterization of the plasmonic structures studied throughout this thesis. Electron Beam Lithography (EBL) is presented starting from the basics of electron-matter interaction and proximity effect and up to a description of complete lithographic process with all the intermediate steps required for the fabrication of the samples. Some notes on FIB lithography and metal deposition techniques are also provided. The chapter ends with the description of the finite element method software used for the different numerical analysis.

Chapter 3: Light Confinement with EOT in 1D Metallic Gratings. The Extraordinary Transmission of Light (EOT) and the light confinement in 1D metallic gratings are the main topics of this chapter. The EOT phenomenon is introduced and then analyzed by a one-to-one comparison between experimental observed data and numerical analysis, in order to correlate the observed peculiar far-field transmission features to the near-field electromagnetic fields profiles. A description of the different resonances processes as function of incident wavelength and polarization and geometrical parameters is provided with a multi-parametric numerical analysis. The 1D grating is then optimized and used in a SERS spectroscopy experiment where thanks to the plasmonic hot spot inside the slits the Raman signal of a benzenthiol (BT) monolayer adsorbed on the metal nanostructure is collected. The last section of the chapter is dedicated to the description of a plasmonic biosensing device based on a plasmonic crystal integrated on a multilayered semiconductor system. The plasmonic resonances of the grating, tuned by local refractive index changes due to the analytes, are transduced into modulations of the photogenerated carriers in the transistor channel and measured as voltage drop between the device terminals.

Chapter 4: Plasmonic Nanofocusing by Means of 3D Tapered Structures. The first part of this chapter reports a summary of the main results on a peculiar focusing structure formed by a metallic cone. In particular the *adiabatic approximation* proposed and developed for the first time by Stockman in 2003 is analyzed in details. The second part of the chapter reports the original results on a plasmonic structure designed, fabricated and tested in order to produce high light intensity enhancement in very small hot-spots. In the last part of the chapter, the properties of a Plasmonic Vortex Lens are used to properly excite a SPP beam which is then coupled to a 3D metallic cone placed in the center of the PVL. This design allows to excite SPP beams with an in-plane radial polarization that coupled with the conical waveguide increases the field enhancement by an order of magnitude respect to a standard configuration.

Chapter 5: Planar Nanofocusing. The possibility of planar nanofocusing along tapered planar metal stripes is analyzed in this chapter. For this purpose a detailed numerical analysis on the focusing effect on a planar tapered waveguide for different configuration is provided, starting from a modal analysis of SPP

propagation on metal stripes waveguides and concluding with a full 3D study of the focusing effect on a planar nanotip for different dielectric environments. The last part of the chapter is dedicated to the application of a novel device which combines the plasmonic planar nanofocusing with the exotic properties of light possessing Orbital Angular Momentum (OAM).

A reference list is provided at the end of each chapter.

31 January 2013

Tommaso Ongarello

1 Surface Plasmon Polaritons

1.1 Introduction

Surface Plasmon Polaritons (SPP) are electromagnetic waves propagating along the interface between a metal and a dielectric medium and have origin from the coupling of the electromagnetic field with electron-plasma density oscillations inside the metal. In this chapter are described the fundamentals properties of SPP; starting from the wave equation, the properties of SPP are analyzed both at single flat interfaces and also in metal/dielectric multilayer systems in terms of dispersion and spatial field profiles. More details on the calculations presented can be found in Appendix A at the end of the thesis. An introduction on the general concept of diffraction limit and how SPP can overcome the problem is also provided. The chapter ends with an introduction on Plasmonic Vortex, showing the basic properties of optical beams possessing Orbital Angular Momentum (OAM) and how they can be generated.

1.2 Diffraction Limit and Surface Plasmon Polaritons

In order to understand the origin of the diffraction limit for optical beams, let's start the analysis considering a plane wave with angular frequency ω propagating in a dielectric medium with refractive index *n*. The dispersion relation is given by:

$$|\mathbf{k}|^2 = n^2 \frac{\omega^2}{c^2} \tag{1.1}$$

Where $|\mathbf{k}| = k$ is the wavevector in the medium and c is the speed of light in vacuum. The component of k must satisfy:

$$k_x^2 + k_y^2 + k_z^2 = (nk_0)^2 = \varepsilon\mu\left(\frac{\omega}{c}\right)^2 \tag{1.2}$$

Where λ_0 and $k_0 = 2\pi / \lambda_0$ are the wavelength and wavevector in vacuum respectively and ε,μ are the relative permittivity (dielectric constant) and permeability of the medium. Since we are considering a propagating wave, all the 3D Cartesian components of the wavevector $k_{j=x,y,x}$ must be real, so that $-k \le k_j \le k$. The maximum variation of the magnitude of the wavevector is then $\Delta k = 2nk_0$. However the uncertainty principle for Fourier transforms holds and the following relation between spatial and a wavevector variation is established:

$$\Delta r \geq \frac{\pi}{\Delta k} = \frac{\lambda_0}{4n} \tag{1.3}$$

Equations (1.3) means that for an optical beam formed by a generic combination of optical 3D waves there is a minimum size in the order of the incident wavelength λ_0 below that the beam cannot be further focalized:

$$\Delta r_{\min 3D} = \frac{\lambda_0}{4n} \tag{1.4}$$

This limit is known as the *diffraction limit* and this limit is due to the nature of the beam itself. As long the optical wave is a 3D wave it will be always limited by diffraction. In standard common waveguide geometries, although the waveguide shape is often 1D, the optical beam is always 3D and thus the width of the optical beam is limited by diffraction, limiting transverse spatial confinement. It's easy now to think that in order to break through the diffraction limit, it's sufficient to increase the Δk value, so that $\Delta r \leq \lambda_0 / 4n$. One way to do that is by reducing one dimension of the optical wave, i.e. considering 2D optical waves. A 2D wave is a wave which is evanescent in one direction (for example the z-direction), like for instance a wave generated by reflection inside a metal surface (see Figure 1.1). In this way $k_z = i\kappa'_z$ is pure imaginary and now holds the following relation:

$$k_x^2 + k_y^2 - \kappa'^2_z = \varepsilon_{ND}\mu\left(\frac{\omega}{c}\right)^2 \tag{1.5}$$

Where $\varepsilon_{ND} < 0$ is the dielectric constant of the reflective medium. For this kind of wave $k_x^2 + k_y^2 > (nk_0)^2$ and so the wave is confined in the $x-y$ plane (a 2D optical beam). It follows immediately that for a 2D optical wave $\Delta k > 2nk_0$ and consequently Δr becomes smaller than the diffraction limit (1.4). However this reasoning is true until there is a 3D optical wave which generates the reflected wave in the metal.

One kind of 2D optical wave that can break through the diffraction limit without the need of an external 3D wave is the eigenmode of an interface between a dielectric and a metal (Figure 1.1). This type of wave, called Surface Plasmon Polariton (SPP), is a self-sustaining mode that, as solution of Maxwell's equations, does exists without the need of an external incident field. In the next paragraph will be explained the basic properties of SPP.

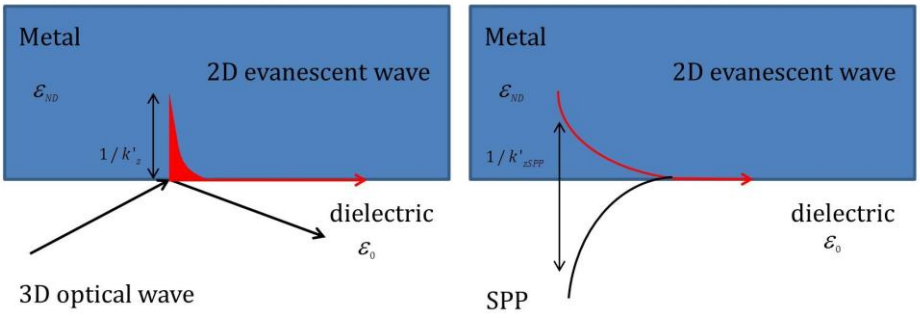

Figure 1.1 Examples of 2D optical waves. Left: Generation of evanescent wave by reflection at metal/dielectric interface. Right: SPP wave excitation at metal/dielectric interface.

1.3 Surface Plasmon Polaritons

Surface Plasmon Polaritons [1,2] are electromagnetic excitations propagating at the interface between a dielectric and a conductor, evanescently confined in the perpendicular direction, with an amplitude that decay exponentially with increasing distance from the surface on both sides. They originate from the coupling of the electromagnetic field with electron-plasma density oscillations inside the metal. The electromagnetic field is then confined to the vicinity of the surface, leading to an enhancement of the field at the interface. For these reasons SPP are very sensitive to surface conditions, geometry of the interface and optical properties of the dielectric environment and incoming radiation.
The first observation of Surface Plasmon Polaritons (SPP) was made in 1902 by Wood [3], who reported anomalies in the spectrum of light diffracted by a metallic diffraction grating. In particular he observed very sharp and narrow peaks and deeps in the collected refracted spectra. These features were strongly dependent on incident angle and wavelength of the incoming radiation. In 1941 Fano [4] showed that these anomalies were associated with the excitation of electromagnetic surface waves on the surface of the diffraction grating. In 1968 Otto demonstrated that the drop in reflectivity in the attenuated total reflection method is due to the excitation of surface plasmons. In the same year, Kretschmann and Rather observed excitation of surface plasmons in another configuration of the attenuated total reflection method. These pioneering works established a convenient method for the excitation and investigation of surface plasmon.

1.3.1 Surface Plasmon Polaritons at Metal/Dielectric Interface

One of the simplest geometry which is able to sustain SPP (see Figure 1.2) is the one formed by of a single flat interface between a semi-infinite dielectric with real dielectric constant ε_2 in $z>0$ and a semi-infinite metal described by an isotropic, frequency dependent, complex dielectric function

$\varepsilon_1(\omega)=\varepsilon_1^{'}(\omega)+i\varepsilon_1^{''}(\omega)$ in $z<0$. In order to calculate the electromagnetic field of a SPP at a dielectric–metal interface Maxwell's equations must be solved in each medium by imposing the appropriate boundary conditions at the interface [5]. We are looking for a solution of the wave equation that is bounded to the interface, i.e. with an evanescent decay in the perpendicular direction. Assuming a one dimensional problem and considering the wave propagating along the x-direction of a Cartesian coordinate system with no spatial variation in the perpendicular in-plane y-direction, the propagating waves can be described as:

$$\mathbf{E}(x,y,z)=\mathbf{E}(z)e^{ik_x x} \tag{1.6}$$

where k_x is the component of the wave vector in the direction of propagation. Assuming harmonic time dependence we get for the wave equation for the electric field:

$$\frac{\partial^2\mathbf{E}(z)}{\partial z^2}+\left(k_0^2\varepsilon-k_x^2\right)\mathbf{E}=0 \tag{1.7}$$

where $k_0=\omega/c$ is the modulus of the wave vector. A similar equation holds for $\mathbf{H}$. Equation (1.7) is the starting point for the study of guided electromagnetic modes in waveguides, and more specifically for the analysis of the dispersion relation of SPP.

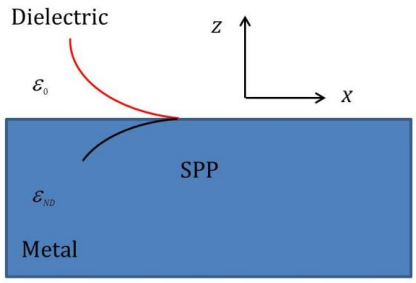

Figure 1.2 Geometry of SPP propagation at a single interface between a metal and a dielectric.

Let's start considering a p-polarized wave propagating along the x-direction (TM wave):

$$\begin{aligned}\mathbf{H}_2&=(0,H_{y2},0)e^{i(k_{x2}x-k_{z2}z-\omega t)}\\ \mathbf{E}_2&=(E_{x2},0,E_{z2})e^{i(k_{x2}x-k_{z2}z-\omega t)}\end{aligned} \tag{1.8}$$

for $z>0$ and:

$$\mathbf{H}_1 = (0, H_{y1}, 0) e^{i(k_{x1}x + k_{z1}z - \omega t)}$$
$$\mathbf{E}_1 = (E_{x1}, 0, E_{z1}) e^{i(k_{x1}x + k_{z1}z - \omega t)} \tag{1.9}$$

for $z < 0$. k_{zi} is the component of the wave vector perpendicular to the interface between the two media. By applying the standard boundary conditions for each component of the electromagnetic field at the interface between metal and dielectric, we obtain the dispersion relation for a SPP expressed in terms of the propagation constant, light frequency and dielectric constants of the two mediums (Appendix A reports the details of the calculation):

$$k_x = \frac{\omega}{c}\left(\frac{\varepsilon_1 \varepsilon_2}{\varepsilon_1 + \varepsilon_2}\right)^{1/2} \tag{1.10}$$

It can be shown that for a s-polarized wave (TE wave) the only solution possible is $E = 0$, meaning that a s-polarized SPP cannot propagate along the interface of a metal-dielectric system. Surface Plasmon Polaritons exist only for TM polarization.

Due to the bound and evanescent nature of SPP, the z-component of the wave vector both in the dielectric and metal is imaginary. This means that the field amplitude of the SPP decrease exponentially as $\exp(-|k_{zi}||z|)$, normal to the surface. The *skin depth* is the z value at which the field falls to $1/e$:

$$z_j = \frac{1}{|k_{zj}|} \tag{1.11}$$

or:

$$\hat{z}_2 = \frac{\lambda}{2\pi}\left(\frac{\varepsilon_1^{'} + \varepsilon_2}{\varepsilon_2^{\,2}}\right)^{1/2}$$
$$\hat{z}_1 = \frac{\lambda}{2\pi}\left(\frac{\varepsilon_1^{'} + \varepsilon_2}{\varepsilon_1^{'\,2}}\right)^{1/2} \tag{1.12}$$

Due to Ohmic losses in the metal, characterized by the imaginary part of the dielectric function of the metal $\varepsilon_2(\omega) > 0$, the energy carried by a SPP decays exponentially as the SPP propagates along the planar dielectric–metal interface. It's important to notice that the penetration depth of the SPP is much smaller than into dielectric, as it can be deduced from equations (1.12). The field profile (E_x, E_z, H_y) of a SPP propagating on air/silver interface at a wavelength of 633 nm is shown in Figure 1.3. The evanescent nature and the confinement of the SPP field in both dielectric and metal are visible in Figure 1.4. The dielectric constant for the silver layer is taken from experimental tabulated data [6].

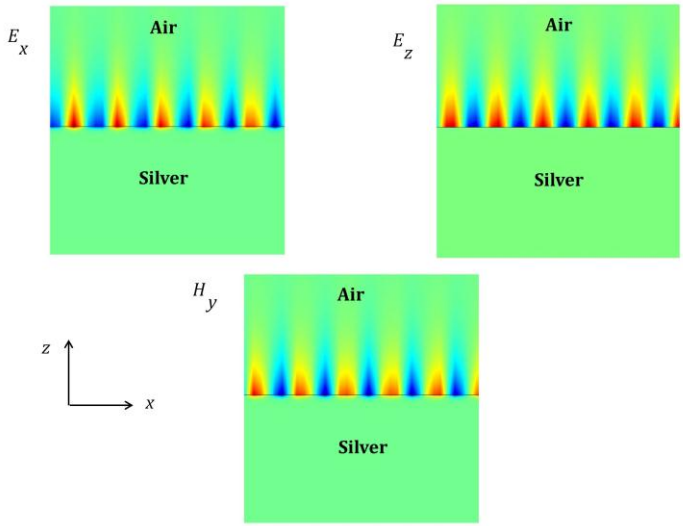

Figure 1.3 EM fields profiles (FEM simulations) for SPP at silver/air interface at $\lambda = 633\text{nm}$. Colors refers to charge sign distributions of the corresponding fields.

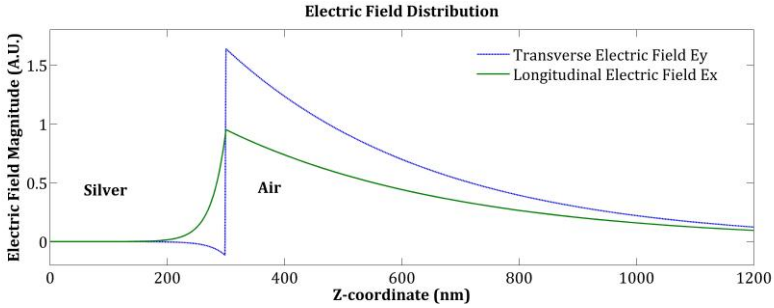

Figure 1.4 Spatial distribution of the two electric field components for an SPP at silver/air interface at $\lambda = 633\text{nm}$.

Figure 1.5 plots the norm of the electric field for a propagating SPP at silver/air interface at $\lambda = 633$ nm .We see that the norm of the SPP field decreases with increasing propagation distance. This means that SPP experience dissipation during the propagation, mainly in the form of Ohmic losses. The length L at which the field intensity decreases to $1/e$ is called *propagation length* and is given by:

$$L = \frac{1}{2\mathrm{Im}[k_x]} \tag{1.13}$$

Typical propagation length values for SPP at the interface between air and a noble metal (Au or Ag), at $\lambda = 633$ nm are 10.0 μm for gold and 38.0 μm for silver.

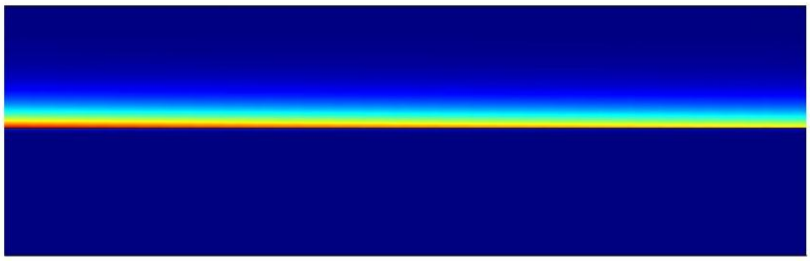

Figure 1.5 Electric Field norm for SPP propagating at silver/air interface. Losses due to Homic effects reduce the propagation length.

A better insight about the properties of the SPP dispersion relation can be obtained by assuming for the dielectric function of the metal the free electron expression, or also called Drude-Lorentz model:

$$\varepsilon(\omega) = 1 - \frac{\omega_p^2}{\omega^2} \tag{1.14}$$

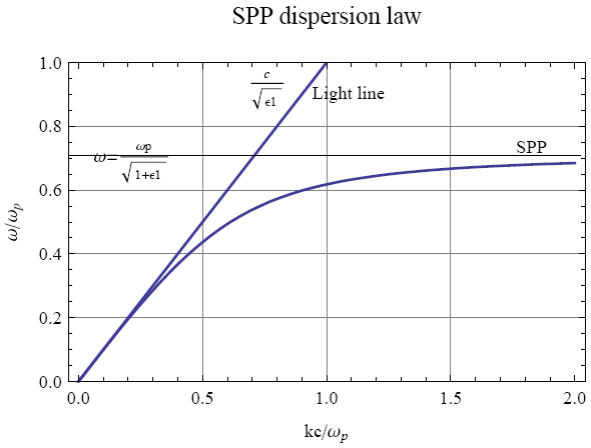

Figure 1.6 Dispersion relation for SPP compared to light dispersion law.

where ω_p is the frequency of bulk longitudinal electron excitations, the plasma frequency. Substituting this expression into SPP momentum relation (1.10), we obtain the SPP dispersion relation, showed in Figure 1.6. Since $\omega / c < k_x$ due to the fact that the EM field of the SPP must decay exponentially into the dielectric medium, the dispersion curve of a SPP lies always at the right of the light dispersion curve $\omega = ck_x$ and so SPP are non radiative waves that cannot be excited directly by incident light.

1.4 Excitation of Surface Plasmon Polaritons

Unlike volume plasmons, SPP can couple with electromagnetic waves, but a difficulty arise from the fact that the dispersion relation of SPP lies right from the light line. If we want a coupling between light

and SPP, the wave vector of incoming radiation must be increased by Δk_x, as shown in Figure 1.6. Once properly excited, an SPP propagates along the interface as far as it is dissipated by metal adsorptions. There are two main methods to achieve this coupling: ATR coupling and grating coupling.

1.4.1 Grating Coupling

Let's consider a wave incident at an angle θ from a dielectric medium on a 1D metal grating with grating constant (period) a. When a light wave with wave vector $\mathbf{k}$ is made incident on the surface of the grating, diffraction generates a series of diffracted waves, each with wave vector:

$$\mathbf{k}_m = \mathbf{k} + m\mathbf{G} \tag{1.15}$$

where m is an integer and denotes the diffraction order. $\mathbf{G}$ is the grating vector and is defined by the relation:

$$\mathbf{G} = \frac{2\pi}{a}\mathbf{x} \tag{1.16}$$

From (1.15) and (1.16) we get:

$$k_{xm} = k_x \pm m\frac{2\pi}{a} = \frac{\omega}{c}\sin\theta \pm m\frac{2\pi}{a} \tag{1.17}$$

We see than the missing momentum, necessary for the coupling of incoming light with SPP, can be provided by the grating vector $\mathbf{G}$ (see Figure 1.7). The coupling condition can be expressed as:

$$k_{sp} = k_{xm} = \frac{\omega}{c}\sin\theta_0 \pm m\frac{2\pi}{a} \tag{1.18}$$

The grating vector lies in the plane of the grating and is perpendicular to the grooves. Therefore the component of the wavevector of the diffracted light perpendicular to the plane of the grating k_z is equal to that of the incident wave, while the component of the wavevector in the plane of the grating k_x is diffraction altered.

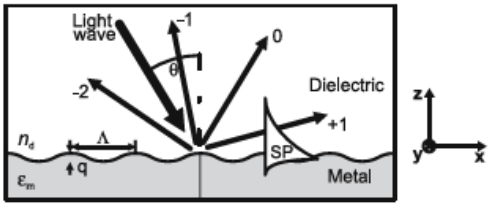

Figure 1.7 Coupling of light to SPP using a grating.

The SPP resonance condition can be observed as a minimum in the grating's reflection spectrum. The coupling condition (1.18) can be fulfilled for various combinations of the angle of incidence, grating pitch, and diffraction order. The characteristic absorption dip can be observed not only in the angular domain, but also when the angle of incidence is kept constant and the wavelength is varied (Figure 1.8). The interaction between the light wave and the surface plasmon results also in a change in the phase of the reflected light.

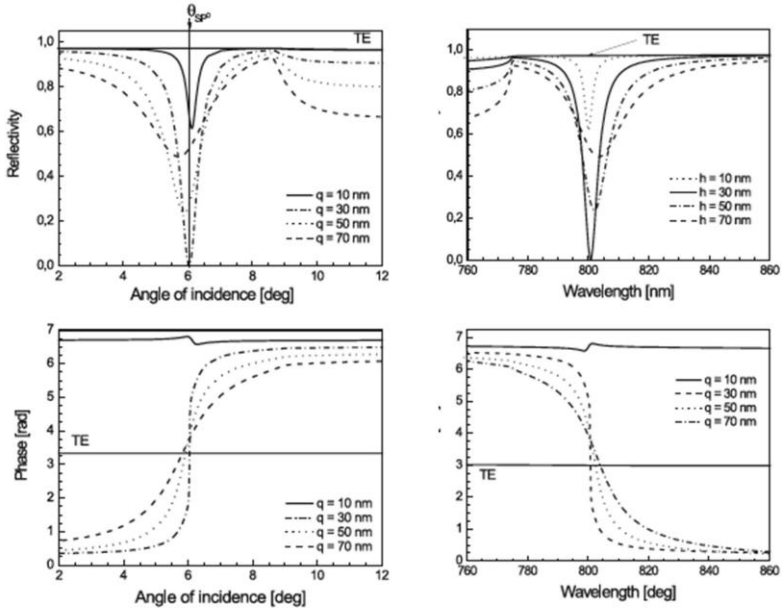

Figure 1.8 Reflectivity (upper plots) and phase (lower plots) as a function of the angle of incidence (left) and of the wavelength (right) for four different depths of a metallic sinusoidal grating and TM polarization. Reflectivity and phase of the TE polarization are shown for comparison (Data taken from [7]).

1.4.2 ATR Coupling

Another way to excite a SPP is by using a three-layer system consisting of a thin metal film sandwiched between two insulator of higher dielectric constant . For simplicity one of the insulator is taken to be air $(\varepsilon_0 = 1)$. The wave reflected at the interface between the dielectric with higher dielectric constant ε ε(usually a prism) and the metal will have a x-component of the wave vector $k_x = k\sqrt{\varepsilon}\sin\theta$, which is sufficient to excite SPPs a the metal/air interface. This is possible because the dispersion curve of the metal/air interface lies between the air and prism dispersion curves (see Figure 1.9).

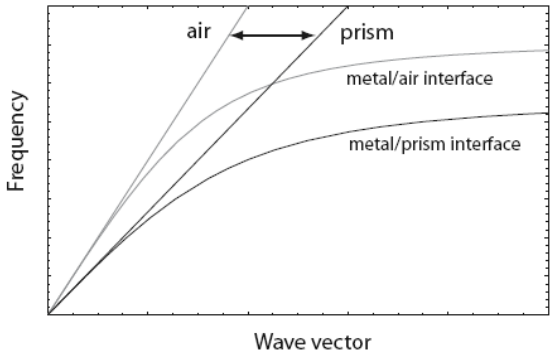

Figure 1.9 Prism coupling and SPP dispersion law.

Two different configurations are available: Otto's configuration [8] and Kretschmann-Raether's configuration [9], as showed in Figure 1.10. In the former a thin metal air gap is placed between the prism and the metal. Total internal reflection takes place at the prism/air interface and the evanescent field couples with the SPP at the air/metal interface. In the latter device a thin metal film is evaporated on top of glass prism. The beam coming from the glass side tunnel through the metal, with EM field decreasing exponentially, and excites the SPP on the metal/air interface.

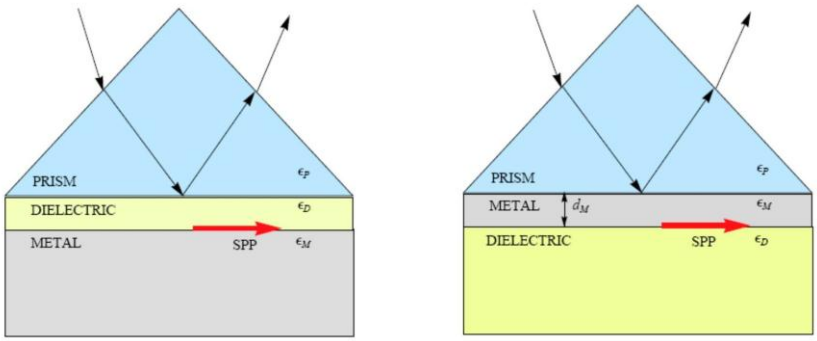

Figure 1.10 Left: Otto's configuration scheme. Right: Kretschmann-Raether's configuration's scheme.

SPP excitation manifests itself as a minimum in the reflected beam intensity from the metal (Figure 1.11). For each wavelength, the matching condition is satisfied for a single angle of incidence on the metal film, the coupling angle, which increases with decreasing wavelength.

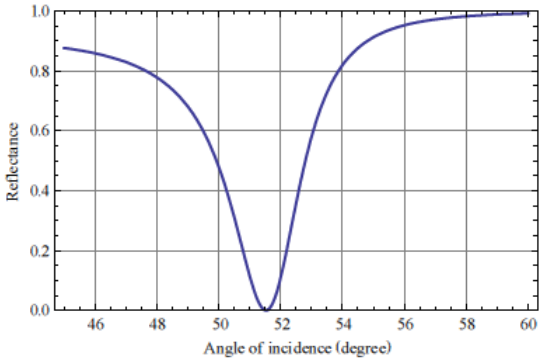

Figure 1.11 Example of reflectivity for TM polarization as a function of the angle of incidence.

1.5 SPP on Thin Metal Films

Besides the semi-infinite dielectric/metal interface, another basic geometry is able to sustain SPP modes. This geometry is a three-layer system where the two external layers can be considered semi-infinite in the transverse direction, while the middle layer has a finite thickness h (see Figure 1.12) [10]. Depending on the choice of the materials, two main cases can be analyzed:

- Insulator/metal/insulator heterostructure (IMI) where a thin metallic layer is placed between two semi-infinite dielectric layers
- Metal/insulator/metal heterostructure (MIM) where a thin dielectric layer is placed between two semi-infinite dielectric layers.

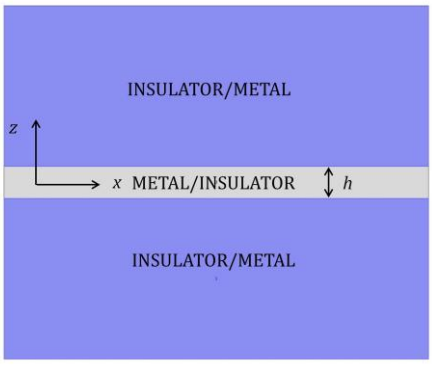

Figure 1.12 Multilayer geometry for IMI or MIM dielectric environment.

In both these systems, due to the presence of an additional layer, the dispersion relation of SPP will change respect to the two-layer case. In fact in such systems, each single interface can sustain bound SPP modes. However when the thickness of the middle layer became comparable or smaller than the decay length of the single mode, the SPPs at the two separate interfaces can interact with each other, giving rise

to different couple modes, called film plasmons or gap plasmons for IMI and MIM geometries respectively [11, 12].

The method for obtain the SPP dispersion relation in a multi-layer system is basically the same as the one used for the single interface case. The details of the calculation can be found in the appendix. Here it will be considered the simplest case, where sub- and super-strates have the same dielectric constants (symmetric environment).

1.5.1 SPP on MIM Structure

By expressing the components of the EM field for TM polarization on each medium and by applying the correct boundary conditions at the two different interfaces, the SPP dispersion relation is formed by a set of two equations [13, 14]:

$$\tanh\frac{k_d h}{2} = -\frac{k_m \varepsilon_d}{k_d \varepsilon_m}$$
$$\tanh\frac{k_d h}{2} = -\frac{k_d \varepsilon_m}{k_m \varepsilon_d} \qquad (1.19)$$

Where $k_{d,m}$ is the z-component of the SPP field in the dielectric or metal layer and $\varepsilon_{d,m}$ is the dielectric constant of the dielectric and metal layer respectively. As it can be seen, the first equation (1.19) describes a mode of even vector parity for the magnetic field component H_y. For this reason this mode is called symmetric SPP mode, since it is symmetric in H_y respect to the middle plane of the gap and consequently it is anti-symmetric for the electric field E_x component. Similarly, the second equation (1.19) describes a mode of odd vector parity for the magnetic field component H_y and this mode is called anti-symmetric SPP mode, since it is anti-symmetric in H_y respect to the middle plane of the gap and consequently it is anti-symmetric for the electric field E_x component. The field profiles for the H_y component for both symmetric and anti-symmetric cases are shown in Figure 1.13 for a silver/air/silver multilayer with $h = 500$ nm at $\lambda = 633$ nm. As it can be seen, the EM field is strongly confined in the dielectric, due to the fact that the penetration depth is very small, especially at visible frequency. The symmetry of the field respect to the middle of the insulator gap is clearly visible for the two different situations.

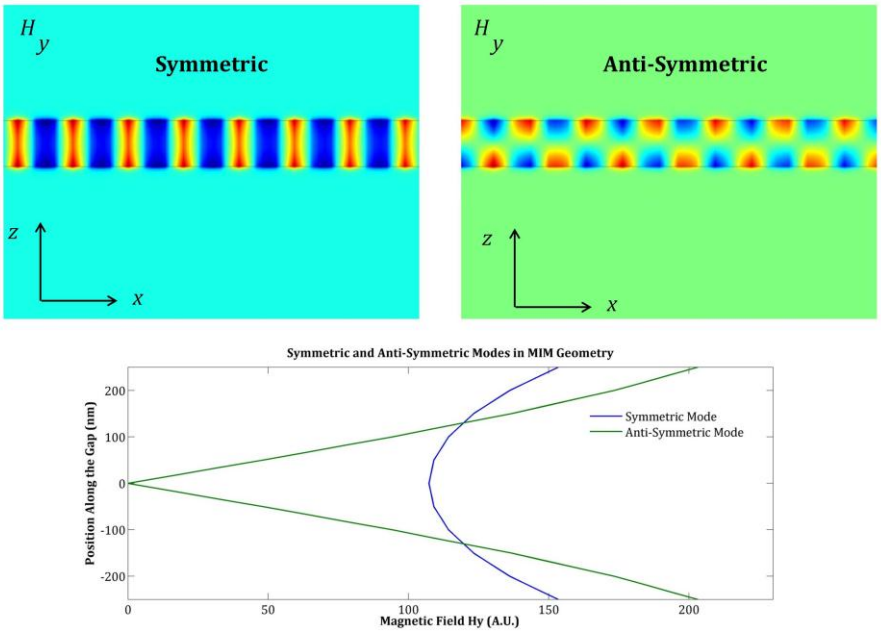

Figure 1.13 Up: field profiles for the magnetic field for symmetric and anti-symmetric configuration on MIM configuration. Down: Symmetric of the y-component of the magnetic field inside the insulator gap. The gap thickness is 500 nm and the 0 position corresponds to the middle plane of the gap.

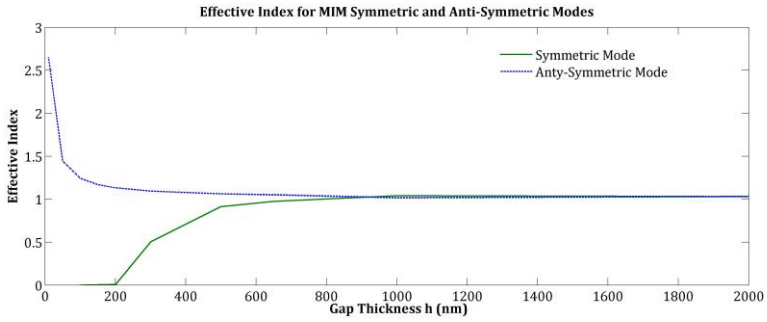

Figure 1.14 Effective plasmonic index for symmetric and anti-symmetric modes on MIM geometry at wavelength of 633 nm for a silver/air/silver multilayer.

If the thickness of the dielectric layer is reduced, the symmetric and anti-symmetric modes behave differently. As the dielectric thickness is reduced, the real part of the wavevector of the anti-symmetric mode also decreases, until there is a critical thickness value where the mode is cut-off and the propagation is stopped (Figure 1.14 plots the real part of the effective index $n_{eff} = k_{xSPP} / k_0$ as function of gap thickness h). The symmetric mode instead experiences the opposite behavior: the wavevector increases with decreasing dielectric thickness, with no sign of cut-off. This is very important for nanofocusing, since as it will be demonstrated in the following chapters, the divergence of the SPP wavevector is a necessary condition in order to effectively condensate SPP in nano-regions. It is worth noting that from Figure 1.14

we see that for gap insulator thickness greater than ~ 1000 nm the symmetric and anti-symmetric modes became degenerate, resembling the SPP mode on single metal/dielectric interface.

1.5.2 SPP on IMI Structure

Also for the IMI structure, the dispersion relation can be split in two equations, one for the symmetric and one for the anti-symmetric SPP mode. Following an identical approach as for the MIM case, the two equations are [13, 14]:

$$\begin{aligned} \tanh\frac{k_m h}{2} &= -\frac{k_d \varepsilon_m}{k_m \varepsilon_d} \\ \tanh\frac{k_m h}{2} &= -\frac{k_m \varepsilon_d}{k_d \varepsilon_m} \end{aligned} \tag{1.20}$$

The first equation describes a SPP mode with symmetric magnetic field distribution across the film, while the second equations describes an anti-symmetric mode. The EM field profiles for the two modes along with the corresponding magnetic field H_y spatial distribution along the metal gap are plotted in Figure 1.15, for an air/silver/air multilayer with $h = 80$ nm at $\lambda = 633$ nm. As it can be seen from Figure 1.16 which plots the real part of the effective index $n_{eff} = k_{xSPP} / k_0$ as function of gap thickness h, this time is the anti-symmetric mode that experiences no cut-off with reducing metal film thickness. This means that for this mode the field localization increase with decreasing film thickness (along with increasing dissipation), so that is this mode that is suitable for nanofocusing. For the symmetric mode instead we see from the field distribution that most of the field is localized in the dielectric medium and so the real and imaginary part of the wavevector decrease with decreasing film thickness. This means that the losses are reduced and so propagation length increase with smaller metal film thickness. This mode is therefore called long range mode [2], and due to the afore mentioned property it very used in plasmonic waveguides. However contrary to the anti-symmetric mode, the long range SPP mode experience a cut-off (Figure 1.16) and for very small metal film thickness the effective modal index approaches the vacuum value, thus the symmetric mode couples with the surrounding environment losing its guided propagation and becoming a radiative mode. This limits the possibility of miniaturization. The trade-off between confinement, propagation length and losses is a crucial topic and must be always kept in mind when designing plasmonic devices [2]. Last, we note that for metal gap thickness greater than ~ 100 nm the two fundamental modes became degenerates, since the metal gap is seen as a semi-infinite optically thick substrate, and the two modes evolve to a single SPP mode on air/silver interface.

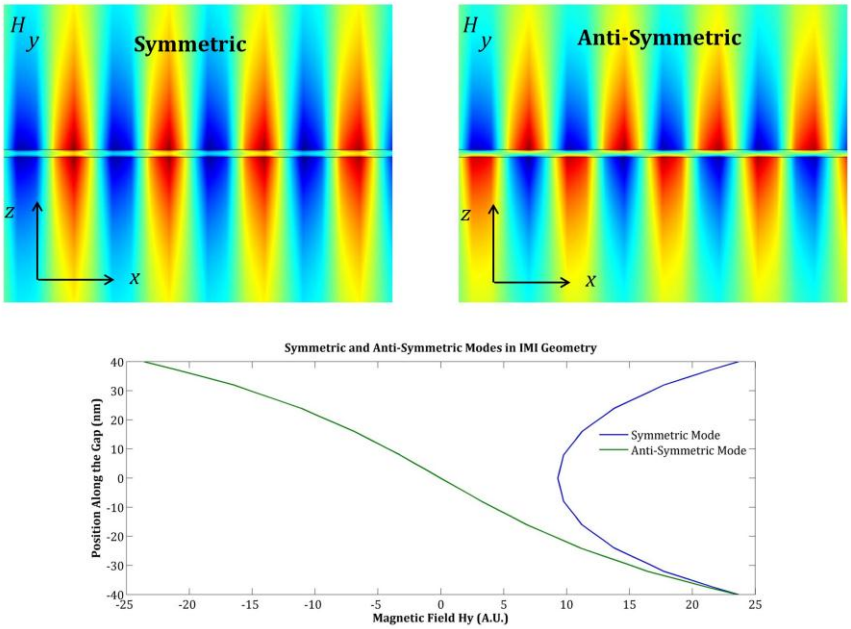

Figure 1.15 Up: field profiles for the magnetic field for symmetric and anti-symmetric configuration on IMI configuration. Down: Symmetric of the y-component of the magnetic field inside the metal gap. The gap thickness is 80 nm and the 0 position corresponds to the middle plane of the gap.

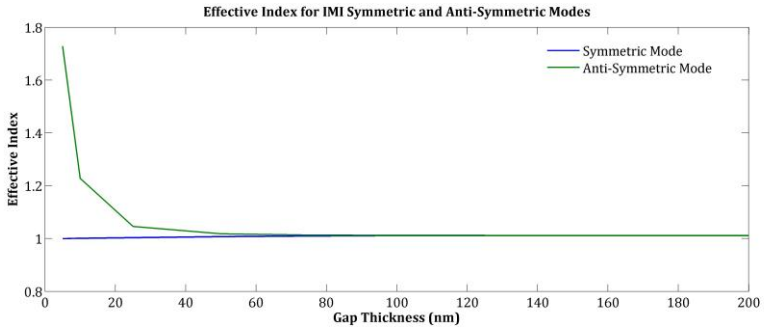

Figure 1.16 Effective plasmonic index for symmetric and anti-symmetric modes on IMI geometry at wavelength of 633 nm for a silver/air/silver multilayer.

1.6 SPP and Diffraction Limit

In the very first section of this chapter we have suggested the idea that by using 2D waves it would be possible to overcome the classical diffraction limit. SPP are 2D confined waves and, as we have seen, some particular geometries, like for instance MIM or IMI waveguides are actually able to give great SPP wavevector values under particular conditions (see Figure 1.14 and Figure 1.16). The SPP dispersion relation (1.10) can be written as

$$k_{SPP} = nk_0 \frac{1}{\sqrt{1 - \frac{|\varepsilon_D|}{|\varepsilon_M|}}} \tag{1.21}$$

Hence k_{SPP} can be made greater than the 3D optical wavevector and can be further increased by changing the materials dielectric constants. The diffraction limit can be indeed overcome by using SPP because from equation (1.21) $k_{SPP} > nk_0$. The minimum beam size of 2D optical waves is given by:

$$\Delta r_{\min 2D} = \frac{\lambda_{SPP}}{4} = \frac{\lambda_0}{4n}\sqrt{\frac{\varepsilon_D + \varepsilon_{ND}}{\varepsilon_{ND}}} \tag{1.22}$$

From equation (1.4) we immediately see that $\Delta r_{\min 2D} < \Delta r_{\min 3D}$. The minimum beam size for a 2D SPP wave is smaller than the corresponding one for a 3D wave, but however is still limited by diffraction. $\Delta r_{\min 2D}$ can be made even smaller by changing the dielectric constant of the metal surface which sustains the SPP propagation; however it is a very difficult task due to the high sensitivity of SPP to surface conditions. As we will see in the following chapters a mode of increasing the SPP wavevector do exists: by carefully choosing a suitable SPP geometry, it is possible to concentrate light in high subwavelength regions, up to few nanometers. Plasmonic gratings, 3D and 2D taper metal waveguides are the structure that will be analyzed in order to find the optimal configuration for SPP concentration beyond the diffraction limit.

1.7 Plasmonic Vortexes

The local excitation of SPP is crucial for all experiments involving plasmonic structures. As we have seen in the previous sections, several methods can be employed for this purpose, like ATR coupling, or plasmonic gratings formed by nano-slits or nano-holes. All of these methods excites SPP as TM-polarized waves, with the wavefront being the one possessed by a plane wave. It has been recently showed [15] that a novel kind of plasmonic structure, named Plasmonic Vortex Lens (PVL) is able to excite Plasmonic Vortexes (PV), i.e. SPP waves carrying Orbital Angular Momentum (OAM) [16]. A full description of OAM properties and their applications to plasmonic structure is beyond the scope of this thesis, but in this section we will give an overview on the basic properties on PV generated by PVL, since PV will be then used as input illumination for the focusing devices proposed in chapter 4 and 5.

Optical Vortex (OV) [17] is a term which refers to topological defects due to phase singularities in light beams, related to the helicoidal shape of the wavefront. When a vortex is presented in a plasmonic wave, we refer to it as Plasmonic Vortex (PV) [16]. The most general solution for the scalar wave equation which describes the OV's propagation is given in cylindrical coordinates by:

$$E(r,\varphi,z,t) \propto r^{\pm|l|} \exp\left[i(kz-\omega+l\varphi)\right] \tag{1.23}$$

Where φ is the azimuthal angle and l is an integer number called topological charge, defined by the path integral:

$$l = \frac{1}{2\pi}\oint \nabla\Phi \cdot d\mathbf{r} \tag{1.24}$$

Taken along a closed circuit **r** around the vortex. It indicates the number of 2π phase changes along any closed circuit around the vortex center, $\nabla\Phi$ being the phase gradient. When $l \neq 0$ the wavefront of the OV is helicoidal: $l\varphi - kz = const$. When $l = 0$ instead we have a plane wave surface. Examples of wavefronts for different l values are shown in Figure 1.17.

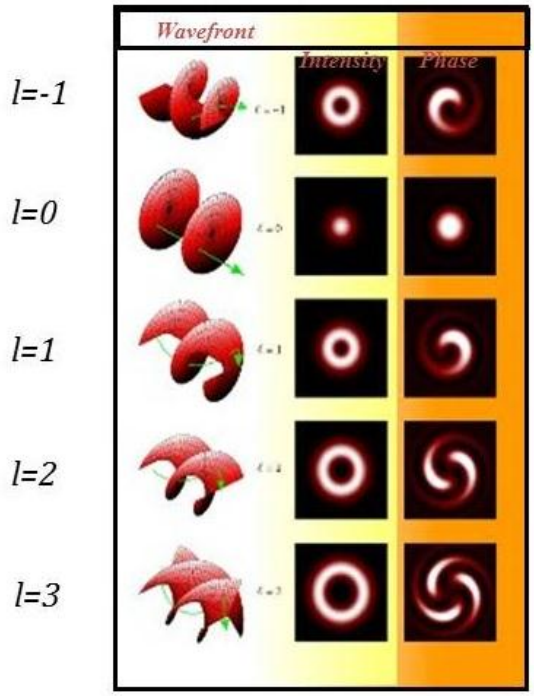

Figure 1.17 Phase wavefront for OV beams for different topological charge l-values. The phase wavefront has a helical shape composed by l lobes disposed around the propagation axis.

OV is intrinsically related to the OAM of light, which can be viewed as a "new electromagnetic degree of freedom". In fact it has been showed that light beams with phase singularities, like OV, can indeed carry orbital angular momentum [18]. This is a property of the EM field, related to the helicoidal shape of the wavefront. That electromagnetic fields can carry not only energy and linear momentum but also angular

momentum has been known for a century. However only recently a full treatment in terms of OAM eigenstates has been developed [19].

The total angular momentum density for an EM wave can be expressed as:

$$\mathbf{J} = \int \mathbf{J} d^3 r = \mathbf{L} + \mathbf{S} \tag{1.25}$$

L is the orbital angular momentum of the photons related to beam vorticity and phase singularities, and **S** is the spin angular momentum, associated to the two states of wave polarization (like left or right circularly polarized light, or the two fundamental TE and TM states of linear polarization). It can be shown that light beams with phase singularities (like OV) can carry OAM. The amplitude of this EM field is usually described in terms of superposition of Laguerre-Gauss (LG) modes, which are a particular set of cylindrically symmetric laser cavity modes. LG modes are characterized by two indices: l which correspond to the topological charge and represents also the number of twists of the helical wavefront within a wavelength, and p the number of radial nodes present in the LG mode (see Figure 1.18).

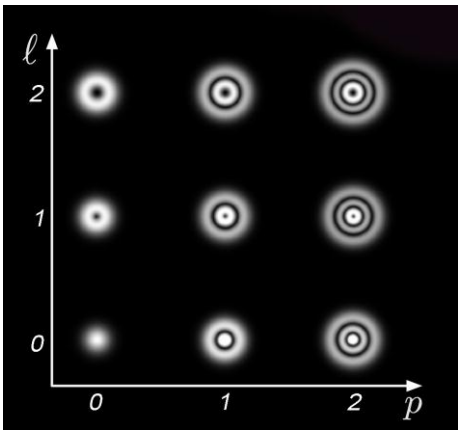

Figure 1.18 Various intensity distributions of LG modes. For each increment of p, an additional concentric ring is added to the mode profile while an increment of l results in an increase in the diameter of the dark core located on the beam axis.

In cylindrical coordinates, in the pane orthogonal to the beam propagation z, the EM field is given by

$$u_{pl}(r,\varphi,z) = \sqrt{\frac{2p!}{\pi(p+|l|)!}} \frac{1}{w} \left(\frac{r\sqrt{2}}{w} \right)^{|l|} L_p^{|l|} \left(\frac{2r^2}{w^2} \right) \times$$
$$\times \exp\left(\frac{-r^2}{w^2} \right) \exp\left(\frac{-ikr^2}{2R} \right) \exp\left[-i(2p+|l|+1)\psi \right] e^{-il\varphi} \tag{1.26}$$

Where w is the beam width, R is the curvature radius, $\varphi(z)=\arctan(z/z_0)$ is the Gouy phase and L_p^L is the generalized Laguerre polynomial. As we can see from equation (1.26) the phase varies linearly with the azimuthal angle φ, as expressed by the term $\exp(-il\varphi)$.

Several method can be used to produce OV in light beams. For example, a computer-generated hologram formed by a diffraction grating with a fork dislocation is able to produce OV [21] (see Figure 1.19). Also a helicoidal transmission optical device that imposes an azimuthally dependent phase retard on an incident optical wavefront (spiral phase plate) is able to imprint OAM to an incident beam [22] (see Figure 1.20).

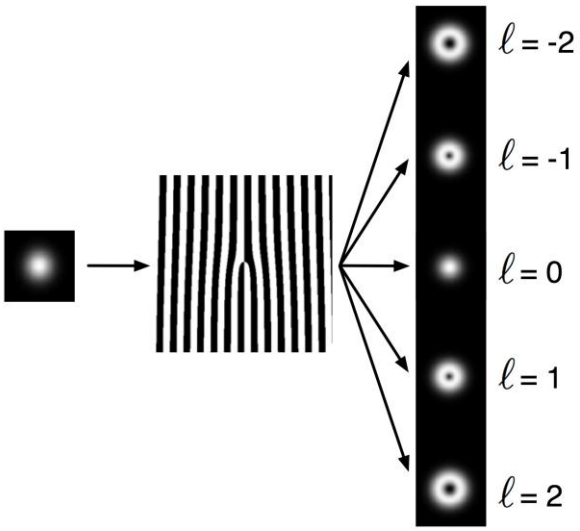

Figure 1.19 A fork hologram crossed by a light beam ideally produces an infinite number of diffraction orders.

However, in order to have a plasmonic vortex, we need a structure that is able to excite plasmons beams and imprint a topological charge on the beam at the same time. Plasmonic Vortices, can be generated by using convenient metallic subwavelength structures illuminated by circularly polarized light [23-26]. The spin angular momentum carried by incident circularly polarized light beam, thanks to the plasmonic structures, is converted into OAM, leading to the generation of helical modes via the coupling with surface plasmons [15, 27]. The plasmonic structures for instance include concentric circular grooves [28], and subwavelength apertures [29, 30]. Here we will focus on a Plasmonic Vortex Lenses [15] consisting of Archimedes's spiral shaped grooves (Figure 1.21) milled in a metal film (gold or silver) in air.

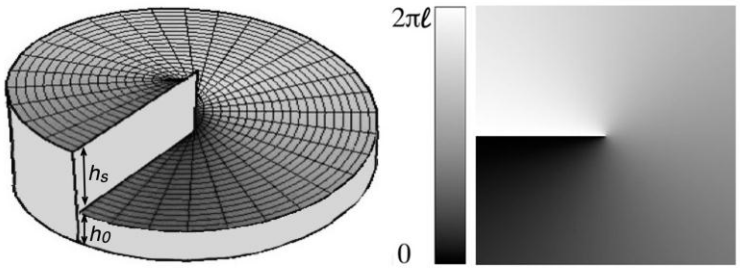

Figure 1.20 Spiral Phase Plate and corresponding phase distribution that imprints onto the transverse plane of an incident beam.

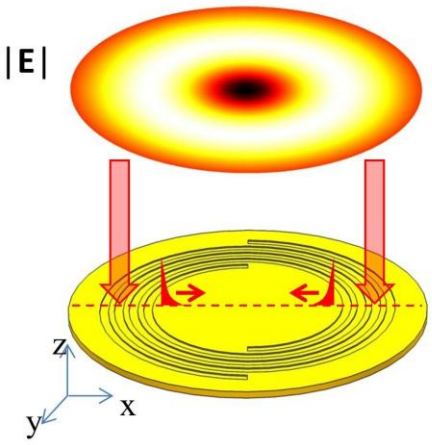

Figure 1.21 PVL formed by Archimedes's spiral shaped grooves milled in a metal film in air. The PVL is illuminated normally by a Gaussian Beam which couples with the PVL itself, generating PV which are focalized in the center of the PVL.

Their geometry is defined by the relation:

$$r_m(\varphi) = r_0 + m\lambda_{SPP}\varphi \tag{1.27}$$

Where φ is the azimuthal angle, λ_{SPP} the SPP wavelength at metal/air interface, m an integer number and r_0 the distance from the center of the PVL to the nearest point of the groove. The complete PVL consists of m spirals, each one rotated of $360/m$ degrees one to each other. For $m=0$ we obtain the bull's eye structure, formed of concentric ring grooves with radial period of λ_{SPP} .The PVL described in equation

(1.27) is able to couple impinging circularly polarized light into PV described by a Bessel surface waves [23], whose longitudinal component is given by

$$E_{z,l_{PV}}(r,\varphi) \propto J_{l_{PV}}(k_{SPP} r)\exp(il_{PV}\varphi) \tag{1.28}$$

Where $k_{SPP} = 2\pi / \lambda_{SPP}$. l_{PV} is the topological charge of the PV, and $J_{l_{PV}}$ is the l-th order Bessel function. As source of illumination we can consider a Laguerre-Gauss beam which impinges normally onto the PVL (see Figure 1.21). As we have seen, the LG beam carries a OV with total angular momentum given by (1.25). The OAM of the PV, resulting from the interaction of the LG beam and the PVL is given then by the following selection rule [15]:

$$l_{PV} = m + l_i + s_i \tag{1.29}$$

Where l_i is the OAM of the LG beam and $s_i = \pm 1$ is the spin of the incident circular polarized beam.

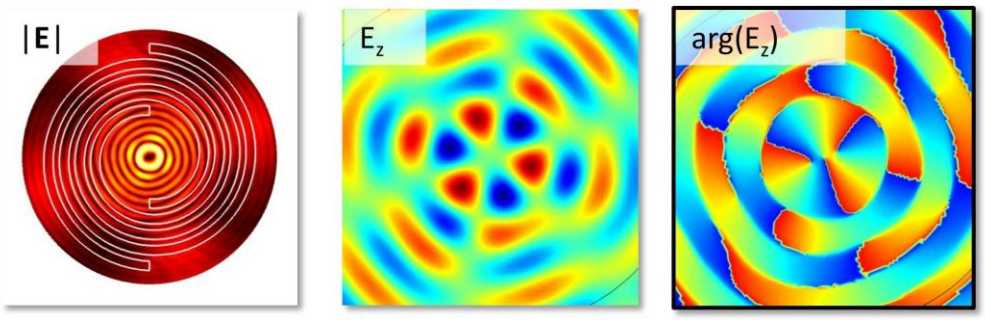

Figure 1.22 Electric field norm, transverse component and corresponding phase distribution for a PV generated by a gold m=2 PVL. The incident beam is a LG circular polarized beam with s=-1 and topological charge l=2. The resulting PV possess a topological charge of l_{PV}=3.

Figure 1.22 shows an example of PV generated by the PVL for $l_{PV} = 3$. The incident wavelength of the LG beam is set to $\lambda = 633\, nm$. We see that in a region sufficiently small around the center of the PVL, the electric field possess a well-defined phase structure, with the phase that possesses a periodic azimuthally spatial dependence in the form of $\exp(il_{PV}\varphi)$. These results suggest the use of PVL as excitation source in order to focalize PV in the center of the PVL itself. If plasmonic structures are placed in the center of PVL, the related plasmonic effect (like nano-focusing for instance) acquires another degree of freedom given by the topological charge l_{PV} of the plasmonic vortex.

1.8 References

[1] H. Raether, Surface Plasmons (Springer-Verlag, Berlin, 1988).

[2] Maier S. A., "*Plasmonics: Fundamentals and Applications*", Springer (2007).

[3] Wood R. W., *Philosophical Magazine* **4**, 396 (1902).

[4] Fano U., *J Opt Soc Am* **31**, 231 (1941).

[5] Jackson J. D. Classical Electrodynamics Third Edition *John Wiley & Sons*.

[6] Palik E. D. Handbook Of Optical Constants Of Solids (1997).

[7] Homola J. (Ed.), "*Surface Plasmon Resonance Based Sensors*", Springer (2006).

[8] Otto A., *Zeits Phys* **216**, 398 (1968).

[9] Kretschmann E., Raether H., *Z Naturforsch* **A 23**, 2135 (1968).

[10] Prade B., Vient J.Y., Mysyrowicz A., Phys. Rev. B, **44**(24), 13556 (1991).

[11] Gramotnev D, Journal of Applied Physiscs, **98** 104302 (2005).

[12] Gramotnev D, Vernon K., Appl. Phys. B, **86**(1), 7 (2007).

[13] Economou E. N., Phys. Rev., **182**(2), 539 (1969).

[14] Dionne J.A., Phys. Rev. B, **73**(035407), 2006.

[15] P. Zilio, E. Mari, G. Parisi, F. Tamburini, and F. Romanato,, Opt. Lett.37(15), 3234-3236 (2012).

[16] L. Allen, M. W. Beijersbergen, R. J. Spreew, and J. P. Woerdman, Phys. Rev. A 45, 8185 (1992).

[17] P. Coullet, L. Gil, and F. Rocca, Optics Communications, vol. 73, no. 5, pp. 403–408, 1989.

[18] L. Allen, Physical Review A, vol. 45, no. 11, pp. 8185–8189, 1992.

[19] M. W. Beijersbergen, R. P. C. Coerwinkel, M. Kristensen, and J. P. Woerdman, Optics Communications, vol. 112, pp. 321–327, Dec 1994.

[20] A. Mair, A. Vaziri, G. Weihs, and A. Zeilinger, "Entanglement of the orbital angular momentum states of photons," vol. 412, pp. 313–316, 2001.

[21] J. Arlt, K. Dholakia, L. Allen, and M. J. Padgett, Journal of Modern Optics, vol. 45,pp. 1231–1237, June 1998.

[22] S. S. R. Oemrawsingh, J. A. W. van Houwelingen, E. R. Eliel, J. P. Woerdman, E. J. K. Verstegen, J. G. Kloosterboer, and G. W. 't Hooft, Applied Optics, vol. 43, no. 3, pp. 688–694, 2004.

[23] Y. Gorodetski, A. Niv, V. Kleiner, and E. Hasman, Phys. Rev. Lett. 101(4), 043903 (2008).

[24] K. Y. Bliokh, Y. Gorodetski, V. Kleiner, and E. Hasman, Phys. Rev. Lett. 101(3), 030404 (2008).

[25] Y. Gorodetski, N. Shitrit, I. Bretner, V. Kleiner, and E. Hasman, Nano Lett. 9(8), 3016–3019 (2009).

[26] H. Kim, J. Park, S.-W. Cho, S.-Y. Lee, M. Kang, and B. Lee, Nano Lett. 10(2), 529–536 (2010).

[27] L. Marrucci, C. Manzo, and D. Paparo, Phys. Rev. Lett. 96, 163905 (2006).

[28] K. Y. Bliokh, Y. Gorodetski, V. Kleiner, and E. Hasman, Phys. Rev. Lett. 101(3), 030404 (2008).

[29] N. Shitrit, S. Nechayev, V. Kleiner, and H. Hasman, Nanolett. 12, 1620 (2012).

[30] S. Yang, W. Chen, R. L. Nelson, and Q. Zhan, Opt. Lett. 34(20), 3047–3049 (2009).

2 Numerical and Experimental Methods

2.1 Introduction

With the advent of modern nanofabrication techniques a wide range of instrumentation and methods is now available for the realization of complex nano-structures for plasmonic applications. In this chapter several techniques for the nanofabrication of metallic plasmonic structures are presented: electron beam lithography, focused ion beam lithography, electrodeposition and thermal evaporation. All these techniques, with particular attention to electron beam lithographic process, have been approached and exploited during this thesis work for the fabrication of the different plasmonic structures that are described in the following chapters. After the fabrication processes, the characterization of the final samples is performed; this step is crucial for the experimental validation of the quality, performance and response of the plasmonic device. However, in order to find the best parameters that optimize the optical response of a plasmonic device, a preliminary optimization process must be performed. This study, conducted usually by means of numerical simulations with finite element method, has the main task to provide the optimal geometrical parameters for the nanofabrication process and also to help to understand the physical mechanisms that are at the base of the plasmonic device's working principle. It appears then clear that the realization of a plasmonic device should consider and overcome each step of this chain of processes: simulation – fabrication – characterization.

2.2 Electron Beam Lithography

Ones of the most widely exploited nanofabrication techniques are represented by lithography processes. The name "lithography" is due to their working mechanism; indeed the main step in a lithographic process is the replication of a pattern on a sample. According to the employed technique, it is possible to distinguish among electron beam lithography (EBL), X-ray lithography (XRL), focused ion beam lithography (FIB) and optical lithography. As suggested by the names of the lithographic processes, their main difference is the pattern transfer action, respectively achieved by means of an electron beam, X-ray radiation, ion beam and ultra-violet radiation (UV). Lithographic processes can also be divided in serial and parallel writing techniques (Figure 2.1). In the former the pattern is prepared with a computer aided design (CAD) software and exposed directly on the resist; in the latter the pattern is on a mask that shadows the incoming radiation and is replicated in one single shot on the resist. EBL and ion beam lithography are serial writing techniques in which the beam is focused on the sample, and deflected according to the CAD pattern; this means that the structures are exposed sequentially, one by one. XRL

and optical lithography are instead parallel techniques in which the mask pattern is replicated with a single shot exposure. Parallel process is faster than the serial one and it allows to replicate a lot of times the same pattern by a mask usually fabricated by means of a serial writing lithography; in this case the mask pattern can not be modified. On the contrary, serial writing technique is more time consuming, but allows to change easily the pattern by means of a CAD software.

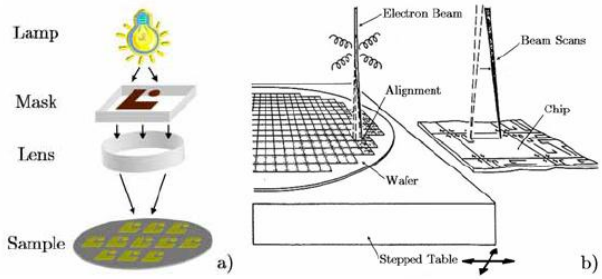

Figure 2.1 Parallel (a) and serial (b) writing techniques.

The electron beam lithography (EBL) is a serial writing technique, as mentioned above, and the pattern is directly exposed on the resist without any mask; as suggested by its name, an electron beam performs the exposure process. As no mask is required, EBL technique is very flexible and it allows to modify or completely change the desired pattern, according to new requests or restrictions that arise during an experimental work. For this reason it is a suitable technique when implementing new devices or facing exploratory works; furthermore it is the usual technique for fabrication of X-ray masks. On the other hand, EBL is a time-expensive process compared to parallel writing techniques, and it is not a convenient choice when a large production of well-established patterns is required. Electron beam lithography appeared in early 1960s evolving from scanning electron microscope (SEM) [1]. The SEM could evolve to e-beam lithography only because of the discovery of an electron-sensitive polymer material, called polymethylmethacrylate (PMMA). Exposure of PMMA resist by e-beam is very much like exposure of photoresists by photons. During EBL exposure, the interaction between electrons and an electron-sensitive material called resist causes the resist to be exposed, and later removed in the development (we consider to the case of a positive tone resist). The mechanism that allows the exposure of a positive resist is the breaking of the polymeric chains due to electron collisions; consequently the average molecular weight of the resist is reduced in the exposed areas, thus increasing their solubility. The result of an exposure is a pattern drawn in terms of solubility in order to produce a contrast as large as possible, where the contrast is the ratio of the exposed areas dissolution rate to the dissolution rate in unexposed areas. Because of the fine beam enabled by electron optics, e-beam lithography using PMMA resist immediately demonstrated much higher resolution capability than optical lithography could dream of

around the time. Nowadays, the state-of the-art e-beam lithography system, combined with special e-beam resist materials and processes, can fabricate structures less than 10 nm [2].

In the following sections it is presented a brief review of the basic concepts regarding a general EBL process, starting from electron-matter interaction and up to a description of the proximity effect. Finally an example of a complete fabrication process of a 1D plasmonic metallic grating by means of EBL is shown.

2.2.1 Interaction between Electrons and Matter

The physics of the electron-beam exposure process is dictated by the nature of electron-solid interactions, both in the resist and in the underlying substrate materials. The main parameters influencing these interactions are those of the beam (primarily the beam energy) and those of the materials (the resist and substrate types and the resist thickness). The electrons in the beam interact with the resist-coated substrate through elastic and inelastic scattering by the resist and substrate atoms. This results in the deposition of energy in the resist and substrate, and in the spreading of the electrons from the point of incidence. The inelastic scattering events are the causes of electron energy deposition in the resist and substrate and determine the absorbed energy distribution. It is this absorbed energy distribution in the resist that determines the developed resist pattern. The electrons generated when an electron beam with energy of several kilo-electronvolts bombards a substrate can be divided into two categories (Figure 2.2):

- The secondary electrons are those ejected from the substrate material itself. They are of low energy, and their energy distribution has a peak at energy of a few electron volts. Due to their low energy, they are readily absorbed by the resist, contributing significantly to the exposure. Fortunately, the low energy also limits their effective range in the resist to a few nanometers, thus limiting the secondary electron contribution to beam broadening to approximately 10 nm [3]. By convention, it is assumed that electrons with energies below 50 eV are secondary.

- The backscattered electrons are primaries that have been reflected from the substrate. For a substrate of silicon (atomic number Z=14), their mean energy is approximately 60% of that of the primary beam [4].

The scattering events are classified as forward scattering and backscattering. Forward scattering is characterized by primarily small-angle scattering, less than 90° from the primary beam direction. The main impact of forward scattering on the lithography process is broadening of the incident beam as it passes from the resist surface to the substrate. Since the scattering angles are characteristically small, the forward-scattered electrons that reach the substrate do not have further statistically significant

interactions with the resist. The beam broadening effects introduced by forward scattering are reduced as resist thickness decreases or accelerating voltage increases.

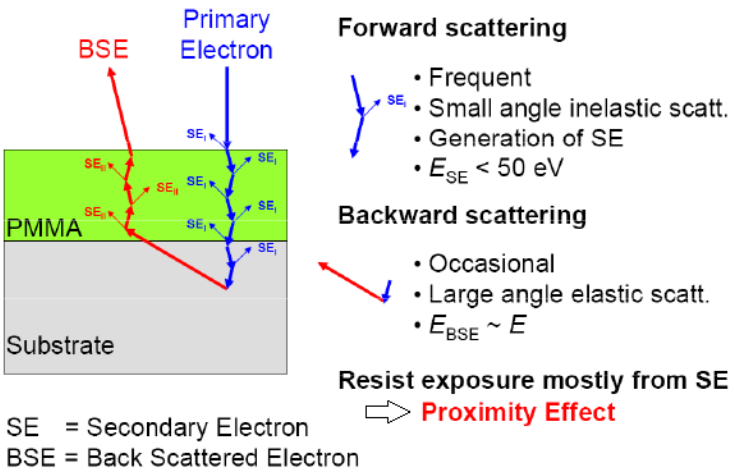

Figure 2.2 Electron scattering events.

Backscattering is characterized by large-angle scattering, to nearly 180° from the primary beam direction. Unlike forward scattering, these large scattering angles make it possible for electrons reaching the substrate to return to the resist. Backscattered electrons may also originate from the resist layer without ever reaching the substrate. This contribution is usually much smaller than that from the substrate, since the magnitude of this scattering is strongly dependent on the atomic number of the material, and typically the ratio of resist to substrate atomic numbers is small. The practical implications are that subsequent scattering events from substrate backscattered electrons can deposit energy in the resist away from the primary beam (i.e., away from the pattern), leading to pattern distortions (the so-called proximity effect). The proximity effect is the major obstacle in the process of achieving high-resolution nanofabrication by charged beams.

The electron collisions can be modeled by Monte Carlo simulations [5,6]. Monte Carlo method makes use of mathematic descriptions of elastic and inelastic scattering cross-sections and electron energy loss in a solid material to calculate how a primary electron from an e-beam is scattered inside a solid material and how it loses its energy. Although each individual electron scattering event is random, simulation of a large number of electron scatterings will generate the general picture of the extent of energy deposition due to the collision and loss of energy from the primary electrons. Figure 2.3 plots out 100 electron trajectories. The electron energy is 20 keV with 1-μm resist layer on top of a silicon substrate. This plot gives a rough idea how deep and how wide the electrons travel inside resist and substrate. Most of electrons scatter forward into substrate but some electrons scatter back into resist layer. These forward scatterings and backward scatterings are the cause of broadening of exposure area in resist. To generate

statistically correct and reliable results, the number of electrons to be simulated has to be between 50,000 to 100,000.

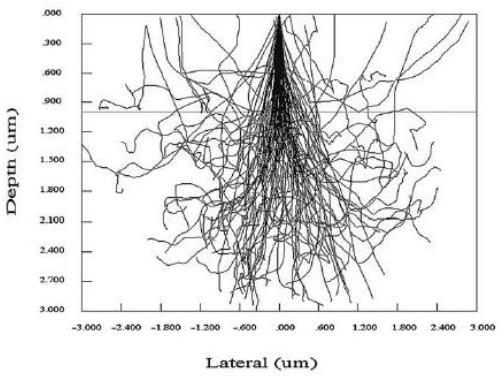

Figure 2.3 Hundred electron trajectories showing the extent of electron scattering.

Instead of counting scattering electrons, forward and backward scattering can also be expressed by a *point spread function* (PSF) which represents deposited energy distribution in resist from single point of incidence. The typical PSF is shown in Figure 2.4, where forward scattering part and backscattering part of energy spread are indicated. The figure also compares the PSFs at 10% and 90% depth of resist. It clearly displays a significant increase of broadening in deposited energy by forward scattering, as well as accumulated energy by backscattering, as electrons going deeper.

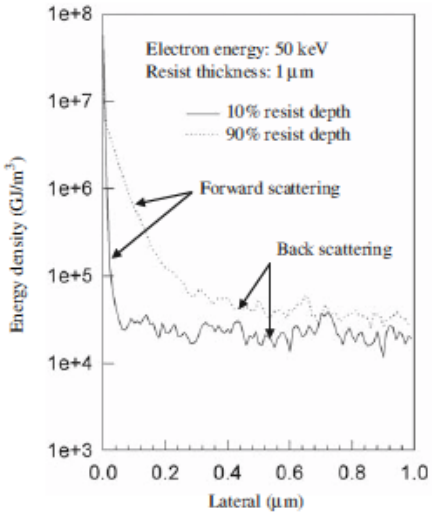

Figure 2.4 Point spread function of electron energy distribution in resist. [7]

The lateral distribution of deposited energy in the resist from the point of incidence is often approximated by Gaussian distributions, assuming initially that the primary beam is a delta function. A

high-amplitude, narrow Gaussian describes the forward-scattered incident (primary) beam broadening due to elastic scattering in the resist. Because the atomic number of the resist (essentially carbon) is low, electrons are only scattered through a small angle in the resist and the exposure area is a narrow "skirt" around the incident beam. A second Gaussian, due to elastic scattering from the substrate, represents the contribution from backscattered electrons. Its amplitude is orders of magnitude less than the first Gaussian, but it is much broader, as shown in Figure 2.5[8]. The forward-scattered Gaussian distribution is dependent on the beam energy, resist type, and resist thickness. It increases in width with either increasing resist thickness or atomic number, and decreases in width with increasing beam energy [9].

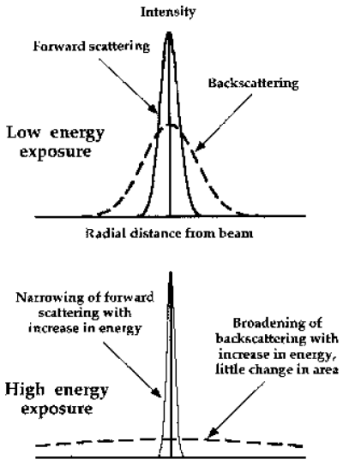

Figure 2.5 Forward scattering and backscattering distributions.

The total quantity of backscattered electrons is characterized by a backscattering coefficient η. This coefficient is strongly dependent on the atomic number of the substrate and only weakly dependent on the incident beam energy. The backscattered Gaussian distribution is therefore highly dependent on the substrate atomic number, increasing in magnitude with increasing atomic number. Although not indicated by η, the width of the backscattered distribution is highly dependent on incident beam energy. The radial spread of backscattered electrons is comparable to the Bethe range, which is the characteristic path length for an electron in the solid that has given up all of its energy. The Bethe range increases with increasing incident beam energy. Thus, the characteristic width of the backscattered electron Gaussian distribution increases with increasing beam energy. Since η is weakly dependent on the beam energy, as the characteristic widths of the backscattered electron Gaussian distribution increase with beam energy, the nearly constant value of η dictates that the integrals of these distributions remain approximately constant. This subsequently implies a decrease in the backscattered electron Gaussian peak height with increasing beam energy.

The comparatively diffuse backscattered energy distribution determines the contrast of the latent image in the resist, and the more compact forward-scattered energy distribution determines the ultimate resolution. Summing up, there are three factors that strongly influence the electron scatterings:

- Electron energy. Higher energy of primary electrons have much smaller scattering angle, therefore, less broadening of the beam due to small-angle forward scattering. Figure 2.6 compares the PSFs from 1 keV to 30 keV electron energies. The higher the electron energy the narrower the PSF. This is another proof that high-energy e-beam is preferred in e-beam lithography, in addition to benefits in lowering chromatic and space charge aberrations.

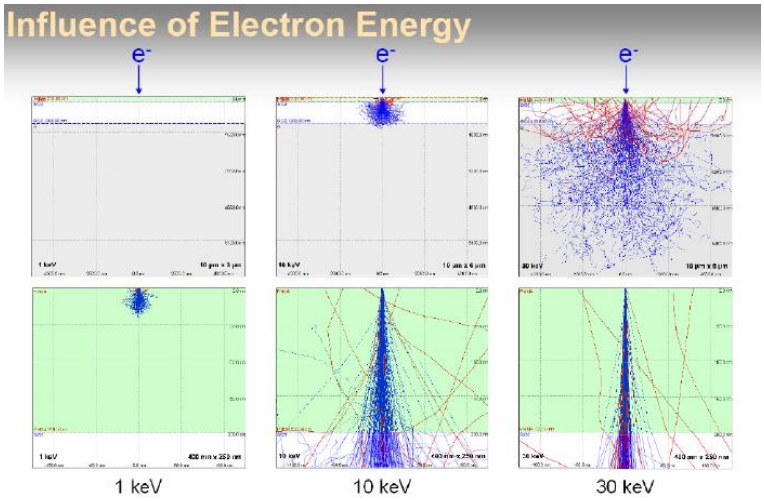

Figure 2.6 Influence of electron energy on the electron scattering.

- Density of substrate material. More electrons will scatter back from substrate if the substrate material is of higher density. Even though the substrate is a light material, such as silicon, the backscattering can still be significant if there is a thin film of heavy metal, such as gold or tungsten, coated at the interface between silicon and resist layer. Therefore, it is more difficult to achieve high-resolution e-beam lithography on high-density substrate.

- *Resist thickness*. It has been apparent from Figure 2.6 that electrons scatter wider forwardly as they go deeper. Therefore, for high-resolution e-beam lithography thin resist layer is preferred.

2.2.2 Proximity Effect

During an e-beam exposure of materials, the region of resist interaction with electrons is larger than the size of the incident probe. This is due to both elastic and inelastic electron scattering in the resist and the substrate. The proximity effect [10] is the exposure of resist by electrons backscattered from the

substrate, constituting a background where the pattern is superimposed. Since this background is not constant, pattern distortions arise.

In order to better understand this phenomenon, we introduce a proximity function $f(r)$ as the energy density distribution produced by a δ shaped electron beam; as we have seen previously, this function can be approximated by the sum of two Gaussian functions:

$$f(r) = C\left[\frac{1}{\beta_f^2} e^{-r^2/\beta_f^2} + \frac{\eta}{\beta_b^2} e^{-r^2/\beta_b^2}\right] \tag{2.1}$$

The widths of the two Gaussian functions, β_f and β_b, are quite different: $\beta_f \ll \beta_b$. The first Gaussian function takes into account the contributions of the forward scattering, while the second function is associated with the back scattering contributions. The η parameter describes the ratio of the back-scattering dissipated energy to the forward scattering energy, while C is a normalizing factor. The proximity function for a real (not shaped) beam is the convolution of (2.1) with the intensity distribution function over a transverse section of the beam. Convolution of a Gaussian beam of radius r_b with (2.1) gives as result again a function of the equation (2.1) type, but with the following parameters:

$$\begin{aligned} \beta_f^{'} &= \left(\beta_f^2 + r_b^2\right)^{1/2} \\ \beta_r^{'} &= \left(\beta_r^2 + r_b^2\right)^{1/2} \end{aligned} \tag{2.2}$$

When writing a pattern, the energy delivered to the resist, i.e. the exposure dose, will be the convolution of the proximity function with the pattern structures; as the pattern is divided in rectangular pixels before exposure, we can limit ourselves to the case of a single rectangle pattern. In Figure 2.7 qualitative results are reported for the exposure of a rectangle; as shown there are exposed areas outside the desired pattern, due to the proximity effect. The delivered dose decreases as the distance from the edges of the pattern increases, following the profile of an error function; in fact if we consider the simpler case of a mono-dimensional rectangle pattern, that is a segment $p(x)$, and calculate the convolution of the mono-dimensional proximity function, $f(x)$, with the segment, it is easy to find the delivered dose $D(x)$:

$$\begin{aligned} p(x) &= \begin{cases} 1 & x_1 < x < x_2 \\ 0 & \text{elsewhere} \end{cases} \\ f(r) &= C\left[\frac{1}{\beta_f^2} e^{-r^2/\beta_f^2} + \frac{\eta}{\beta_b^2} e^{-r^2/\beta_b^2}\right] \end{aligned} \tag{2.3}$$

$$D(x) = C\left\{\sqrt{\frac{\pi}{2}}\left[erf\left(\frac{x_2 - x}{\sqrt{2}\beta_f}\right) - erf\left(\frac{x1 - x}{\sqrt{2}\beta_f}\right)\right] + \eta\sqrt{\frac{\pi}{2}}\left[erf\left(\frac{x_2 - x}{\sqrt{2}\beta_b}\right) - erf\left(\frac{x1 - x}{\sqrt{2}\beta_b}\right)\right]\right\} \tag{2.4}$$

In the two-dimensional case similar results are obtained.

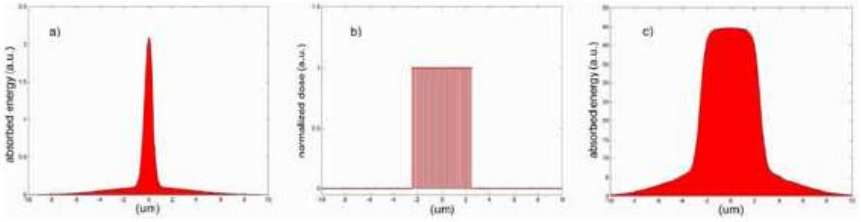

Figure 2.7 Exposure of a rectangular pattern (one dimensional scheme): a) Proximity function, b) pattern scanned by the electron beam, c) the result of the exposure. Exposed resist (c) is the convolution of the proximity function (a) with the pattern profile (b).

When high resolution, high density structures are desired, the proximity effect must be taken into account and corrections for the addressed dose must be calculated in order to have well defined and well separated shapes. Purpose of the corrections is to obtain a roughly uniform delivered dose for the pattern, with fast decay of absorbed energy at the edges of desired structures. Consequently the pattern really exposed will be different from the desired one; in general, the corrected pattern will require a multi-level exposure (in which each level has a different dose), also if the desired pattern is a single level one.

In considering an arbitrary point in the resist, this point will be developed out as part of the resist image if the deposited energy at the point exceeds a certain accumulated dose. We have seen that since the total contribution at a point in the resist is pattern-dependent, dense features will become overexposed and very isolated features will be underexposed, creating the so-called intershape and intrashape proximity effect. Consider a specific example of the exposure of an isolated square pattern of dimensions comparable or larger than the Bethe range for the given exposure conditions. The exposure conditions will be fixed such that the primary energy deposited in the resist will be equal for all points in the pattern. At the center of the pattern there is a total contribution of deposited energy that is the sum of the primary energy plus backscattered energy contributions from nearby points exposed in all directions. However, in the corners of the square there are nearby backscattered contributions only over one quadrant, reducing the total deposited energy relative to the center point. The result, after development to a constant energy contour, is the rounding of the corners. This is an example of intraproximity effect, the variation of total deposited energy *within* the pattern (see Figure 2.8).

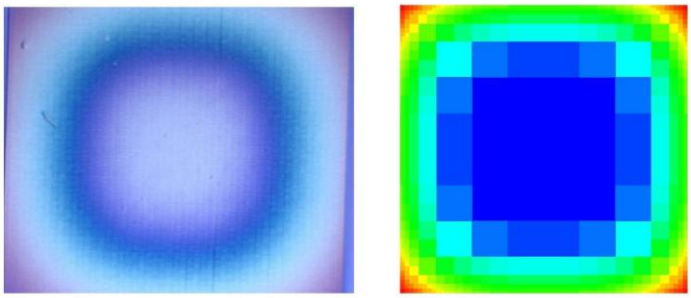

Figure 2.8 Left: optical microscope image of a developed square pattern with an equal dose assigned to all points. Right: proximity effect can be corrected assigning different doses (shown in the image by different colors) to different points.

Next consider the exposure of an isolated cross pattern of dimensions comparable or larger than the Bethe range for the given exposure conditions, as shown in Figure 2.9. At the tips, the outside corners will have backscattered contributions integrated over one quadrant (similar to the square example above) and will thus exhibit the characteristic intraproximity rounding. Now consider a point just outside of the pattern area, at one of the inside corners where the two cross arms intersect. At some points sufficiently close to but still outside the pattern, the integrated backscattered electron contribution will exceed the energy threshold for development. This will result in a fillet or web across the corner. This is one example of the interproximity effect, the variation of total deposited energy outside the pattern.

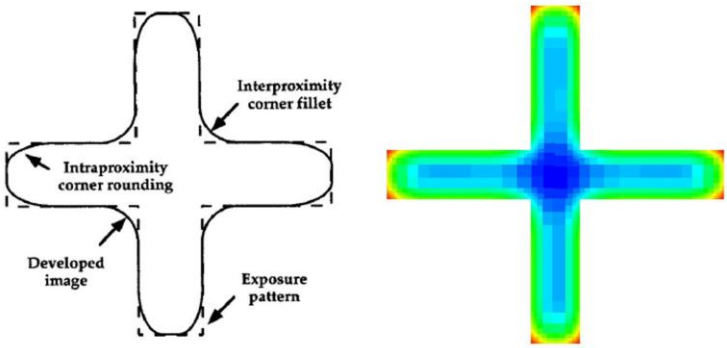

Figure 2.9 Left: cross pattern distortion due to proximity effects. Right: proximity effect correction for a cross pattern (different colors indicate different doses).

Although the proximity effect poses serious problems, it does not constitute a fundamental resolution limit to electron lithography. A number of methods for compensating for the effect, or at least reducing the gravity of the problems, have been developed. The most popular form of proximity effect compensation is probably *dose correction*. To implement this method, the dose delivered by the lithography instrument is

varied in such a way as to deposit the same energy density in all exposed regions of the pattern. Examples of dose correction applied to a square and a cross pattern with the GenISys Layout BEAMER™ software are shown in Figure 2.8 and Figure 2.9.

In some cases the proximity correction can be done by resizing the pattern geometry. The resizing, also called biasing, is best suitable for simple and highly repeated patterns, such as lines and squares.

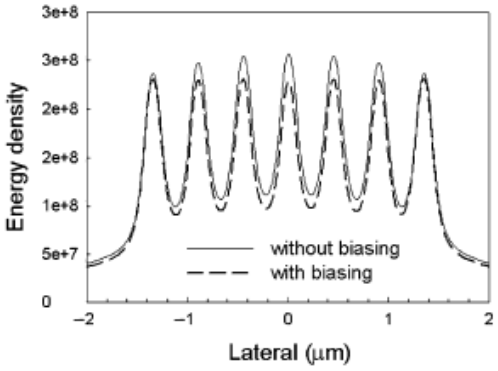

Figure 2.10 Comparison of pattern biasing for proximity effect correction (150-nm lines and 450-nm pitch, exposed with 20-keV beam energy into 0.5-μm resist on silicon). [7]

For a group of repeated lines, the lines in the middle of pattern area can be resized narrower (negative biased) than nominal design to compensate the higher-than-average energy contributed from neighboring lines, or the lines at the outer rim of pattern area can be resized wider (positive biasing) to compensate the lower-than-average energy due to electron scattering. The overall result is a relatively uniform distribution of energy across the whole pattern area. The amount of biasing can be determined empirically or from simulation of electron energy distribution. An example is shown in Figure 2.10. The figure shows deposited energy for a group of seven lines with line width of 150 nm and pitch of 450 nm exposed by 20-keV e-beam into 0.5-μm thick resist on silicon. If all lines are exposed at equal width, the lines in the middle receive higher energy (solid line plot) because electron scatterings from both sides contribute energy to the middle lines. If the middle lines are negatively biased, all the lines receive more or less the same energy (dash line plot).

2.2.3 Nanofabrication by Means of EBL

To achieve high-resolution patterning is essential to attain a complete control on the geometry of the fabricated patterns with a resolution of few nanometers. This is especially true for the fabrication of plasmonic structures, where the optical response of the final device depends strongly on the accuracy of the optimized geometrical parameters. To this aim Veneto Nanotech (VN), the hi-tech district of Veneto Region in the field of nanotechnologies applied to materials, purchased in 2009 an Electron Beam

Lithography (EBL) machine (Figure 2.11) for its new Research Center LaNN (Laboratory for the Nanofabrication of Nanodevices) located in Padova, a tool that can create structures smaller than 10 nm.

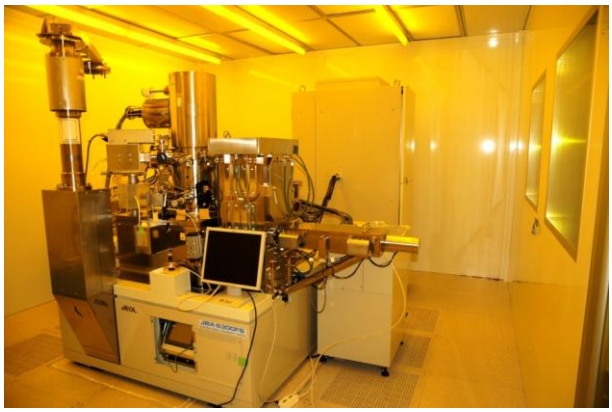

Figure 2.11. The JEOL JBX-6300FS EBL system located at LaNN (Laboratory for Nanofabrication of Nanodevices).

All the experimental samples made (and tested) by means of EBL in this thesis work have been fabricated with the machine showed above. In this section we give a full description of a standard EBL process with all of the intermediate steps, taking as example the fabrication of plasmonic gratings which will be used in chapter 3.

These are the main features of the EBL JEOL JBX-6300FS system used:

- ZrO/W Thermal field-emission gun
- Spot-beam vector scanning combined with a step-and-repeat stage movement
- 4-stage electron-beam focusing system
- Accelerating voltage up to 100 kV
- Beam scanning speeds up to 12MHz
- Scan increments down to 0.125 nm
- Beam diameter as low as 2 nm
- Stage positioning resolution of $\lambda/1024$ (about 0.62 nm)
- Deflector amplitude correction and objective-lens focus correction using the substrate height detector
- 2-stage objective lens enabling both submicron writing for small-volume production and ultra-fine processing
- Writing performance: minimum feature size at 100 kV (high-precision writing mode) $\leqq$ 8 nm

In order to check the writing performance of the machine, exposures were made to determine the minimum feature dimension that the EBL system can fabricate.

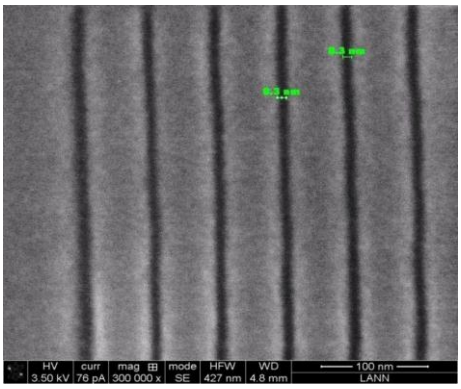

Figure 2.12 A minimum line width of 8nm was fabricated using a 50nm thick ZEP 520A resist.

As we can see in Figure 2.12 using a 50nm thick ZEP 520A resist, developed in MIBK:IPA 1:1 at 7°C, we were able to fabricate slits 8nm in width (with a period of 60nm).

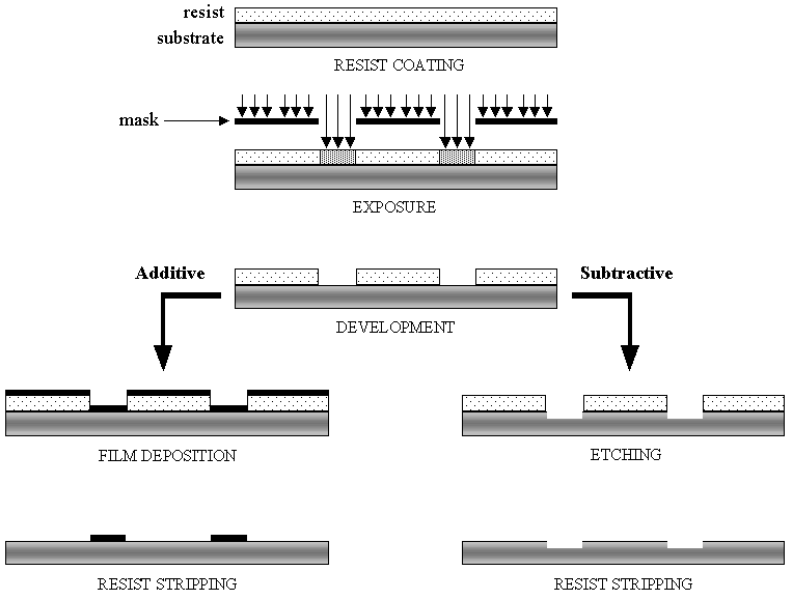

Figure 2.13 Scheme of the fabrication process for additive and subtractive processes.

The typical nanofabrication process followed is described in Figure 2.13, and can be divided in the following steps:

- Spin coating and soft baking
- EBL patterning
- Resist development
- Metal deposition (electrolytic growth or thermal evaporation)
- Resist stripping (or etching)

The resist used in our nanofabrication processes is mainly the poly(meth)acrylate (PMMA) AllResist AR-P 671.05, with molecular mass 950K, viscosity 57 mPa s, solids content 5% (dissolved in chlorobenzene). For a lift-off process (see next section on thermal evaporation) it is normally used a by-layer of two different resists: an electron-sensitive resist like PMMA on the top and a layer of PMGI (polymethylglutarimide) on the bottom used as a mask. Each resist comes along with a specifications document where the thickness of the resist is plotted vs the solid content, for different molecular weights and a definite coating speed. The resist is applied to the substrate by spin coating to form a film of uniform thickness (e.g. spinning the AR-P 671.05 resist at 4000 rpm to obtain a nominal thickness of 490nm). The resist is then soft baked on a hot plate at 180°C for 10 minutes to remove solvents and stress and to promote adhesion of the resist layer to the substrate. To prevent stress arising during the cooling process, a suitable decreasing temperature ramp has been set. Spin coating is a procedure used to apply uniform thin resists films to flat substrates: an amount of solution is placed on the substrate which is then rotated at high speed in order to spread the fluid until the desired thickness of the film is achieved. The time need to obtain a certain thickness is calculated by tabulated data provided for each type of resists. The film thickness depends mainly on three factors: spin speed, solution concentration and molecular weight. An explicit expression for the thickness is given by the following equation:

$$T = \frac{KC^{\beta}\eta^{\gamma}}{\omega^{\alpha}} \tag{2.5}$$

where T is the film thickness, K is a calibration constant, C the polymer concentration in grams per 100 ml solution, η the intrinsic viscosity, and ω the number of rotations per minute (RPM). α,β,γ are experimental exponents.

The next step in the fabrication process is the generation of the pattern to be exposed. This is usually accomplished by the use of CAD software like Layout Editor™. To correct the pattern for the proximity effect, a commercial software has been used, GenISys Layout BEAMER™ [11], which besides providing the tools for advanced process correction, offers a lot of complementary functions, e.g. the possibility to model the absorbed energy or showing the e-beam shot placement. When applying the proximity effect correction, choosing the appropriate correction function (the Point Spread Function (PSF)) is very important. This approach corrects the scattering effects of electrons in the material stack. The range of scattering will depend on the electron energy (acceleration voltage), resist and other layer materials and their thicknesses, including the substrate material, and it is divided into two types:

- *Forward scattering / short range correction.* The energy deposition of the forward scattering range, also called short range, is in the range of a few nanometers for 100keV machines and is designated by

α. In addition to the forward scattering the beam size (beam blur) needs to be considered for short range effects. The beam blur is dependent on the beam current of the exposure and is typically in the range of a few nanometers for low beam currents (>1nA) and may become few 10nm for very high beam current. The forward scattering and beam blur can be combined to an "*effective α*". Depending on this effective alpha short range correction may be needed or not. For most 100keV Gaussian beam exposures short range correction will not be needed for feature >50nm.

- *Back scattering / long range correction.* The deposited energy of backscattered electrons as a function of the distance from the beam can be approximated by either single or multi Gaussian function(s) with the width $\beta, \gamma_1, \gamma_2$ .The function strongly depends on electron energy and the stack, especially the substrate. β is on the order of 35μm for a 100keV, when writing on a silicon substrate. On the other hand, it is in the range of 10μm when writing on GaAs. The shape of the backscatter (long-range) PSF is simpler and can be approximated with just one Gaussian (beta) when using a 100kV machine writing on silicon. The PSF is more complex, with greater energy contributions in the mid-range (100nm-1μm), for 100keV on GaAs, requiring the approximation by multiple Gaussians or better yet by using a numerical PSF table.

There are several ways of determining the right correction functions (PSFs):

- Monte Carlo simulation [5,6]. Monte Carlo simulation software can simulate the PSF using computational models to calculate the scattering of electrons in the material for a given stack and electron energy. The result is a table with energy as a function of distance from the beam position. This PSF function table can be used directly, or approximated with Gaussian functions.
- Experimental methods [12]. A correction function can also be determined by using experimental methods (writing and measuring of test patterns) by providing a table equivalent to energy deposition as a function of distance. Such experimental methods can cover process effects, e.g., resist bake, development and etching, in addition to the electron scattering effects, and the calculated PSF is thus the most reliable.

In Figure 2.14 is shown the PSF calculated by Monte Carlo simulations for 500nm PMMA on ITO/glass substrate, along with its approximation with Gaussian functions.

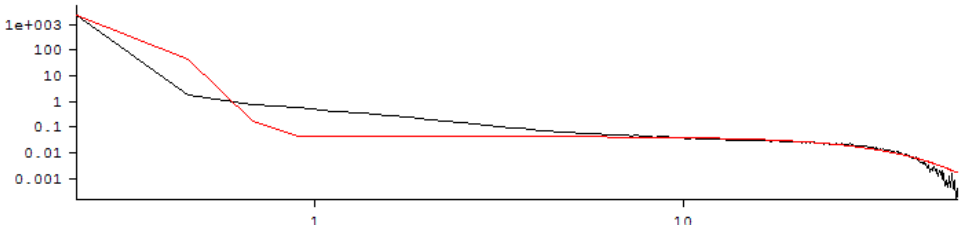

Figure 2.14 The PSF function calculated for the PEC correction of our samples.

In Figure 2.15is shown the result of the PEC correction calculated for a 500x500um^2 array of slits, with grating period of 300 nm and slit width of 120 nm, applying to the pattern the PSF shown in Fig. 9.13.

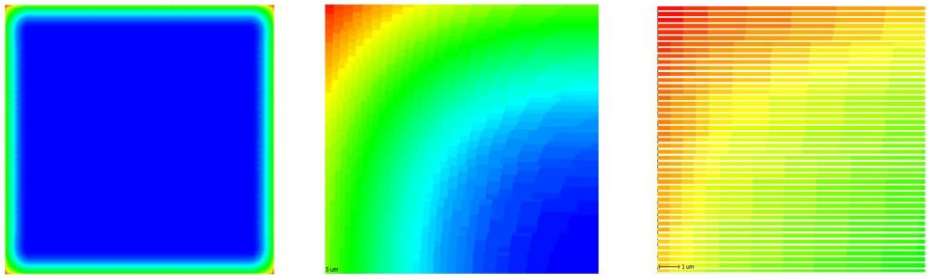

Figure 2.15 Proximity effect compensation; detail of the dose correction at a pattern corner; further zoom (single slits and fracturing are visible).

In Figure 2.16 is shown an optical microscopy image of a dose metrics of squares, where is apparent the effect of the proximity. Due to backscattering, at every dose the center of the square receives more energy than the borders and even more than the corners, which are in fact the last to be cleared. This is a typical example of a dose metrics used to calculate the contrast curve of a resist.

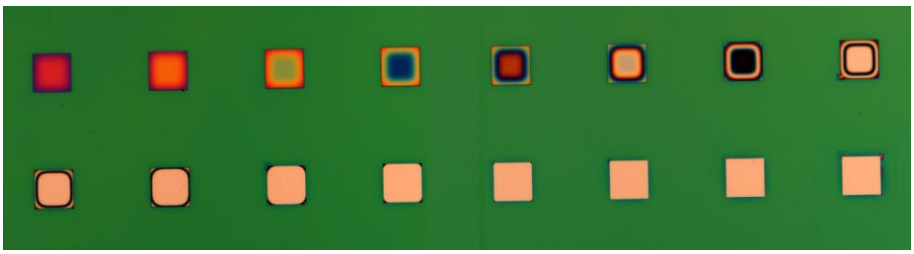

Figure 2.16 From top left to bottom right: sequence of increasing dose squares. It is apparent the effect of the proximity.

After the correction of the patter, the EBL exposure can be performed. The JBX-6300FS e-beam lithography system can work in a high-speed writing mode for small-volume submicron production and a nanometer-writing mode for ultra-fine processing. In the high-speed writing mode the EBL exposure is performed typically at 100KeV with a current ≥ 2nA, a beam diameter of 6nm, a scan pitch (distance

between two successive shots) of 12nm, an objective aperture of 60µm and a field size of 500x500µm^2 (EOS mode 3). In the high resolution mode the exposure is performed at 100KeV with a current of 100pA, a beam diameter of 2nm, a scan pitch of 1.5nm, an objective aperture of 25µm and a field size of 62.5x62.5µm^2 (EOS mode 6).

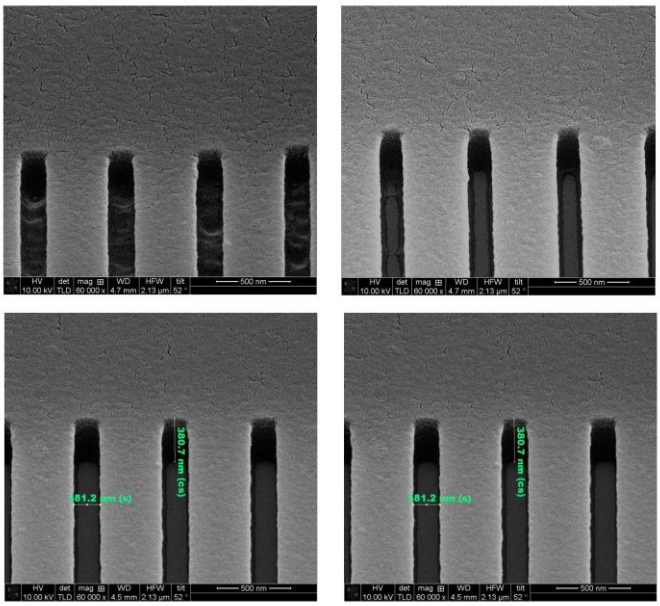

Figure 2.17 From top left to bottom right: cross section SEM images of increasing dose patterns (slit nominal width: 180nm).

Every nanofabrication process by EBL needs a preliminary stage where the correct dose to apply to the specific pattern to expose has to be determined. A dose metrics is meant to investigate the correct dose through the exposure of an array of patterns identical in size and shape to the pattern to expose, slightly differing in dose. After the development, the best dose has to be determined through a comparative analysis of the resulting patterns.

In Figure 2.17 a series of cross section SEM images of a dose metrics for an array of slits (period 610nm, slit width 180nm) is shown, where can be observed: (a) the residual resist inside the slits in case of insufficient dose; (b) the progressive clearing of the slits at the increase of the dose; (c) the right replication of the pattern for a dose equal to the clearing dose; (d) the broadening of the slits in case of excessive dose.

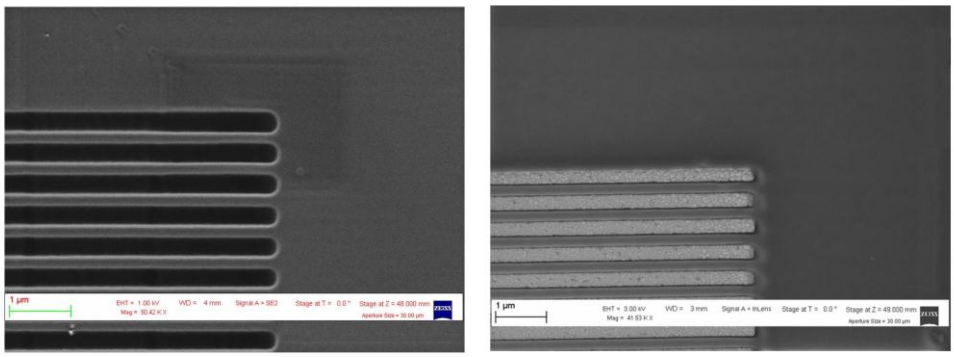

Figure 2.18 Particular of the grating pattern before (left) and after (right) electrolytic growth.

The next step after the exposure is the resist development step, in order to obtain the desired pattern. Commonly used developers for PMMA are 1:3 methyl isobutyl ketone (MIBK): isopropanol (IPA) for higher contrast and 1:1 MIBK:IPA for higher sensitivity. However, recently isopropanol mixed with a small proportion of water, has been demonstrated to have superior lithographic performance [13]. In a recent paper [14] we noted that the surface roughness of partially developed (in 1:3 MIBK:IPA) PMMA resist (where the resist was intentionally under-dosed in order to create the 3D features) was acceptably smooth only in the lower dose range (0 to 250 μC/cm^2); for higher doses, R_q was very high (up to hundreds of nm), due to a "phase separation effect" of the resist (see Fig. 9.20) [13]. Using the 3:7 deionized water:IPA developer we were able to improve the roughness R_q value of one order of magnitude. For this reason the water:IPA developer is preferred and has been used in all lithographic processes in this thesis work.

After the development, the sample is ready to be post-processed. In particular, for the realization of plasmonic structures a metal deposition step is mandatory. This can be obtained by two main techniques: electrolytic growth (for and additive process) or thermal evaporation (in a lift-off process). The description of these two techniques is given in the next section. Here we show just an example of a metallic grating which has undergo the electrolytic growth step. For ITO/glass substrates we used typically a voltage of 2.9V and a growth current of 100 mA DC, since previous work has demonstrated to be a good value to control the growth, with a growth rate calibrated to be from variable from 3 to 10 nm/sec. In Figure 2.18 a particular of a lithographed grating pattern is shown, before (left) and after (right) electrolytic growth.

The final step is the removal (or stripping) of the remaining resist left on the sample. Depending on the type of resist employed different solutions can be used. For PMMA the stripping is done by dipping for 3 minutes the sample into hot acetone (60°), and rinsing it in cold acetone and then in IPA. For PMGI the

stripping is performed in MF:319 solution for 10 minutes. Finally, in Figure 2.19 are shown images of the fabricated structures.

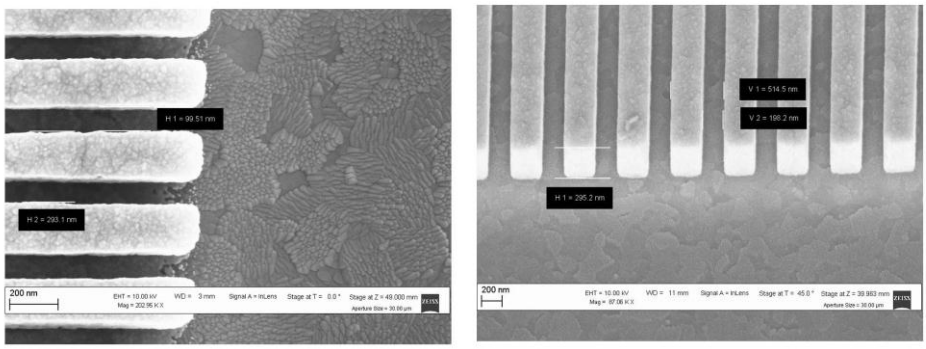

Figure 2.19 SEM images of the nanofabricated structures.

2.3 Focused Ion Beam Lithography

Focused Ion Beam (FIB) lithography [15] uses a collimated and focused beam of accelerated ions that directly hit the sample surface and sputter a small amount of material. Depending on the accelerating voltage and on the selected ion current, sample surface is milled and the desired pattern is recorded on the exposed area. Since this technique consists in directly milling the exposed surface, the pattern profile which is usually obtained by performing FIB lithography on a metal surface is almost digital, with amplitude values strictly related, at a fixed accelerating voltage, to current intensity and exposition time. FIB instrument consists of a source for the generation of the ion beam, an accelerating, focusing and scanning system of electromagnetic lenses, a vacuum chamber directly connected to the ion column, where the sample is located and exposed. The use of an ion beam provides an interaction with the exposed area that is imitated to its surface: ions interact and remove surface atoms, and dwell time and size are controlled with great resolution down to a nanometer scale. Since the exposed surface is scanned with a nanometric-size writing spot, FIB lithography requires longer times comparable to the one of EBL. However, also FIB technique provides highe resolution on lithography and a complete control on pattern design, and allows to use a complete top down approach, where the pattern is transferred directly into the material, without the need of other post-processes. A full description of a FIB system is beyond the scopes of this thesis work, but some processes used in the work presented in the following sections used FIB steps for the fabrication of the final devices. In this work FIB lithography was performed by means of the gallium ion source (Ga+) of the dual beam system FEI Nova 600i instrument (which acts also as a SEM microscope). This system guarantees a resolution down to 5 nm for an accelerant voltage of 30 kV. Ion beam can be selected in the range from 1.5pA up to 20 nA. This instrument also provides an Energy-

Dispersive X-ray spectroscopy (EDX) analysis system for the elemental and chemical analysis of the sample. The stimulated emission of characteristic X-rays from the specimen is produced by the high-energy ion or electron beam that is focused on the sample. Since an X-ray energy pattern is characteristic of the energy difference between electron shells and thus of the element from which they are emitted, this allows the elemental composition of the inspected target to be detected and estimated. Energy-peak intensity provides information on the relative percentages of the detected elements.

2.4 Metal Deposition Techniques

As we have seen in the previous section, in order to get to a final device, a single step fabrication process is not possible in most cases, even with a powerful tool like an EBL system. In particular since plasmonic devices need the presence of metallic structures, some sort of metal deposition techniques must be employed. In this work thesis, the metal samples were obtained by means of two main techniques: electrodeposition (or electrolytic growth, like the one used for the gratings in Figure 2.19) and thermal evaporation.

2.4.1 Electrodeposition

A metallic coating can only be deposited onto a substrate from an aqueous solution of a metal salt if there are sufficient electrons available, from whatever source, to neutralize the metal ions in solution, allowing the metal itself to form in the zero-valent state. In a typical electrodeposition process, a metal conductor material must be deposited on a substrate. In order to do so, the substrate must be conductive. The problem is solved if the substrate itself is a metallic layer, but if the substrate is a dielectric (like for instance silicon or glass), it is then must be made conductive first by sputtering a thin adhesion metal layer, and then a conductive seed layer. The adhesion metal layer is usually formed by 10 nm Cr, while the seed layer is formed by 20 nm Au. The thickness of the thin refractory metal adhesion layer may be as small as 50 to 100 Å, while the thickness of the conducting seed layer can range from 150 to 300 Å. The key requirement for seed layer is that it is electrically continuous and offers low sheet resistance. After forming a pattern in a spin-coated polymer by UV exposure, e-beam, or X-ray radiation and developing away the exposed resist, contact is made to the seed layer and electrodeposition is carried out. The use of solvent-containing development agent ensures a substrate surface completely free of grease and ready for plating. If a transparent substrate is needed, like for example for a transmission grating (Figure 2.19), then a glass substrate covered with a thin layer of ITO can be used. Indium tin oxide (ITO, or tin-doped indium oxide) is a solid solution of indium(III) oxide (In_2O_3) and tin(IV) oxide (SnO_2), typically 90% In_2O_3, 10% SnO_2 by weight. It is transparent and colorless in thin layers while in bulk form it is yellowish to grey. In the infrared region of the spectrum it acts as a metal-like mirror. Indium tin oxide is one of the most

widely used transparent conducting oxides because of its two chief properties, its electrical conductivity and optical transparency, as well as the ease with which it can be deposited as a thin film. As with all transparent conducting films, a compromise must be made between conductivity and transparency, since increasing the thickness and increasing the concentration of charge carriers will increase the material's conductivity, but decrease its transparency. Thin films of indium tin oxide are most commonly deposited on surfaces by electron beam evaporation, physical vapor deposition, or a range of sputter deposition techniques.

2.4.2 Thermal Evaporation

In some cases, a different metal deposition technique is preferred respect to electrodeposition. In fact although electrodeposition is a fast and cheap technique, the resolution and roughness of the metal layer grown depend strongly on the type of substrate used for the process. Moreover, the choice of metals to be growth is limited the number of electrolic solutions available: every different type of metal requires its own solution and experimental setup.

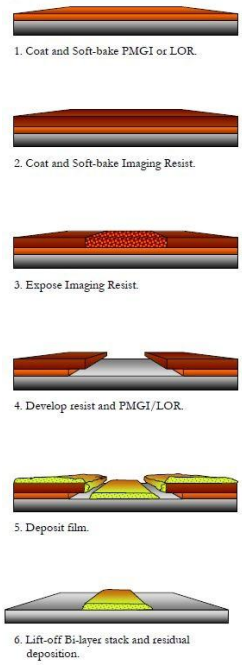

Figure 2.20 Generic lift-off process with thermal metal evaporation.

Thermal evaporation on the other hand allows to deposit metal thin films with a very low roughness and the control of the final thickness of the layer is very precise, since a typical deposition rate is 0.5 nm/s. Moreover, thermal evaporation is the best choice when a lift-off lithographic process is employed. The lift-off process is summarized in Figure 2.20 Generic lift-off process with thermal metal evaporation.. The lift-

off allows to deposit a thin film from above, using a PMGI resist as a mask. This allows to increase the final resolution of the lithographic exposition compared to electrodeposition.

Thermal evaporation represents one of the oldest of thin film deposition techniques. Evaporation is based on the boiling off (or sublimating) of heated material onto a substrate in a vacuum. From thermodynamic considerations, the number of molecules leaving a unit area of evaporant per second or flux F is given by:

$$F = N_0 e^{-\Phi_e / kT} \tag{2.6}$$

Where N_0 is a slowly varying function of temperature (T) and Φ_e is the activation energy (in eV) required to evaporate one molecule of the material. The activation energy for evaporation is related to the enthalpy of formation of the evaporant, H, as:

$$H = \Phi_e \times e \times N(J/mol) \tag{2.7}$$

Where N is the Avogadro's number. A good vacuum is needed during the evaporation: even at a pressure of 10^{-5} Torr, 4.4 contaminating monolayer per second will redeposit on the substrate. Moreover, to avoid reactions at the source (e.g., oxide impurities being formed), the oxygen partial pressure needs to be less than 10^{-8} Torr.

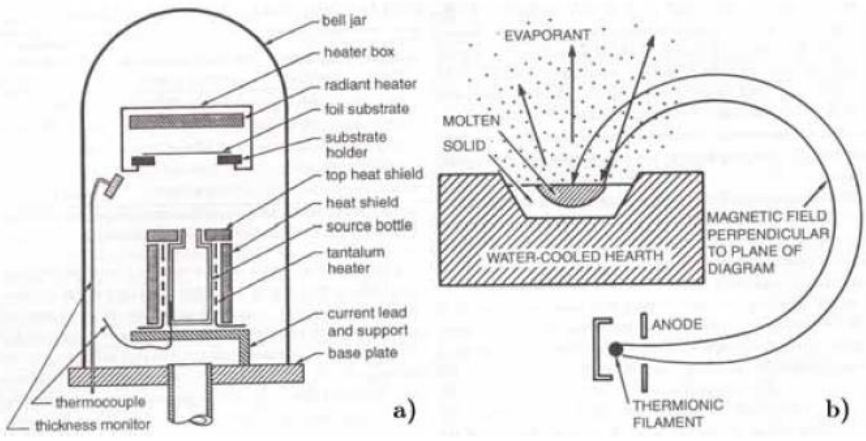

Figure 2.21 Thin film deposition: a) typical evaporation setup; b) Diagram of magnetized deflection electron-beam evaporation system.

In laboratory settings, a metal is usually evaporated by passing a high current through a highly refractory metal containment structures (e.g., a tungsten boat or filament). This method is called "resistive

heating" (Figure 2.21). Resistive evaporation is simple but easily spreads contaminants that are present in the filament, and the small size of filament limits the thickness of the deposit film.

Evaporation is fast (e.g., 0.5 μm/min for Al) and comparatively simple; it registers a low-energy impact on the substrate (~0.1eV); that is, no surface damage results except when using e-beam evaporation. Under proper experimental conditions, evaporation can provide films of extreme purity and known structure. In cases where the purity of the deposed film is of prime importance, evaporation is the preferred technique. As we just learned, evaporators emit material from a point source (e.g., a small tungsten filament), resulting is shadowing and sometimes causing problems with the deposition, especially on high-aspect structures. Difficulties also arise for large areas where highly homogeneous films are required, unless special setups are chosen. The different problem to overcome arises from the source materials decomposing at high evaporation temperature. While this risk does not exist when evaporating pure elements, it becomes a problem in the evaporation of compounds and substance mixtures. Evaporated thin film are usually under tensile stress, and the higher material's melting point the higher stress. Tungsten and nickel, for example, can have stress in excess of 500 MPa, which may lead to curling or peeling. Raising the temperature of the substrate tends to lower the internal stresses in the thin films.

2.5 Optical Characterization Techniques

In order to verify and investigate experimentally the different properties predicted and expected from the modeling of a plasmonic structure, several characterization techniques must be employed. The quality and fidelity of the sample are analyzed usually by means of Scanning Electron Microscopy (SEM); far-field quantities like reflectance and transmittance are obtained through ellipsometric measures, which also allow to determine the dielectric constant of different materials over a wide range of wavelengths. Near-field properties, like for instance the electromagnetic field distribution or enhancement can be collected with the help of a Scanning Near-field Optical Microscope (SNOM). In this section the basics on these techniques are reviewed.

2.5.1 Scanning Electron Microscope

Scanning electron microscope (SEM) [16] images the sample surface by scanning it with a high energy electron beam. A schematic of a SEM is reported in Figure 2.22. Electrons interact with the atoms that make up the sample producing signals that contain information about the target surface topography, composition and physical properties like electrical conductivity. Primary electrons are emitted thermionically from a metallic filament cathode (usually tungsten or lanthanum hexaboride) or by a

thermal field emission tip (Schottky emitter) and they are accelerated towards an anode. The electron beam, which typically has an energy ranging from a few hundred eV up to 40 keV, is focused by one or two condenser lenses into a beam with a very fine focal spot sized 0.4 nm to 5 nm. The beam passes through pairs of scanning coils or pairs of deflector plates in the electron column which deflect the beam horizontally and vertically so that it scans in a raster fashion over a rectangular area of the sample surface. Both the column and the sample chamber are under high vacuum (10^{-6} - 10^{-7} mbar) in order to avoid the electron scattering by gas molecules.

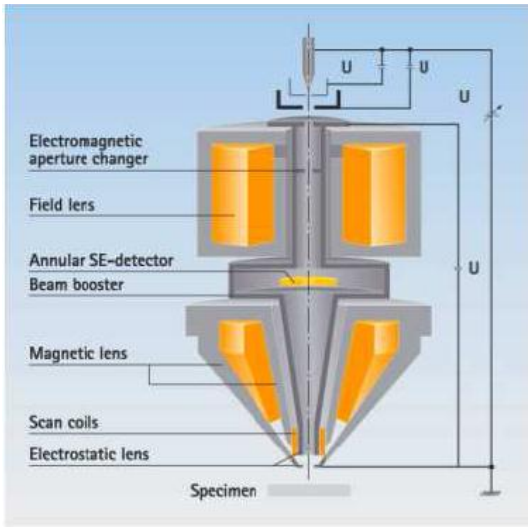

Figure 2.22 SEM Electron column scheme.

When the primary electron beam interacts with the target, the electrons loss energy by repeated scattering and absorption within a teardrop-shaped volume (interaction volume), which extends from less than 100 nm to around 5 μm into the surface. The size of the interaction volume depends on the electrons energy, the atomic number and density of the sample. The interaction between primary electrons and the sample results in the reflection of high-energy electrons by elastic scattering, emission of secondary electrons by inelastic scattering and the emission of electromagnetic radiation. The image displayed is a distribution map of the intensity of the signal being emitted from the scanned area of the sample. The most common imaging mode collects the low energy (< 50eV) secondary electrons. These electrons originate within a few nanometers from the surface. The electrons are detected by an Everhart-Thornley detector which is a type of scintillatorphotomultiplier device and the resulting signal is displayed as a two-dimensional intensity distribution. The brightness of the signal depends on the number of secondary electrons reaching the detector: if the beam enters the sample perpendicular to the surface, then the activated region is uniform around the axis of the beam and a certain number of electrons are emitted. As the angle of incidence increases, the escape distance of one side of the beam will decrease and more

secondary electrons will be emitted. In this way steep surfaces and edges tend to be brighter than flat surfaces, which results in images with a well-defined, three dimensional appearance. The spatial resolution depends on the size of the electron spot, which depends on both the electrons wavelength and the optical system which produces the scanning beam. The resolution is also limited by the size of the interaction volume. Depending on the instrument, the resolution can be from 1nm to 20 nm.

2.5.2 Ellipsometry

Ellipsometry [17] is a useful technique for the characterization of optical properties from the reflection of a circularly polarized monochromatic wave incident on a multilayer flat sample. Analyzing the polarization of the reflected beam, information about thickness and refractive index of each layer can be obtained. Moreover, ellipsometry can be used to compute transmission spectra as function of wavelength and polarization of incident radiation. This can be considered as a nondestructive, flexible and sensitive technique. We describe now the physical basis of ellipsometric analysis [17]. The most general polarization of a monochromatic light wave is elliptic, in which the endpoint of the electric-field vector processes along an elliptic trajectory in any plane perpendicular to the direction of propagation. The time evolution can be viewed as a superposition of two harmonic vibrations along perpendicular axes, with a phase shift Δ. Assuming the wave propagating along the z-axis, the amplitude of the electric field in the x-y plane can be described in the form:

$$\mathbf{E}(t)=\begin{pmatrix}E_x(t)\\E_y(t)\end{pmatrix}=\mathrm{Re}\left\{\begin{pmatrix}Xe^{i\Delta}\\Y\end{pmatrix}e^{i\omega(t-t_0)}\right\} \tag{2.8}$$

Besides the phase shift, the state of elliptic polarization is determined by the amplitudes X and Y. More precisely, only relative amplitude X/Y is relevant in ellipsometric measurements, since multiplying both X and Y by a common constant changes merely the light intensity. Using the angle ψ defined by $\tan\psi = X/Y$ and varying from zero to $\pi/2$, elliptic polarization can be represented by *Jones Vector:*

$$\begin{pmatrix}\sin\psi e^{i\Delta}\\\cos\psi\end{pmatrix} \tag{2.9}$$

which is determined by the two real angles ψ and Δ. Simple special cases of a general elliptic polarization are:

- linear polarization, for $\Delta = 0$ or π
- circular polarization for $\psi = \pi/4$ and $\Delta = \pm\pi/2$

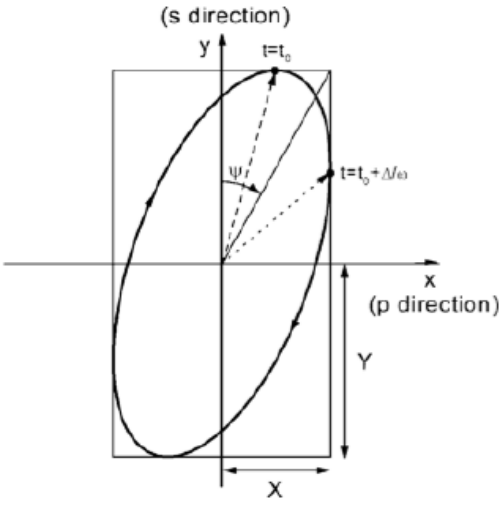

Figure 2.23 Polarization ellipse.

Ellipsometric technique is based on a suitable manipulation of the polarization state by auxiliary polarizing elements and measured sample. The basic configuration consists of a light source, a linear polarizer (P), a retarder (called compensator - C), the sample (S), a linear polarizer (called analyzer - A) and a detector (PCSA configuration, Figure 2.24). The arm with source, polarizer and retarder prepares a known polarization state of light incident on the sample. The arm with analyzer and detector is used to detect the change of polarization produced by the sample. A planar sample is assumed, with the angle of incidence denoted by φ. The beams incident on and reflected from the sample lie in the plane of incidence, which contains also the normal to the sample surface. The directions of linearly polarized light transmitted by the polarizer and the analyzer are defined by the angles P and A, respectively. The azimuth of the fast axis of the compensator is C. All of these angles are measured from the local x-axis lying in the plane of incidence, with the positive values for the clockwise rotations when looking the positive z-direction. Assuming E_P the complex amplitude of the linearly polarized wave transmitted by the polarizer, the wave incident on the compensator is a superposition of the component aligned along the fast axis, having the complex amplitude $E_p \cos(P-C)$, and the orthogonal component along the slow axis, $E_p \sin(P-C)$. The transmitted wave is modified by multiplying the two components by the complex transmittance t_f and t_s respectively, so the field amplitudes transmitted by the compensator along its fast and slow axes are:

$$\begin{aligned} E_f &= t_f E_p \cos(P-C) \\ E_s &= t_s E_p \sin(P-C) \end{aligned} \tag{2.10}$$

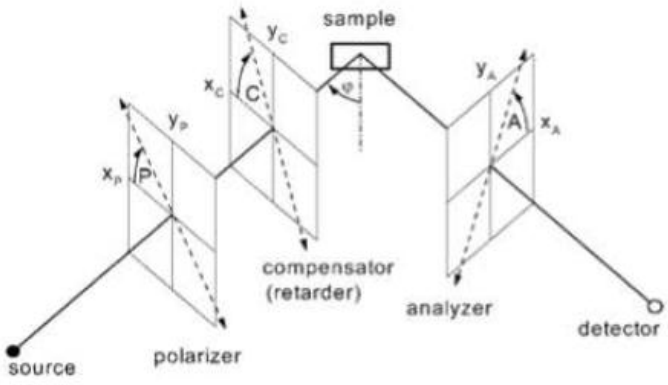

Figure 2.24 PCSA configuration.

The wave incident on the sample is a superposition of the component parallel and perpendicular to the plane of incidence (p and s polarization). The reflected wave is modified by multiplying the two components by the complex reflectivity r_p and r_s. Consequently, the amplitudes of p and s-polarized components reflected from the sample are:

$$\begin{aligned} E_{rp} &= r_p\left(E_f \cos C - E_s \sin C\right) \\ E_{rs} &= r_s\left(E_f \sin C + E_s \cos C\right) \end{aligned} \tag{2.11}$$

Finally, the wave transmitted by the analyzer results from the addition of incident p and s-polarized components, projected onto the direction of the azimuth A:

$$E_A = E_{rp}\cos A + E_{rs}\sin A \tag{2.12}$$

A simpler ellipsometric scheme is the polarizer-sample-analyzer (PSA) configuration, resulting by removing the compensator from PCSA. The field amplitude on the detector results:

$$E_A = E_p\left(r_p \cos P\cos A + r_s \sin P\sin A\right) = E_p r_s\left(\rho\cos P\cos A + \sin P\sin A\right) \tag{2.13}$$

where ρ is the complex reflectance ratio:

$$\rho = \frac{r_p}{r_s} = \tan\psi e^{i\Delta} \tag{2.14}$$

Photometric ellipsometry is based on measurements of intensity for a number of suitably chosen settings of the optical components influencing the polarization state of light. In the PSA configuration, light

intensities are measured for several properly chosen azimuths of the polarizer and analyzer. Since the analyzed state of polarization is independent of absolute intensities, one of them can be used as a reference for the measurement of relative values. Consequently, at least three independent intensities are required to determine the two real ellipsometric parameters. For fixed azimuth P, the intensity transmitted by the analyzer is:

$$I(A) = I(P)|r_s|^2 \cos^2 P(\tan^2\psi \cos^2 A + \tan^2 P \sin^2 \\ +2\tan\psi\cos\Delta\tan P\cos A\sin A) \tag{2.15}$$

Taking the intensity for $A = \pi/2$ as a reference, the ellipsometric angle ψ is obtained from the relative intensity measured for $A = 0$ as:

$$\tan\psi = |\tan P|\sqrt{\frac{I(0)}{I(\pi/2)}} \tag{2.16}$$

the third intensity can be measured for $A = \pi/4$ and provides the value of the ellipsometric angle Δ:

$$\cos\Delta = \mathrm{sgn}(P)\frac{2I(\pi/4) - I(0) - I(\pi/2)}{2\sqrt{I(0)I(\pi/2)}} \tag{2.17}$$

The PSA scheme with fixed polarizer is usually operated with a large number of intensity measurements at different analyzer azimuths. With the rotating analyzer configuration, the signal at the analyzer as a function of time (uniform rotation) is:

$$V(t) = DC + \alpha\cos(2\omega t) + \beta\sin(2\omega t) \tag{2.18}$$

(one AC component on a DC background). Normalized intensity at the analyzer is from previous calculations:

$$\frac{I(A)}{2\left(\tan^2\psi + \tan^2 P\right)} = I(P)|r_s|^2\cos^2 P(1 + \alpha\cos 2A + \beta\sin 2A) \tag{2.19}$$

where:

$$\alpha = \frac{\tan^2\psi - \tan^2 P}{\tan^2\psi + \tan^2 P} \\ \beta = \frac{2\tan P\tan\psi\cos\Delta}{\tan^2\psi + \tan^2 P} \tag{2.20}$$

α and β results from the discrete Fourier transform of the measured signal. Once computed, they are used to calculate the ellipsometric angles:

$$\tan\psi = |\tan P|\sqrt{\frac{1+\alpha}{1-\alpha}}$$
$$\cos\Delta = \mathrm{sgn}(P)\frac{\beta}{\sqrt{1-\alpha^2}} \tag{2.21}$$

2.5.3 Scanning Near-field Optical Microscopy

It has been assumed for many years that imaging could only occur with classical propagating-mode solutions to Maxwell's equations. However, imaging with the so-called "non-propagating" exponential (evanescent) modes is also possible. This rather unconventional technique is referred to as near-field optical microscopy. According to Abbe's theory, the resolving capability of conventional optical microscopy is ultimately limited by diffraction. Near-field scanning optical microscopy (SNOM) [18] is a microscopic technique for nanostructure investigation that breaks the far field resolution limit by exploiting the properties of the non-propagating fields that exist only near the surface of the object. These fields carry the high frequency spatial information about the object and have intensities that drop off exponentially with the distance from the object. Because of this, the probe must be placed very close to the surface (typically a few nanometers), much closer than the wavelength of the light. This region is the "Near-Field zone" and hence the name of the technique.

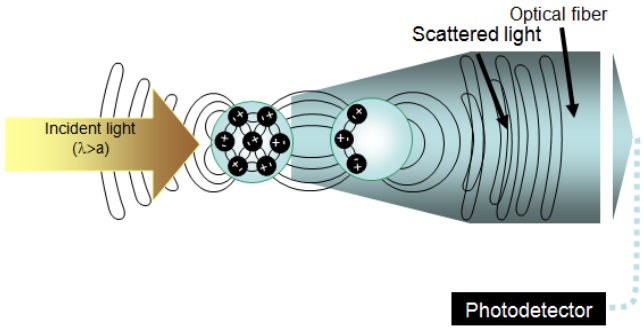

Figure 2.25 Detection of Optical Near Field.

With this technique, the resolution of the image is limited by the size of the detector aperture and not by the wavelength of the illuminating light. SNOM offers the use of a very small light source as the imaging mechanism. By using a quasipoint light source with a diameter much smaller than the wavelength of light, one can achieve resolutions better than the diffraction limit. Typically, laser light is fed to the aperture via an optical fiber (see Figure 2.26). The aperture (Figure 2.27) can be a tapered fiber coated with a metal (such as Al), a microfabricated hollow AFM probe or a tapered pipette. Normally, the size of the point light source determines the resolution obtainable.

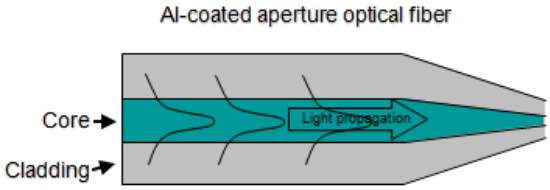

Figure 2.26 Scheme of the aperture illumination via optical fiber.

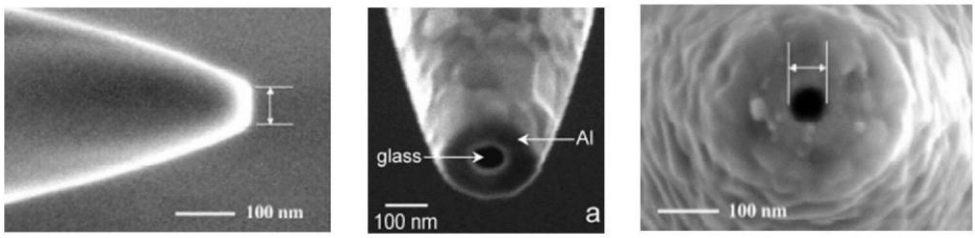

Figure 2.27 Images of optical fiber apertures [17].

There are two types of feedback typically used to maintain the proper working distance of the probe to the sample. One method is quite similar to how feedback works with an AFM - by using a cantilevered probe the normal force is monitored, typically by using a beam-deflection setup as in most AFMs. The second method uses a tuning fork. By attaching the fiber to a tuning fork, which oscillates at its resonant frequency, we can monitor changes in the amplitude as the tip moves over the surface. The tip is moved laterally, and this techniques is normally referred to as "shear-force" feedback.

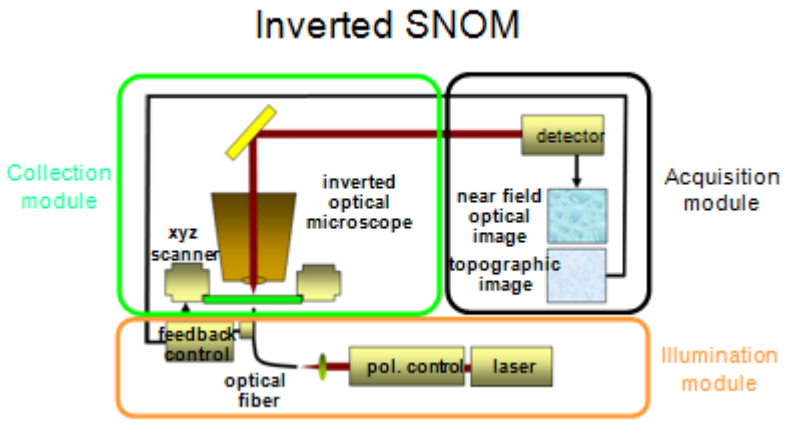

Figure 2.28 Inverted SNOM experimental setup.

Depending upon the sample being imaged, there are multiple modes of operation for SNOM:

- Transmission: laser light travels through the probe aperture and transmits through the sample (requires a transparent sample). This is the mode of operation we used: light comes from the back side of the sample and is collected, in transmittance, from the top of it (see Figure 2.28);
- Reflection: light source travels through the probe aperture, and reflects from the surface. Lower light intensity, and tip-dependent, but allows for opaque samples;
- Collection: sample is illuminated from large outside light source, and the probe collects the reflected light;
- Illumination/Collection: the probe both illuminates the sample and collects the reflected light.

Detection of the signal can be handled in a number of different ways: Spectrometer, APD (Avalanche Photo Diode), Photomultiplier Tube, or CCD.

2.6 Numerical Methods

The basic plasmonic properties derived in chapter 1 have been calculated starting from Maxwell's equations; as long as the geometry of the problem allows to explicit apply the correct boundary conditions, analytical solutions can be found for the dispersion relation of SPP, and also for field profiles and energy distributions. However, when the geometry of the structure supporting a plasmonic resonance allows no more analytical solutions, then numerical methods must be employed. Indeed numerical simulations play an essential role in the understanding of all plasmonic phenomena giving a quantitative description of the various parameters that govern the different process. In this thesis work, by means of the Finite Element Method (FEM), a variety of plasmonic nanostructures have been modeled, with two main aims: the first is to understand, at least at a qualitative level, the physical behavior which leads to the observed plasmonic phenomena. The second is to find the optimized geometrical parameters which give the best response of the plasmonic device. This kind of response depends on the particular structure considered, and could be maximize the far field transmission for a plasmonic grating, or the field enhancement for a plasmonic tip.

The Finite Element Method (FEM) [19] is a numerical technique for finding approximate solutions of partial differential equations (PDE), as well of integral equations, with proper boundary conditions. The software used for the different FEM simulations is COMSOL [20] (versions 3.5 to 4.3) in particular the RF Module, which is a package expressly dedicated to the solutions of Maxwell's equations, and allows a variety of applications to RF devices, optics, photonics and plasmonics.

Several steps are required in order to make FEM simulation. After the definition of the geometry of the problem, the crucial point in FEM simulation is to create a mesh i.e. a partition of the geometry into small units of simple shapes, called mesh elements. The introduction of a mesh defines a discretization of the geometry, allowing approximations to the dependent variables that defines the problem. The idea is to approximate the main functions of the problems with functions that can be described by a finite numbers of parameters, or elements. Inserting this approximations into the PDE that governs the problem, generates a set of ordinary differential equations which are then numerically integrated using standard techniques such as Euler's Method, Runge-Kutta, Lagrange's Method and others. The typical PDE for a TM wave can be expressed as:

$$\mu_0 \varepsilon_0 \frac{\partial}{\partial t}\left(n^2 \frac{\partial \mathbf{A}}{\partial t} \right) + \nabla \times \left(\nabla \times \mathbf{A} \right) = 0 \tag{2.22}$$

Where $\mathbf{A}$ is the potential vector and n^2 is the refractive index.

Usually, the first step in a FEM simulation is to define the geometry of the problem (see Figure 2.29).

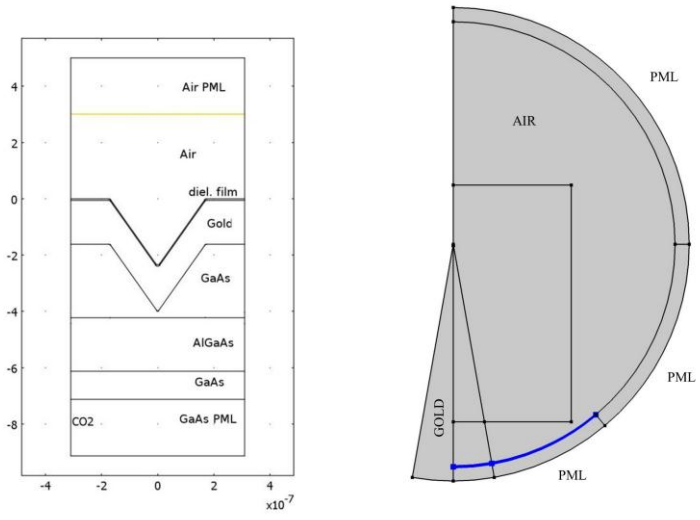

Figure 2.29 FEM model for two different geometries. Left: 1D v-shaped plasmonic grating (see chapter 3). Right: Metal cone waveguide (see chapter 4). Both possess a symmetry and so the model can be solved only partially without loss of generality. The different domains are also showed, together with the port used as input source (color lines).

The key element in this step is to find the symmetries of the problem, since this will allow to reduce the computation only to the symmetric part of the geometry, thus optimizing computational effort. For instance, a 1D plasmonic grating is simulated only for one period, while for an axial-symmetric cone only

one half of the cone it is simulated. The symmetries allow also to reduce the dimensions of the problem. 1D grating can be reduced to a 2D problem in the same way as a 3D cone is reduced to a 2D triangle. In most cases it is useful to parameterize the geometry, in order to perform multi-parametrical studies that allow fully exploring the phase space and finding the best configuration. The critical parameters depends strictly on the geometry considered, and could be the period and depth of a 1D metal grating, or the aperture angle of a metal cone. Once the geometry is defined, the next step is the definition of boundary and domains; the materials must be set, with appropriate dielectric constants (usually taken from experimental data) and the corrected boundary conditions must be imposed. The excitation incident wave is usually launched in the model by means of a "port" boundary condition. This particular condition allows to set a known incident wave as input source for the problem, usually in the form of an analytical expression. In this way, all parameters of the incident wave can be controlled, like wavelength, polarization, power flow and so on. Sometimes the simulated structure possesses a set of eigenmodes like for instance a waveguide. In this case COMSOL allow to perform an out of plane modal analysis, which calculates numerically the different modes, giving as result the effective index and field profile for each mode found. The modes found can then be used as input source on a port on the complete geometry. Example of this kind of analysis can be found in chapter 4 and 5, where it is applied to the study of nanofocusing on different waveguides. Very often is useful to add to the geometry also PMLs (Perfectly Matched Layers), which are additional domains that absorb the incident radiation without producing reflections. They provide good performance for a wide range of incidence angles and are necessary to correctly absorb scattered waves at the top of the models and transmitted ones at the bottom. The final step prior to launching the simulation is the creation of the mesh (see Figure 2.30). The mesh generation is an automatic process handled by the software, which chooses according to the geometry and to calculator power where to make a more refined mesh. A refinement of the mesh can be imposed also by the user; also the minimum element size, and the shape of the mesh elements can be manually varied, accordingly to the desired level of accuracy. The solved model allows to visualize different electromagnetic quantities, all related to Maxwell's equations, like electric and magnetic field components, power flow, current density and similar. Transmission, reflectance and absorption can be calculated also in every part of the simulated domain, thus demonstrating the power and flexibility of this numerical tool. Unless noticed, all numerical results presented in this thesis work have been calculated by means of FEM simulations.

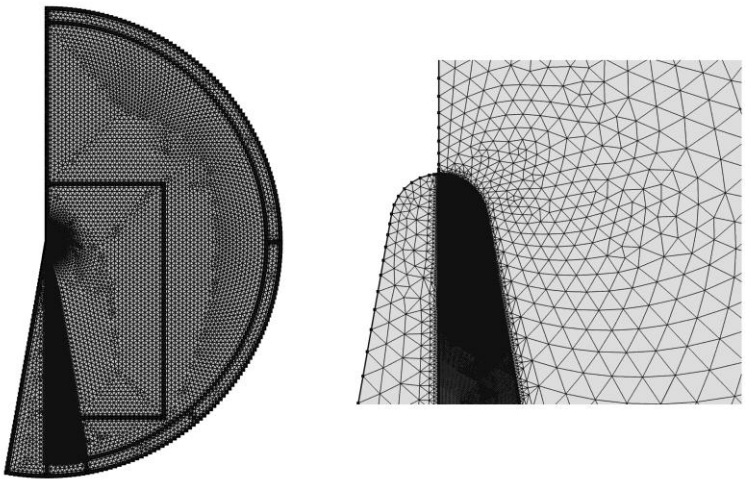

Figure 2.30 Meshing of the FEM model. Left: the adaptive mesh refinement is clearly visible. Near the cone's tip the mesh is more dense, thus providing an accurate solution. Right: zoom near the tip. The refinement function in COMSOL allows to refine also only certain areas of the model, like for instance the metal part of the cone.

2.7 Conclusions

In this chapter a description of the different experimental and simulation methods used throughout this thesis work have been presented and analyzed. The aim of this part is to give a basic idea on the different steps required in order to get to a complete nano-device. As it clearly appears, the modeling, fabrication and characterization of a device are not isolated parts of a single problem, but instead they must interact with each other. Modern nano-science is mainly based on multi-disciplinary steps and the fundamental task of a scientist working in the modern nano-science field is to have the most possible complete view of the entire problem, in order to make the different steps compatible with each other. Further details on the different processes can be found in the next chapters, where descriptions are given for any particular case.

Unless otherwise noticed, all experimental and modeling work presented in this work has been conducted in LaNN (LAboratory for the Nanofabrication of Nanodevices) in Padova, Italy.

2.8 References

[1] McCord, M. A.; M. J. Rooks (2000). SPIE Handbook of Microlithography, Micromachining and Microfabrication.

[2] Broers, A. N. et al. (1996). "Electron beam lithography—Resolution limits". Microelectronic Engineering **32**: 131–142.

[3] Broers A., J. Electrochem. Soc.: Solid State Sci. & Technol. **128**, 166 (1981).

[4] Liddle J. et al., Microlithography World **6**, 15 (1997).

[5] Murata K. et al., Jpn. J. Appl. Phys. **10**, 678 (1971).

[6] Parikh M., Kyser D.F., J. Appl. Phys **50**, 1104 (1979).

[7] Cui Z., "Nanofabrication", Springer (2008).

[8] Chang T. et al., IBM J. Res. Develop. **32**, 464 (1988).

[9] Broers A. N., IEEE Electron. Dev. **ED-28**, 1268 (1981).

[10] Chang, T. H. P., Journal of Vacuum Science and Technology , vol.12, no.6, pp.1271-1275, 1975.

[11] http://genisys-gmbh.com/web/products/beamer.html.

[12] Hauptmann M., Choi K..H., Jaschinsky P., Hohle C., Kretz J., Eng L.M., Microeletronic Engineering 86 (2009) 539.

[13] Yasin S. et al., Microelectronic Engineering **61**, 745 (2002).

[14] Massari M. et al., *Microelectron. Eng.* **88**, 2675 (2011).

[15] B. Bhushan, Handbook of Nanotechnology, Springer (2004).

[16] N. Yao, Z. L. Wang, Handbook of Microscopy for Nanotechnology, Springer (2005).

[17] H. Fujiwara, Spectroscopic Ellipsometry – Principles and Applications, Wiley (2007).

[18] Schiavuta P., "Near-Field Optics and Scanning Near-Field Optical Microscopy (SNOM)", IMN Interuniversity Master in Nanotechnologies (2007).

[19] Coccioli, R.; Itoh, T.; Pelosi, G.; Silvester, P.P., Antennas and Propagation Magazine, IEEE , vol.38, no.6, pp.34-48, 1996.

[20] http://www.comsol.com/.

3 Light Confinement with EOT in 1D Metallic Gratings

3.1 Introduction

The main topic of this chapter is the description of Extraordinary Optical Transmission (EOT) phenomena in 1D metallic gratings and how it can be exploited in order to concentrate and tunnel the light trough sub-wavelength apertures, in order to create electromagnetic (EM) field hot-spots. This effect can be used for different applications, like sensing, spectroscopy and polarization elements. As we will see, EOT based structures are very sensible to surface conditions, and the related EOT-phenomena range from near-field EM field enhancement to far-field transmission peaks.

This chapter is organized as follows: first an historical introduction on the problem of light transmission trough small apertures is provided. Then detailed description of the EOT phenomena in 1D metallic gratings is performed by a one-to-one comparison between experimental observed data and numerical analysis. This analysis allows to identify the different resonant mechanisms which lead to EOT, and thus to understand how the different parameters of a 1D grating can be varied in order to precisely tune the different resonances . The possibility to obtain EM field hot-spots inside nano-slits is then exploited for spectroscopy application, in particular to Raman spectroscopy, showing that an optimized 1D gold grating is indeed able to boost the Raman signal of active molecules. The last part of this chapter is dedicated to the description of the optimization and fabrication process of a novel biosensing compact electro-optical device, which combines light concentration due to EOT with a highly sensitive and scalable photo-detection scheme inspired by high electron mobility transistors (HEMTs).

3.2 Light Transmission Trough Small Apertures

The study of light transmission trough small apertures has always been a crucial topic in physics. The first studies go back to seventeenth century, when Grimaldi (1618-1663) first described diffraction from circular apertures, contributing to the foundation of classical optics. Huygens (1629-1695), enunciating the principle named after him, greatly improved the wave theory of light, deriving the laws of reflection and refraction. In the following years, several experiments were performed; the most famous of them being the Young's double slits experiment (1773-1829). This experiment represented a decisive step in leading to general acceptance of the wave theory. The diffraction theory was further improved by Fresnel (1788-1827) and later by Kirchoff (1832-1887), which his scalar theory gave for the first time a complete

mathematical formulation of the diffraction problem. In the twentieth century, as the technology evolved towards longer wavelength of the electromagnetic spectrum, the interest shifted to the study of light transmission trough sub-wavelength holes, i.e. holes with dimension smaller than the wavelength of incident radiation. In 1944, Bethe [1] treated the diffractive properties of an idealized sub-wavelength hole, that is, a hole in a perfectly conducting metal screen of zero thickness. The geometry of the problem is represented in Figure 3.1.

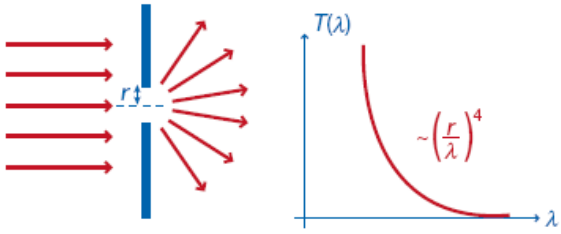

Figure 3.1 Diffraction from a small hole.

The Bethe's method consists of applying the standard Maxwell's boundary condition at the screen position ($x=0$) for the tangential components of the electromagnetic (EM) field:

$$\begin{aligned} \hat{n}\times\mathbf{E}&=0 \\ \hat{n}\cdot\mathbf{H}&=0 \end{aligned} \tag{3.1}$$

where $\hat{n}$ is a unitary vector directed along the normal direction of the screen. Since the screen is taken as a perfectly conducting metal screen, the EM field at $x=0$ is zero everywhere on the screen but not inside the hole, where **H** and the normal component of **E** are discontinuous. The problem is then to calculate the EM field on the right-hand side of the screen subject to the boundary conditions (3.1). For the effective calculation of the EM field, Bethe first derives the magnetic current density and charge density in the hole by defining the correct integration domain, and then he evaluates the fields assuming to be at large distance from the hole. The transmission coefficient is defined as the ratio of the total transmitted intensity to the incidence intensity:

$$T=\frac{\int I(\theta)d\Omega}{I_0} \tag{3.2}$$

where I is the intensity of the wave. Assuming a normal incident radiation, the transmission coefficient computed by Bethe is given by:

$$T=\frac{64}{27\pi}k^4r^6 \tag{3.3}$$

where $k = 2\pi/\lambda$ is the norm of the wave vector of the incoming radiation, and r is the radius of the aperture. The transmission coefficient normalized to the aperture area is then:

$$\eta = \frac{64}{27\pi^2} k^4 r^4 \propto \left(\frac{r}{\lambda}\right)^4 \tag{3.4}$$

It's immediate to see that as λ becomes larger than r, we would expect the optical transmission to drop rapidly. Equation (3.4) is valid for both TM and TE polarization at normal incidence. The Bethe theory predicts that the transmission of light through a sub-wavelength aperture should be very low, on the order of 10^{-4}. In 1998, Ebbesen et Al. [2], reported for the very first time the phenomena of Extraordinary Optical Transmission (EOT). Ebbesen collected several transmission spectra for normally incident light on a silver screen of thickness $h = 200\,\text{nm}$ perforated with an array of circular holes of diameter $r = 150\,\text{nm}$ arranged on a square lattice with period $a = 900\,\text{nm}$. The spectra are reported in Figure 3.2. The spectra show a number of distinct broad peaks, two of which occur at wavelength greater than grating period. Moreover, the peaks become gradually stronger at longer wavelengths. Even more surprising is that the absolute transmission efficiency, calculated by dividing the fraction of surface area occupied by the holes, is greater than unity at the maxima. This means that more light is transmitted respect to the incident one as impinges directly on the holes. These results are clearly in contrast with the Bethe theory, and must imply that the array itself is an active element, not just a passive geometrical object in the path of the incident beam.

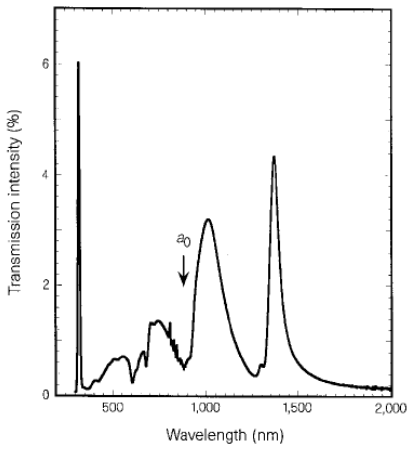

Figure 3.2 Zero-order transmission spectrum of an Ag array (a=900 nm, d=150 nm, t=200 nm) [2].

In the following years, others experiments were done ([3] [4]), on several types of arrays with different geometries and metals, varying also the properties of incident radiation, such as angle of incidence and polarization. The results showed that the peak's intensity and spectral position changes

with different materials. The hole's shape affects also transmission spectra; in particular rectangular holes have different transmission properties from circular holes. EOT can be seen also in 1D structures (transmission gratings) as shown by [5]. It's clear that the origins of EOT peaks cannot be explained by a simple diffraction analysis. Indeed, a fundamental role in the EOT process is played by Surface Plasmon Polaritons (SPP). Referring to Ebbesen's experiment, there is one important clue relating EOT to surface plasmons: the absence of EOT in hole arrays fabricated in Ge films, which points out the importance of the metallic film. The understanding of the EOT was then associated to the role of the metallic grating: due to grating coupling, SPP can be excited, leading to an enhanced light field on the top of the holes. After tunneling through the aperture, the energy in the SPP field is scattered into the far field on the other side.

A qualitative, first approximation description of the structure of the transmission spectrum can be given by assuming that the incident light couples with the metallic grating, thus exciting SPP on the dielectric-metal interfaces. The coupling condition can be expressed with the phase-matching condition:

$$k_{SP} = k_x \pm iG_x \pm jG_y = k_0 \sin\theta \pm (i+j)\frac{2\pi}{a_0} \tag{3.5}$$

Assuming a square array and a normal incidence light $(\theta = 0)$, and using (1.10), we find that the transmission maxima occur at wavelength fulfilling the condition:

$$\lambda_{SPP} = a\left(i^2 + j^2\right)^{-1/2}\left(\frac{\varepsilon_1\varepsilon_2}{\varepsilon_1 + \varepsilon_2}\right)^{1/2} \tag{3.6}$$

Equation (3.6) is only a first approximation, and the peaks position predicted are slightly shorter than those observed experimentally, but it is another clue of the role of SPP in EOT process. In the next sections we limit our analysis to the simplest case of 1D metallic gratings. Contrary to 2D subwavelength structures (which do not possess subwavelength propagating modes), in 1D gratings the interaction of plasmonic mediated resonances with the geometrical resonances of a standard 1D grating leads to a new sets of near and far field features that needs to be fully investigated.

3.3 EOT on 1D Plasmonic Gratings: Polarization, Near and Far-Field Analysis

Despite EOT has been discovered on 2D arrays of holes, 1D metallic gratings have become soon object of study, since this geometry is easier to threat. In particular, 1D geometry represents the ideal choice for the transmission analysis of TE and TM polarization. Theoretical studies, performed using different analytical and computational methods [6-9], showed that the optical response of a metallic grating is given by a combination of three main phenomena [10,18]: Surface Plasmon Polaritons (SPPs) resonances,

whose nature can be only TM, cavity mode resonances (CM), and Wood-Rayleigh anomalies that can be excited both for TE and TM polarization. Since SPPs do exist only for TM-polarization, this case was studied mainly, whereas few references report investigation about TE-polarization transmission properties. Although these resonances have a different field distribution compared to TM case, they lead to transmission efficiency with intensity comparable to the TM case. One of the works that treated the s-polarization case is the one presented by Crouse *et al.* [11] in 2007. In this work it is shown that even for s-polarization (TE), cavity modes resonances in 1D metal-dielectric structures can occur. In particular, by placing inside the grooves a high dielectric constant material, they present a computation focused to optimize EOT for TE and TM polarization simultaneously. The polarization dependence was also investigated by Lu et al. [12] in 2008 for pure metallic gratings in the infrared part of the electromagnetic spectrum and by Marquier et al. [13] in 2008 where the influence of polarization on thermal emission was studied.Experimental analyses of 1D gratings are much less than those performed on 2D gratings. Barbara et al. [14] in 2002 presented a first study in the optical regime, using a silica grating covered with gold. Later, Pang et al. [15] presented an experimental study in which different geometrical grating's parameters were analysed. In both cases only the p-polarization case was studied deeply. Other two experimental studies on 1D gratings were presented by Crouse et al. [16] in 2008 and Collin et al. [17] in 2010. These studies were performed in the microwave spectral region for p and s-polarization and for p-polarization and in the infrared spectral regime respectively.

The aim of this section is to show, both experimentally and numerically, the different physical mechanisms which are at the base of the EOT phenomena in 1D gold gratings with subwavelength dimensions. It will also be shown that under particular conditions EOT trough 1D gold grating becomes polarization independent in the optical regime. This study provides correlation between the far field and near field analysis of the optical modes involved in the transmission process and allows to understand the physical role of the different near and far field resonances observed, both experimentay and numerically. In this way an optimization process can be done for application purposes, and two examples of possible applications are given in the next sections.

3.3.1 Fabrication and Optical Characterization

The fabrication process of 1D gold gratings is made by means of an Electron Beam Lithography (EBL) system JEOL 6300FS operating at 100 keV, with 2 nA current, on a glass substrate coated with 350nm of PMMA resist. The typical chip patterned area has a dimension of 2x2 mm^2. After the resist patterning, the metallic structures were obtained by means of electrolytic growth. A thin layer of ITO on the substrate acts as conductive layer necessary for the electric contact during the galvanic growth. A growth current of

100 mA, voltage of 2.9 V and growth time of 45 sec has been used. The growth rate was calibrated to be 3.3 nm/sec. A typical fabricated gold grating is shown in Figure 3.3.

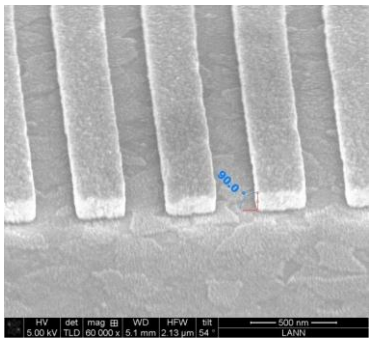

Figure 3.3 Example of a fabricated gold grating. It's clearly visible the ITO structure underneath the gold ridges.

The optical characterization of the samples is made through ellipsometric measures; in particular we focus on the far-field transmission properties of the system. Experimental measures have been performed by using a variable angle spectroscopic ellipsometer (J.A.Woollam Co.) (see chapter 2 for more details). The equipment allows to perform measurements over a wide spectral range from 193nm up to 2200nm and its variable wavelength and polarization angle of incidence light allows flexible measurements. In particular, our measurements have been performed at normal incidence, and the polarization angle has been varied from 0° (tangential component of electric field perpendicular to the slits axis - TM) to 90° (tangential component of electric field parallel to slits axis - TE).

3.3.2 Numerical Simulations

FEM simulations have been performed using COMSOL Multiphysics, RF package. In order to minimize computational time and to improve precision, the full EM field distributions have been computed with FEM only in one period of the grating, setting periodic boundary conditions. The simulated structure includes both the ITO and glass substrate along with two layers of PML (Perfectly Matched Layer) on the upper and lower sides of the geometry. The ratio between slit width and period (duty cycle) is kept constant to 50%, in order to have resonances for both TE and TM polarization and match the value of the experimental sample. The metal thickness is fixed to a value of 200 nm, and the light impinges normally to the sample. The dielectric constants of the metal and different substrates are taken directly from ellipsometric experimental measures performed on the samples used for the experiment. A scheme of the simulated structure is shown in Figure 3.4.

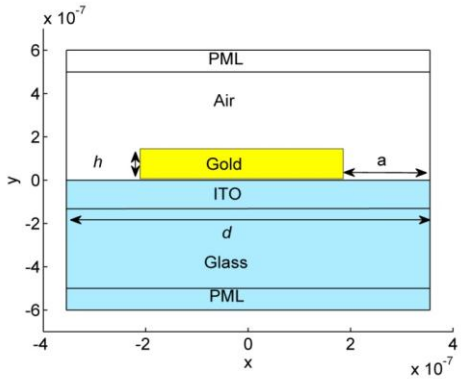

Figure 3.4 ***Scheme of the simulated structure.***

3.3.3 Results and discussion

Several numerical and theoretical studies have been performed in the past years in order to explain the physics that governs the EOT phenomena for 1D grating structures. They take into account SPP contribution, analyze single apertures and band structure or explain the transmission process by means of a diffracted evanescent wave model. The modal analysis presented by F.J. Garcia-Vidal and L. Marin-Moreno [10] is a simplified analytical model which is able to catch the main physic effects and it has the advantage of leading to a simple analytical expression for far-field quantities. The model was developed for an ideal infinite 1D grating, setting surface impedance boundary conditions on the interfaces, and considering only the p-polarization case. According to this model, neglecting all the evanescent modes and keeping only the fundamental propagating eigen-mode inside the slits, it is possible to give an analytical expression for the transmittance:

$$T = \frac{1}{\sqrt{\varepsilon_s}} \frac{\left|\tau_{12}\right|^2 \sum_{i=-\infty}^{i=+\infty} \cos\theta_i \left|\tau_{23,i}\right|^2}{\left|1-\left|\rho_{12}\right|\left|\rho_{23}\right| e^{i\phi_{tot}}\right|^2} \tag{3.7}$$

where τ and ρ represent, respectively, the transmission and reflection coefficients at the different interfaces of the grating; ε_s is the dielectric constant of the substrate, θ_i the i-th diffraction order angle and ϕ_{tot} is the total phase accumulated by the single propagating waveguide mode travelling forth and back inside the slit:

$$\phi_{tot} = \arg(\rho_{12}) + \arg(\rho_{23}) + 2k_0 h \tag{3.8}$$

where h is the metal thickness, and k_0 the vacuum wave vector. A derivation of (3.7) for the simplest symmetric configuration can be found in Appendix B. In Figure 3.5a is reported an experimental

transmission spectra for a 1D gold grating (period 516 nm, slit width 258 nm and metal thickness 200 nm) as function of incident wavelength, for different polarization angles. The transmission reaches a remarkable value as high as 55% for the TM polarization.

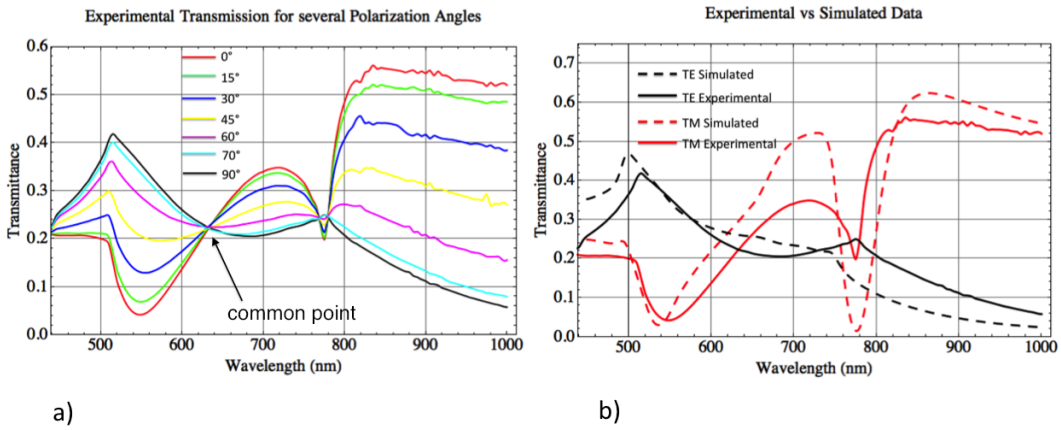

Figure 3.5 a) Experimental transmission spectra as function of incident light wavelength and polarization angle, from 0° (TM) to 90° (TE). At 630nm a point common to all polarization values is observed. b) Comparison between experimental (continuous lines) and simulated (dashed lines) data for TE and TM transmission spectra.

Different features in the transmission spectra appear for TM and TE polarization and with the help of equations (3.7) and (3.8) we are able to identify the main mechanisms that govern the transmission properties of 1D metallic gratings: Surface Plasmons Polaritons (SPP) resonances, Cavity Modes (CM) resonances, and Wood-Rayleigh (WR) anomalies [18,19]. These different types of resonances can couple in different way generating the complex behaviour of the transmitted spectra (Figure 3.5a). CM is a single mode Fabry-Perot like-resonance standing inside the slits, which occurs when the phase difference between the different waves transmitted to the substrate is a multiple of 2π. Since this type of resonance can be excited for both TE and TM polarizations, any given combination of the two fundamental polarizations can give rise to a CM. SPP resonances are due to the matching between the in-plane component of the TM polarized incident radiation and the grating vector $G = 2\pi / d$ (where d is the grating's period):

$$nG = k_0 \,\mathrm{Re}\left(\sqrt{\frac{\varepsilon_d \varepsilon_m}{\varepsilon_d + \varepsilon_m}}\right) \tag{3.9}$$

and where ε_m and ε_d are the dielectric constants of the metal and the dielectric (air or substrate depending on the interface considered). SPP resonances are related to transmission extinction and high EM field enhancement at the top surface of the slits [18]. WR anomalies [19] are abrupt changes in

transmission that occur both in TE and TM polarization when a diffraction order lies in the plane of the grating, i.e. when:

$$d_n = n\lambda / N \tag{3.10}$$

where n is the diffraction order, d the period, N the refractive index of the substrate and λ the wavelength. These configurations mark a discontinuity since for $d > d_n$ the n-th diffraction order does exist while for $d < d_n$ it does not. It's worth noting that WR are not resonant phenomena but are due to geometrical parameters and are not related to CM and SPP. Both Equations (3.9) and (3.10) refer to normal incidence.

In the experimental spectrum (Figure 3.5a) we observe all of these features. In Figure 3.5b is reported a comparison between an experimental spectrum and a simulated one, for both TE and TM polarization. As we can see, the spectral locations of cavity modes and transmission dips are in fairly good agreement with theoretical data, discrepancies being due to fabrication artifacts.

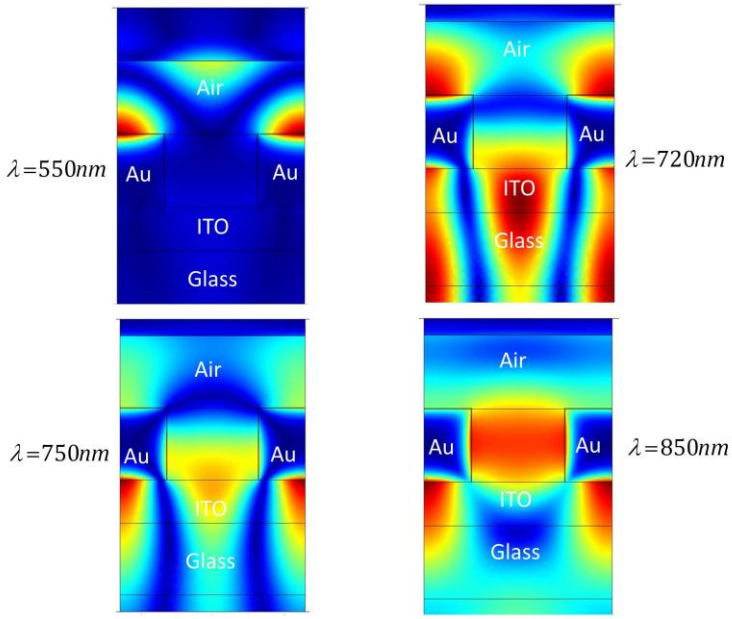

Figure 3.6 Fem simulations of magnetic field norm for 1D plasmonic gold grating at different wavelengths. The geometry is the same as the experimental data of Figure 3.5. According to the spectral position on the transmission spectra, different near-field magnetic resonances are observed.

With the help of FEM simulations we are able now to give a physical interpretation of the different resonances observed in the transmission spectra. For TM polarization we see that at a wavelength of 550 nm a transmission dip is present. The dip spectral location is very close to the one predicted by equation (3.9) (at 550 nm the dielectric constant of the gold is ε_m=-6+2.09i), thus confirming the plasmonic nature

of this anti-resonance. In fact, at this wavelength, SPP are excited on the air-gold interface of the grating, and the electromagnetic (EM) field is confined on the top of the metallic structures, leading to transmission extinction and high near-field enhancement [20] (see Figure 3.6 for the magnetic field distribution inside the slits at different wavelengths). The peak at 720 nm is due to a hybrid SPP-CM mode formed by the combination of planar SPP on the top of the grating and by SPP cavity modes excited on the vertical walls of the slits [18]. In fact, as many authors pointed out, CMs and SPPs resonances are not independent each other [20,21] and they can couple in order to generate a hybrid mode that presents both CM and SPP resonant characteristics. The transmission dip at 775 nm is another SPP excitation; this time SPP are excited on the gold-ITO interface of the grating (at 775 nm the dielectric constants of the gold and ITO substrate are respectively ε_m=-24+1.62i and ε_d=2.28+0.077i). Finally at a wavelength of 850 nm a more intense hybrid SPP-CM mode is excited, reaching a sort of plateau in the transmission spectrum. This time the CM resonance couples with the SPP resonance at the substrate side and for this type of resonance, the EM field is distributed uniformly within the slits [18]. As we have seen, for a 1D metallic grating, the different transmission features cannot be explained by taking into account only a single transmission mechanism, but instead is often the presence of different resonances which leads to the transmission peaks and dips observed. For a fixed grating geometry, different near and far-field responses are observed just by varying the incident wavelength. Tthe results in Figure 3.6 show also that this kind of plasmonic structure is able to confine the EM radiation in vary narrow subwavelenght regions if for instance a hybrid SPP-CM mode is excited. Of course the plasmonic contribution is the most peculiar, and due to the well-known SPP properties, the plasmonic response of such gratings can be easily adjusted and tailored depending on the final application. For instance, the plasmonic dips observed at 550 nm or 775 nm in Figure 3.5 can be moved spectrally by changing the grating's period or the substrate material. Also the cavity mode resonances can be moved at precise spectral position by changing the geometry of the resonant cavity (height and width of the slit). The response of 1D plasmonic gratings depends then on different parameters, which goes from the materials to the particular geometry of the grating. Since plasmonic gratings are mostly employed in biosensing and spectroscopy applications, where a monochromatic laser is used as excitation source (usually at wavelength of 514 nm, 633 nm or 780 nm), in order to fully control the transmission features, it is useful to perform multi-parametrical studies at fixed wavelength which allows to explore the full phase-space and point out the different resonances.

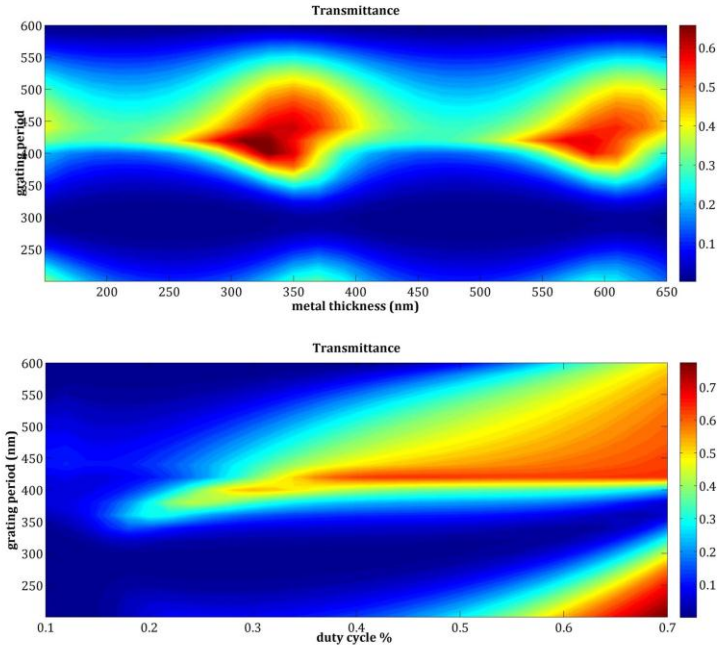

Figure 3.7 Transmission maps for a 1D gold grating at incident wavelength of 633 nm. Up: the duty cycle is fixed to a value of 40%. Down: the metal thickness of the slits is fixed to 300 nm.

Figure 3.7 shows a transmission map for a plasmonic 1D gold grating as function of grating's period d and metal thickness h at a wavelength of 633 nm for a duty cycle of 40%. As we can see, even if we are at a fixed spectral position, again different transmission maxima and minimum are observed with a periodic pattern. The transmission maxima correspond to the excitation of CM resonances inside the slits, which due to their geometrical nature, occurs at very precise value of the height of the resonant cavity. Figure 3.7 also shows the transmittance as function of grating's period d and duty cycle at a wavelength of 633 nm for metal thickness $h = 300$ nm . Again we see areas with different transmission values; if the duty cycle is too low, we are in an extreme subwavelength condition and the total far-field transmittance drops significantly. However this not means that there is no resonance inside the slits; field concentration is possible even in very narrow slits, as demonstrated by [10]. Increasing the slit width instead produce an enhanced in the transmission value, as expected.

So far we have focused our attention on the transmission properties for TM polariziation, since SPP are excited only for this kind of incident polarization. For TE polarization, SPPs cannot be excited [22]; however looking at Figure 3.5 a resonance is observed for this polarization at a wavelength of 516 nm (equal to grating's period). This is due to the excitation of a cavity mode, but the EM field distribution within the slits is completely different respect to the TM case. For this polarization, the field is located at the center of the slits, with no SPP field mode located on the vertical walls (very similar to the profile shown in Figure 3.8a). These cavity modes strongly depends on the geometry of the slits and grating, like

slits width and metal thickness [11,12]. For TE polarization we also observe a WR anomaly, represented by a less intense transmission peak located at 780 nm. Its spectral location is well predicted by (3.9) (the refractive index of the ITO substrate at 780 nm is n=1.517+0.025i), thus confirming the nature of this peak. Experimental data also clearly show that, by a rotation of polarization from 0° to 90°, all the spectral features have a progressive suppression or enhancement and that the TM spectrum gradually transform into the TE one. A peculiar behavior is represented by a "*common point*" for all the different polarization angles, located at a wavelength of about 630 nm and having a transmission of 23%. This point represents a symmetry of the system: at that particular wavelength, no matter the polarization angle, the far field transmission remains constant. The polarization independence, however, does not hold also at microscopic level where the EM configuration changes dramatically. Switching from TE to TM polarization, the resonant EM field distribution inside the slits changes from a cavity mode to a direct SPP excitation, as shown by the FEM simulations at common point wavelength, reported in Figure 3.8.

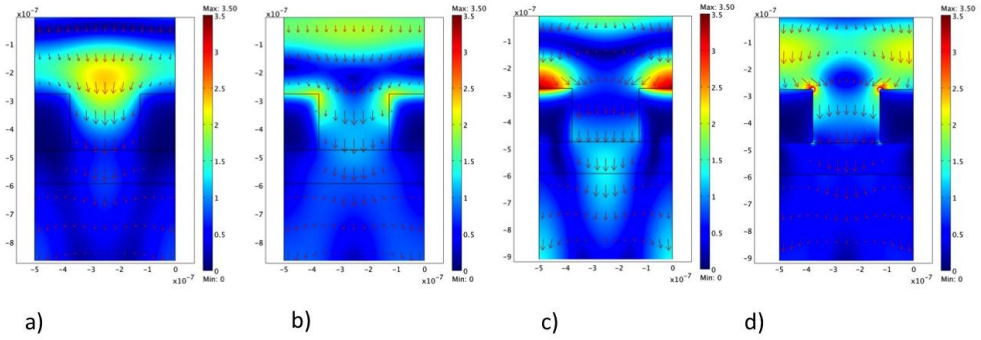

Figure 3.8 FEM simulation of EM field configuration and average power flow at the common point wavelength (630nm) for a gold grating with period of 516 nm, duty cycle set to 50% and gold thickness of 200nm. The colour scale is normalized to the incident EM field a) and b) TE polarization, electric and magnetic field respectively c) and d) TM polarization, electric and magnetic field respectively.

For TE polarization (Figure 3.8a) the norm of electric field has its maximum localized in the centre of the slits, while the magnetic field is located mostly in the upper region of the grating (Figure 3.8b). For TM polarization (Figure 3.8c,d) the norm of the EM fields presents both the typical SPP excitation on the upper side of the grating, related to transmission extinction, and a cavity mode field pattern within the slits, which leads to EOT [16]. Thus, contrary to the far field behaviour, at *common point* the EM field keeps strong polarization dependence. Thanks to Maxwell's equations linearity, however, the two completely different near-field behaviours combine linearly and give rise to the polarization-independent transmittance spectra experimentally observed (Figure 3.5a). This is confirmed by the average power outflow (red arrows in Figure 3.8), which is very similar for both polarizations.
Is the *common point* found for this sample a real singularity? In order to answer this question we have

performed multiparametric FEM simulations that allow to explore the phase map and look for the configurations which show to be polarization independent.

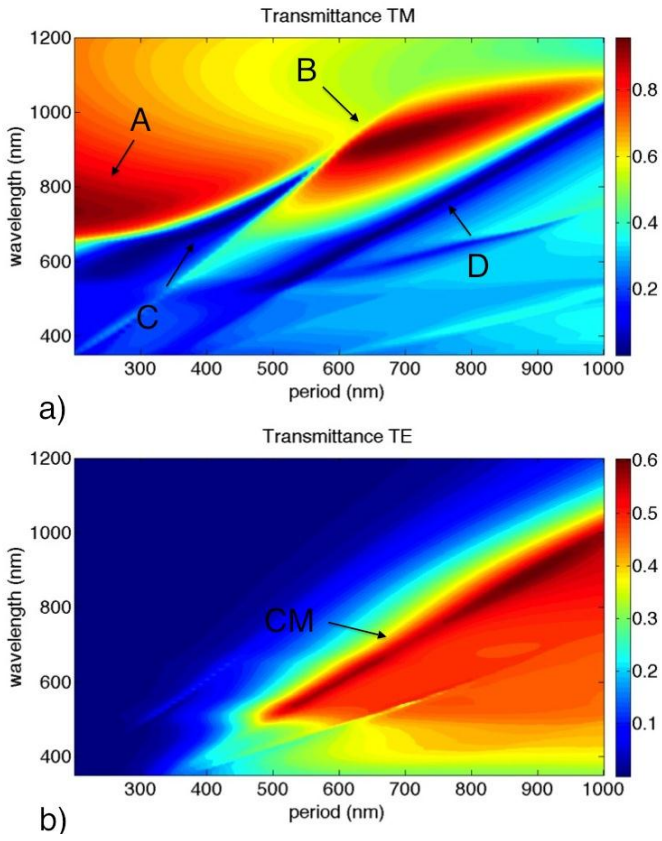

Figure 3.9 FEM transmission map (colour scale) as function of grating's period and incident light wavelength. The duty cycle is kept fixed to 50% and the gold thickness is set to 200nm. Fig. a) refers to TM case. Fig. b) refers to TE case. The letters refers to the different transmission resonances described in the main text.

In Figure 3.9a and Figure 3.9b the transmission maps are reported as function of incident wavelength and grating period respectively for TM and TE polarization. For TM two distinct high-transmission areas are present, corresponding to both hybrid cavity modes-SPP and CM resonances. The first one (marked with A on the map) is located in the low-period region of the map, and starts at a wavelength of 670 nm up to 1000 nm. The second one (marked with B) is located at higher period values (stating from 600 nm) but has a narrower wavelength bandwidth compared to the previous one. In this map are also presents anti-transmission bands; the first one (marked with C) corresponds to period values in the range from 250 to 550 nm, while the second one (marked with D) is located at period values higher than 550 nm. These bands correspond to direct SPP excitation at the different interfaces (air-gold and gold-ITO), as confirmed by their spectral positions, which in first approximation fits the prediction of grating-coupling formula for SPP excitation(3.9). For TE we can see that only cavity modes (marked with CM on the map) are present,

as expected. The fact that TE cavity modes appear to wavelengths near the grating period must not be confused with the presence of WR anomalies, as Eq. 2 might suggest, but instead to the particular geometry we have choose in our analysis. In fact TE cavity modes are strongly dependent on slits width [11,12] and metal thickness and in our calculations we found that if these two parameters are varied, the TE cavity modes are strongly modified (both spectral location and transmission intensity).

In order to study the properties of the common point, we made also a map that plots the absolute value of the difference between TE and TM transmission (Figure 3.10). Since at the *common point* the transmission is the same for both polarizations, we expect to see in the map transmission minima corresponding to the common point. In fact, a *common point* band appears (marked with CP), starting from a wavelength of 500 nm and up to 1050 nm. This band represents the dependence of the common point on grating's period and wavelength. As we can see, the spectral location of common point as function of period follows an almost linear dependence behavior; this means that we can choose the particular wavelength at which the common point occurs just by varying the grating's period. This can be useful exploited to design the common point configuration at a particular wavelength. It's worth noting that for this kind of structures the absorption has significant value (values between 40% and 80%) only in the low-wavelength regime of the spectrum (from 350 to 500 nm). For longer wavelengths, the absorption drops significantly up to less than 3%. This means that the transmittance and reflectance for wavelengths larger than 500 nm are complementary each other, thus opening the possibility to obtain also a reflectance polarization independence.

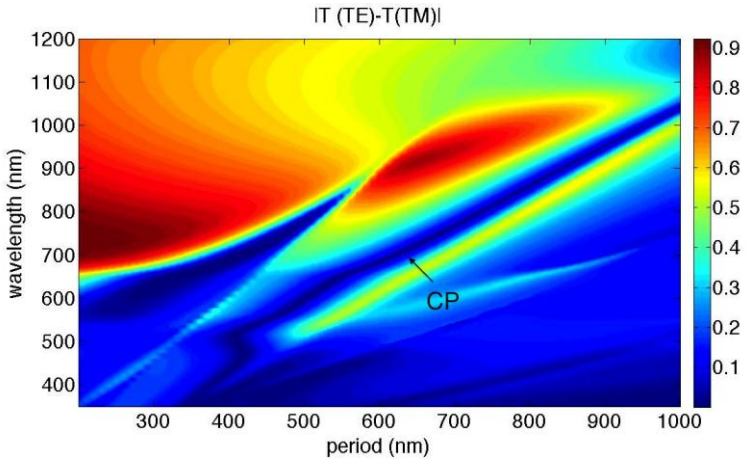

Figure 3.10 FEM map that plots the absolute difference between TE and TM transmission values (Fig. 4) as function of incident light wavelength and grating's period. Letter CP refers to the "common point" band.

In order to connect the different EM filed profiles found with FEM simulations to the transmission resonances observed in the transmission spectra (Figure 3.5), experimental near field analyses have been

performed, by using a Scanning Near-field Optical Microscope (SNOM). The SNOM (scanning near field optical microscopy) technique is a microscopy technique that is able to overcome the resolution limit of the far field, which is due to diffraction. Exploring with a probe the evanescent fields at the surface of the samples and propagating such waves to a detector in the far field, resolutions much higher than the incident light wavelength can be obtained. In the present work the grating was illuminated upside down, in a configuration known as inverted SNOM (see chapter 2). Figure 3.11a reports the intensity profile of the light emitted from the slits as function of the direction along the grating (periodicity direction) for a 1D grating. The measurements have been collected by using un-polarized light with wavelength at a distance of few tens of nanometers from the sample. The grating was designed in order to obtain a SPP-CM resonance at the excitation wavelength of 514 nm with unpolarized light.

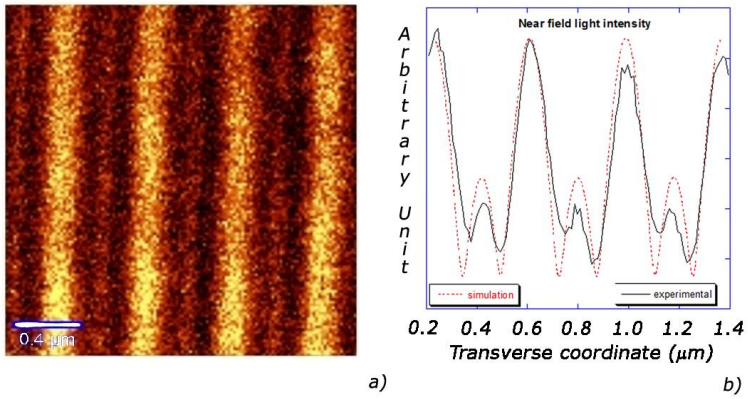

Figure 3.11 (a) SNOM light intensity image; (b) comparison of experimental (solid line) and simulated (dotted line) SNOM light intensity profile. The FEM simulation plots the magnitude of the square of the electric field amplitude. The major peaks and the brighter areas correspond to SPP excitations on the gold ridges of the array, while the small peaks and the less bright areas correspond to the light directly scattered inside the slits.

In Figure 3.11 is reported the SNOM light intensity image and two types of peaks are present. The more intense peaks appear to be coherent to the grating's period and are related to the TM SPP excited on the top of the grating gold ridges while the less intense peaks are present between major peaks. In the near field regime, the small peaks correspond to the TE cavity modes excited inside the slits, which are related to the excitation of the evanescent waveguide modes. This interpretation is further confirmed by the SNOM light intensity profile (Figure 3.11b). Also in this picture the more intense areas correspond to the gold ridges in perfect correlation with the SNOM intensity profile providing a direct vision of the SPP excitation. The less intense areas correspond, on the contrary, to the light passing directly through the slits. A FEM simulation of the SNOM intensity has been also performed in Figure 3.11b which plots the magnitude of the square of the electric field amplitude. In particular we can see the alternation of peak

intensity whose location fits very good the experimental data. This result confirms that using un-polarized light both the two the SPP and cavity modes resonances can be excited at the same time. EOT 1D gratings then allows not only a transmission enhancement in the far-field regime, but allows also an efficient EM field concentration in subwavelength regions.

3.3.4 Conclusions

To conclude this section transmission trough 1D gold grating has been studied both experimentally and numerically. Transmission spectra show EOT for both TE and TM polarization, although with different transmission mechanisms, reaching a maximum transmission value of 55% for the TM case. The polarization dependence of the system shows a symmetry property highlighted by the presence of a point common to all the different polarization angles. FEM simulations were used in the analysis in order to understand the transmission properties of the system both on the near and far field regime. In particular we have shown that the far-field polarization independence does not hold on the near-field regime. SNOM data show that at in the near field two types of peaks intensity profile are present. The more intense corresponds directly to the SPP excited on the gold ridges of the grating confirming the active role played by SPP on EOT process. The weaker peaks correspond to light directly scattered inside the slits, which are related to the excitation of the cavity modes. These preliminary results can be usefully exploited for bio-sensoristic applications, when a highly sensitive response to functionalization is needed. 2D maps allow to point out the different aspects involved in the transmission process for the two fundamental TE and TM polarizations, showing the presence of a common point band whose spectral location depends linearly on grating's period. Moreover we have shown that the different optical responses of 1D plasmonic gratings can be tailored and optimized just by varying the geometry of the grating, thus allowing the use of such structures to different applications, depending if a far-field transmission enhancement or a near-field light concentration is needed. In the next sections two example are provided of EOT application for spectroscopy and biosensiong applications.

3.4 Design, fabrication and characterization of plasmonic gratings for SERS

3.4.1 Introduction

In the previous section we have shown that 1D plasmonic gratings can give rise to high EM concentration inside subwavelength regions (i.e. inside the slits) if the geometry of the grating is optimized. This behavior can be exploited for instance in spectroscopy, where EM field "hot-spots" can boost by several orders of magnitude the signal coming from active molecules. One of the techniques that take advantage of plasmonic effects is without doubt Raman spectroscopy [23]. Identifying molecules at

very low concentrations is critical for many analytical applications such as forensics, medical diagnostics, drug discovery, and chemical development. The molecular fingerprint information present in Raman spectra makes the technique specific and quantitative. Moreover Raman measurements are nondestructive and noninvasive. As a result of these qualities, this spectroscopy has lately gained lots of attention as a detection tool. Surface Enhanced Raman Scattering (SERS) [24], which relies on the amplification of the Raman signal induced by suitable metal nano-structured surfaces, allows to overcome a drawback of Raman spectroscopy, which is its lack of sensitivity. The larger the amplification factor, the higher is the sensibility to the detection, and identification, of molecules deposited on the surface of the nanostructures. Plasmonic nanostructures can generate strong light concentration in such a way that Raman scattering can be increased by several orders of magnitude up to the possibility of single molecule detection. (SM-SERS) [25-30]. Despite high sensibility and specificity, SERS is not a quantitative technique for detection in the sense that it is extremely difficult to perform accurate measurements of the amount of functionalized molecules. This is due to the combination of several factors related mainly to the geometry of the nanostructures and to the intensity and distribution of the electromagnetic (EM) fields. A strategic topic is the combination of theoretical tools, which allow to foresee and tailor the features of metal nanostructures, with experimental fabrication techniques. Nano-lithography is useful to realize plasmonic substrates possessing the geometrical parameters optimized from the theory. By choosing simple geometries, with a high degree of symmetry, it is possible to provide a better insight in the field distribution on the metal surfaces with shorter computational time. To our knowledge, only a few works have previously computed and measured the SERS enhancement factor [31]. The aim of this work is to design, fabricate and characterize a 1D Gold grating, in order to exploit its plasmonic properties for SERS. In particular the grating is theoretically optimized for concentrating electromagnetic (EM) radiation inside the slits. A chip with the proper geometrical parameters is then fabricated by Electron Beam Lithography (EBL) and electrolytic growth. Finally, the Raman enhancement factor of the chip is measured and compared with the theoretical estimation.

3.4.2 Design

As in the previous section, numerical analysis was performed using Finite Element Method (FEM). The software used is COMSOL Multiphysics 3.5a with Matlab, in particular the RF package. The simulated structure is like the one shown in Figure 3.4. The dielectric constants of the various layers were taken from ellipsometric data, obtained directly from the samples used for the experiments. The gold grating has been illuminated from the air side at normal incidence with TM polarization at a wavelength of 633 nm. In order to minimize computational time, perfect periodic boundary conditions have been imposed, and calculations were made only for one period.

The simulated structures were designed in order to obtain a particular EM field configuration: the presence of hot-spots inside the slits (Figure 3.12). Since the presence of hot-spots is linked with the full excitation of plasmonic resonances, far field quantities, such as reflectance, transmittance and absorbance can be evaluated in order to extrapolate useful information about EM field configuration. In Figure 3.12 the optimized EM field configuration for TM and TE polarization are shown.

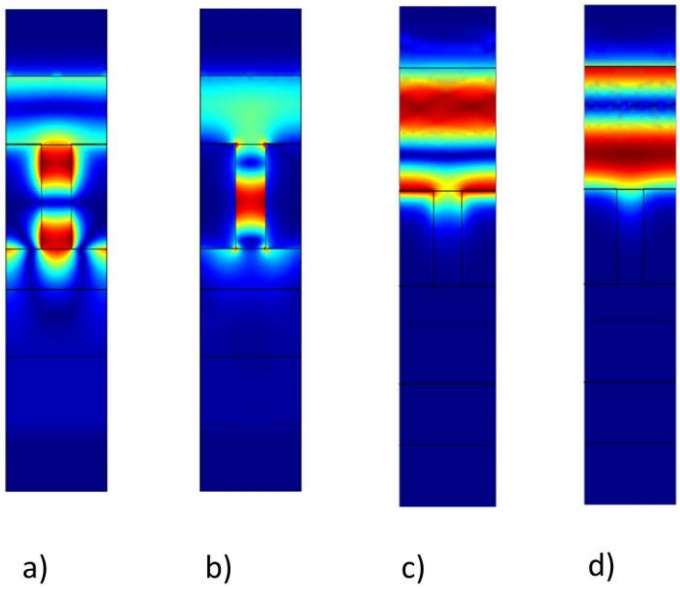

Figure 3.12 Optimized field configuration for SERS hot-spots (d=300 nm, h=350 nm, a=120 nm). a) norm of the magnetic field for TM polarization; b) norm of the electric field for TM polarization; c) norm of the magnetic field for TE polarization; d) norm of the electric field for TE polarization.

It clearly appears that TE polarization is forbidden to penetrate the trances of the slits. On the contrary in TM polarization the EM generates plasmonic standing waves whose intensity has been optimized changing the geometrical parameters of the grating. In fact, the EM field distribution is, in principle, dependent on all the geometric parameters: metal thickness (h), slits width (a), and period (d). The duty cycle (slit width/period ratio) has been fixed to 40% in order to have a large zone of active SERS surface. Bidimensional maps of transmittance, reflectance and substrates absorbance have been computed as function of period and thickness (Figure 3.13), keeping the incident wavelength set to 633 nm, i.e. the laser wavelength used in the experiments. The simulation also takes into account a thin (2nm) dielectric layer of a non-absorbing conformal to the plasmonic grating surface profile that resembles the benzenthiole functionalization. As can be clearly seen, a periodic pattern in the maps is present. The areas of minimum reflectance and maximum metal absorbance correspond to Fabry-Perot CM resonances excited by plasmonic effects. Looking at the maps, these two conditions are verified for a gold thickness (h) of 100, 350 and 600 nm, and up to a grating period (d) of 400 nm.

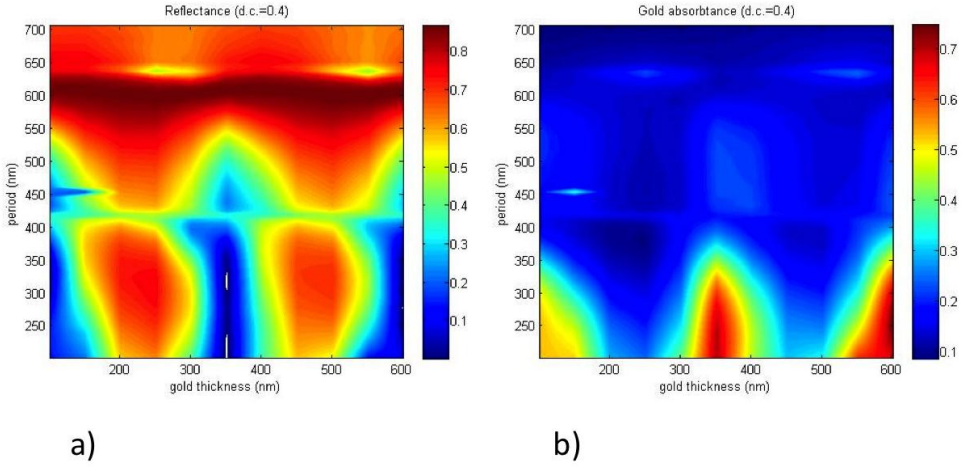

Figure 3.13 a) reflectance and b) gold absorbance maps as a function of gold grating and thickness. The interesting areas, corresponding to plasmonic excitations, lie in the period range 200-400 nm and in metal thickness range 320-380 nm.

From these results the geometrical parameters, useful for the required EM field configuration, can be easily obtained. Exploring the full range of periods, from the reflectance map of Figure 3.13 it can be seen that with a period d=300 nm the resonance is completely excited. A metal thickness of h=350 nm has been chosen: it presents two hot spots well localized inside the slits. The other resonance values found for metal thickness presents hot spots that are not well localized (h=100 nm) or have a low intensity (h=600 nm). The final optimized geometry is shown in Figure 3.12.

3.4.3 Fabrication

The fabrication process consists of two main steps. Electron beam lithography (EBL), by using a JEOL EB6300FS EBL system operating at 100 keV, with 2 nA current, has been performed on a glass substrate. A thin layer of ITO on the substrate acts as conductive layer necessary for the following electrolytic growth. The substrate was previously spinned with a 490 nm thick PMMA resist layer. After the spin coating, the resist has been soft baked at 170 °C on a hot plate for 10 minutes. A dose of 1200 $\mu C/cm^2$ has been used during the exposure. The area patterned on the substrate by the EBL process has a dimension of 2 mm x 2 mm. Although a smaller area could be fabricated, samples with large and uniform SERS active surfaces can be more easily implemented in practical devices. After the exposure, a methyl-isobutyl-ketone (MIBK) solution diluted with isopropyl-alcohol (IPA) (volume ratio: MIBK:IPA=1:3) has been used for the resist development (30 sec at room temperature). After the development the resist has been rinsed in pure IPA. The metallic structures were obtained through an electrolytic growth made on the ITO layer. The electrolytic bath used in the process is the commercial solution Karatclad™ 265 HS, with 4.5 nominal ph. The deposition temperature was 36° C, Au 8 gr/l, density 15 Bè. A growth current of 100 mA, voltage

of 2.9 V and growth time of 45 sec have been used for the process. The growth rate was calibrated to be 3.3 nm/sec. As pointed out in the previous sections, in order to obtain hot spots inside the slits, we need a precise geometry. Due to the critical sensitivity of the grating design all the fabrication parameters have been precisely controlled. For this reason dose correction to compensate for the proximity effect was required to obtain good shape definition. Remarkable is that the gold grating has been grown on a transparent substrate, necessary for the optical characterization. In Figure 3.14 is shown a fabricated gold grating.

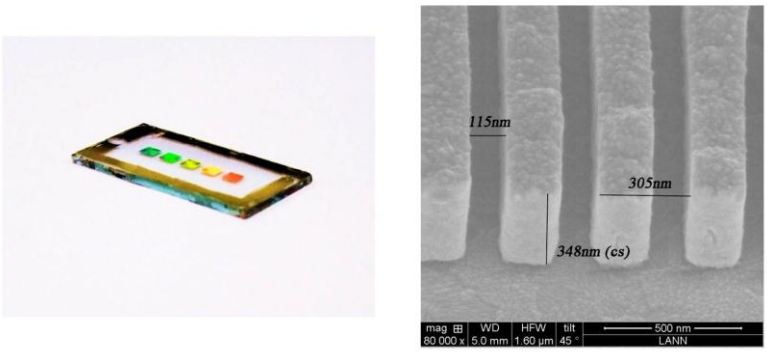

Figure 3.14 1D gold grating used for SERS measurements and SEM image of the fabricated geometry. It's clearly visible the ITO structure underneath the gold ridges. The period is about 305 nm, slits width about 115 nm and metal thickness about 348 nm. The geometrical parameters correspond to the optimized geometry found with FEM simulations.

3.4.4 Experiments and results

SERS measurements have been performed with a Renishaw micro-Raman instrument employing a 50x microscope objective and the 632.8 nm line of a He-Ne laser as laser source. Spectra are acquired with different laser polarization, transverse magnetic (TM) and electric (TE) modes. The determination of the SERS enhancement factor is performed by recording the SERS signal of a benzenthiol (BT) monolayer adsorbed on the metal nanostructure. BT presents an intense Raman signal at 992 cm^{-1}, corresponding to the breathing of the benzenic ring, with a well-known Raman cross-section [27]. The SERS Substrate Enhancement Factor (SSEF) can be evaluated by using the formula [27]:

$$SSEF = \frac{I_{SERS} / N_{Surf}}{I_{RS} / N_{vol}} = \frac{I_{SERS}}{I_{RS}} \frac{C_V H_{eff}}{C_S} \frac{\sigma_{toluene}}{\sigma_{BT}} \frac{1}{A} \tag{3.11}$$

where I is the Raman signal intensity of the molecule monolayer absorbed on the metal surface ($SERS$) and the liquid used as reference (RS), C_V and C_S are the volumetric and packing density of the reference liquid and the BT adsorbed, H_{eff} is the collection efficiency of the experimental set-up, σ is the Raman

differential cross section and A is the ratio between the patterned area and a flat one. As liquid reference we have used Toluene, instead of Benzenethiol, for technical reasons. The volumetric density of Toluene and the packing density of Benzenethiol are known from the literature: $C_V = 5.69 \cdot 10^{21}$ molecule/cm^3 and $C_S = 6.8 \cdot 10^{14}$ molecule/cm^2 [28-30]. The ratio $\sigma_{Toluene}/\sigma_{BT}$ was measured to be 0.56. Figure 3.15 shows SERS spectra of BT: the Raman signal recorded with TM polarization is much more intense than the one recorded with TE polarization, as foreseen by simulations.

The experiment is characterized by the possibility to compare the SERS intensity I_{SERS} for the two polarizations without changing any other experimental parameter. The ratio of the SSEF factors in equation (3.11) allows to identically eliminate all the other factors except for the I_{SERS} contribute for the two perpendicular polarizations, according to the following formula:

$$R = \left[\frac{SSEF_{TM}}{SSEF_{TE}}\right]_{\exp} = \left[\frac{I^{SERS}{}_{TM}}{I^{SERS}{}_{TE}}\right]_{\exp} = \left[\frac{SSEF_{TM}}{SSEF_{TE}}\right]_{theor} \tag{3.12}$$

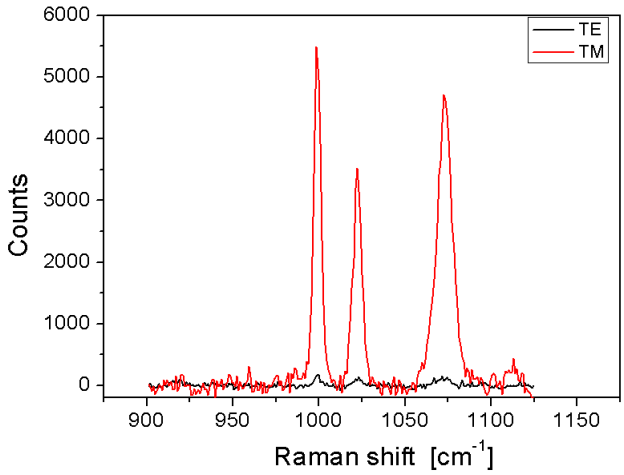

Figure 3.15 SERS spectrum of BT recorded with TM (red line) and TE (black line) polarization.

A similar reasoning can be performed for the simulation data (the fourth term in equation (3.12)). The SERS EF for a specific molecule functionalization on a specific substrate can in principle be computed by spatial averaging of the enhancement factor of a single molecule, $M_{Loc}(\omega L)$, $M^{PW\text{-}P}{}_{Loc}(\omega_R)$, averaged over the entire metallic surface:

$$SSEF^P = \left\{ M_{Loc}(\mathbf{r},\omega_L) M^{PW-P}_{Loc}(\mathbf{r},\omega_R) \left[T(\alpha_N, \mathbf{e_{Loc}}(\mathbf{r},\omega_L), \mathbf{e^{PW\text{-}P}_{Loc}}(\mathbf{r},\omega_R)) \right] \right\} \tag{3.13}$$

Rigorous definitions about the terms in equation (3.13) are provided in Ref. [27]. The curly brackets {...} denotes spatial averaging; the square brackets instead [...] represent the averaging over allowed molecular orientations of the $T(\alpha_N, \boldsymbol{e_L}, \boldsymbol{e}_R)$ surface selection rules factor which couples the excitation and re-emission problems through the normalized Raman polarizability tensor (characterizing the symmetry of the Raman tensor and the molecular orientation). Substantially the total SERS Enhancement Factor is due to two multiplicative factors: the electromagnetic M factor and the chemical one [27]. The M factors can be computed taking into account the field distribution provided by simulation code within the $|E|^4$-approximation [27]. On the contrary, the contribute in the square brackets is independent of the EM field and depends only on the molecule orientations of the molecules on the surface of the grating being simplified when we compute the ratio between the theoretical estimation of SSEF in equation (3.13).

Equation (3.12) allows to directly compare the experimental and the theoretical enhancements factors (Table 3.1). The error associated to the experimental SSEFs is calculated from experimental data collected in different sample regions and it gives an estimation of the homogeneity of the device. Although a polarization dependence is shown in Figure 3.15 and a match between the experimental and theoretical ratio in equation (3.12) has been achieved (see Table 3.1), for a systematic confirmation of this preliminary result, further investigation is required in order to figure out the role played by other factors in the experimental determination of the ratio R.

THEORY		**EXPERIMENT**	
EM EF_{TM} (SEM)	**EM EF_{TE} (SEM)**	**$SSEF_{TM}$**	**$SSEF_{TE}$**
6.43 (A=4.2)	0.17 (A=4.2)	245.67 ± 9.82	7.51 ± 1.51
R		**R**	
37.43		32.68 ± 6.52	

Table 3.1 Comparison of the theoretical and the experimental EFs. EM EFTM/TE (SEM) is evaluated in the $|E|^4$-approximation [3], using the SEM measured geometrical parameters. Experimental SSEFs are evaluated using equation (3.11). R is the ratio defined in equation (3.12).

To this purpose we realized a second series of samples, with geometrical characteristics slightly different from the previous (period d = 300 nm and metal thickness h = 400 nm, optimized for a slit width a = 80nm), from the analysis of which we experimentally determined the ratios R as: R = 46 ± 5. Due to the different grating parameters, the theoretical R ratio has been recalculated. The obtained value is R = 42. This result confirms the agreement between the experimental and theoretical ratios and supports the

reliability both of the numerical simulations and of the nanofabrication process, thus confirming the validity of the $|E|^4$-approximation in the evaluation of the Enhancement Factor and the potentiality of the nanofabrication technique in the engineering of plasmonic substrates.

In order to experimentally characterize the relation between the SSEF factor and the polarization angle (ϕ) of the incident light, i.e. the dependence of SSEF on a generic hybrid polarization, we must sum together the contributions of SSEF_{TM} and SSEF_{TE} at the different polarization angles. To estimate it theoretically, we must simply calculate the percentage of the incident power polarized in the TM and TE modes. The Malus's law says that when a polarizer is placed in a plane polarized beam of light, the intensity, I, of the light that passes through is given by:

$$I = I_0 \cos^2(\phi) \tag{3.14}$$

where I_0 is the initial intensity and ϕ is the angle between the light's initial polarization direction and the axis of the polarizer. Therefore, $I_{TM} = I_0 cos^2(\phi)$ and $I_{TE} = I_0 sin^2(\phi)$. Since SSEF is proportional to $|E|^4$, the expected dependence of the SSEF factor on the polarization angle will be approximately of the type $Acos^4(\phi) + Bsin^4(\phi)$, where, due to the absence of plasmonic effects, the contribution of the TE mode will be in general very small.

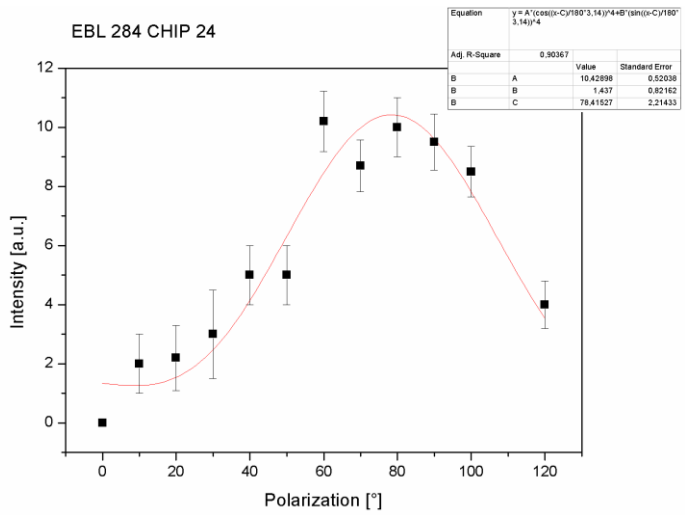

Figure 3.16 SERS signal intensity dependence on the incident polarization angle. The error bars have been estimated from the signal to noise ratio of the single measures.

Measuring experimentally the variation of the SERS signal intensity to the changing angle ϕ, we obtained the plot showed in Figure 3.16, which appears to be properly fitted by a curve of the type $Acos^4(\phi) + Bsin^4(\phi)$, thus confirming the theoretical predictions and the reliability of the SERS measurements.

The optical characterization of the device has been made through ellipsometric measures. In Figure 3.17 are shown the experimental transmission spectrum (red line) and the simulated spectrum (blue line). As can be seen, the agreement between theory and experiment is very good. Since the light spot impinging on the device is quite broad (hundreds of μm of diameter), the ellipsometer delivers global information of the sample analyzed: the good agreement between the simulated and experimental spectra is therefore indicative of the quality of the device. A plasmonic peak is observed at 570 nm, followed by a dip at 633 nm, which is exactly the wavelength of the SERS laser beam used. Note also the scattering of the cavity mode on the ITO substrate, generating a SPP on the gold-ITO interface. Around 900 nm there is a very intense cavity mode, with a transmission experimental value of 63%. The difference in intensity and position between theory and experiment can be due to the uncertainty on gold thickness and on the determination of the dielectric constant of the glass substrate.

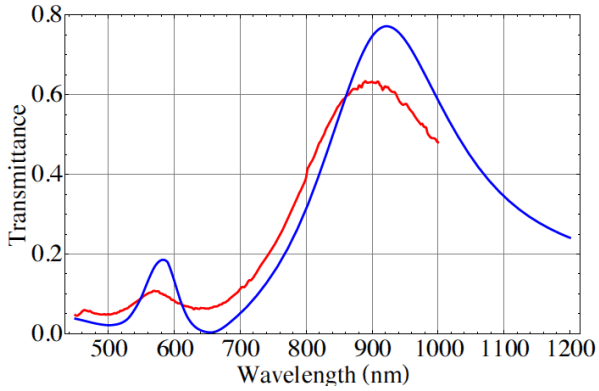

Figure 3.17 Experimental (red line) and simulated (blue line) transmission spectra.

3.4.5 Conclusions

In conclusion, a 1D digital gold grating has been simulated varying its geometrical parameters in order to find an EM field configuration showing hot-spots inside the slits. The Enhancement Factor of the optimized structure has been evaluated in the $|E|^4$-approximation. A device with the optimized geometry has been fabricated by Electron Beam Lithography and electrolytic growth developing an easy and reliable nanofabrication process, and Raman performances have been measured with a 632.8 nm laser line. Thanks to the simple geometry, the SERS Enhancement Factor (SSEF) of the realized nanostructures and its dependence on a generic hybrid polarization have been measured and compared with the theoretical calculated estimations. A good agreement between the experimental and numerical $SSEF_{TM}$ to $SSEF_{TE}$ ratio, added up to a well-tested nanofabrication process able to guarantee a good uniformity and reproducibility of the device, have confirmed the potentiality of the nanofabrication technique in substrate engineering to provide local fields of the desired intensity and location. This result is a good

starting point for tailoring the properties (like field distribution) of more complex nanostructures, which can be optimized and exploited for example in SERS and micro-fluidics applications.

3.5 Integration of plasmonic gratings on GaAs HEMT photodetectors for biosensing application

Biosensing [37] is a cutting-edge topic in 21st century scientific research, revolving around multidisciplinary contributions from various fields: materials science, physics, chemistry, biology, as well as engineering and medicine. A biosensor is a device able to detect target molecules by converting the biological response of an analyte sensitive receptor into a quantitative optical or electrical signal. This determination can be qualitative, identifying a specific compound, and/or quantitative, extracting the analyte concentration. Such a technology is attracting a significant amount of interest, since its applications are widespread and involve also health-related purposes, namely diagnostics. Plasmonics has been found particularly suitable to be integrated in this context [32-34, 37]. As we have seen in the previous chapter, phenomena like surface plasmon polaritons (SPPs) and extraordinary optical transmission (EOT) at a metal/dielectric interface are intrinsically sensitive to surface properties variations, as in the event of a bio-recognition process. As a consequence, light transmission and absorption properties are modified, meaning that high sensitivity devices can be realized. Surface plasmon resonance sensors are the most known example. In this section we present an optical biosensor based on a plasmonic crystal integrated on a multilayered semiconductor system. The high sensitivity of plasmonic resonances to variations of the local refractive index due to functionalization is coupled with a highly sensitive and scalable photo-detection scheme inspired by high electron mobility transistors (HEMTs). In more detail, the device is a modulation-doped AlGaAs/GaAs epitaxial heterojunction creating a two-dimensional electron gas (2DEG) at the interface, patterned at the top with an array of V-grooves and coated by a thin gold film. The plasmonic resonances of the grating, tuned by local refractive index changes due to the analytes, are transduced into modulations of the photogenerated carriers [35] in the transistor channel and measured as voltage drop between the device terminals.

The employ of HEMTs as photodetectors has not drawn much attention yet, though their renowned sensitivity under low illumination is perfectly suited for this kind of applications. There are two major advantages which this structure provides. The first is the simplicity of the detection scheme, as the system is a monolithic device whose working principle is to collect just a voltage or current measure, instead of requiring angular resolved reflectivity measurements like in spectroscopic ellipsometry based devices. The second is scalability efficiency. In fact, while photodiode based biosensors show limited possibility of miniaturization due to the dependence of the extracted signal on the area of the active surface, the current

device's performances are almost independent on its size. Light acts as an optical gate and the extracted signal can be controlled with and external driving voltage. As a consequence, a smaller quantity of analyte is required. This is a fundamental aspect for bio-medical applications. The high sensitivity has a twofold advantage: first the total amount of light transmitted toward the HEMT by the structure can be very low due to the fact that the higher sensitivity to functionalization is often reached at low absolute transmission. Second, a low light irradiance (Wcm^{-2}) can be used to extract the information. This can be advantageous in removing problems connected to the heating of the biological materials by light and convenient in order to irradiate large area of a device containing many independent HEMTs. This configuration is suitable for organizing a scheme for performing parallel biological detections on an array of biosensors.

The schematic cross section of the device together with band structure diagram for the GaAs/AlGaAs/GaAs HEMT multylayer is reported in Figure 3.18. The phototransistor used is a modulation-doped $Al_{0.42}Ga_{0.58}As$/GaAs heterostructure featuring a two-dimensional electron gas (2DEG), grown by molecular beam epitaxy and with the Al concentration chosen so that the spacer layers are transparent to the design wavelength. The top GaAs capping layer is nanopatterned with a V-groove grating, fabricated by electron beam lithography followed by anisotropic wet etching that realizes a V aperture angle of 70.5°. As it can be deduced, the working principle which is at the base of the device proposed in Figure 3.18 embrace several topics, ranging from solid state physics, to plasmonic and sensing, with different nanofabrication techniques employed for the several processes required for the completion of the final device. Of course the full description of all the phenomena and techniques is beyond the scope of this thesis' work; here we will give the description of the part regarding the plasmonic grating used as sensitive element of the final device. In particular we will show the optimized plasmonic grating's geometry and the complete fabrication process of the plasmonic grating on the final device. Regarding the electro-optical design and set-up, including the fabrication steps for the realization of the HEMT structure, a detailed description can be found in [36].

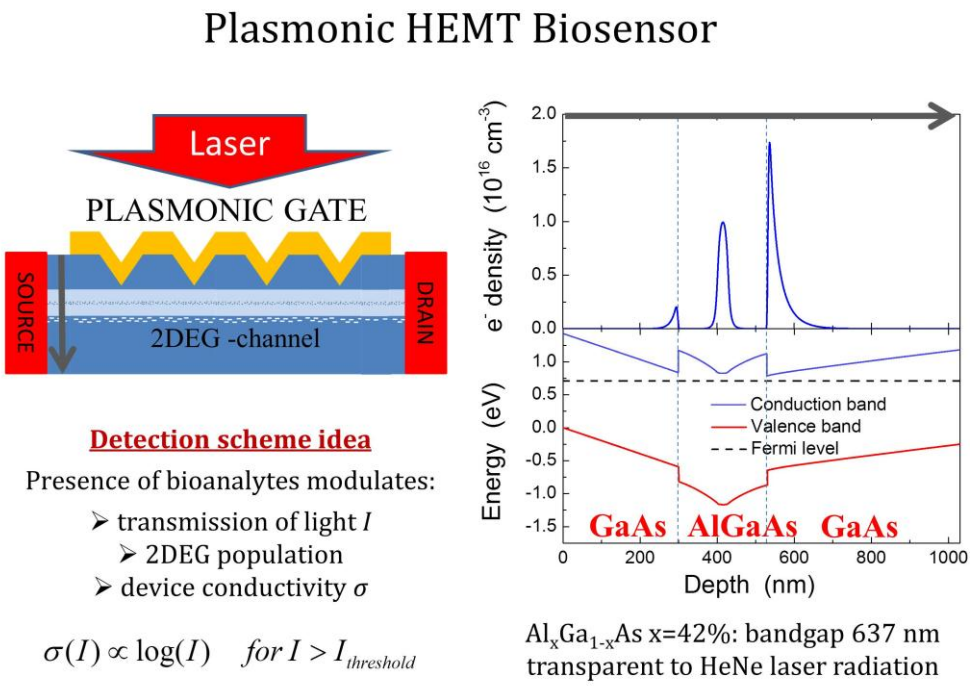

Figure 3.18 Schematic of the HEM biosensor and band structure of HEM luty-layer.. The basic idea is that the presence of bioanalytes changes the transmission properties of the grating, and consequently the 2DEG population and conductivity. By measuring the difference in voltage or current before and after the functionalization event, the binding event can be recognized.

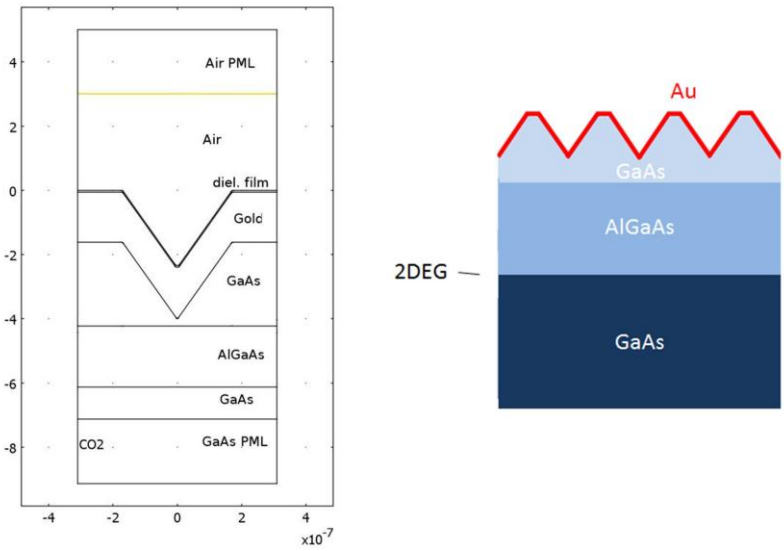

Figure 3.19 FEM model set up for the simulated V shape grating.

3.5.1 Plasmonic Grating Optimization

As we have seen in the previous parts of this chapter, plasmonic gratings which exploit EOT phenomena could be designed in order to generate EM field hot-spots in subwavelength regions at the metal/air interface. Since SPP are very sensitive to surface conditions, if the grating is designed to support a plasmonic resonance at a given configuration, a change in the environment (like a functionalization event) will dramatically change the near and far field response of the grating. This will change quantities like reflectance, transmittance and EM field profile. Depending on the working principle of the final biosensor and on the particular events that have to be recognized, an accurate modeling and optimization of the grating's geometry must be performed. In our particular case, the plasmonic crystal layout is designed, by full EM field numerical simulations, to maximize transmittance variation between the bare surface (refractive index n=1) and the surface coated by a 5 nm-thick layer with refractive index n=1.45, for TM-polarized normally impinging light at normal incidence (0°) and fixed wavelength of 633 nm.

In particular the optimization process is carried out in the same fashion of the one used in the previous section for SERS, by performing multi-parametrical simulations in order to fully explore the phase-space of the geometrical parameters.

Although initially the geometry chosen was a simple 1D metal grating, some difficulties arose in the fabrication process, since the most sensitive configuration to transmittance variation required the realization of 10 nm wide metal slits. A new configuration is then proposed, which consists of a V-shaped grating. Figure 3.19 shows the FEM model and grating's geometry used for the simulations. The grating is placed on a GaAs/AlGaAs/GaAs stack which forms the HEMT structure and it is responsible of the generation of the 2DEG. The V-shaped grating is covered by a gold layer in order to make it a plasmonic device. The aperture angle of the V is fixed to 70.5° by an anisotropic etching process of planar (100) GaAs which exposes sidewalls in the {111} orientation for grooves aligned to the $[01\bar{1}]$ direction (more details of the fabrication process will be given in the next section). The optimized configuration, which maximizes the transmission variance between a bare and a functionalized surface is the one corresponding to a grating with period 628 nm, duty cycle of 58% and gold thickness of 180 nm. Figure 3.20 shows the field profiles for the optimized configuration before and after the functionalization event (which correspond to a change of the refractive index of the 5-nm thick layer from 1 to 1.45). The bare configuration corresponds to the excitation of a SPP on the upper surface of the grating, like the one observed in the first of Figure 3.15. When the functionalization layer is placed, we observe instead how the field profile has changed. Although the SPP signature is still present on the upper interface, we observe also the presence of a field concentration in the bottom of the V. This kind of resonance corresponds to the excitation of a local geometrical vertical resonance, like a Fabry-Pérot resonator [38]. The SPP and Fabry-Pérot

resonances are spectrally close, and their interaction lead to the configuration with the maximum transmittance variation, as it can be seen from the plot of transmittance versus incidence angle in Figure 3.20. With the optimized configuration, the transmittance variation at 0° incidence angle is $\Delta T = 530\%$, and the total transmittance from the grating to the HEMT structure is $T \sim 10^{-4}$, grating high sensibility and high responsivity of the device.

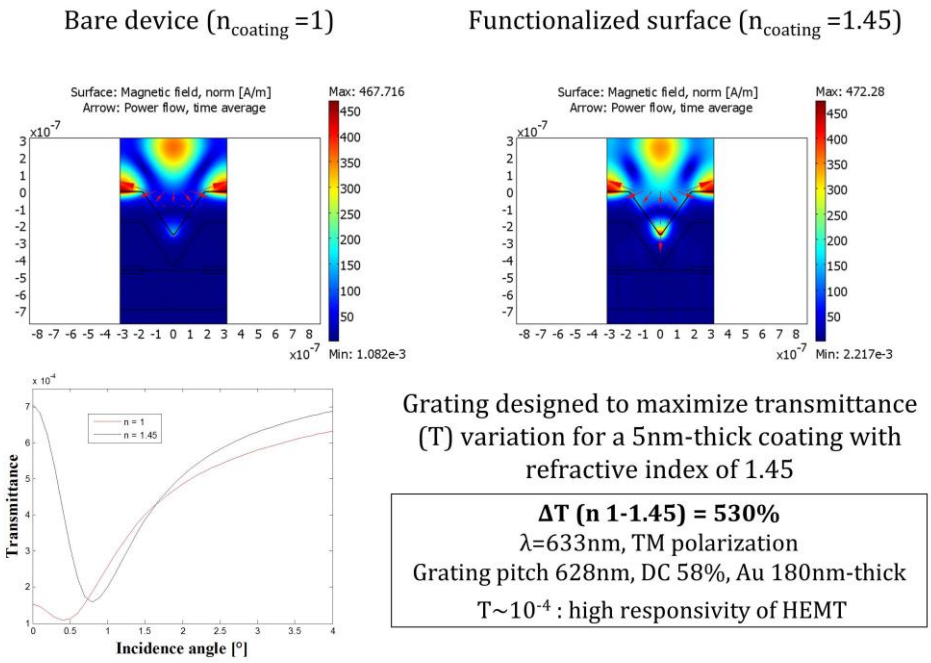

Figure 3.20 Optimized geometry for the V shape grating. Electric field norm shows the two different field distribution between the bare and functionalized configuration. The absolute transmittance difference is maxium at 0° incidence angle, with a value of 530%.

3.5.2 Fabrication of the Plasmonic Grating

With the correct geometrical parameters found, the fabrication process of the plasmonic grating can be performed. The fabrication of the plasmonic grating is the last step of the fabrication of the final device, and it is performed on a previously fabricated MESA, which includes the HEMT layers and the hall bar contacts for the detection of the signal. The main challenge in this case is to expose the grating area with nanometric precision on the gate of the HEMT structure, between source and drain. Figure 3.21 shows the CAD image of the MESA where the darker areas indicates where the plasmonic grating must be placed. Few microns of misalignment could compromise the contact on the active area. Moreover, also a perfect

orthogonal alignment between the grating direction and the hall-bar is required, in order to provide the correct polarization excitation of the SPP resonances. An example of exposed area is also shown in Figure 3.21. The patterned area is the blue zone in the center of the picture, and has a dimension of 500x500 μm^2 . Also the cross mark used for EBL alignment is visible.

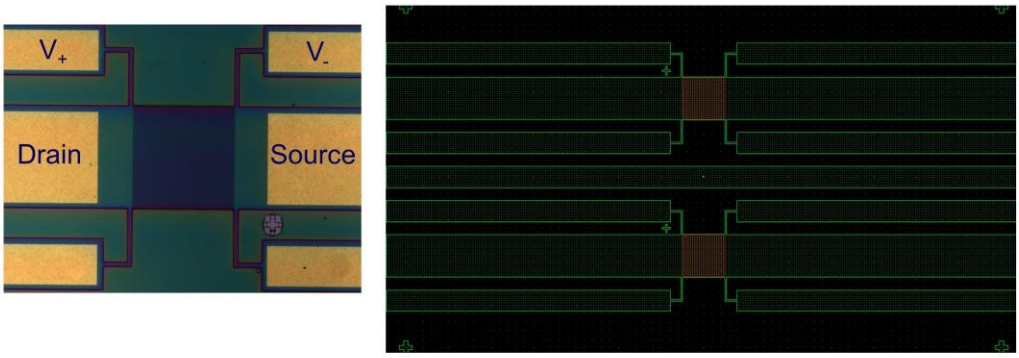

Figure 3.21 Left: optical microscope image showing a detail of the active area (the blue area) where the plasmonic grating must be expose. A cross alignment bar is visible in the lower-right corner. Right: CAD file showing the final layout for the active areas (red areas) with the alignment cross marks.

The fabrication steps can be summarized as follows:

- Electron Beam Litography (EBL) is performed on the active area between source and drain.
- After the exposure and development, the pattern created with EBL is used as a resist mask for an anisotropic wet etching of GaAs layer; this ensures the creation of the V shape pattern.
- Finally the metal grating is created by means of thermal evaporation of gold, followed by a lift-off and stripping of the resist mask.

In more details, the EBL exposed pattern consists of an array of straight lines with period of 628 nm. The exposure is made directly on the HEMT multi-layer, with a 500 nm PMMA layer as positive resist. The EBL machine operates at 100 keV, with 2 nA current in order to assure both high resolution and speed. The final geometry of the optimized device requires the duty cycle to be precisely 58%, which means that the upper aperture of the V must be 360 nm. However, the EBL step has the purpose to create only the mask for the following etching process of the GaAs layer. If a 358 nm wide line is exposed directly, the etching process would make the final width of the grating a lot larger. Also the proximity effect in the lithographic process is another cause of line width broadening. To compensate all of these effects, we perform several tests on a GaAs wafer in order to find the best and more consistent parameters for initial pattern line width, exposure dose, PMMA developing time and etching developing time. The final

parameters are the following: the pattern exposed has a line width of 50 nm and exposure dose of 860 $\mu C / cm^2$, and it is developed in water:IPA=3:7 solution for 60 seconds. After that, the unexposed areas of PMMA are used as mask for the wet etching of the GaAs layer. The etching solution is made by H_2O:H_2O_2:H_2SO_4=40:8:1 solution. The etching time has been fixed to 25 seconds in order to prevent the complete etching of the GaAs layer down to the AlGaAS layer.

Whit all of the fabrication parameters known, it is then possible to perform the entire process on the complete HEMT structure. As said before, a perfect alignment is required. To do so, we include in the HEMT a cross-marker near the active area to be exposed. The EBL machine is able to recognize this marker, and in particular, by performing a double scan along the two arms of the cross, to calculate and memorize the marker position. By telling the machine the distance of the active area from the marker, is then possible to perform the EBL exposure with the required precision level. The samples can be then fully processed, and the final results after the metal evaporation step is showed in Figure 3.22a,b. As it can be seen, the V-shape geometry is obtained, with the desired geometrical parameters. A picture of the complete device is also shown in Figure 3.22c,d.

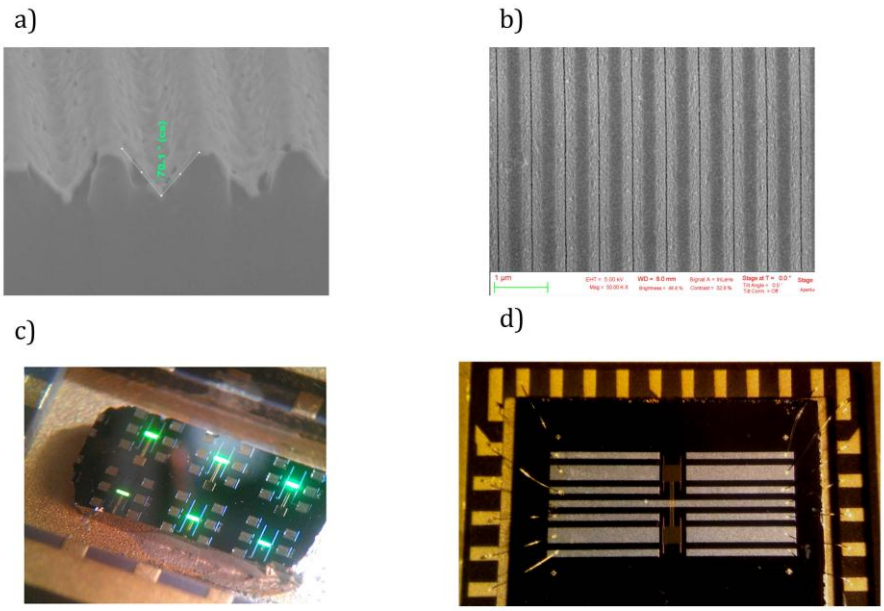

Figure 3.22 a): cross section of the V grating after the etching and metal deposition processes. The etching angle of 70° is visible. b): top view of the V grating after etching and gold deposition. The period is 628 nm and the width of the V grooves at the top is 360 nm, as desired. c): image of an array of completed devices. d): detail of a complete device with two active areas where the plasmonic gratings are placed. The electric bonding for electrical measures is also visible.

3.5.3 Experimental Measures

To conclude this section, we report some preliminary optical and electrical measures on a complete device. The optical measure consists of a reflective spectrum taken in the wavelength range between 500 and 800 nm. The angle of incidence is set to 15°. Although the device is designed to work at normal incidence, unfortunately the ellipsometric set-up located at LaNN laboratory does not allow to perform reflectivity measures at angles smaller than 15°. This fact prevents the direct far field observation of the plasmonic resonances supported by the grating, but the measure can still be used as a check with the corresponding simulated spectra at 15°. If at least a similar qualitative behaviour is observed, than we should expect that also at 0° the fabricated device behaves very similar to the simulated one. Figure 3.23 reports a comparison between the experimental and simulated data. We can see that on a qualitative level, the reflective trends are similar, with the same sequence of dips and peaks. The wavelength mismatch and also the fact that the absolute transmission at wavelengths greater than 780 nm exceeds the value of 1 can be attributed to technical problems of alignment between the incident light and the sample. In fact, the active area of the grating is 500x500 μm^2 and even with using a focusing probe the impinging light spot may not illuminates completely the grating area, leading thus to some artifacts; however the artifacts give only normalization problems, without affecting the shape of the reflection spectrum.

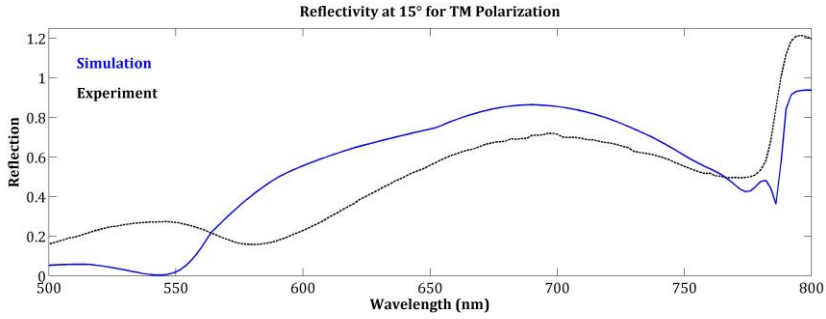

Figure 3.23 Comparison between experimental and simulated reflection spectrum for HEMT device at 15° incidence angle.

Finally it was also possible to perform preliminary measures to test the electric response on the complete device, even after a functionalization event. Figure 3.24 shows measurement of channel resistance (V_{ds}) as a function of incidence angle (θ) for a bare and functionalized configurations. As we can see, the device is able to detect the resistance variation due to the presence of the avidin layer, but it isn't able to do the same for the biotin layer. This can be attributed to the fact that at this stage the device is still a prototype and further optimization steps are required, especially on the electronic part. Nevertheless, the measured trend of the conductivity versus incidence angle (Figure 3.24), before and after the sequential coating of the active area with a biotin-avidin bilayer, is in excellent agreement with the

simulated transmittance curves. Comparing optical modelling and experimental results, we calculated that the resolution achievable by this scheme is about $2 \cdot 10^{-5}$ refractive index units.

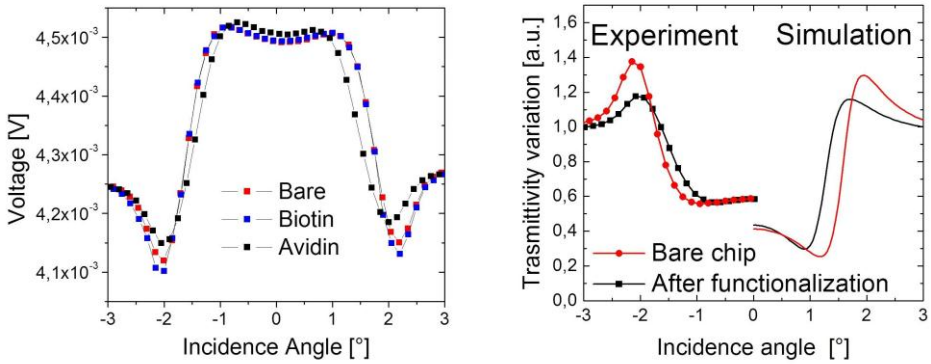

Figure 3.24 Left: Conductivity vs incidence angle for three different HEMT device configurations. The difference in signals between the bare and avidin functionalized configurations is visible. Right: Transmittance variation as function of incidence angle between bare and functionalized configuration. Experimental and simulated data show good agreement.

3.5.4 Conclusions

In conclusion, in this section we have shown the implementation of a plasmonic structure on a prototype of a complete biosensor device. Starting from a studied plasmonic effect (light concentration by means of EOT), it has been possible to design and model a plasmonic grating in order to maximize the transmittance variation trough a HEMT multilayer geometry. With the optimized parameters, the plasmonic grating has been fabricated and integrated on the HEMT structure, in order to be experimentally tested under different conditions. The preliminary measures show good agreement with theoretical predictions. These results are a good example on how plasmonic can be successfully applied and integrated to other branch of physics towards the development of a practical device. For this purpose, every part of the modelling-fabrication-characterization chain must be carefully analyzed and developed with particular care to the following step.

3.6 References

[1] Bethe H. A. Theory of diffraction by small holes. Phys. Rev. 66, 163-182 (1944).

[2] Ebbesen T. W., Lezec, H.J., Ghaemi, H.F., Thio, T. & Wolff, P. A. Extraoridanry optical transmission thorugh sub-wavelength holes arrays. Nature 391, 667-669 (1998).

[3] Pang Y., Genet C., Ebbesen T. W. Optical transmission through sub-wavelength slit apertures in metallic films. Opt. Comm. 280, 10-15 (2007).

[4] Degiron A., Ebbesen T. W. The role of localized surface plasmon modes in the enhanced transmission of periodic sub-wavelength apertures. J. Opt. A: Pure Appl. Opt. 7, S90–S96 (2005).

[5] Garcia-Vidal F. J., Martin-Moreno L. Tranmission and focusing of ligth in one-dimensional periodically nanostructured metals. Phys. Rev. B 66, 155412 (2002).

[6] P. Lalanne, J.P. Hugonin, J.C. Rodier, "Theory of surface plasmon generation at nanoslits apertures", Phys. Rev. Lett. 95, 263902 (2005).

[7] L. Salomon, F. Grillot, A.V. Zayats, F. De Fornel, "Near field distribution of optical transmission of periodic subwavelength holes in a metal film", Phys. Rev. Lett. 86, 1110 (2001).

[8] J. A. Porto, F.J. Garcia-Vidal, J.B. Pendry, "Transmission resonances on metallic gratings with very narrow slits", Phys. Rev. Lett. 83, 2845 (1999).

[9] S.G. Rodrigo, F.J. Garcia-Vidal, L. Martin-Moreno, "Influence on material properties on extraordinary optical transmission through hole arrays", Phys. Rev. B 77, 075401 (2008).

[10] F.J. Garcia-Vidal , L. Martin-Moreno, T.W. Ebbesen , L. Kuipers, "Light passing trough subwavelength apertures", Rev. Mod. Phys. 82, 729 (2010).

[11] D. Crouse, P. Keshavareddy, "Polarization independent enhanced optical transmission in one-dimensional gratings and device applications", Opt. Exp. 15, 4 (2007).

[12] Y. Lu, M.H. Cho, Y. Lee, J.Y. Rhee, “Polarization-independent extraordinary optical transmission in one-dimensional metallic gratings with broad slits”, Appl. Phys. Lett., 93, 061102 (2008).

[13] F. Marquier, C. Arnold, M. Laroche, J.J. Greffet, Y. Chen, “Degree of polarization of thermal light emitted by gratings supporting surface waves”, Opt. Exp. 16 (8), 5305 (2008).

[14] A. Barbara, P. Quemerais, E. Bustarett, and T. Lopez-Rios, “Optical transmission through subwavelength metallic gratings”, Phys. Rev. B 66, 161403 (2002).

[15] Y. Pang, C. Genet, T.W. Ebbesen, "Optical transmission through subwavelength slit apertures in metallic films" Opt. Comm., 280, 10 (2007).

[16] D. Crouse, A.P. Hibbins, M.J. Lockyear, “Tuning the polarization state of enhanced transmission in gratings”, Appl. Phys. Lett., 92, 191105 (2008).

[17] S. Collins, G. Vincent, R. Haidar, N. Bardou, S. Rommeluère, J. Pelouard, "Nearly perfect fano transmission resonances trough nanoslits drilled in a metallic membrane", Phys. Rev. Lett. 104, 027401 (2010).

[18] P. Zilio, D. Sammito, G. Zacco, and F. Romanato, "Absorption profile modulation by means of 1D digital plasmonic gratings", Opt.Expr. 18 (19), 19558 (2010).

[19] Lord Rayleigh, "On the dynamical theory of gratings", P. Roy .Soc. Lond. A Mat., 79, pp. 399-416 (1907).

[20] F. Marquier, J.J Greffet, S. Collin, F. Pardo, J.L. Pelouard, "Resonant transmission through a metallic film due to coupled modes", Opt. Expr. 13 (1), 70 (2005).

[21] P. Lalanne, J.P. Hugonin, J.C. Rodier, "Theory of surface plasmon generation at nanoslits apertures", Phys. Rev. Lett. 95, 263902 (2005).

[22] H. Raether, Surface Plasmons (Springer-Verlag, Berlin, 1988).

[23] Gardiner, D.J. (1989). Practical Raman spectroscopy. Springer-Verlag.

[24] E. C. Le Ru, E. Blackie,M. Meyer, and, and P. G. Etchegoin The Journal of Physical Chemistry C 2007 111 (37), 13794-13803.

[25] X. Zou, S. Dong, J. Phys. Chem. B, 110, 21545-21550 (2006).

[26] K. Kneipp, H. Kneipp, I. Itzkan, R. R. Dasari, M. S. Feld, Chem. Rev., 99 (10), 2957-2975 (1999).

[27] E. C . Le Ru, P. Etchegoin, Principles of SERS, Oxford, Elsevier, 2009.

[28] K. B. Biggs, J. P. Camden, J. N. Anker, R. P. Van Duyne, J. Phys. Chem. A, 113 (16), 4581-4586 (2009).

[29] R. N. Favors, Y. Jiang, Y. L. Loethen, D. Ben-Amotz, Rev. Scien. Inst., 76, 033108 (2005).

[30] C. L. Haynes, R. P. Van Duyne, J. Phys. Chem. B, 107, 7426-7433 (2003).

[31] T.H. Reilly, S. H. Chang, J.D. Corbam, G. C. Schatz, K. L. Rowlen J. Phys. Chem. C, 111 (4), 1689-1694 (2007).

[32] F. Romanato, K. H. Lee, G. Ruffato, and C. C. Wong, Applied Physics Letters 96, 111103 (2010).

[33] G. Ruffato and F. Romanato, Optics Letters 37, 2718 (2012).

[34] G. Zacco, F. Romanato et al., Microelectronic Engineering 88, 1898 (2011).

[35] P. Zilio, D. Sammito, G. Zacco, and F. Romanato, Optics Express 18, 19558 (2010).

[36] G. Bovo, Master Degree Thesis, 2012.

[37] Homola, J. Surface plasmon resonance based sensors; Springer: Berlin, 2006.

[38] T. Sondergaard, S.I. Bozhevolni, Phys. Rev. B 80, 195407 (2009).

4 Plasmonic Nanofocusing by Means of 3D Tapered Structures

4.1 Introduction

In the previous chapters we have considered SPP propagation along flat surfaces or in multi-layers geometries; and we have shown that plasmonic hot-spots can be generated by exciting plasmonic resonances in 1D metallic gratings. However, there are other different geometries that can be used to guide and confine SPP. Due to their 2D and evanescent nature, we have seen that SPP can provide strong subwavelength localization of electromagnetic energy beyond the diffraction limit of light. The possibility of efficient concentration of optical energy into nanoscale regions as small as a few nanometres is one of the major advantages offered by plasmonics, which is expected to lead to a variety of new applications. This phenomenon is called nanofocusing and it cannot be achieved in conventional optics using dielectric focusing elements [1-3]. The plasmonic focusing efficiency, i.e. the electromagnetic field enhancement due to the focusing effect respect to the intensity of the incident field, can be boosted by several orders of magnitude with a careful choice of the waveguide geometry. One of the most used and studied method to overcome diffraction limit and therefore focus SPP waves, consists of slowing down an SPP wave (i.e. reduce the phase and group velocity of the wave). If the process is done very fast and the dissipation is weak, the energy can be concentrated and confined to nanoscale regions. The slowing-down process can be easily obtained by using metallic nanostructures such as tapered rods and tapered optical fibers with metal coating [4-9] along with other numerous structures such as tapered circular paraboloidal metallic gaps and nanowedges, [10–13] tapered metal films, [14] nanoparticle lenses, [15] and pyramid tips covered in a metal film [16]. All these structures are designed in order to couple an incident wave to SPP which in turn coherently propagate toward a nanometric tip. In particular, conical tips are capable of focusing light energy into regions as small as a few nanometres with a substantial local electromagnetic field enhancement up to hundreds of times near the tip. [7, 17] Strong local field enhancement near the tip opens new opportunities for giant nonlinear optical effects at the nanoscale, including possible solitary pulse propagation, surface-enhanced Raman scattering, nanoscale refractometry, etc.

The first part of this chapter reports a summary of the main results regarding plasmonic nanofocusing on a peculiar structure formed by a metallic cone. In particular it is analyzed in details the *adiabatic approximation* proposed and developed for the first time by Stockman in 2003. The dependence of the focusing effect on materials and geometry is investigated in order to find the optimized conditions. The

second part of the chapter reports the original results on a plasmonic structure designed, fabricated and tested in order to produce high light intensity enhancement in very small hot-spots. Finally in the last part of the chapter, the properties of a Plasmonic Vortex Lens (see chapter 1) are used to properly excite a SPP beam which is then coupled to a 3D metallic cone placed in the center of the PVL. This design allows to excite SPP beams with an in-plane radial polarization that coupled with the conical waveguide increases the field enhancement by an order of magnitude respect to a standard configuration.

4.2 Adiabatic Nanofocusing

In this section we will analyze in details the plasmonic nanofocusing effect by using the adiabatic approximation. One of the first studies about the effects of SP's propagating towards the tip of a metal tapered rod was done by Babadjanyan and colleagues [23]. They solved the wave equation in spherical coordinates approximately and studied the behavior of the electric and magnetic field at the tip of the rod. However the first complete analytical description of the problem was introduced by Stockman [24] in 2004. He analyzed the propagation of a SPP along a tapered metal cylinder embedded in vacuum. The cylindrical geometry allows to calculate an exact dispersion relation for the SPP propagation for any arbitrary radius of the metal cylinder giving us a complete insight about the physical mechanisms that lies at the base of the plasmon adiabatic focusing. This is not the case instead for other waveguide geometries, like for instance planar metal tapered stripes, where only numerical solutions can be found. For this reason we will take the Stockman theory as a starting point for the understanding of the nanofocusing problem, which can be then extended (at least as a first approximation) to other more complex nanofocusing structures.

The basic structure considered by Stockman consists of a metal conical waveguide with dielectric constant ε_m embedded in vacuum $(\varepsilon_d = 1)$ like the one in Figure 4.1.

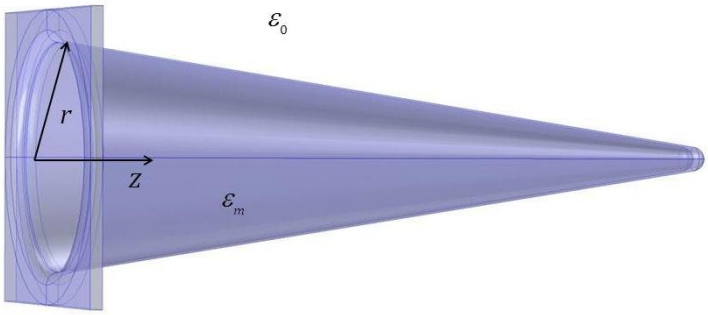

Figure 4.1 Geometry of the conical waveguide. z denotes the propagation direction, while r refers to the local radius at a given section z. The cone's tip is rounded with a curvature radius of 10 nm.

The propagation is assumed along the z-axis. Here for the calculations we follow the same approach prosed by M. Vogel [25], considering the cone at a given z position as a cylinder with a radius equal to the base radius of the cone at that given cross section. In fact, a conical waveguide can be treated as a series of cylinders whose radius continually decrease as moving towards to the tip of the cone. The dispersion relation for a SPP travelling along this type of waveguide can then be derived considering a cylindrical problem, and then the effective modal index k_{SPP}/k is expressed as a function of the local radius. Due to the symmetry of the problem, the wave equation can be expressed in cylindrical coordinates:

$$\begin{aligned}\nabla^2\mathbf{E}+k^2\mathbf{E}&=\nabla^2_{rad}\mathbf{E}+\frac{\partial^2\mathbf{E}}{\partial z^2}k^2\mathbf{E}=0\\ \nabla^2_{rad}&=\frac{1}{r}\frac{\partial}{\partial r}\left(r\frac{\partial}{\partial r}\right)+\frac{1}{r^2}\frac{\partial^2}{\partial\varphi^2}\end{aligned} \tag{4.1}$$

Where $k=\omega/c$ is the free space wavevector and c is the speed of light in vacuum. We seek a solution in the form of:

$$\mathbf{E}(r,\varphi,z)=\mathbf{E}(r,\varphi)e^{-iq_z} \tag{4.2}$$

Where q_z is the component of the wavevector along the propagation direction. Substituting equation (4.2) into equation (4.1) and by a separations of variables we get:

$$\begin{aligned}&r^2\frac{\partial^2R(r)}{\partial r^2}+r\frac{\partial R(r)}{\partial r}+\left(h^2r^2-n^2\right)R(r)=0\\ &\frac{\partial^2\Phi(\varphi)}{\partial\varphi^2}+n^2\Phi(\varphi)=0\\ &h^2=k^2-q_z^2\end{aligned} \tag{4.3}$$

Where n is an integer index. The solutions of this set of equations must be found in the form of Bessel functions, in particular the modified Bessel function of the first and second kind I_n and K_n [26]. With this choice, the component of the SPP field along the propagation direction can be expressed as:

$$\begin{aligned}E_z&=A\left\{A_1I_n(hr)+A_2K_n(hr)\right\}e^{in\varphi}\\ H_z&=B\left\{B_1I_n(hr)+B_2K_n(hr)\right\}e^{in\varphi}\end{aligned} \tag{4.4}$$

Where $A,A_{1,2}$ and $B,B_{1,2}$ are amplitude coefficients to be determined. The dispersion relation is then obtained by solving Maxwell's equation with the appropriate boundary conditions, which yields to:

$$\left(\frac{n}{r}\right)^2\left(\frac{q_z}{k_0}\right)^2\left(\frac{1}{h_d^2}-\frac{1}{h_m^2}\right)^2=\left(\frac{1}{h_2}\frac{K_n(h_d r)'}{K_n(h_d r)}-\frac{1}{h_1}\frac{I_n(h_m r)'}{I_n(h_m r)}\right)\left(\frac{\varepsilon_d}{h_d}\frac{K_n(h_d r)'}{K_n(h_d r)}-\frac{\varepsilon_m}{h_m}\frac{I_n(h_m r)'}{I_n(h_m r)}\right)$$
$$h_{m,d}=\sqrt{q_z^2-k_0^2\varepsilon_{m,d}} \qquad (4.5)$$

Where r is the radius at a given point, k_0 the free space wavevector, q_z the wavevector component along the propagation direction, and n is the index which indicates the order of the Bessel functions. Equations (4.5) allows to derive the different bound modes supported by the conical metal waveguide for any values of the local radius r, up to the tip ($r=0$).

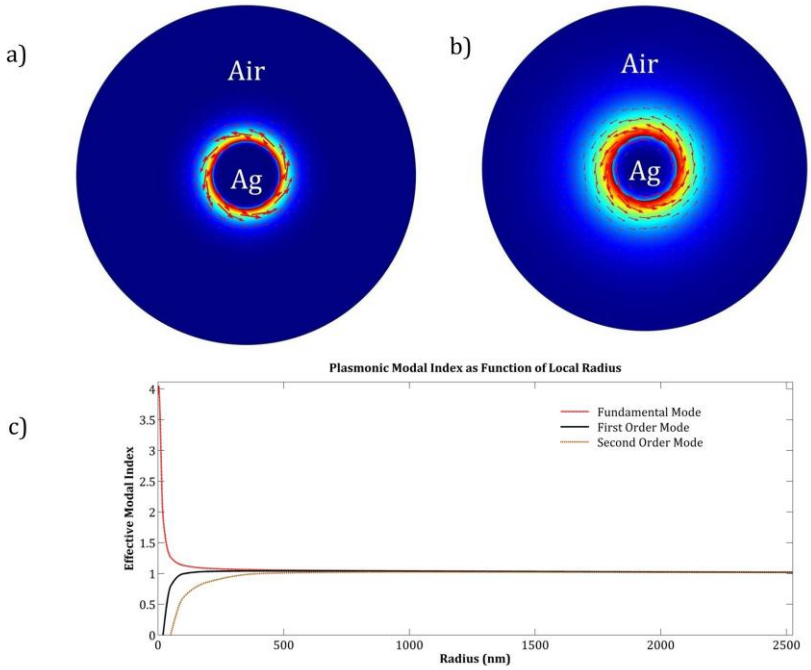

Figure 4.2 a) Electric field norm for the fundamental TM mode for a silver cylinder in vacuum at λ=633 nm for local radius of 600 nm. The mode is well confined to the metal interface. Red arrows refers to the the radial component of the electric field, which is the dominant one. b) Field profile for local radius of 150 nm. The mode is not cut-off for small radius. c) Effective index of the first three modes as function of local radius. No cut-off is observed for the fundamental mode, even for small radius.

The index n must be an integer number in order to ensure the continuity of the solutions for $\varphi=0$ and $\varphi=2\pi$. From the solution equation (4.5) it can be demonstrated that the fundamental TM mode ($n=0$) experience no-cut off with decreasing cylinder radius. This can be better understood looking at the mode profile of the fundamental TM mode. Figure 4.2a shows a FEM simulation of the norm of the electric field

for the fundamental mode for a silver cylinder in air at a wavelength of 633 nm for a local radius of 600 nm. The mode is bounded to the metal/air interface and remains well defined and confined even for very small radius, as shown in Figure 4.2b for a radius value of 150 nm. The dominant field component of the fundamental mode is the radial one and for this reason the mode can be considered a radial one.

Equation (4.5) for the fundamental mode $n=0$ can be re-written in the form:

$$\frac{\varepsilon_m}{\kappa_m}\frac{I_1(k_0\kappa_m r)}{I_0(k_0\kappa_m r)}+\frac{\varepsilon_d}{\kappa_d}\frac{K_1(k_0\kappa_m r)}{K_0(k_0\kappa_d r)}=0 \tag{4.6}$$

Where this time $n(z)=q_{zSPP}/k_0$ is the effective index of the plasmonic mode at a point z along the waveguide and $\kappa_m=\sqrt{n^2-\varepsilon_m}$, $\kappa_d=\sqrt{n^2-\varepsilon_d}$ are the complex decrements of the plasmonic filed in the metal and in the dielectric respectively. Equation (4.6) determines n as a function of the wire radius r at a given point. If the grading dependence $r=r(z)$ of the metal cylinder is known, then it's possible to calculate the effective index $n(z)$ at any point along the waveguide. Two main cases can be distinguished:

- Thick metal cylinder ($k_0 r \gg 1$): the solution of equation (4.6) tends to the case of an SPP propagating at the interface between a metal and a dielectric: $n=\sqrt{\varepsilon_m\varepsilon_d/(\varepsilon_m+\varepsilon_d)}$
- Thin nano-cylinder ($k_0 r \ll 1$): the equation can be approximated as:

$$n(r)\approx\frac{1}{k_0 r}\sqrt{-\frac{2\varepsilon_d}{\varepsilon_m}}\left[\ln\sqrt{-\frac{4\varepsilon_m}{\varepsilon_d}}-\gamma\right]^{-1} \tag{4.7}$$

Where $\gamma\approx 0.57721$ is the Euler constant. The approximation used to derive the dispersion relation (4.7) in the limit of very small cone radius r was made by Stockman in order to have an analytical expression for the plasmonic effective index $n(r)$. This approximation is called *adiabatic approximation.* Accordingly to Stockman's theory, "*the nanofocusing can be achieved by exciting SPP and then adiabatically, but as rapidly as possible, transforming them into localized Surface Plasmons (SP). The latter are purely electric oscillations that can nano-localize"* [27]. What actually happens is the following: an SPP wave excited for example by means of a grating propagates along a graded plasmonic waveguide (like the metal cone shown in Figure 4.1). If the geometrical parameters of the waveguide slowly (or *adiabatically*) change along the SPP propagation direction, then the phase velocity of the SPP tend to zero near the end of the waveguide. Of course it is mandatory that the excited SPP mode experiences no cut-off during all the propagation along the waveguide. If these conditions are fulfilled, then the SPP will adiabatically convert

from propagating to a localized SP. This adiabatic approximation is also called WKB (Wentzel-Kramers-Brillouin) approximation and it is often used in quantum mechanics [28].

As we have seen in chapter 1, in order to break through the diffraction limit and thus produce a nanofocusing effect, a great wavevector value is required in order to increase the spatial confinement of the plasmonic wave (see equation (1.22)). From equation (4.7) we see that at $r=0$ (tip position) the effective index $n=k_{SPP}/k_0\to\infty$ and consequently both the phase velocity $v_p=c/n$ and group velocity $v_g=c\left[d(n\omega)/d\omega\right]^{-1}$ tend to zero for $r\to 0$. The increase of the modal index and confinement of the plasmon (and the decrease of the group velocity) is usually associated to a severe increase in absorption losses that reduces the propagation length (the so-called trade-off between confinement and loss), thus limiting the possibility of an efficient focusing enhancement. Adiabaticity however allows to overcame this limitations; if the thinning of the conical rod is not abrupt and occurs slowly over wavelengths much larger than the effective plasmon wavelength, the transition of the SPP from propagating to localize occurs sufficiently rapid to minimize absorption leading to an efficient nanofocusing. The divergence of the wavevector in the limit of a null volume can be then considered as a necessary condition for plasmonic nanofocusing. The adiabatic stopping of the SPP mode at the end of the tapered waveguide leads maximum SPP field confinement in a very small volume with no reflection from the tip, and the concentration efficiency depends of several parameters like the length of the adiabatic waveguide, tapering angle, losses and absorption. This result demonstrates that a conical metallic waveguide is able to sustain a SPP bound mode which propagates along the entire waveguide and then it focalizes at the tip position. Figure 4.2c plots the effective modal index for the fundamental TM mode $n_{eff}=k_z/k_0$ as function of the local radius r for a silver cylinder in air at a wavelength of 633 nm calculated by means of a FEM simulation. For decreasing r values, n_{eff} remains always greater than the free space wavevector (equals to one in air) and in the limit $r=0$ it diverges. This is not the case for higher order modes which instead are cut off below a certain critical radius (see Figure 4.2), and so will be not further considered. Figure 4.3 shows the plasmonic effective index calculated accordingly to (4.7). As it can be seen the behavior is the same as the one found with FEM method thus confirming the validity of the adiabatic approximation in the limit of small cone radius. It is worth noting that besides limitations due to absorption and losses effect, the limits on the maximum field enhancement that can be obtained depends also on the minimum radius of curvature at the tip: the smallest radius, the biggest enhancement. In conclusion, as long as the tapering grading is sufficiently smooth, the adiabatic compression is valid along the entire waveguide.

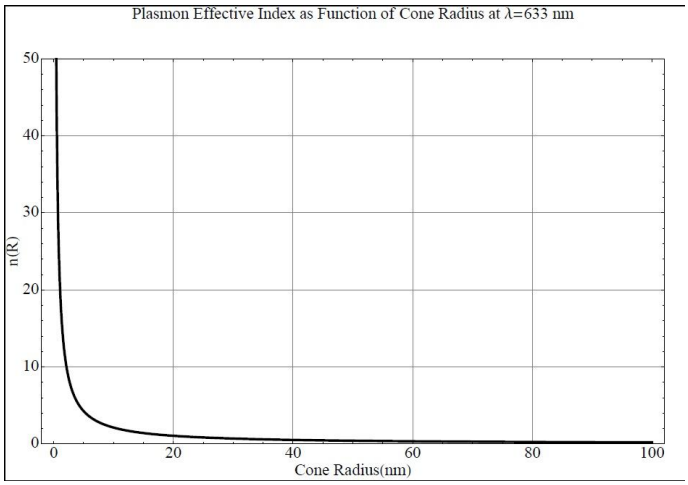

Figure 4.3 Effective plasmonic index as function of cone radius at λ=633 nm calculated using equation (4.7). The same diverging behavior of FEM simulation (Figure 4.2c) is observed.

The main problem of the analytical, but yet approximated adiabatic theory, is to find a criterion of applicability of the adiabatic approximation. For this purpose, it is convenient to express the WKB approximation under another point of view: the adiabatic propagation and compression of an SPP mode along a tapered geometry is valid as long as the SPP "sees" the waveguide at a given cross section always as a non-tapered geometry. The tapering of the guide must be very small and slow so that the variations of the plasmonic wavenvector within one plasmon wavelength are negligible at all distances from the tip of the rod and avoid also any back reflection from the waveguide's end. To express mathematically this condition, it is useful to define the adiabatic parameter δ :

$$\delta = \left| \frac{r' d\left(k_0 n\right)^{-1}}{dr} \right| \tag{4.8}$$

Where $r' = dr / dz = \tan(\alpha / 2)$ is the cone grading. For the applicability of the adiabatic approximation, accordingly to Stockman, is sufficient that:

$$\delta \ll 1 \tag{4.9}$$

It' s important to note that from equation (4.8) and (4.7) we see that at the tip position $r = 0$ the adiabatic parameter δ remains finite and so the adiabatic approximation is valid for the entire waveguide, including the stopping point at the tip. Looking at the expression of the dispersion relation and at the definition of the adiabatic parameter, we see that if the distance of the SPP from the tip is sufficiently far, the adiabatic condition is satisfied for nearly any taper angles values α . This is justified by the fact in this condition the cone diameter is larger than the plasmon wavelength, and the SPP mode is just the flat SPP mode at metal/air interface. However when the diameter of the cone became smaller than

the SPP wavelength, if the taper angle is large, then the plasmon wavenumber n starts to vary significantly thus breaching the constrain imposed by equation (4.9), which is then valid only for small enough tapering angles. As we will see later, the critical angle at which the adiabatic approximation fails depends on several parameters like the geometry of the waveguide and the kind of metal.

The structure and theory proposed by Stockman set the base for a series of different works regarding plasmonic nanofocusing on 3D cylindrical geometries, both theoretical and experimental. The adiabatic theory sets a criterion in order to have a maximum field enhancement at the tip, but it does not take in account other effects like reflection, losses and absorption that could affect the SPP propagation along the tapered rod. In 2007 Issa et al. [29] studied in details the optical nanofocusing on tapered metallic waveguides by means of FEM simulations, with particular attention to the above mentioned effects. Their results showed that in the nanofocusing process the geometrical parameters of the waveguide play a crucial role. There is an optimal tip angle of $35°$ for gold cones which gives the best field enhancement and it is independent from the initial radius of the rod. Moreover the length of the rod is not an arbitrary parameter but must be set in order to minimize the loss and attenuation at a given wavelength. Also the choice for the waveguide material is crucial, since the attenuation and losses can be minimized by choosing a metal with a low attenuation constant at the desired wavelength. Finally they showed that the maximum enhancement at the tip is obtained when the adiabatic parameter $\delta \sim 1$ meaning that the adiabatic condition is poorly satisfied. This result demonstrates that the focusing effect is not given only by the adiabatic part, but also the interactions between radiative and reflective losses give their contribution to the total field enhancement. The validity of the adiabatic approximation for conical geometries has been addressed also by Gramotnev et al. [30] in 2008. In their paper they propose a numerical optimization process for a conical rod in order to achieve the highest field enhancement at the tip. Their results show that exists an optimal taper angle which maximize the local field enhancement and at the same time minimize reflection from the tip itself. Also an optimal rod length value was found (numerically and analytically) which represents the best compromise between plasmon amplitude enhancement due to the tapering of the rod and dissipation due to plasmon propagation. The validity of the adiabatic theory for a conical tapered waveguide has been also investigated over a wide range of taper angles, and the result found showed that the approximation is still valid up to $\sim 35°$ (for gold rods) taper angle. This fact is quite remarkable, since this value is significantly larger than the one found initially by Stockman and also is larger than the one found for other focusing geometries, like for instance a tapered groove [31]. This means that the applicability of the adiabatic approximation depends also on the geometry of the waveguide.

The results found by Issa and Gramotnev highlight the fact that applicability condition (4.9)proposed initially by Stockman is too restrictive, and therefore it can be rewritten for a conical rod as:

$$\delta = \left| \frac{r' d\left(k_0 n\right)^{-1}}{dr} \right| \sim 1 \tag{4.10}$$

The aperture angle of the tip which gives the maximum enhancement is also the critical angle at which the adiabatic theory is not valid; this is expected since the largest field enhancement is obtained when the angle is large enough to collect the maximum energy but at the same time is still not too large to make reflection from the tip became significant.

To conclude the discussion about the focusing properties of a conical metallic waveguide, a complete full-field FEM simulation of a metal cone in vacuum at a wavelength of $\lambda = 633\, nm$ is shown. Due to the rotational symmetry of the problem, the model is solved without loss of generality only for one half-section of the cone, in order to reduce computational effort. This in turns allows to refine the mesh at the very end of the cone in order to get the most accurate solution of the problem. As input source it is used the fundamental TM bound plasmonic mode of the cone, like the one showed in Figure 4.2. The mode is launched at the base of the cone with a port as a boundary condition and the intensity of the associated electric field $\left|E_{BASE}\right|^2$ is used to calculate the enhancement factor at the tip as:

$$\eta = \frac{\left|E_{TIP}\right|^2}{\left|E_{BASE}{}^2\right|^2} \tag{4.11}$$

Where $\left|E_{TIP}\right|^2$ is the squared norm of the maximum of the electric field at the tip's position. By using experimental values for the dielectric constant of the metal (in this case silver or gold), and by launching the plasmonic mode at the base of the cone, it is assured that attenuation effects due to adsorption and losses are taken into account. The length of the cone is set to the optimal value calculated using the derivation proposed by Gramotnev [30]:

$$L_{opt} = \frac{\mathrm{Re}(\varepsilon_m)(1+\varepsilon_m)}{\mathrm{Im}(\varepsilon_m)\mathrm{Re}(k_{SPP})}\cos(\alpha/2) \tag{4.12}$$

Where ε_m is the dielectric constant of the metal, k_{SPP} is the SPP propagation constant at metal/air interface and α is the angle of the cone. At $\lambda = 633\, nm$ $L_{opt} \sim 25\, \mu\mathrm{m}$ for silver while for gold $L_{opt} \sim 10\, \mu\mathrm{m}$. L_{opt} is poorly dependent on the aperture angle of the cone and depends mainly on the wavelength since the dielectric constant of the metal is wavelength dependence too. Figure 4.4a plots the

enhancement as function of the apex angle for both silver and gold. We see that there is an optimal angle at which the electric field enhancement is maximum. This value is different from silver respect to gold (20° respect to 35°) due to the different propagation that the SPP undergoes along the tapered waveguide. The trend yet is similar for both metals. Of course the total enhancement depends not only on the geometry but also on losses. For most metals at visible wavelengths losses due to metal adsorption could play a crucial role in the final focusing efficiency. Therefore is mandatory to choose the proper material accordingly to the desired wavelength and application of the device. Silver for instance due to the very low value of the absorption coefficient, grants high propagation lengths and low attenuations in the visible spectrum therefore giving an highest field enhancement at the tip compared to other metals like gold and aluminum. On the other hand, due to high momentum mismatch, coupling between far field radiation and SPP is not so efficient for silver. Moreover silver has the tendency to oxide quickly making it not suitable for most optical devices. The effect of the radius of curvature of the tip has been also investigated. In Figure 4.4b is reported η as function of the tip radius. The enhancement shows a strong dependence on the radius and variations of few nanometers can give large variations of the local field enhancement. The precise control of the tip fabrication process is therefore crucial in order to precisely control the focusing effect.

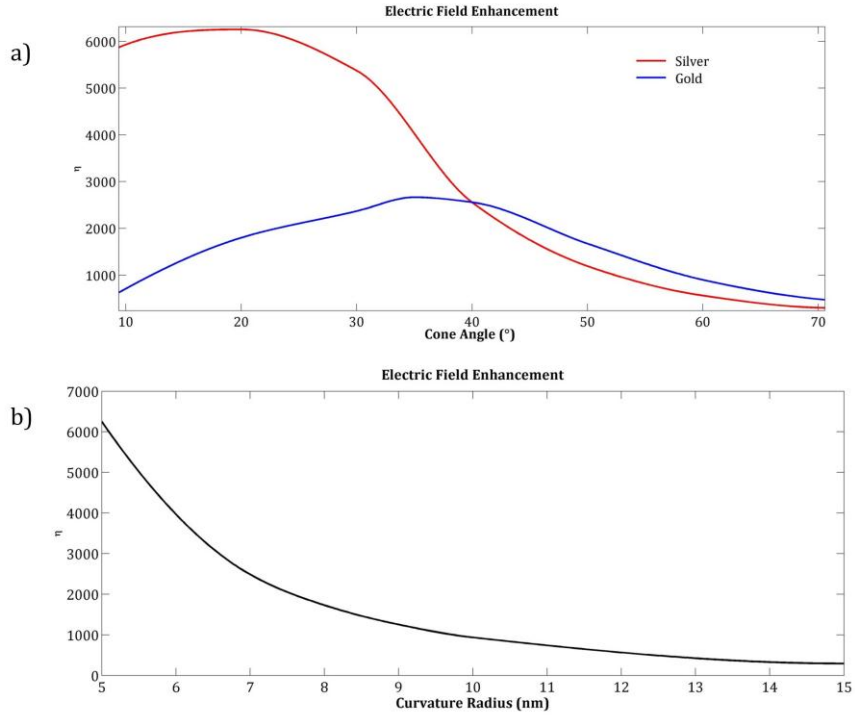

Figure 4.4 a) Electric field enhancement as function of cone angle, for gold and silver cones in vacuum at λ=633 nm. b) Electric field enhancement for a silver cone in vacuum as function of tip's curvature radius at λ=633 nm.

Figure 4.5a shows the norm of the electric field near the tip, along with the z-component (corresponding to the main axis of the cone) of the electric field for a silver cone. The aperture angle of the cone is 20° while the radius off curvature at the tip is 5 nm. The focusing effect and associated field enhancement is clearly visible. Looking at the z-component of the electric field (Figure 4.5c), it can be seen the propagation of the SPP mode at the gold/air interface. In the proximity of the tip (Figure 4.5b) the plasmon amplitude dramatically increases leading to the adiabatic condensation at the end of the tapered waveguide. Little reflection and irradiation from the tip is observed, accordingly to Stockman's theory. The enhancement factor for an angle of 20° is $\eta \sim 6300$ which proves the efficiency of the type of geometry as a light focusing device. If we now consider a larger aperture angle (40°) (Figure 4.6) we see that the enhancement factor decreased to a value of ~ 2500 and also the reflections from the tip are significantly increased, in perfect agreement with the fact that the adiabatic condition is not more valid at large angles. In these conditions a significant part of the light energy carried by the SPP is not confined anymore at the tip which leads to irradiations and back reflections. A comparison between Figure 4.5 and Figure 4.6 allows to highlight the different physical behavior of the plasmonic focusing effect when the adiabatic condition is satisfied at the tip or not. For a 20° angle the condition is still valid and we see how near the tip the SPP are compressed and slowed down. On the other hand for a 40° angle, the spatial variation of the section of the cone near the tip is too fast, and the SPP are not able to stop and condensate efficiently. In this case the adiabatic condition is valid only far from the tip, and the focusing observed at the tip is due to the fact that waveguide acts basically as a plasmonic lens, but no adiabatic compression is observed. Figure 4.7 plots the radial component of the electric field E_r for the SPP mode travelling along the lateral surface of the cone at interface metal/air, as function of the distance from the tip (the cone angle is 20°). The radial component shows slow oscillation far from the tip, while in the proximity of the tip itself the oscillation are much more quicker and wider, meaning that the plasmonic stopping and compression is actually taking place. From this behavior follows the definition of the plasmonic focusing also as "tsunami" effect, due to the dramatic increase of electric energy near the tip in the same fashion as the mechanical energy carrier by an ocean wave near a shore.

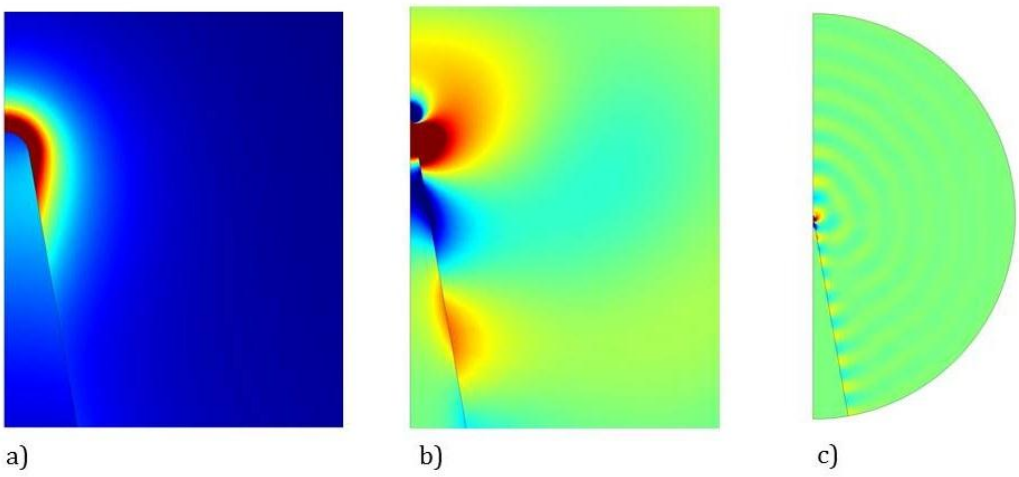

Figure 4.5 a) Electric field norm at the tip at λ=633 nm for a silver cone in air with vertex angle of 20°. The maximum enhancement is 6300 for a curvature radius of 5 nm. b) E_z component of the electric field showing SPP compression and stopping at the tip. c) SPP propagation along the entire conical waveguide. Little reflection from the tip is observed.

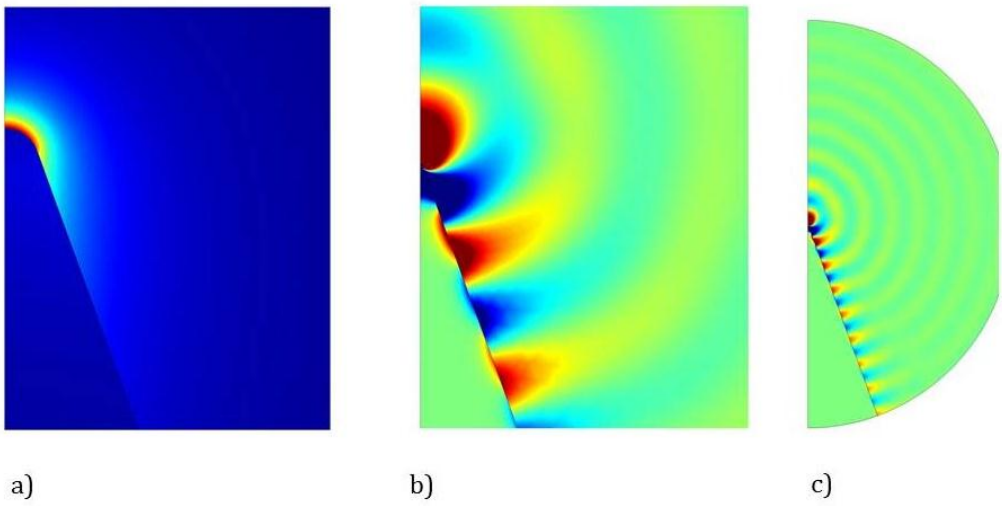

Figure 4.6 a) Electric field norm at the tip at λ=633 nm for a silver cone in air with vertex angle of 40°. The maximum enhancement is 2500 for a curvature radius of 5 nm. b) E_z component of the electric field showing that for larger angles the SPP confinement is less efficient. c) SPP propagation along the entire conical waveguide. Higher reflections from the tip are observed compared to the 20° case.

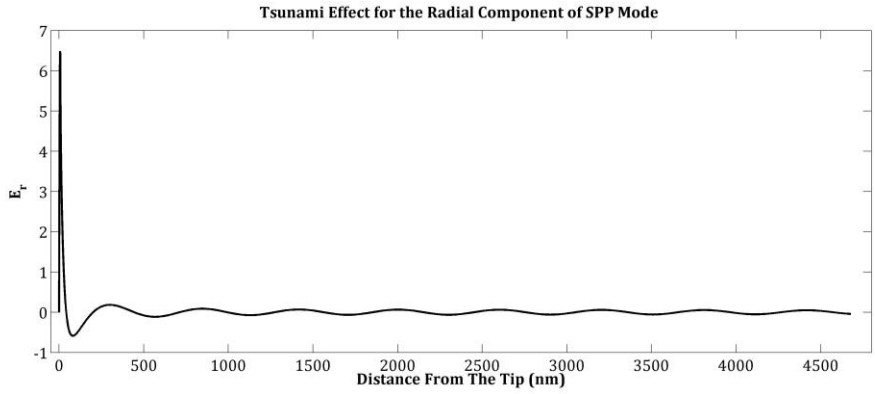

Figure 4.7 Radial component of the SPP mode propagating along the cone waveguide, as function of distance from the tip (0 is the tip's position).

4.2.1 Conclusions

In this section, the adiabatic nanofocusing on a cylindrical metal waveguide has been analyzed in details. With the help of an analytical model and FEM simulations it has been possible to point out the different physical mechanisms that generate the adiabatic nanofocusing on a metallic nanotip. The response for different materials and different geometrical parameters has been also investigated, with comparison with the results found in literature, allowing to find the best geometrical paramters for maximum field enhancement.

4.3 Fabrication of "nano-rocket-tips" for plasmonic nanofocusing

In this section are reported the results (both numerical and experimental) of an original device which consists of nano-rocket-tips used for plasmonic nanofocusing. In the previous section we have reported a detailed analysis of plasmonic conical structures with particular attention to the physical mechanisms that undergo the nanofocusing process. In the last years other studies have been conducted by several research groups using approximate methods [6, 7] analytical approach combined with perturbation methods [10] and rigorous numerical methods [17,18]. It was demonstrated that the nanofocusing capabilities of the conical tip are only weakly dependent upon variations of the tip angle and cone length around their optimal values. On the contrary, strong dependence of the local field enhancement at the rounded tip of the cone on radius of the tip was demonstrated with the typical variations of the enhancement between 100 times for the tip radius of 10 μm and 1600 times for the tip radius of 2 nm for the metallic rod of the taper angle of 35° and vacuum wavelength 632.8 nm [19]. It appears clear that the requirement of a precise geometry control of the conical tips sets a challenge for the experimental fabrication of samples in order to verify and exploit the plasmonic nanofocusing effect. Most of the experimental studies regarding focusing on conical shapes have been conducted in order to quantify the

effective field enhancement at the tip and also to find the best way to optimize the coupling between the plasmonic beam and waveguide in order to minimize losses and absorption effects. Several fabrication techniques have been employed like UV-nanoimprint lithography [32], metal etching and FIB [33], template-stripping methods [34], standard metal deposition. From these studies it emerges that not only the tip's radius of curvature is crucial in the focusing effect, but also other fabrication defects like surface roughness and impurities can affect the final focusing effect. Nonconical shapes of tapered rods may be also quite common during the fabrication processes, and their analysis will be essential for the detailed understanding, experimental investigation, and practical applications of plasmon nanofocusing in tapered rods. In addition to fabrication challenges, experimental measurements requires a nontrivial optical excitation and detection. 3D conical shape for instance requires a radial-polarized beam as a source of illumination, in order to excite with maximum efficiency the proper SPP mode . Also the near-field detection of the signal is nontrivial, since for instance with a SNOM tip, interaction between the probe and the plasmonic structure could give rise to artefacts and misleading signals. These difficulties somehow justify the fact that theoretical treatments of the focusing problem exceed the number of the experimental ones. The promising applications of the plasmonic focusing by means of 3D structure have found great interests in the field sensing, spectroscopy, in particular TERS and SERS, high-density data storage, near-field probing and microscopy [32-34].

One of the techniques to couple incident light to SPPs is the so-called Kretschman-Raether setup which consists of a thin metal film sandwhiched between transparent dielectric media with different refractive indexes (see chapter 1). Light impinging with proper angle onto the film from the high refractive index side may excite SPP modes of the film. In this experiment we try to follow this coupling scheme and to exploit it for nanofocusing purposes. In particular we report on nanofabrication of transparent metal-coated conical tips that we call "nano-rocket-tips". Focused Ion Beam (FIB) is used for the fabrication of masters. Two steps replica in transparent polymers coupled with metal evaporation allows to obtain high quality structures with good tip's radius. The transparencies of the substrate match the requirements for a precise SNOM and transmittance optical characterization.

4.3.1 Experimental methods

The fabrication of our nano-rocket-tips array requires few steps of process: focused ion beam (FIB) lithography; first negative mold replica; second mold replica; metal evaporation. A schematic illustration of the process is reported in Figure 4.8. Focused ion beam lithography were carried out by a FEI Nova i600 Dual Beam System. A focused Ga+ ion beam with energy of 30 keV and a probe current of 9–21 nA was used for the milling process. Nano-tips were milled in silicon in arrays by following the criteria illustered in fig.1. Due to "proximity" effects related with the high current used conical structures have been

obtained on the not-milled zone. The cones have been prepared with base ranging from 0.75 up to 2μm large and with maximum heigth of 7μm. FIB fabricated silicon nano-rocket tips arrays were analyzed in order to derive the 3D structure of the cones. Once chosen the proper dielectric material (NOA) and metal layer (Ag) thickness, the FIB fabricated tips were used as masters for making negative copies in PDMS using RTV615 silicone. The PDMS masters were plasma bonded to glass slides. The PDMS stamps thus obtained were used to produce positive copies of the tips in NOA61 a thiolene optical adhesive (Norland Optical Adhesive) by UV curing a drop of the resin squeezed between a glass slide and the PDMS stamp. Curing was carried out using a 100 Watt UV flood lamp (SB100P Spectroline) optimized for 365 nm wavelength emission at a distance of 10 cm from the sample and for a duration of 20 min. For reliable demolding a motorized tension stage was used, allowing detachment at a controlled displacemnet rate. Finally replicated NOA copies were metallized by 40nm Ag evaporation by means of e-beam. Optical characterization of the prepared tips array was performed by means of Scanning Near-Field Optical Microscope (SNOM). This microscopy technique allows the investigation of nanostructure that breaks the far field resolution limit by exploiting the properties of evanescent waves. This is done by placing the detector very close (distance much smaller than wavelength λ) to the specimen surface and allows a surface inspection with high spatial, spectral and temporal resolving power. With this technique, the resolution of the image is limited by the size of the detector aperture and not by the wavelength of the illuminating light. In particular, lateral resolution of 20 nm and vertical resolution of 2–5 nm have been demonstrated [21]. In this experiment SNOM measurements over the rocket tips array were performed in transmittance mode at a λ=633nm (HeNe laser source). Moreover, in order to evaluate the enhancement effect at the tip a blank measurement of the incoming wave are needed. Hence, SNOM spectra was also measured on a transparent substrate.

4.3.2 Results and discussion

SEM micrographs of the milled tips array are reported in Figure 4.9 along with detail of the tip radius. Values below 20nm have been obtained with all the prepared samples. The 3D profile of the tips has been derived from direct measurements on SEM micrographs by using the internal meter of the system. Angles at the tip ranging from 16° up to 30° depending on the conditions of the beam (beam current and focus offset). Other few examples are illustrated in Figure 4.9. Figure 4.10 reports SEM micrographs of replicated nano-rocket tips array. After the two steps mold-replica and metal evaporation the tip radius increase up to 40nm (figure 4b). We can argue that this is mainly related with the first replica step. The PDMS used for the negative replica of the cone tips, in fact, has a small density and this does not allow to maintain the low tip radius during the strip process. Although the PDMS polymer fills perfectly the Silicon

master, after the stripping it tends to partially collapse increasing the radius of the sharp edges [22]. Naturally, also the metal evaporation can introduce an additional tips radius.

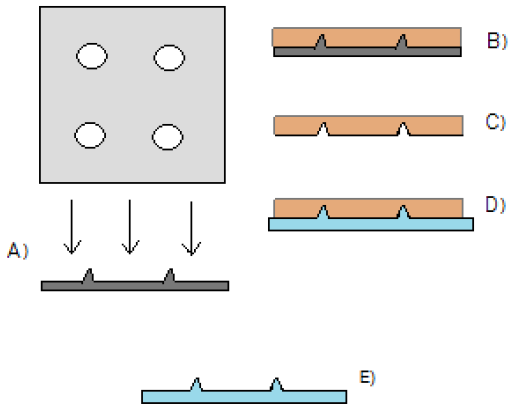

Figure 4.8 Schematic diagram of the nanofabrication procedures. A) FIB lithography; B) PDMS mold replica; C) PDMS Stripping; D) NOA mold replica; E) NOA Stripping and metal evaporation

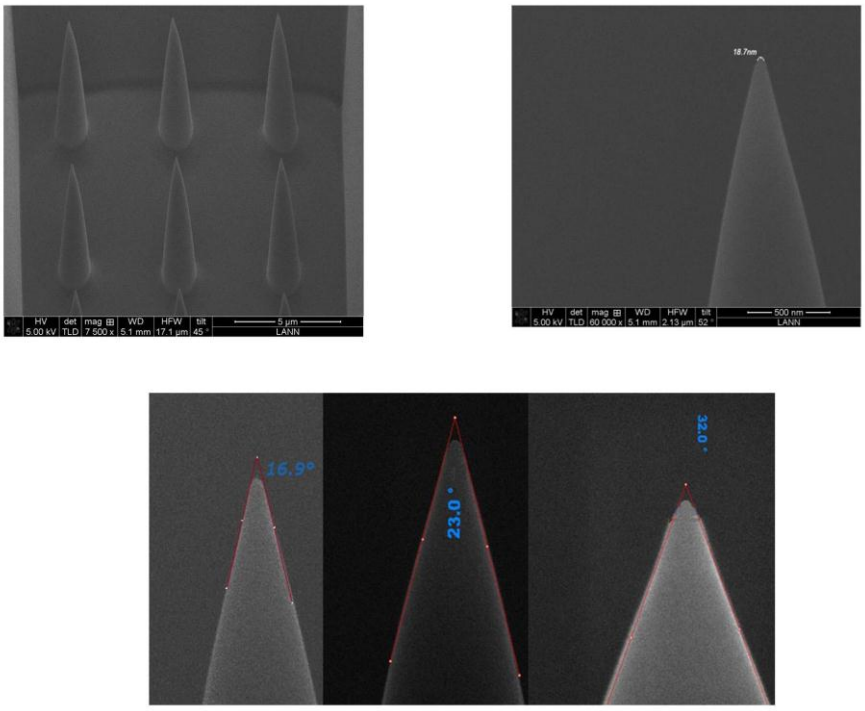

Figure 4.9 SEM micrograph of typical tips. Comparison between angle at the tip.

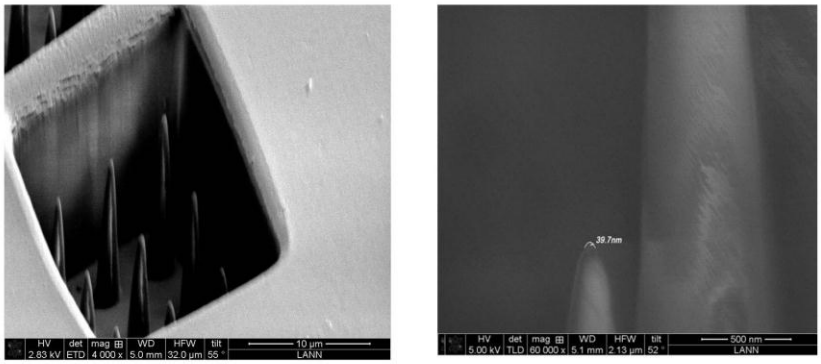

Figure 4.10 SEM micrographs of the replicated with NOA 79 and metallized nano-rocket tips array.

Experimental near field analyses have been performed by using Near field Scanning Optical Microscopy (SNOM). SNOM analyses have been performed on the sample in order to collect the spatial intensity profile of the light emitted from the rocket-tips. Figure 4.11 reports the map of the light intensity over an area of 10 x 10 μm and shows the details on 4 tips of the array. The measurements have been collected in contact mode by using unpolarized light at 633nm. As can be seen, an intensity peak is present at the tip. Moreover, in order to evaluate possible enhancement effects the measurements at the tips have been compared with a blank measurement of the source by using a transparent substrate. While the transparent substrate get 2500 counts, the max photon counts at the tip is 27000. Hence, an enhancement field factor of about 11 has been measured. The differences between the photon counts peaks showed in Figure 4.12 are essentially due to small differences in tip radius, in fact, as previouly demonstrated, small differences can lead to important decrement in the enhancement effects (Figure 4.12).

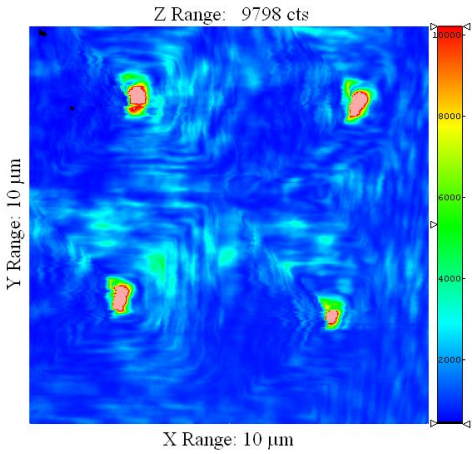

Figure 4.11 SNOM signal over an array of 4 tips.

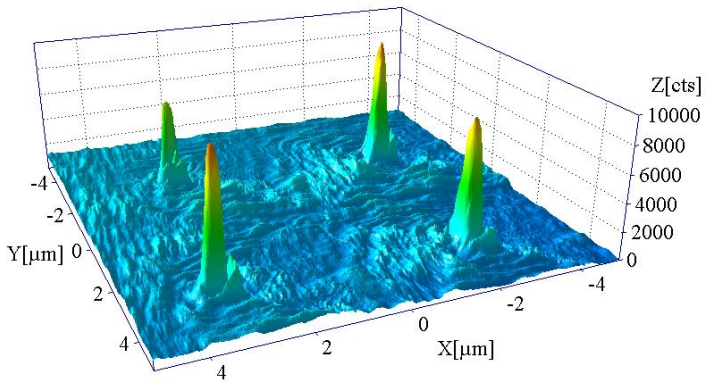

Figure 4.12 3D plot of the SNOM measurements.

Simulations of the optical response of the device have been performed by means of COMSOL Multiphysics commercial software which implements the Finite Elements Method (FEM).The simulation set-up is almost identical to the one used for simulate the "Stockman"'s conical structure in the previous section. The only main difference lies in the excitation source. In fact, in order to best approximate the available experimental setup, we simulated a conical NOA-tip covered with a 40nm-thick Silver film, illuminated form the NOA side with a 633nm linearly polarized incident wave. The curvature radius at the tip is realistically assumed to be 40nm. This setup is not optimal for nanofocusing since the tip aperture angle is very low and only a fraction of incident can couple to the film SPPs. More important, radially polarized incident light would be required in order to generate a coherent SPP "ring" propagating toward the tip which adiabatically condensates. In fact, as shown in Figure 4.2, the fundamental TM bound mode which is the one able to nano-focus is a radial mode. By using linear polarized light as input source, only a fraction of the incident electromagnetic field will couple with the proper fundamental mode of the structure, thus reducing the coupling and focusing efficiency. However, despite the unideal experimental configuration, the simulated electric field norm distribution, reported in Figure 4.13, shows nevertheless a relevant near field enhancement in the metal film regions close to the tip in the x-axis direction due to excitation of SPPs. The maximum calculated field enhancement with respect to the incident wave in vacuum is about a factor 18.5, which correspond to an intensity enhancement of $\eta \sim 320$. This value is consistent with the factor 11 found experimentally, considering that the SNOM probing tip has a finite width of 100nm and has therefore a finite intensity lateral resolution. It should be noted also that the excitation with a radial polarized beam is not trivial: a perfect alignment with the cone's axe is required and also radial polarizers works only for few visible wavelengths, thus limiting the application of the device. A possible method to overcame this limitation is presented in the next section.

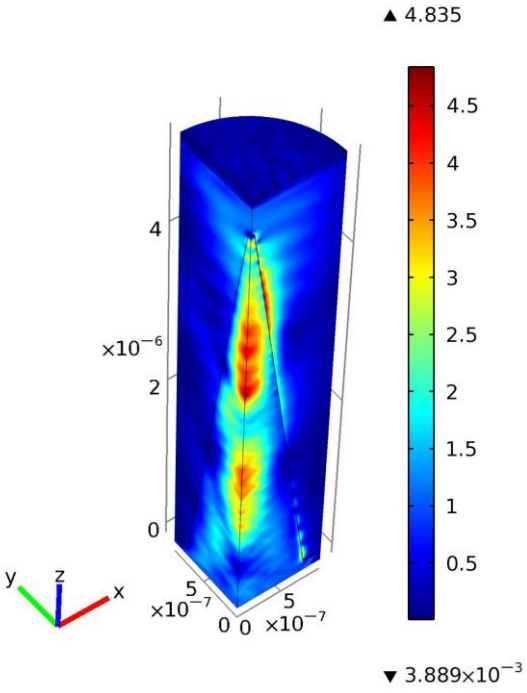

Figure 4.13 3D FEM simulation of the conical tip illuminated by 633nm incident light polarized along x-axis. Color scale: electric field norm enhancement with respect to field in vacuum.

4.3.3 Conclusions

In this paper a simple and reproducible procedure for the fabrication of nanorods (nano-rocket tips) array has been presented. The multi-step process allows to obtain conical tips with good aspect ratio (up to 10) and small tip radius (<20nm). The double mold replica lead to the realization of tips array that shown important nanofocusing effects and field enhancement. Finite element methods simulations have been used to design the structure and to verify the physical/plasmonic effects. FEM simulations demonstrate to be a powerful tool for the nanostructure design. Near field optics characterizations by means of SNOM demonstrate the performances of the prepared nanostructure, although in this experiment no polarization of the impinging light has been used. We have demonstrated that a cone/nano-rocket with convex shape and dielectric constant ε, covered with an uniform metalic layer can experience plasmon localization when illuminated with proper polarized light. This is in agreement with previous works [20] and ensures important advantages in the fabbrication procedure. Future works on this kind of structures comprising suitable polarizator elements should lead to high level of field enhancement at the tips. This will permit the application of the proposed nanostructure to high sensivity molecular detection useful in biosensor, cell analysis, DNA hybridization studies, etc.

4.4 Enhanced 3D Nanofocusing by Means of Plasmonic Vortexes

In the previous section we have discussed one of the major problems about experimental verification and employment of the 3D nanofocusing effect in a practical device: the need of a perfect radial polarized beam as input source in order to properly excite the fundamental TM bound mode supported by a conical metal waveguide. A standard radial-polarizer requires a perfect alignment with the axis of the conical waveguide, since few tens of degrees of misalignment could reduce the coupling efficiency of several orders of magnitude. Moreover this would require a complex optical set-up, thus limiting the possibility of miniaturization and making almost impossible to have a compact final device. The problem could be overcome by using a structure which is able to couple the incident radiation (like a laser source) to generate a plasmonic mode with the correct radial polarization, and then the excited SPP mode is coupled to a 3D conical waveguide, which is also part of the final device. In this way the radial polarization is impressed on the excitation source by the device itself, without the need of any external element. With this goal in mind, we propose here a structure based on this concept, which showed in Figure 4.14.

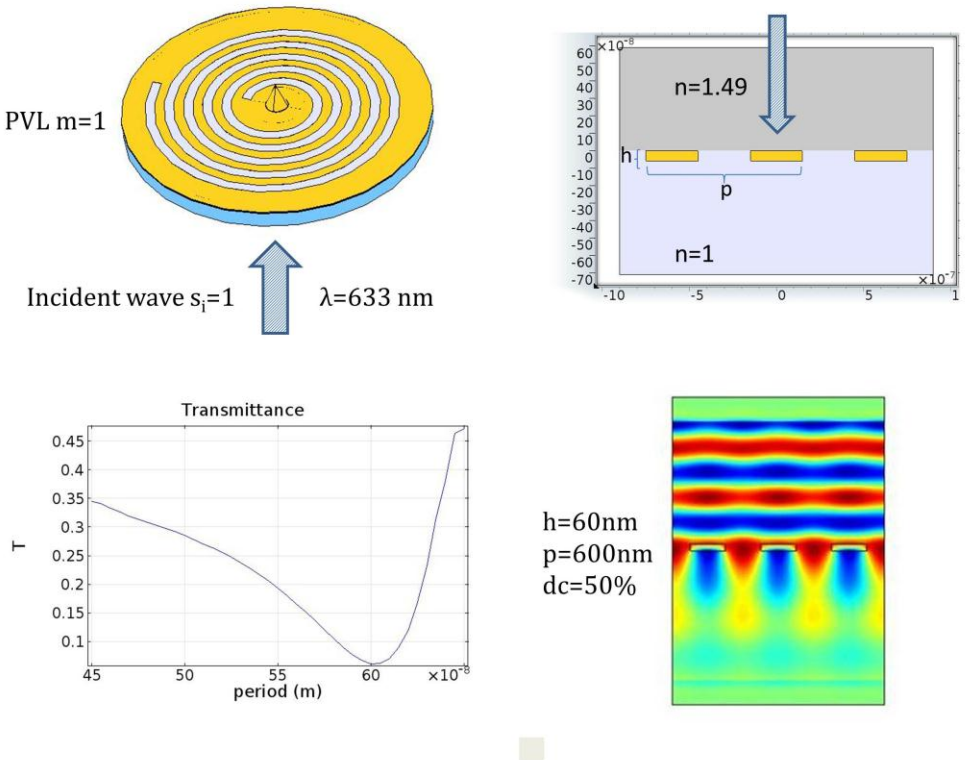

Figure 4.14 Scheme of the simulated structure and optimization process for the coupling between the incident circular polarized wave and the plasmonic PVL grating. The optimized configuration is the one which minimize the far-field transmission at air/gold interface.

It consists of an Archimede's spiral Plasmonic Vortex Lens (PVL, like the one discussed in chapter 1) with $m=1$ where in the centre it is placed a 3D metallic cone. The PVL and cone material is gold, and the structure lies on a glass substrate. It is illuminated from the bottom by means of a left hand circular polarized wave at a wavelength of 633 nm. The period of the spiral's arms and the metal thickness of the PVL are chosen in order to efficiently excite SPP at the air/gold interface. For this reason a FEM mutli-parametric simulation has been performed in order to find the optimized geometrical parameter of the PVL. The simulation process is the same described in chapter 3 for EOT gratings, and given the symmetry of the problem, the model has been solved in two dimensions. Figure 4.14 shows the results of the optimization process. The optimal configuration for SPP coupling is the one which minimize the transmission at the air/metal interface, and hence maximize the SPP excitation at air/gold interface. The field profile of this configuration is reported also in Figure 4.14. The PVL period is then 600 nm, with a gold thickness of 60 nm and duty cycle of 50%.

In chapter 1 we have seen that a Plasmonic Vortex Lens (PVL) illuminated by a Gaussian beam is able to generate a Plasmonic Vortex (PV). The phase distribution and hence the polarization nature of the PV depends on the value of the topological charge l_{PV} of the PV itself. Illuminating the $m=1$ PVL with a left-hand circular polarized beam ($s_i=-1, l_i=0$) results in the generation of a PV with total OAM value:

$$l_{PV}=m+l_i+s_i=0 \tag{4.13}$$

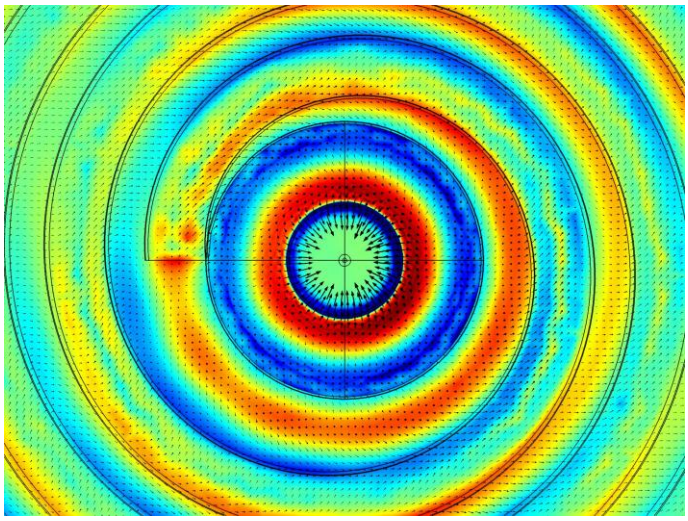

Figure 4.15 Coloroscale: E_z component of the PV excited by the PVL. As we can see, the topological charge of the PV is $l_{PV}=0$. The arrows represents the in-plane electric field E_x and E_y components, showing the radial symmetry of the field.

It has been showed [35] that the dominant component of the electric field for a PV with $l_{PV}=0$ is the transverse component respect the PVL plane (E_z component). However the in-plane components of the electric field are such that for l_{PV}=0 they are directed radially, towards the centre of the PVL. Figure 4.15 shows the E_z component and the in-plane electric field component generated by the PVL of Figure 4.14. As we can see, near the centre the electric field is truly radial and axial-symmetric. If now we place the 3D gold cone right in the centre of the PVL, then we should expect that the SPP PV mode is coupled to the taper geometry and the fundamental TM bound mode is excited. The cone has been modelled in order to represents in the most precise way a possible fabricated device. For this reason at the very end of the cone, the tip is shaped to resemble a fabrication defect that occurs in the nano-fabrication process (examples of the fabricated device are shown in the next paragraph). Contrary to what we have observed in Figure 4.13, this time the mode possesses the right polarization, which give the maximum nanofocusing enhancement. Figure 4.16 shows the norm and the transverse component of the electric field for the complete structure consisting of the whole PVL and conical waveguide. A clear focusing effect is visible at the tip. The transverse E_z electric field component shows the PV excitation and coupling to the conical waveguide. Also the symmetry of the SPP mode which propagates and condensate on the tip is visible. Since the adiabatic process is identical to the one discussed in the previous sections, the optimal angle is still 36° for gold at $\lambda = 633\,nm$. The height, radius, and distance from the PVL instead have been optimized in order to give the maximum field enhancement at the tip. In this geometry not only the contribution to the final field enhancement given by the cone must be considered, but also the contribution of the PVL must be taken into account. In fact, has demonstrated by [34], the PVL itself is able to focalize the PV towards the centre, adding its contribution to the final effect. Indeed, as recently demonstrated by [36], the 3D cone waveguide sourranded by a PVL can be considered as the best option for plasmon nanofcousing, when the highest possible field enhancement is seek. Following this argumentations, it appears clear that the optimized geometry is the one which maximize the plasmonic focusing towards the base of the cone and at the same time minimize scattering and losses. The results of this optimization process are listed in Figure 4.16. The maximum field enhancement reaches a value of $\eta \sim 30000$ for a radius of curvature at the tip of 5nm. With this high enhancement value it is possible to deliver optical energy to nanoscale regions as small as few nanometers for particle trapping, imaging, sensing opening the way for a new generation of nano-optical detectors.

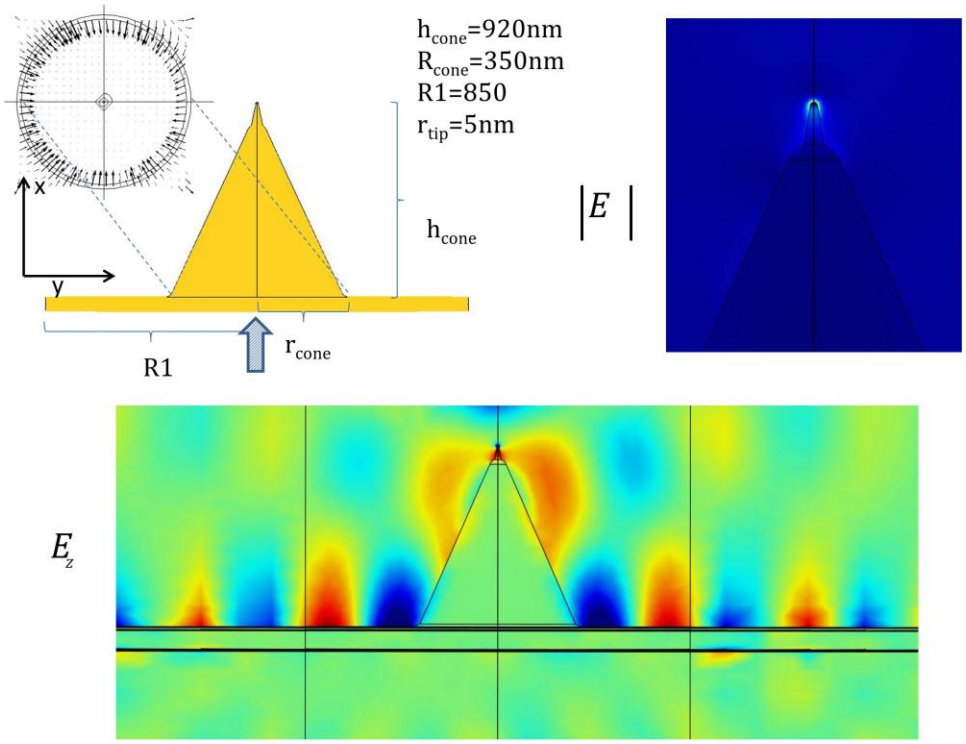

Figure 4.16 Optimized parameters of the complete structure and field distributions. The electric field norm shows a clear focusing effect at the tip

4.4.1 Nanofabrication

The proposed structure has been fabricated in order to perform future experimental testing and characterization of the device. Images of a fabricated sample are shown in Figure 4.17. The fabrication process consists of few different processes: electron beam lithography; electrolytic grown and electron beam induced deposition. A glass substrate was firstly covered with 5 nm of thermal evaporated gold in order to obtain a conductive transparent substrate for the following steps of process. The substrate has been then coated with negative resist AR-N of 200 nm thickness by means of spin coating and then exposed by electron beam lithography. Since the resist is negative, the resist area exposed by the electron beam will remain after the development process. The choice of a negative resist over a positive one is dictated by the need of having a complete opaque gold area around the spiral, in order to prevent direct illumination in a future experimental test. The CAD pattern has been also corrected for the proximity effect with the software LayoutBeamer (Figure 4.17). The exposed spiral structure allows to perform the following electrolytic deposition step. A gold layer of 180 nm has been grown. Finally, at the centre of the structure a gold nanotip with a conical shape (base diameter 350nm, height 900nm) has been locally deposited by means of electron beam induced deposition by means of FIB system (Figure 4.17). Thanks to the metal deposition, the radius of curvature of the tip is very small, in the order of 5 nm.

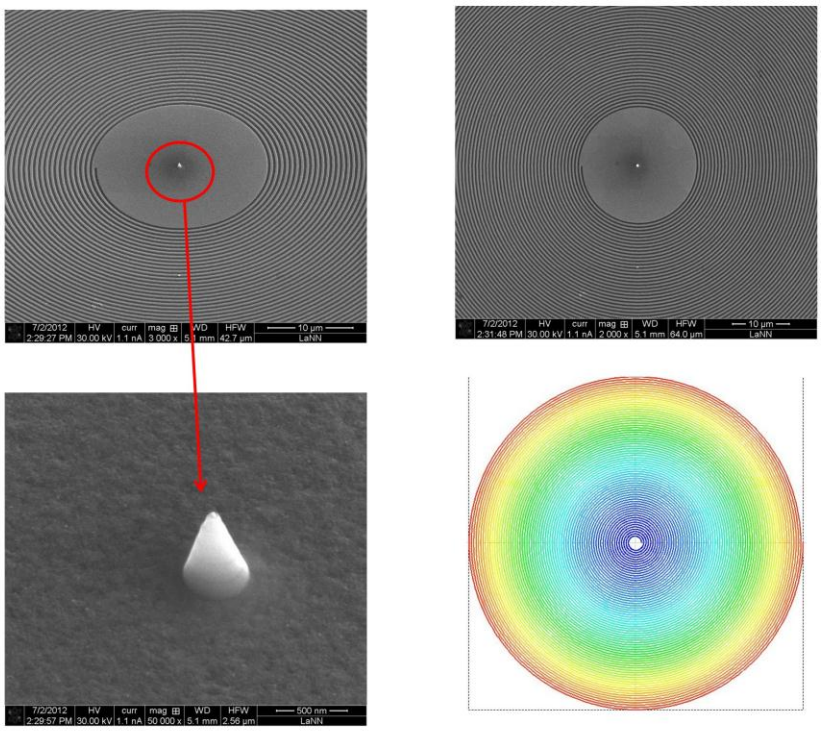

Figure 4.17 Examples of fabricated structure. The geometrical parameters are the ones described in Figure 4.16. The last image shows the proximity-effect corrected pattern for the negative resist EBL exposure. The different colors represents the different exposures doses assigned to the different parts of the pattern in order to compensate the sovra-exposure.

4.4.2 Conclusions

In this section we have shown how the problem of generating and coupling a SPP radial mode to a conical waveguide can be overcame by using as excitation source a PVL. The generated PV possesses an in-plane radial polarization at the centre of the PVL itself. If a conical waveguide is placed in the centre of the PVL, the plasmonic mode can propagates and adiabatically focus on the cone's tip. Due to the optimal polarization nature of the SPP mode and also due to the presence of the plasmonic lens, the observed focusing effect is greater by an order of magnitude than the one observed with a conventional SPP excitation scheme. The proposed structure has been also fabricated with a combination of different nanofabrication techniques, in order to ensure the highest process resolution grating a radius of curvature of the cone's tip of 5 nm. Future work will include a near-field optical characterization of the device with a SNOM setup.

4.5 References

[1] L. Novotny and B. Hecht, Principles of Nano-Optics Cambridge University Press, Cambridge, 2006

[2] S. Kawata, M. Ohtsu, and M. Irie, Nano-Optics, Series in Optical Sciences Vol. 84 Springer, New York, 2002

[3] Topics in Applied Physics in Near-field Optics and surface plasmonpolaritons, edited by S. Kawata Springer-Verlag, Berlin, 2001, Vol. 81.

[4] L. Novotny, D. W. Pohl, and B. Hecht, Ultramicroscopy 61, 1 1995

[5] F. Keilmann, J. Microsc. 194, 567 1995

[6] A. J. Babadjanyan, N. L. Margaryan, and K. V. Nerkararyan, J. Appl. Phys. 87, 3785 2000.

[7] M. I. Stockman, Phys. Rev. Lett. 93, 137404 2004.

[8] A. Bouhelier, J. Renger, M. R. Beversluis, and L. Novotny, J. Microsc. 210, 220 2003.

[9] N. Anderson, A. Bouhelier, and L. Novotny, J. Opt. A: Pure Appl. Opt. 8, 227 2006.

[10] K. Kurihara, J. Takahara, K. Yamamoto, and A. Otomo, J. Phys. A: Math. Theor. 42, 185401 2009.

[11] D. K. Gramotnev, D. F. P. Pile, M. W. Vogel, and X. Zhang, Phys. Rev. B 75, 035431 2007.

[12] D. K. Gramotnev, J. Appl. Phys. 98, 104302 2005.

[13] D. F. P. Pile and D. K. Gramotnev, Appl. Phys. Lett. 89, 041111 2006.

[14] E. Verhagen, L. Kuipers, and A. Polman, Nano Lett. 7, 334 2007.

[15] K. Li, M. Stockman, and D. J. Bergman, Phys. Rev. B 71, 115409 2005

[16] K. Tanaka, M. Tanaka, and T. Sugiyama, Opt. Express 14, 832 2006

[17] A. V. Goncharenko, H.-C. Chang, and J.-K. Wang, Ultramicroscopy 107,151 2007.

[18] N. A. Issa and R. Guckenberger, Plasmonics 2, 31 2007.

[19] D. K. Gramotnev, M. W. Vogel, and M. Stockman, J. Appl. Phys. 104,034311 2008

[20] M.W. Vogel and D.K. Gramotnev, J. Appl. Phys. 107, 044303 2010

[21] Y. Oshikane et al. (2007). Sci. Technol. Adv. Mater. 8: 181.

[22] H. Schmid and B. Michel, Macromolecules, 2000, 33 (8), pp 3042–3049.

[23] Babadjanyan A.J., Margaryan N.L., Nerkararyan K.V., J. Appl. Phys. **87**, 3785 (2000).

[24] Stockman M., Phys. Rev. Lett., 2004 **93**(13).

[25] Vogel M.W., Gramotnev D.K., Phys. Lett. A 363 (2007) 507.

[26] G.E. Andrews, R. Aaskey and R. Roy, *Special Functions,* Cambridge University Press 1999.

[27] Bozhevolni S., Stockman M., *Plasmonic Nanoguides and Circuits,* Pan Stanford Publishing (2009).

[28] C. Cohen-Tannoudji, B. Diu, F. Laloe, *Quantum Mechanics*, Wiley (1977).

[29] N. A. Issa, R. Guckenberger, Plasmonics (2007) 2:31-37.

[30] D.K. Gramotnev, M.W. Voegel and M. Stockman, J. Appl. Phys. **104**, 0311(2008).

[31] D.F. Pile and D.K. Gramotnev, Appl. Phys. Lett. **89**, 041111 (2006).

[32] J.M. Kontio, J. Simonen, J. Tommila, M. Pessa, Microelectronig Eng. (2009) 0167.

[33] S. Berweger, J.M. Atkin, R.L. Olmon, M.B. Raschke, JPCL 2012, 3, 945-952.

[34] Nathan C. Lindquist; Prashant Nagpal; Antoine Lesuffleur; David J. Norris; Sang-Hyun Oh Nano Letters 2010;10(4):1369-1373.

[35] P. Zilio, E. Mari, G. Parisi, F. Tamburini, and F. Romanato,, Opt. Lett.37(15), 3234-3236 (2012).

[36] D.K. Gramotnev, M.W. Vogel, Phys. App. Lett. A 375 (2011) 3464-3468.

5 Planar Nanofocusing

5.1 Introduction

In chapter 1 we have seen that a multilayer system (IMI or MIM) is able to sustain SPP and in particular exists a set of solutions of the Maxwell's equations which give rise to couple modes, called symmetric and anti-symmetric, depending on the particular field symmetry (see Appendix A for details). The geometry considered was formed by an infinite-wide multilayer in the direction normal to the propagation direction, while the thickness of the central core has a finite value. In this chapter we want to investigate the possibility of SPP waveguiding on thin metal stripes which lateral dimension has a finite value. In particular the lateral confinement of the SPP modes will be investigated along with their propagation properties as function of the waveguide geometry and the dielectric environment. The possibility of planar nanofocusing along tapered planar metal stripes is then analyzed. This geometry presents several advantages respect to other plasmonic focusing structures, like for instance a 3D metal cone (chapter 4) where the proper SPP excitation with a radial mode is a non-trivial experimental issue, or a metallic wedge where the fabrication of a very precise geometry and very sharp tip is a challenging process. A planar geometry in fact can be illuminated with standard linear polarized light and usually the SPP excitation is obtained by means of prism coupling or grating coupling, and also the fabrication process is usually performed with FIB or EBL techniques which allow very high resolution performances and an accurate geometry control. On the contrary, a planar tapered waveguide usually does not provide a huge electromagnetic field enhancement compared to a 3D geometry. A detailed numerical analysis on the focusing effect on a planar tapered waveguide for different configuration is provided. The last part of the chapter is dedicated to the application of a novel device which combines the plasmonic planar nanofocusing with the exotic properties of light possessing Orbital Angular Momentum (OAM). The new degree of freedom possessed by the SPP beam opens up to the possibility of charge control in nanometric volumes, besides granting an highest field enhancement at the tip respect to standard illumination.

5.2 SPP Modes on Metal Stripes

In this section we consider a waveguide geometry based on the IMI structure seen in chapter 1 and consisting of a thin metal stripe sandwiched between two thick dielectric cladding layers. We have seen that for a sufficiently small metallic core layer, interaction between SPP on the two interfaces create a set of couple modes. For a symmetric dielectric environment, where the super- and sub-strate have the same dielectric constants, the couple modes can have a symmetric or anti-symmetric field distribution respect

to the middle plane. For the symmetric mode the real and imaginary parts of the wavevector decrease with decreasing film thickness. This means that the losses are reduced and so propagation length increase with smaller metal film thickness. This mode is therefore called long range mode.

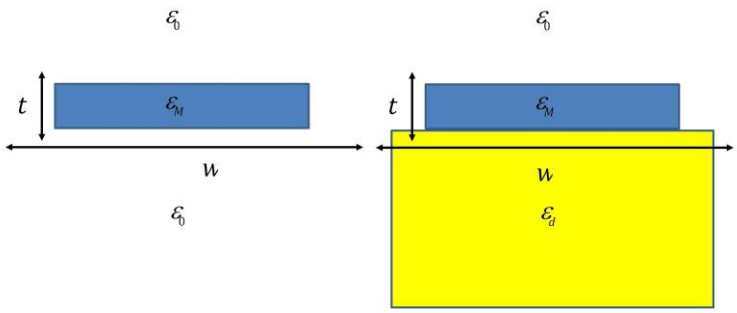

Figure 5.1 Geometry of a metal stripe of thickness t and width w embedded in vacuum (symmetric environment) and placed on a substrate (anti-symmetric environment).

We want to see if a similar behavior is observed in a slightly different geometry (Figure 5.1) which consists of a metal stripe of finite width w and thickness t under the condition $w/t \ll 1$ where only the metal thickness t is subwavelength. The metal stripe is embedded in vacuum. This geometry was first analyzed theoretically by Berini in 2000 [1], and his results showed that if the width of the stipe is sufficiently large and the metal thickness is small enough, two fundamental bound modes of opposite symmetries do exist. Figure 5.2 shows the field profile of these two modes, calculated by means of a FEM modal analysis for a gold stripe with $w = 1\ \mu\text{m}$, $\lambda_0 = 633\ \text{nm}$ and $t = 60\ \text{nm}$. The dispersion relations of these modes are plotted in Figure 5.3 as function of metal stripe thickness. The fundamental symmetric mode seems to behave very similar to the long range mode of the infinite IMI structure. The attenuation decreases dramatically with decreasing t and therefore it can be called the long-rage mode of the metal stripe. These results would lead to the conclusion that in a plasmonic waveguide the long range mode should be the preferred one, since it can assure very high propagation lengths in order of several hundreds of microns in the visible range and up to a 1cm in the near-infrared. However the decrease in attenuation length observed for the long range mode is accompanied by an equal loss in confinement. In fact as the film thickness is reduced, the mode evolves in a plane wave (without cut-off) and the corresponding TEM mode extends over many wavelengths into the dielectric medium. Consequently the field confinement, defined by the fraction of the power flowing through the stripe to the total power of the mode, decrease with decreasing film thickness. This behavior can be observed looking at the field profile of the symmetric mode for a very a very thin metal stripes $t = 15\ \text{nm}$ (Figure 5.4): the mode is almost all spread in the surrounding medium. The anti-symmetric mode instead possess a very localized field

(Figure 5.4), concentrated near the edges of the metal stripe, but in this case the attenuation constant is very high and increase dramatically with increasing film thickness (see Figure 5.3) thus limiting the propagation length of an SPP wave. If a high degree of miniaturization is needed (like for instance in photonic circuits) or a need of electromagnetic field confinement (like in the case of nanofocusing) is required, it appears clear that the long range mode cannot be used, despite of long propagation lengths. This is a demonstration of the general principle of the trade-off between localization and loss which always occurs in plasmonic devices. Field concentration in subwavelength dimension on metal surfaces implies that a significant amount of the total mode energy is inside the metal itself, leading to great propagation losses due to Ohmic heating. Electromagnetic energy concentration in subwavelength scales will necessarily imply micron or sub-micron propagation lengths in the visible spectrum range. Concluding the discussion on the metal stripe in a symmetric environment, we see from Figure 5.3 that the two fundamental modes do not present a cut-off thickness and as the metal film thickness increase, both the symmetric and anti-symmetric mode become degenerate, like in the case of the infinite IMI structure, with their propagation constant converging to that of a SPP supported by the interface between two semi-infinite metallic and dielectric regions.

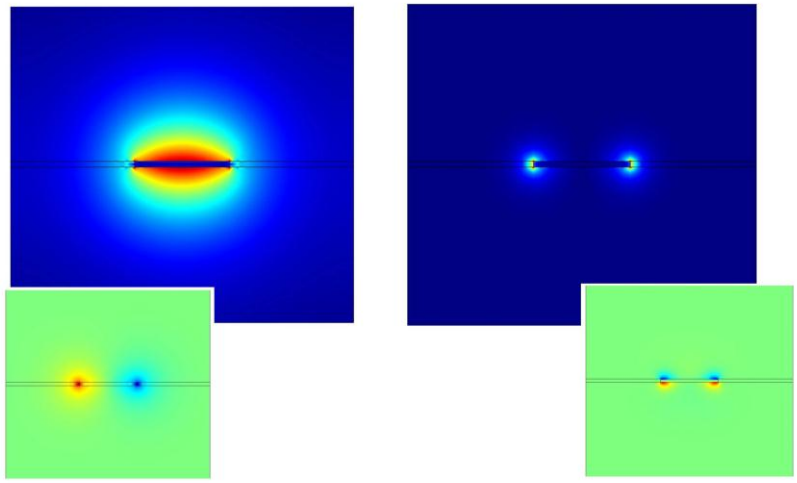

Figure 5.2 Symmetric and Anti-symmetric modes of a silver stripe embedded in vacuum at $\lambda = 633\,\text{nm}$. The stripe width is $w = 1000\,\mu\text{m}$ and the thickness is $t = 60\,\mu\text{m}$. Left: Electric field norm of the fundamental symmetric mode and corresponding H_z magnetic field component, showing the symmetry of the mode. Right: Electric field norm of the fundamental anti-symmetric mode and corresponding H_z magnetic field component.

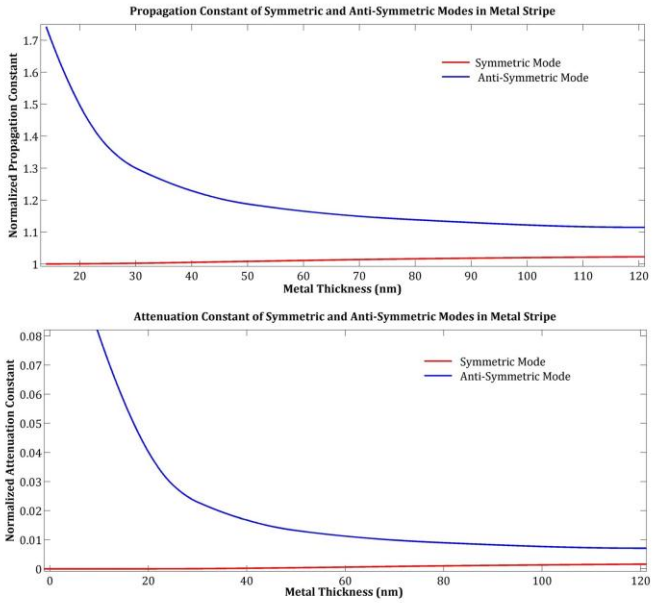

Figure 5.3 Up: normalized propagation constant $\mathrm{Re}(k_x)/k_0$ for symmetric (red) and anti-symmetric (blue) modes of a silver stripe in vacuum as function of metal stripe thickness at $\lambda = 633\,\mathrm{nm}$. Down: normalized attenuation constant $\mathrm{Im}(k_x)/k_0$.

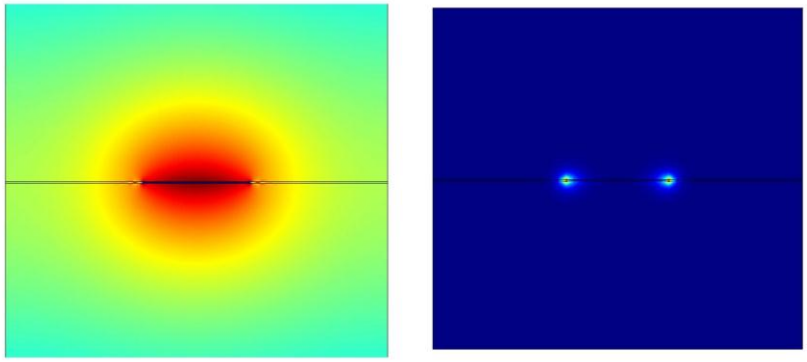

Figure 5.4 Left: norm of the electric field for the symmetric mode of a silver stripe of thickness 15 nm and width 1000 nm in vacuum at $\lambda = 633\,\mathrm{nm}$. The field is spread all across the surrounding medium. Right: norm of the electric field for the anti-symmetric. The field is almost all localized on the edge of the stripe.

The next SPP waveguide geometry that is considered is the one formed by a metal stripe placed on a dielectric substrate (Figure 5.1) with refractive index $n_d = \sqrt{\varepsilon_d}$. The dielectric environment is not symmetric anymore and in this case the spatial distribution of the mode fields is not truly symmetric or anti-symmetric [2,3]. The long and short range modes observed in the symmetric environment do not exist anymore, due to the phase mismatch between the SPP at the two different interfaces, which prevent

the formation of couple modes. Rather, the mode field distributions are symmetric-like or asymmetric-like. In particular the field distributions have the general form of those found in the symmetric structure but the fields are localized near only one interface. With a generalization, we can still call these new modes as symmetric and anti-symmetric modes, where the symmetric one has a mode field distribution with a maximum at the interface with the dielectric with the lowest permittivity and the opposite holds for the anti-symmetric one. As like the symmetry, also the polarization nature of the modes supported by this kind of waveguide is not well-defined. Pure TM or TE modes are not supported, but if the aspect ratio $w/t>1$, then the component E_y of the electric field perpendicular to plane dominates, and the modes are called quasi-TM modes.

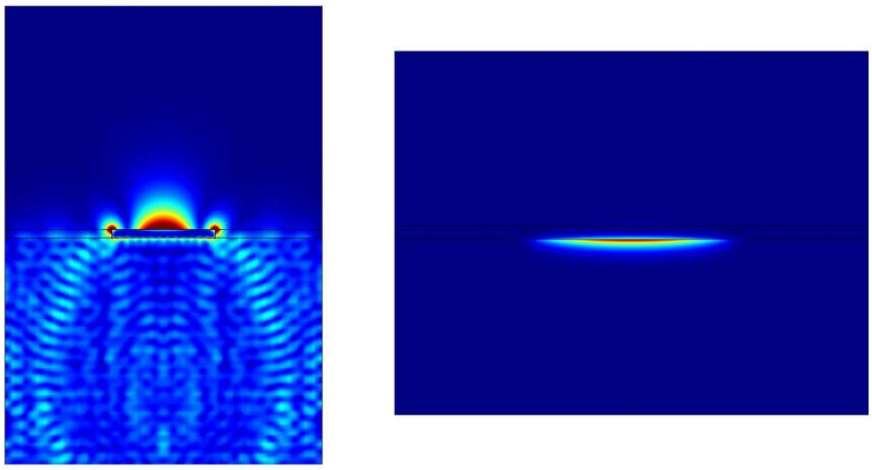

Figure 5.5 Symmetric (right) and anti-symmetric modes (left) of a silver stripe of thickness $t = 120\,\text{nm}$ and width $w = 1500\,\text{nm}$ on a dielectric substrate ($n_d = 2$) at $\lambda = 633\,\text{nm}$. Right: electric field norm of the leaky mode at air/silver interface. Left: electric field norm of the bound mode at silver/substrate interface.

Figure 5.5 shows the two fundamental symmetric and anti-symmetric modes for a gold stripe in air, placed on a high-index dielectric substrate $(n_d = 2)$ at a wavelength of $\lambda_0 = 633\,\text{nm}$. The mode localized at the air/metal interface, called the symmetric mode, radiates significantly into the surrounding air and also through the dielectric substrate. For this reason it is called leaky mode [3], and shows that Ohmic losses are not the only attenuation factor for a propagating SPP, but also re-radiation into the higher-index substrate plays a crucial role for this type of geometry. The dispersion relation for SPP leaky modes is such that it is always between the light line and the substrate line, as it can be seen in Figure 5.6, and for this reason the re-radiation process is possible. Leaky modes along metal stripes has been the object of several experimental studies, due to the fact that they can be easily excited in an ATR set-up and they present a great momentum overlap with SPP modes on a flat surface. However as the experimental

studies have been demonstrated, these leaky modes present low propagation lengths due to the afore mentioned mechanisms of losses. Moreover a leaky mode presents a critical stripe width value under which the propagation is stopped, thus making its use for any type of focusing application unsuitable.

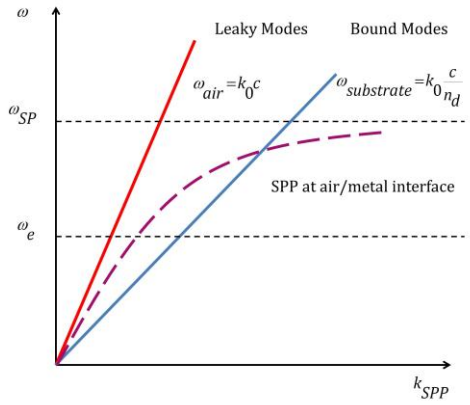

Figure 5.6 Dispersion relation of SPP modes in an anti-symmetric dielectric environment. The red line is the light line, while the blue line is the substrate line. Modes between the light and substrate line are called leaky modes. When the SPP dispersion curves crosses the substrate line, the leaky modes are irradiated in the substrate.

The anti-symmetric fundamental mode presents a field distribution localized on the highest-index dielectric (the glass substrate) and contrary to the symmetric leaky mode, the anti-symmetric has a bound nature, with no sign of radiation through the substrate or air (Figure 5.5). All of the electromagnetic field energy is confined near the metal stripes, and this mode has a modal behavior very similar to the one observed for a metal cylinder in chapter 4. The propagation constant as function of the metal stripe width is plotted in Figure 5.7. As it can be seen, the fundamental bound mode presents a diverging wavevector for decreasing stripe width, meaning that it can be efficiently used for nanofocusing application, while the highest-order modes are cut off (for the symmetric mode even the fundamental mode presents a cut-off stripe width value, which limits its employment for nanofocusing). The observed mode profile resembles a Gaussian-like mode profile, with a quasi-TM polarization nature as discussed before. These features allow a more straightforward excitation of the desired mode compared for instance to the metal stripe embedded in the symmetric dielectric environment (Figure 5.2), where the mode is mostly localized on the waveguide edges.

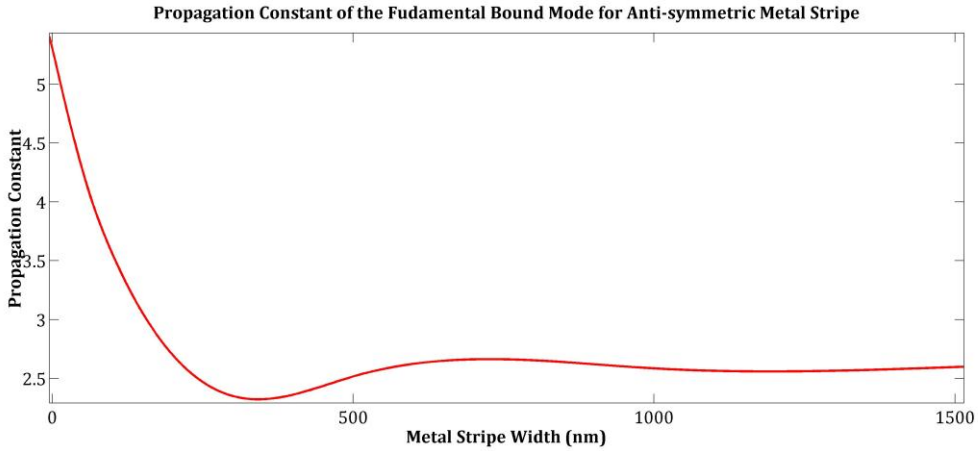

Figure 5.7 Propagation constant of the fundamental bound mode of a silver metal stripe at silver/substrate interface, as function of stripe width. The geometry is the same as in Figure 5.5.

Indeed the asymmetry of the dielectric environment is the responsible of the observed Gaussian-like profile.

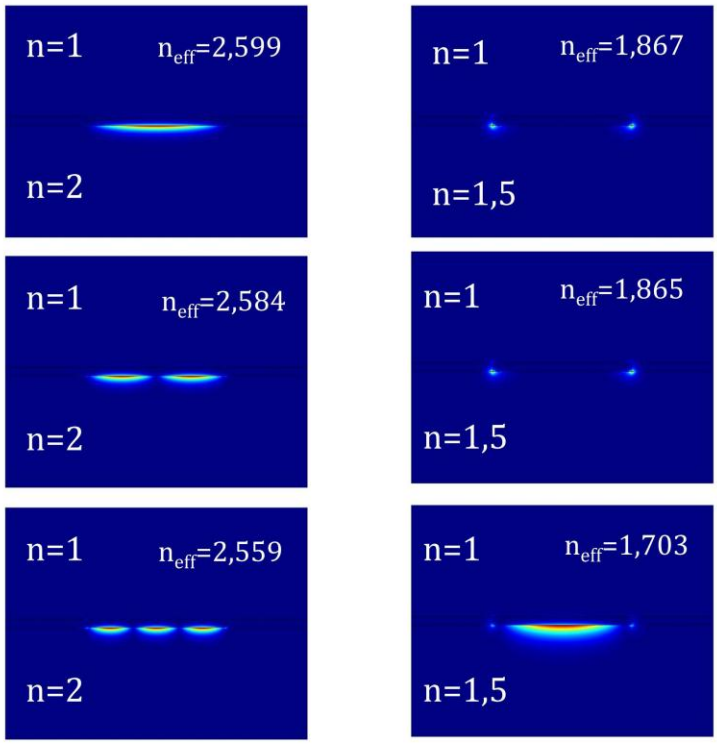

Figure 5.8 Mode profiles of electric field norm for the three lowest order bound modes of a silver metal stripe 1500 nm wide and 120 nm thick. The wavelength is 633 nm. The super-strate is air while the substrate has a refractive index of 2 (left) and 1.5 (right).

Figure 5.8 shows a comparison between two identical metal stripes with different surrounding mediums. The superstrate is kept the same for both cases (air), and the substrates refractive indexes are 2 and 1.5. It's clearly visible that the configuration with a highest refractive index contrast presents a more Gaussian-like mode profile with the maximum of the intensity spread all across the entire width of the metal stripe and therefore it is most likely to be excited in an experimental situation where a Gaussian laser beam is used. On the other hand the configuration with the lowest dielectric contrast has the fundamental mode with most of the energy localized on the waveguide edges, like the case of the symmetric configuration. In order to have a Gaussian-like distribution, we must look at the third order mode which unfortunately at some width value is cut-off.

5.3 Nanofocusing on Planar Tapered Waveguides

In the previous section we have seen that the fundamental bound mode of a metal stripe placed on a high-index dielectric substrate does not present cut-off when the transverse width of the stripes is reduced, even in subwavelength regime. This is not the case instead for a dielectric core waveguide, where the subwavelength confinement is limited by diffraction. In fact, for propagation along the z-direction, the relationship between the propagation constant β, the transverse components of the wave vector k_x, k_y and the frequency ω of the guided mode is given by:

$$\beta^2 + k_x^2 + k_y^2 = \varepsilon_{core}\frac{\omega^2}{c^2} \tag{5.1}$$

Since in a dielectric waveguide $\varepsilon_{core} > 0$ and k_x, k_y are real, equation (5.1) implies that $\beta, k_x, k_y \le \sqrt{\varepsilon_{core}}\,\omega / c = 2\pi n_{core} / \lambda_0$. According to the uncertainty relation between wave vector and spatial coordinates, the mode confinement for such 3D optical wave is limited by the effective wavelength in the core medium:

$$d_x, d_y \ge \frac{\lambda_0}{2n_{core}} \tag{5.2}$$

However, if the guiding medium in the core is of metallic character then $\varepsilon_{core} < 0$. If this is the case, in order for equation (5.1) to be fulfilled, either one of both k_x, k_y must be purely imaginary, i.e. the guided modes are two or one dimensional. Recalling the discussion in chapter 1 and 4, we see that an SPP mode which does not present cut-off (like the one showed in Figure 5.5) is actually able to produce a transverse field confinement well below the diffraction limit, and as in the case of 3D conical shapes, to produce a nanofocusing effect even if a taper planar geometry is used.

Studies on metal nanowires with subwavelength transverse dimension have been conducted since 2000. Dickson [4] and Krenn [5] performed experimental studies in the visible range on metal stripes by exciting SPP at air/metal interface using prism coupling. With a conventional near-field microscopy set-up they both show the existence of SPP guided modes which propagate along the metal nanowire. However, as discussed above, the mode excited in those experiments is essentially a leaky mode, and, besides of the low propagation length values, at some point the mode is cut-off, thus limiting the possibility of an efficient nanofocusing.

The first concrete planar nanofocusing geometry was the one presented by Verhagen et al. [6] in 2008. They presented the possibility to achieve nanofocusing of SPPs with a laterally tapered metal stripe waveguide on a dielectric substrate, both in experiments and simulations. In order to do so, they excited the purely bound SPP mode at the high-index side of the tapered waveguide, like the one discussed in Figure 5.8 , with light of a wavelength of 1.48 μm in air. Since the SPP propagation and focusing take place in the substrate, in order to observe the focusing of SPPs in the tapered waveguide they detected up-conversion luminescence from erbium ions implanted in the substrate [7,8]. As predicted, no sign of a cutoff width was observed for the mode excited at the metal/substrate interface and consequently a great electric field enhancement at the very end of the taper waveguide is observed.

Here we present the fundamental results on a planar metal tapered waveguide, showing the focusing effect for different configuration. The tool used for this numerical investigation is a full 3D FEM model. The SPP mode is assumed to be properly excited by standard SPP excitation techniques. A precise control of the SPP momentum is needed in order to properly couple the incident SPP wave to the SPP bound mode of the structure; for this reason the most used technique of excitation is the grating coupling. Equation (1.18) allows to calculate with good approximation the exact period of the grating once known the dielectric constants of the material and the incident wavelength and so the propagation constant of the mode can be precisely controlled. Since a complete simulation of the full structure made off the waveguide plus the grating would require a huge computational effort, only the last part of the waveguide is simulated, i.e. the one where the actual SPP propagation and focusing is taking place. As input source in the model, a boundary mode analysis is performed at the beginning of the waveguide. The desired SPP fundamental bound mode is found, and thanks to its focusing properties, it is then used as boundary condition. The set-up of the FEM model, with the mesh geometry and input boundary mode, is shown in Figure 5.9. Differently from the study presented by Verhagen which used a near-infrared excitation wavelength $\left(\lambda_0 = 1480nm\right)$, here a visible wavelength $\left(\lambda_0 = 633nm\right)$ is preferred, which correspond to the frequency of a He-Ne laser typically used in most optical experiments. Moreover the investigation of the

focusing effect in the visible range is of great interests for application purposes, like for instance photonics circuits, telecommunications, bio-sensing, spectroscopy. The main difference between the visible and infrared regimes lies in the fact that in the visible range the losses for most of the noble plasmonic metals (like silver and gold) is even more accentuated, leading to propagation lengths which hardly reaches $\sim 20\ \mu$m (especially if the mode used is the one at the high-index substrate/metal interface). This requires an even more miniaturization of the focusing devices, but with modern nanofabrication techniques this requirements can be fulfilled. The behavior of the SPP bound mode instead is less-sensitive for different wavelengths (at least in the visible and near-infrared range) and the only change is that as the wavelength is reduced towards the UV, the effective index of the plasmonic mode increases. The mode profile instead for the fundamental mode at the high-index substrate/metal interface possess always its Gaussian-like shape, as we have previously shown.

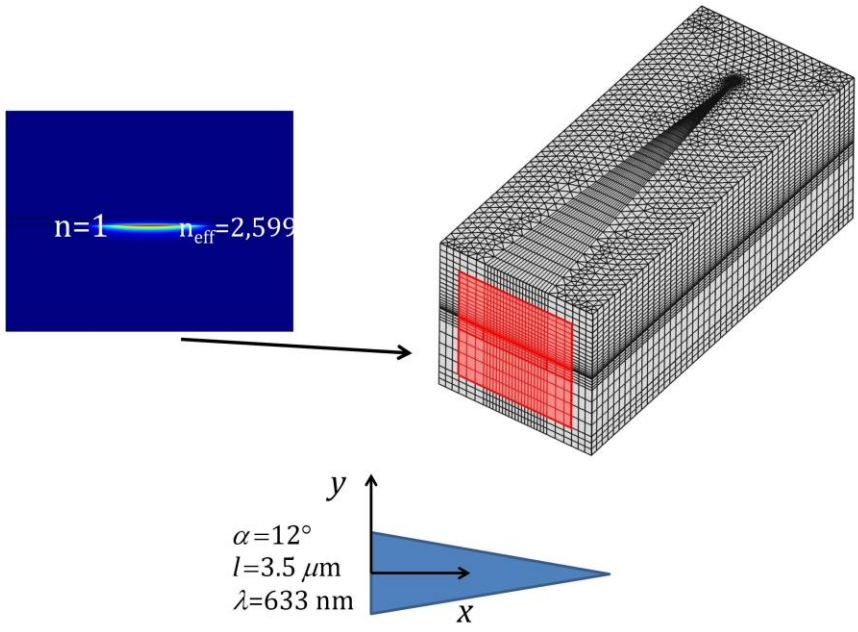

Figure 5.9 FEM model set-up for a planar silver tapered waveguide on a dielectric substrate. The red part indicates the excitation port where the fundamental bound mode of a silver metal stripe is launched.

Figure 5.10 shows the electric field profile of a silver planar tapered waveguide placed on a dielectric substrate with refractive index of $n_d = 2$ excited like shown in Figure 5.9. The triangular waveguide is $3.5\ \mu$m long and has a vertex angle of 12°, while the curvature radius of the tip is set to 10 nm. The metal thickness of the waveguide is 100 nm. The field profiles are taken just at the interface between the lower part of the silver waveguide and the dielectric substrate.

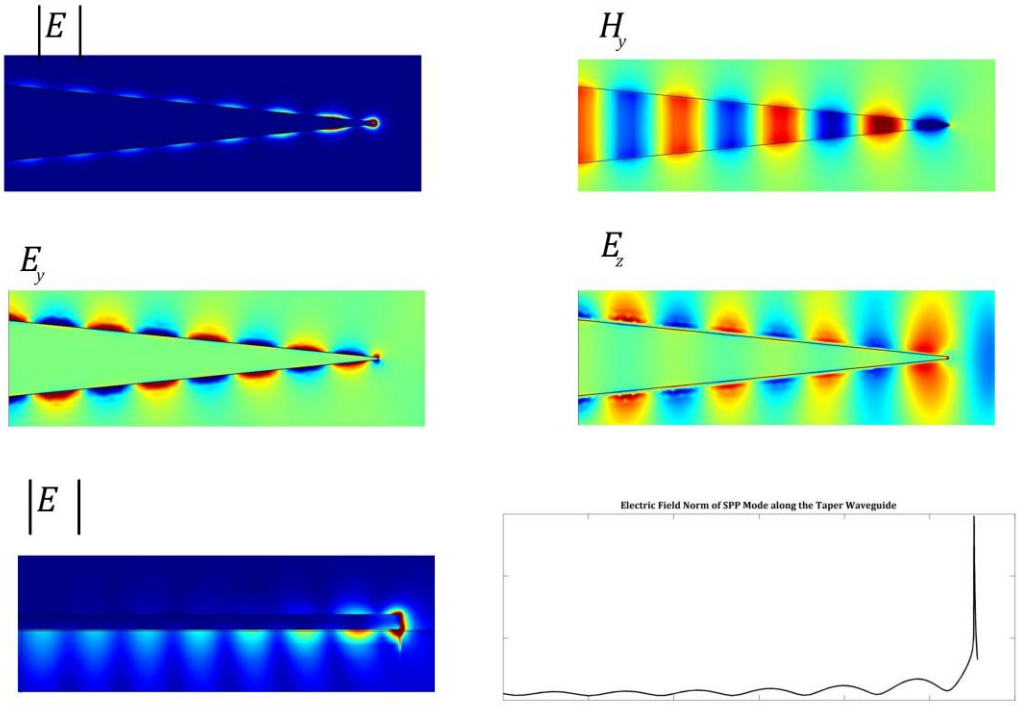

Figure 5.10 Tapered waveguide geometry and field profiles of the SPP mode propagating at silver/substrate interface at a wavelength of 633 nm. The slices are taken along the x-y plane at the silver/substrate interface. The maximum field enhancement at the tip position is 750. Color scales are saturated for better visualization.

As for the 3D metal cones, also in this case a condensation of the SPP mode is observed near the tip, leading to nanofocusing. The physical mechanism of this effect is basically the same as the one observed for the metal cones. This is due to the fact the SPP bound mode for the two geometries behave basically the same, as we have seen previously. Both modes possess a diverging wavevector as the critical dimension (the radius of the cone and the width of the metal stripe) is reduced, which leads in both cases to an adiabatic compression of the SPP modes and consequently SPP stopping at the very end of the waveguide. Although an analytical expression for the dispersion relation on a stripe waveguide is not available, the results obtained for the cylindrical geometry are expected to be still valid even for the planar geometry, at least on a qualitative level. We see that the transverse components E_y and E_z (as recalled, the bound mode used as excitation source is not a pure TM mode, due to the asymmetry of the environment. However the strongest electric field components are still the transverse ones respect to the direction of SPP propagation) behaves very similar to the components of the cylindrical bound mode seen in chapter 4 (see Figure 4.4), with strong localization to the metal/dielectric interface and also with strong lateral confinement. The symmetry of the bound mode excited at the metal/dielectric interface is clearly

visible: the E_y component of the electric field is anti-symmetric respect the triangle's axis, while E_z is symmetric. The norm $|E|$ of the electric field clearly shows the enhancement at the very end of the tapered waveguide due to focusing effect. The propagation of the SPP mode takes place at the silver/substrate interface and near the tip we observe a rapid increase in the plasmon amplitude which leads to SPP stopping and condensation just at the tip position. This is very similar to the "tsunami" effect observed for the conical geometry seen in chapter 4. Although the SPP propagation and condensation takes place in the substrate, we see from Figure 5.10 and Figure 5.11 that at the tip's position the electric field is spread all across the waveguide, reaching also the air/silver interface; however the field is still strongly localized and confined to the metal edge of the tapered waveguide, and the confinement increase at the SPP mode approaches to the tip's position. This is not the case when the SPP mode is far from the tip (Figure 5.11): when the adiabatic compression is not taking place, the mode is spread all across the waveguide and also it extends in the dielectric substrate.

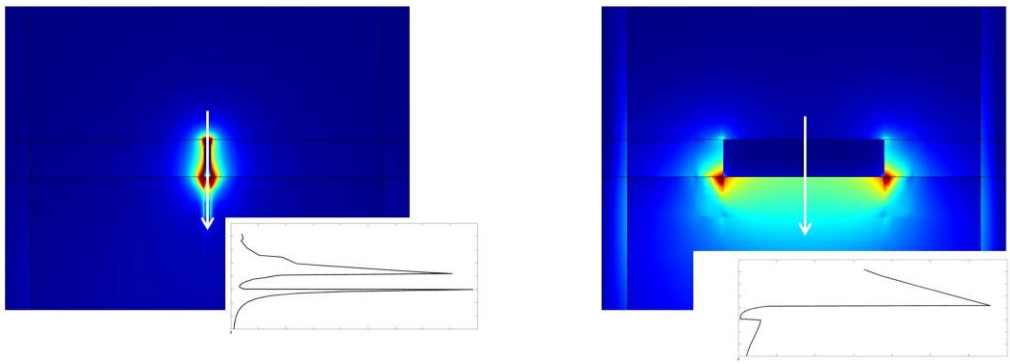

Figure 5.11 Top: Electric field norm at two different cross section of the tapered waveguide. Left: Electric field norm at 5 nm near the tip. The field is very transverse localized near the waveguide's edges. The inset shows the field norm along the direction of the white arrow. Right: Electric field norm at 2 μm from the tip. Inset shows how the field is poorly localized.

Like for the 3D cone, there is an optimal taper angle value (calculated as 12°) which maximize the focusing effect and at the same time minimize the reflection from the tip, giving another proof that the adiabatic theory is still valid also in this case. The main difference between a planar and a 3D nanofocusing is that the SPP mode condensates and adiabatically stops in two dimensions instead of three, leading to a smaller maximum field enhancement compare to the 3D conical geometry. The maximum field enhancement is ~ 750 , calculated with the formula (4.11) at a distance of 10 nm from the tip (this distance value is comparable with the average distance of a near field SNOM probe) which is roughly an order of magnitude smaller than the one obtained with a 3D geometry at the same wavelength and with the same dielectric

environment [9]. Also the polarization nature of the two SPP modes which condensate plays an important role for the total enhancement. A 3D geometry requires a radially polarized incident beam in order to properly excite the fundamental mode while a planar geometry works with a simple linear polarized beam (TM polarization). Although a radial polarized beam excitation and the corresponding coupling to an SPP mode is a non-trivial experimental issue, it assures a more efficient coupling with the proper cylindrical mode, minimizing scattering processes. On the other hand the planar waveguide geometry could be excited with no particular efforts, for example with a standard plasmonic grating.

The focusing effect observed for the presented planar geometry has a fundamental limitation: in order to excite a SPP bound mode which does not presents cut-off for any width of the metal stripe, the mode must be an anti-symmetric mode at the high-index substrate/metal interface. Although at the very end of the waveguide the field extends also at the air side, most of the focused energy lies in the substrate. This fact presents several practical drawbacks, the most important being the difficulty of a near-field detection of the signal, and low propagation length compared to a mode excited at the air/metal interface. Some experimental studies tried to avoid the detection problem by using active substrates which are able to re-emits in the far field the propagation signature of the SPP mode along the waveguide. These substrates include erbium ions implanted in a sapphire substrate or fluorescence materials like a matrix of rhodamin. It appears clear that the possibility of obtaining a focusing effect on the air/metal interface would improve the near-field detection and consequently the possibility to apply and integrate a planar focusing device in different fields. Some studies were performed by Ditlbacher [10] and Weeber [11], which showed the existence of an SPP mode at air/metal interface for a nanowire which seemed to not have a cut off during the propagation. Although this effect was only observed but not explained, this opened up the possibility to obtain nanofocusing effect even at the air side of the waveguide, with obvious advantages for experiments, detection and application. The key element inside the work of Ditlbacher and Weeber [10,11] lies in the small metal layer (chromium or silver) they placed underneath the metal nano-stripe waveguide. This thin layer was placed only to prevent direct illumination of the waveguide during their measurements, since the SPP mode excitation was obtained by means of ATR coupling, illuminating from the glass substrate side. However, as we will show, it is the presence of this thin (but yet optically thick) layer which allows the existence of a SPP bound mode which is able to propagate and adiabatically condensate at the metal/air interface.

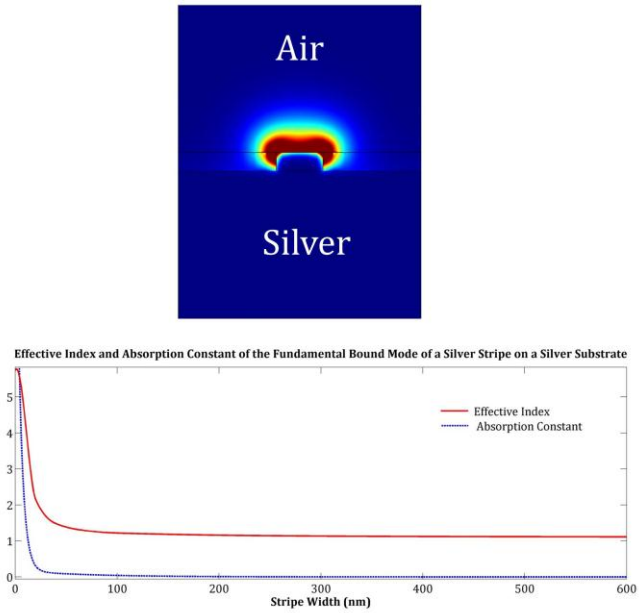

Figure 5.12 Up: mode profile of the fundamental bound SPP mode of a silver stripe waveguide on a silver substrate at a wavelength of 633 nm. The stripe thickness is 100 nm and the width is 600 nm. Down: dispersion relation (normalized effective index and absorption constant) of the SPP mode as function of waveguide width.

Figure 5.12 shows the mode profile for a silver metal stripes placed on a silver substrate. The geometry is basically the same as the one considered in Figure 5.5 with the only difference being the substrate. As we can see, the mode possesses the same Gaussian-like shape as the one observed in Figure 5.5, but this time the mode is localized at the air/metal interface. The effective index dependence on the waveguide width is also plotted in Figure 5.12. This SPP mode could be mistaken for a leaky mode, as the one shown and discussed in Figure 5.5, since the effective index remains close to 1 for width value down to ~ 100 nm . However we see that for width stripe value below ~ 50 nm the effective index begins to diverge, like the bound mode used previously for obtain the nanofocusing effect. What makes this mode a true bound mode which is able to condensate lies in the dielectric environment. In fact, as we have seen, air/metal/high index dielectric multilayers allow the presence of symmetric and asymmetric modes localized at the two different interfaces. Instead, our configuration comprises a metallic bulk as substrate for the metal waveguide. This is the reason why a waveguide bound mode is present at the air/metal interface. This mode, for large width values, resembles the typical SSP mode profile on an extended metal film region [3,12] and once excited and coupled to the waveguide remains confined even for small waveguide width, without cut-off. Moreover, the presence of the optically thick metal layer underneath the waveguide actually prevents any form of re-radiation process into the substrate. With this configuration a more direct experimental verification of the focusing effect is possible, since direct near

field measurement at the air side would be possible, and the mode propagation at the air side allows to increase the SPP propagation length up to $\sim 35\ \mu$m for silver at $\lambda_0 = 633$ nm compared for instance to the propagation length of the mode used previously at silver/substrate interface, which has a value of $\sim 8\ \mu$m .

The mode found opens then the possibility to obtain a focusing effect on a planar geometry even at the air side. To investigate this possibility, the mode shown in Figure 5.12 is used as input source for a tapered silver waveguide on a silver bulk layer. The geometry and simulation parameters are the same as the one used for the simulation of Figure 5.10. Figure 5.13 shows the electric field profile for this case.

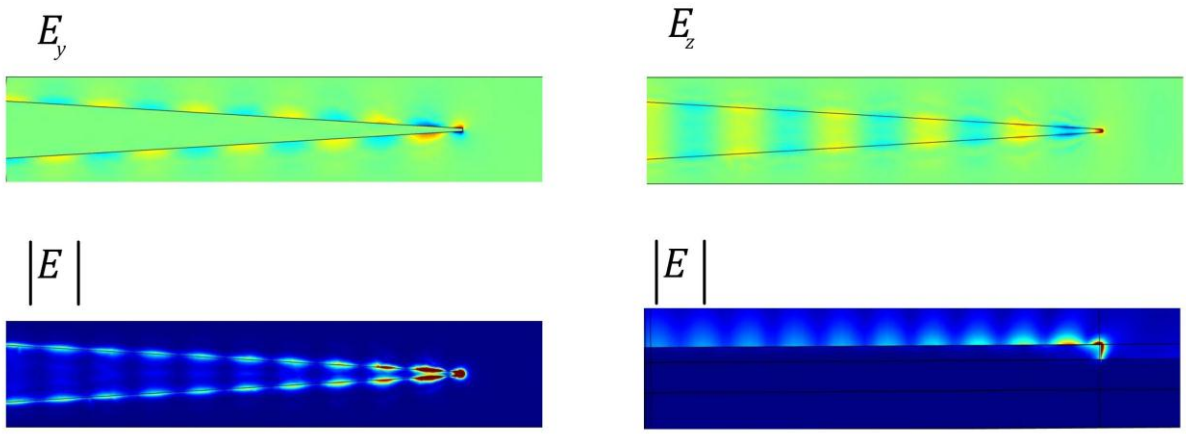

Figure 5.13 Electric field profiles of the SPP mode propagating at air/silver interface at a wavelength of 633 nm. The slices are taken along the x-y plane at the air/silver interface. The maximum field enhancement at the tip position is 1500. Color scales are saturated for better visualization.

The modal behavior and focusing effect is the same observed in Figure 5.10, with the only difference that the SPP propagation and condensation takes place now at the air/side, meaning that the geometry proposed and the mode used is actually able to produce a focusing effect. From the electric field norm distribution we see that also in the case at the tip position the field is spread all across the waveguide cross section, again with strong localization around the edges. Also the symmetry of the SPP mode at air/silver interface for E_y and E_z is similar to the one observed in the silver/substrate situation. Besides of the obvious advantage of air/silver excitation and propagation, this configuration allows also a more pronounced focusing enhancement with a maximum optimized value of 1500 which is twice the value found with the silver/substrate excitation. This is simply due to the fact that a mode propagating in air suffers less absorption and scattering process, leading to an increased field energy carried along the propagation. The adiabatic condensation process is basically the same as the one discussed for the

excitation at the substrate/metal interface, and so all the physical features discussed previously are the same even in this case.

5.3.1 Conclusions

In the first two sections of this chapter a detailed study on SPP propagation on planar metal waveguides has been provided. In particular we have shown that a planar nanofocusing effect, in the fashion of the one observed for 3D conical waveguides, is possible if the correct mode is excited accordingly to the dielectric environment. We have also shown an original method to overcome the limitations in the focusing effect observed at metal/substrate interface. By using a bulk metallic substrate it is possible to excite a SPP bound mode which does not present cut-off during the propagation and hence produces a focusing effect at air/metal interface. The results found will be used in the next section where a novel device, which combines the focusing properties of a plasmonic planar structure with the exotic properties of OAM light, is presented in details. The details of the OAM of light and how it can be generated by means of a Plasmonic Vortex Lens can be found at the end of chapter 1.

5.4 Focusing dynamics on circular distributed tapered metallic waveguides by means of Plasmonic Vortex Lenses

Orbital Angular Momentum (OAM) of light is a degree of freedom which has not still been fully investigated and has recently opened up new possibilities in the field of optics. It is related to electromagnetic beam vorticity and phase singularities [13]. The potential applications of OAM of light in applied physics, and in particular in plasmonics have only begun to be explored. Very interesting and promising new effects have been demonstrated, like plasmon-induced spin-orbit interactions [14], optical spin Hall effect in nanoapertures arrays [15] and spin dependent plasmonic effects [6,16-20]. It has also been shown that Surface Plasmon Polaritons (SPP) waves carrying OAM, i.e. Plasmonic Vortices (PVs), can be generated by using convenient metallic subwavelength structures illuminated by circularly polarized light [14-16]. The spin angular momentum carried by incident circularly polarized light beam, thanks to the plasmonic structures, is converted into OAM, leading to the generation of helical modes via the coupling with surface plasmons [21,22]. The plasmonic structures include concentric circular grooves [15], Archimedes's spiral shaped grooves, also called Plasmonic Vortex Lenses (PVLs), [15-18,20] and subwavelength apertures [18,19]. An example of combining SPP modes generated by a PVL with nanofocusing capabilities of a plasmonic conical structure is given in [23], where high field enhancement on the nanoscale region is observed.

In this section we propose a SPP focusing structure based on tapered planar waveguides illuminated by OAM light by means of a PVL. The outer part consists of *m* spiral grooves with a central circular metallic area. The inner part inside a circular area is designed with four circularly distributed planar nanotips with apex curvature radius of 10nm (Figure 5.14). These metallic planar nanotips are placed on a 200 nm metallic layer of silver and as we have seen, are able support plasmonic modes that can be guided and focalized up to few nanometers [24-27]. As illuminating the PVL with a circular polarized light and exploiting the spiral arm design, we can control the OAM topological value (l_{PV}) of the PVs [22]. The control of the PV modes is used to modulate in phase the SPPs propagation along the nanotips and their corresponding focusing dynamics.

The numerical analysis in this work have been performed using software package COMSOL Multiphysics® which implements the finite elements method for rigorous numerical simulations.

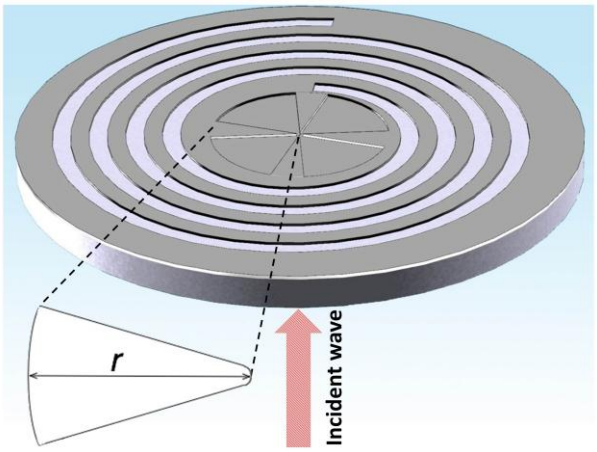

Figure 5.14 The PVL consists of m Archimede's spiral grooves milled in a 200 nm silver film on glass substrate, while at the center four silver planar rounded nanotips of thickness 70 nm are grown on a silver disk of thickness 230 nm in order to avoid direct nano-tips illumination from the incoming radiation (λ=633nm). The refractive index of silver is nAg=0.13+i3.8. Inset: the tipbase is curved. The tip is r=3.1μm in length, while the tip angle value is set to 12°. The PVL groove period for SPP coupling at silver/air interface is 617 nm with duty cycle of 50%.

In the previous section, we have proven that the focusing effect at the apex of a silver nanotip lying on a silver bulk takes place at the air/metal interface. The optimized geometry is then the same as the one discussed in the previous section (see Figure 5.15). After the optimization of the single tip, we considered the structure made by four circularly distributed planar nanotips. In order to reduce the computational efforts, without loss of generality, we simulate only the central inner part of the structure discarding the spiral grating and its contribution to the total enhancement. In this way, the field enhancement is given only by the tip itself. In particular a boundary modal analysis has been performed which allows to lunch a

PV mode with an arbitrary l_{PV} value from a circular port 600 nm distant from the tips base. If the exact geometrical parameters of the spiral are needed for experimental purposes, they can be found by calculating the exact period and thickness of the spiral grating by means of a multi-parametric FEM simulation, like the ones performed for EOT gratings in chapter 3. Indeed, the symmetry of the problem is the same for an EOT grating. For completeness we report the parameters of the spiral grating in order to properly excite a SPP mode at air/silver interface at a wavelength of 633 nm; the PVL groove period for SPP coupling at silver/air interface is 617 nm with duty cycle of 50% and the total metal thickness is 270 nm.

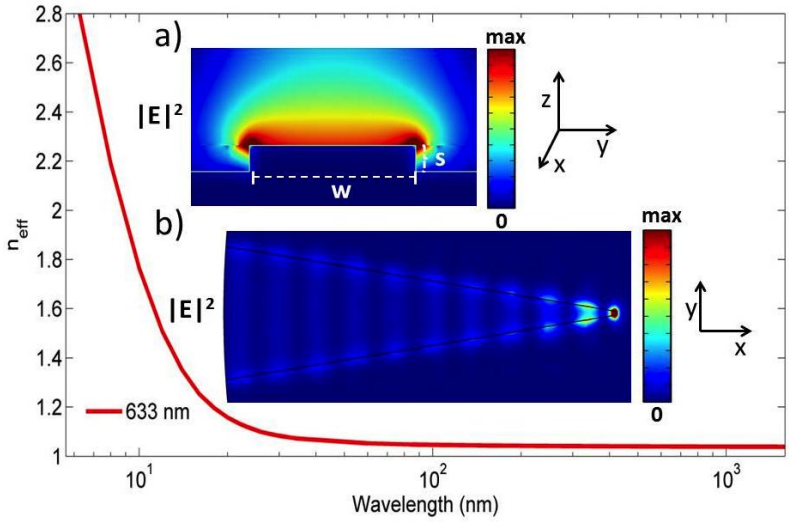

Figure 5.15 red line: SPP mode behavior for a silver stripe waveguide on a silver substrate for different widths value (w) for λ=633nm. The silver thickness is *s*=100nm. a) Electric field intensity of the bound mode at silver/air interface for *w*=680nm. b) Electric field intensity for single nanotip. The focusing effect is shown at silver/air interface. Color scale is saturated for better field visualization.

As we have shown in chapter 1, a spiral PVL [23] with m-arms illuminated by a circular polarized beam with topological charge l_i and spin s_i generates a PV whose OAM is $l_{PV}= m+l_i+s_i$. We analyze the behavior of the structure for different values of l_{PV} recalling that SPPs carrying OAM are characterized by a helicoidally phase structure. Depending on the phase of the input PV, a different configuration can be obtained. For $l_{PV}=0$, the obtained phase distribution leads to a strong focusing effect at the apex of each tip (Figure 5.16). The enhancement field intensity at the tip is ≈ 4900, which is far higher than the value previously found for the single tip, reaching a value near to the one found for the conical geometry. This enhancement is given by the fact that the SPP mode excited is also a PV mode, and due to the circular polarized nature of this mode, the energy concentration towards the center of the structure where the tips are located is maximized. This proves the reliability of the structure for the focusing production compared to other planar focusing structure [24-27]. The intensity enhancement is calculated as usually as $|E_{tip}|^2/|E_{bmax}|^2$

where E_{tip} is the electric field amplitude calculated at 10 nm upon the tip's apex and E_{bmax} is the maximum value of the electric field mode excited as boundary condition. Figure 5.16 shows the intensity of the electric field, together with that of the boundary field mode used as input source. A symmetric and simultaneous enhanced charge distribution at the four tips is observed.

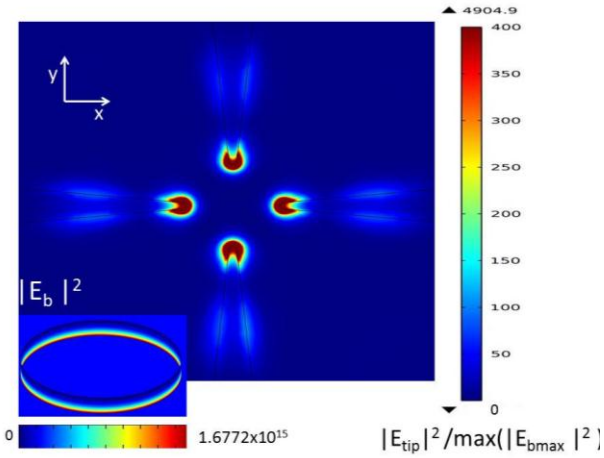

Figure 5.16 Intensity of the electric field for the structure of Figure 5.14 illuminated with a PV with $l_{PV}=0$. Lower inset shows the boundary mode used as input source. Color scale is saturated for better field visualization.

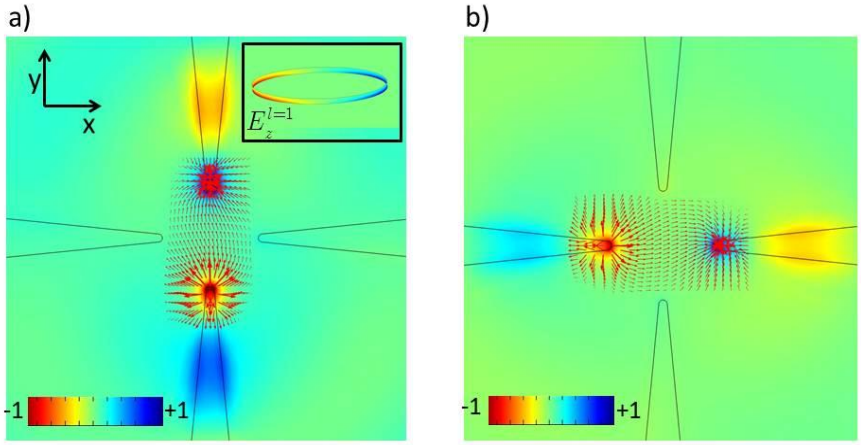

Figure 5.17 Color scale (a.u.) represents transverse electric field component E_z for $l_{PV}=1$. Red arrows indicate the in plane electric field (E_x and E_y). Upper inset shows the boundary mode used as input source. a) Charge distribution at T=0. b) Charge distribution at T/4 time later.

For higher l_{PV} values, the phase of PV possesses a periodic azimuthally spatial dependence in the form of $\exp(il_{PV}\varphi)$. This behavior affects the charge distribution at the tips apex depending on the input electric field phase distribution. For $l_{PV}=1$ the phase of the incoming PV azimuthally increases from 0 to 2π (see inset of Figure 5.17a). As a consequence, two diametrically opposed tips (the verticals ones in Figure

5.17a) acquire an enhanced charge distribution on the apex with opposite sign, while the remaining two tips (the horizontal ones in Figure 5.17b) are 'switched off''. This configuration is not static in time, in fact, at an instant t=*T/4* time later, where T=2π/ω, the phase profile evolves so that the charge distribution has now rotated leading to the excitation of the two opposite horizontal tips (Figure 5.17b).

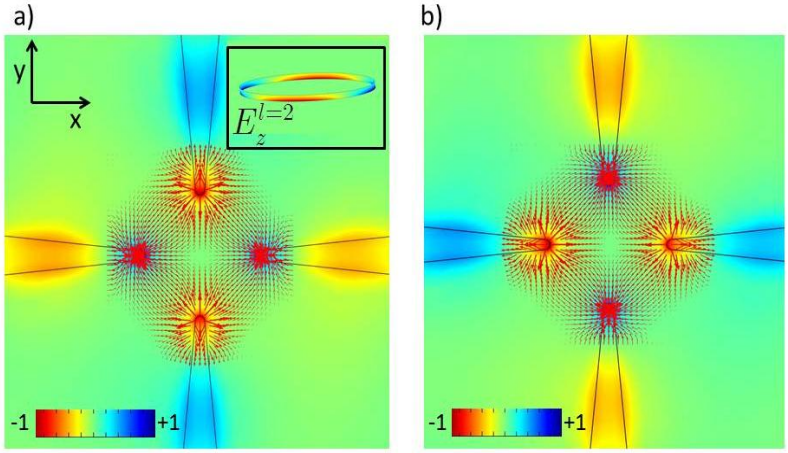

Figure 5.18 Color scale (a.u.) represents transverse electric field component E_z for $l_{PV}=2$. Red arrows indicate the in plane electric field (E_x and E_y). Upper inset shows the boundary mode used as input source. a) Charge distribution at T=0. b) Charge distribution at T/2 time later.

For $l_{PV}=2$ (Figure 5.18a) the electric field phase azimuthally increases from 0 to 4π (see inset of Figure 5.18a). At *t*=0 a simultaneous enhanced charge distribution results at the tip apex so that the two couples of diametrically opposite tips have the same charge sign respectively (see Figure 5.18a). Looking at t=*T/2* time later (Figure 5.18b) we see that the four tips are still simultaneously excited with the same behavior observed before, the only difference is that as the phase evolves in time, the charge distribution at the tips apex is opposite respect to the previous case.

For even larger l_{PV} values the charge sign at the tips apex for the four tips configuration can be easily deduced from the azimuthal phase field distribution of the PV. Let's imagine that the four tips are disposed in an azimuthal coordinates system φ where the left horizontal tip is placed in the 0° position, and the remaining three tips are placed in 90°,180° and 270° position in a clockwise direction. Since the phase of PV possesses a periodic azimuthally spatial dependence in the form of $\exp(il_{PV}\varphi)$, the maxima and minima of the PV at the base of each tip follows curve in the form of $y=\cos\left(l_{PV}\varphi\pi/180°\right)$. Figure 5.19shows this behavior for l_{PV} ranging from 1 to 4. It's easy to see then that for odd l_{PV} values at a given time only two opposite tips will be excited with opposite charge distribution at the apex (just as the $l_{PV}=1$ case). For even l_{PV} values with $l_{PV}>2$, all the four tips will be excited at the same time, but differently from the $l_{PV}=2$ case, the charge sign at the apex will be equal for all four tips (resembling the $l_{PV}=0$ case). It's

important to note that this reasoning is valid for arbitrarily large l_{PV} only if the taper angle of each tip is small enough to allow the input phase to be quite constant and well defined along each of the tapered waveguides bases.

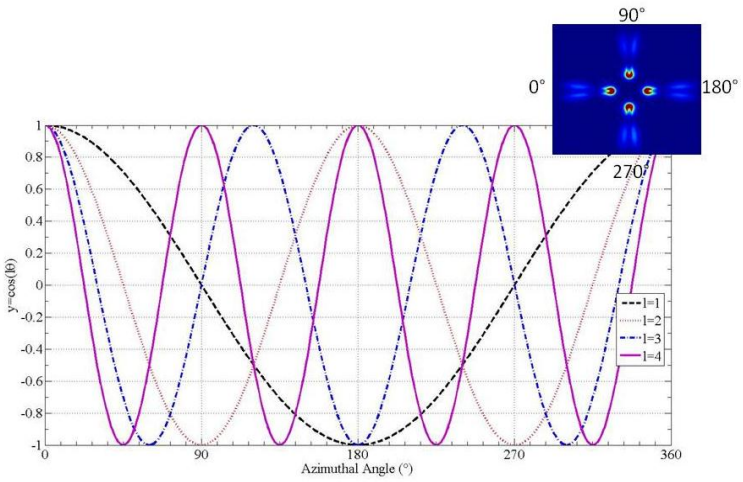

Figure 5.19 Azimuthal dependence of PV phase at the base of each tip for different l_{PV} values. Inset shows the azimuthal position of the tip.

5.4.1 Nanofabrication

In order to investigate also experimentally the structure presented in the previous section, a complete fabrication process of the device has been developed. The crucial aspect of the fabrication process is to fabricate the inner part where the four tips lies over a silver bulk substrate, while on the other hand the gap between each spiral's arms must be completely open to allow the SPP coupling with the PVL. For these reasons, the fabrication process consists of different fabrication steps with different techniques and can be summarized as follows. First, on a glass substrate is evaporated a silver layer of 230 nm on the top of that a double layer of PMGI/PMMA resist is spinned. The silver layer acts as the silver substrate for the entire structure. The double stack resist layer is required in order to perform EBL process with a following lift-off step (see chapter 2 for further details). The PMMA layer of 60 nm is the one where actually the lithography takes place, while the PMGI layer, which is not exposed acts as a masking layer. The EBL exposure is performed in high-resolution mode to assure the highest lithographic quality, in order to achieve the smallest possible radius of curvature at the tip's position. The beam current is set to 100p A and the exposure dose to 300 $\mu C/cm^2$. For high resolution process, the control and correction of the proximity effect is crucial. For this reason the exposed pattern has been PEC corrected, as shown in Figure 5.20. The exposed pattern consists of the four tips and a full circle with no PVL at the moment. After the EBL exposure, the PMMA layer is developed in water:IPA=3:7 solutions for 30 second, while the PMGI layer is developed in MF 319:water=1:1 solution for 6 minutes. The solution concentration and time

development for the PMGI has been chosen after several tests, in order to find the best compromise between etching time and undercut rate. The next step is the evaporation of 70 nm silver layer on the entire structure. The 70 nm silver layer is the actual thickness of the tips, respect to the plane of the PVL. After the metal deposistion, the PMMGI/PMMA layer is stripped by means of hot acetone and pure MF 319 in ultrasonic bath for 10 minutes. This assures the complete removing of the remaining resist. The last step is the creation of the PVL. For this scope, a FIB process is performed on the structure: with the help of an alignment marker it is possible precisely drill the PVL in the silver bulk layer. In this way, the PVL grating is cleared all the way down to the glass substrate, while only the four tips area lies on the silver bulk. This process prevents the four tips to be directly illuminated from the input radiation, and more important, the right dielectric environment for the focusing at air/silver interface is provided. Figure 5.20 and Figure 5.21 show the schematic of the process along with images of the fabricated samples. As we can see, the tip's radius of curvature is very low, thus granting high field enhancement.

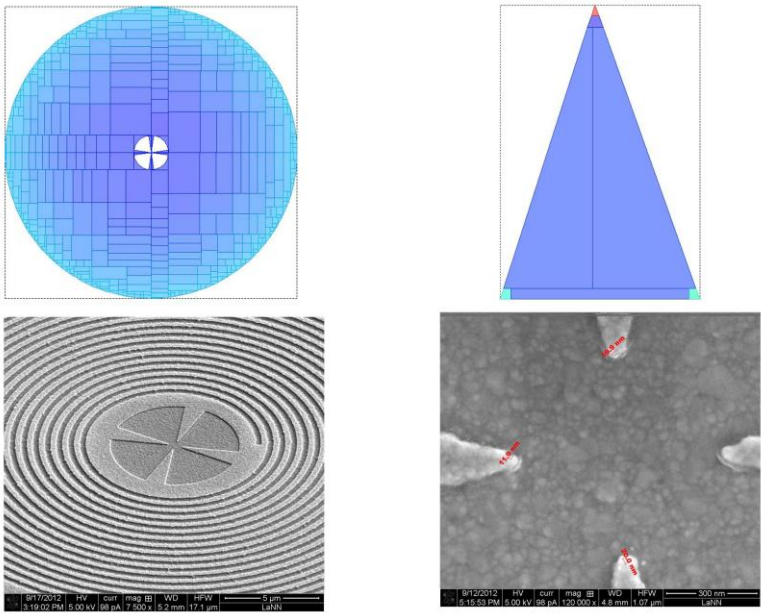

Figure 5.20 Up: CAD pattern files with PEC for EBL exposure. The colors indicate the different dose classes in order to compensate the proximity effect. A detail of the tip pattern is also shown. Down: complete fabricated samples. The four tips lie on a silver substrate, while the PVL is drilled down to the glass substrate. The detail shows the radius of curvature of the tips, which is in the order of 10 nm.

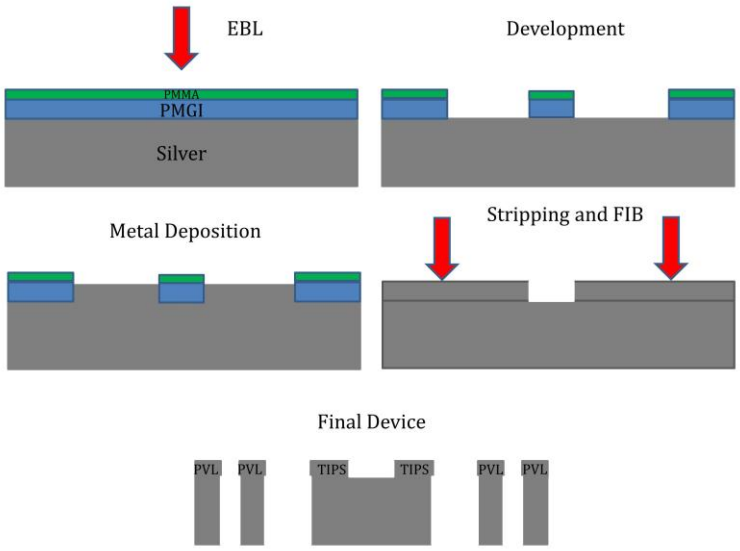

Figure 5.21 Flowchart of the fabrication steps described in this section. The images show a cross section of the device. After the EBL exposure and resist development, a metal deposition is performed in order to assure the presence of the silver substrate underneath the four tips. A FIB milling creates the PVL structure.

5.4.2 Conclusions

Summarizing, we have shown that an efficient focusing structure can be obtained by exploiting the modal properties of metal tapered waveguides illuminated by means of a PV. By acting on the l_{PV} value of the PV it is possible to induce a time-variable charge distribution at the tips'apex thus gaining an additional degree of control on the final focusing effect. Different behaviors have been observed, which depend on the phase structure of the PV generated by the PVL. Moreover the maximum field enhancement observed is higher than the one obtained by means of linear-polarized illumination source on a planar structure. The proposed structure has been also fabricated, by using a multi-step high-resolution nanofabrication process which combines EBL and FIB lithography process and assures a radius of curvature at the tip as lows as 10 nm.. Future work will be aimed to the optical characterization of the device. It must be noted that with a conventional SNOM near-field detection scheme (see chapter 2), the only visible effect would be the simultaneous enhancement of the four tips in the $l_{PV}=0$ case. In fact, at visible frequencies, the "switching charge" effect described for $l_{PV}>0$ occurs in the THz frequency range and no optical detector is so fast to track the signals coming from the different tips. Moreover, a femto or aven atto-second laser source is needed in order to not mask the switching effect, but these technologies are still under development and very expensive. A possible solution of these problems could be to shift in the infrared wavelength regime and use the experimental set up developed by Sandtke et al. [28], which consists of a phase-sensitive near field microscope which yields information on both the local electric field amplitude and phase. It is based on a near-field microscope detection scheme which collects the

evanescent field by scanning with a coated near field probe. The system is incorporated in one branch of a Mach-Zehnder interferometer; in this way the light collected in the probe interferes with a frequency-shifted reference beam. The time-dependent interference signal can be then detected and analyzed with a lock-in amplifier. By adjusting and vary the delay time between the two reference branches, they were able to track and follow the time evolution of a SPP wave packet travelling along a metal waveguide. With this set-up it would be then possible to observe, at a fixed space position of the probe, the phase evolution and consequently the charge switching effect at a single tip. A possible application of this effect would be in the optical tweezing field; in the last years the problem optical trapping to the nanoscale has been addressed [29] and metallic nanostructures have proved to be an ideal choice for controlling light at subwavelenght scales, allowing the accurate positioning of single nano-objects, nano trapping and biosensing [30].

5.5 References

[1] Berini P., Phys. Rev. B, 61 (15):10484 (2000).

[2] Berini P., Phys. Rev. B, 63 (12):125417 (2001).

[3] R. Zia, M. D. Selker, and M. L. Brongersma, Phys. Rev. B 71, 165431 (2005).

[4] Dickson R.M.,Andrew L.L., J. Phys. Chem. B, 104:6095-6098.

[5] J.R. Krenn, B. Lamprecht, H. Ditlbacher, G. Schider, M. Salerno, A. Leitner and Aussenegg F.R., Europhys. Let. 60(5):663-669 (2002).

[6] E. Verhagen, A. Polman, and L. Kuipers, Opt. Express 16 (1), 45 (2008).

[7] F. Azuel, Chem. Rev. 104, 139 (2004).

[8] G.N. van den Hoven, E. Snoeks, A. Polmann, C. van Damm, J.W.M. van Uffelen and M.K. Smit, J. Appl. Phys. 79, 1258 (1996).

[9] N. A. Issa and R. Guckenberger, Plasmonics 2, 31 2007.

[10] H. Ditlbacher, A. Honheau, D. Wagner, U. Kreibig, M. Rogers, F. Hofer, F. Aussenegg, R. Franz and J.R. Krenn, Phys. Rev. Lett. 95 257403 (2005).

[11] J. Cs. Weeber, J. R. Krenn, A. Dereux, B. Lamprecht, Y. Lacroute, and J. P. Goudonnet, Phys. Rev. B 64, 045411 (2001).

[12] Stefan A. Maier, Plasmonics Fundamentals and Applications (Springer 2007).

[13] L. Allen, M. W. Beijersbergen, R. J. Spreew, and J. P. Woerdman, Phys. Rev. A 45, 8185 (1992).

[14] Y. Gorodetski, A. Niv, V. Kleiner, and E. Hasman, Phys. Rev. Lett. 101(4), 043903 (2008).

[15] K. Y. Bliokh, Y. Gorodetski, V. Kleiner, and E. Hasman, Phys. Rev. Lett. 101(3), 030404 (2008).

[16] Y. Gorodetski, N. Shitrit, I. Bretner, V. Kleiner, and E. Hasman, Nano Lett. 9(8), 3016–3019 (2009).

[17] H. Kim, J. Park, S.-W. Cho, S.-Y. Lee, M. Kang, and B. Lee, Nano Lett. 10(2), 529–536 (2010).

[18] L. T. Vuong, A. J. L. Adam, J. M. Brok, P. C. M. Planken, and H. P. Urbach, Phys. Rev. Lett. 104, 083903 (2010).

[19] N. Shitrit, S. Nechayev, V. Kleiner, and H. Hasman, Nanolett. 12, 1620 (2012).

[20] S. Yang, W. Chen, R. L. Nelson, and Q. Zhan, Opt. Lett. 34(20), 3047–3049 (2009).

[21] S.-W. Cho, J. Park, S.-Y. Lee, H. Kim, and B. Lee, Opt. Express 20, 10083 (2012).

[22] L. Marrucci, C. Manzo, and D. Paparo, Phys. Rev. Lett. 96, 163905 (2006).

[23] P. Zilio, E. Mari, G. Parisi, F. Tamburini, and F. Romanato, Opt. Lett.37(15), 3234-3236 (2012).

[24] D. K. Gramotnev, M. W. Vogel, Phys. Lett. A 375 (39), 3464-3468 (2011).

[25] E. Verhagen, A. Polman, and L. Kuipers, Opt. Express 16 (1), 45 (2008).

[26] E. Verhagen, M. Spasenovic, A. Polman, and L. Kuipers, PRL 102, 203904 (2009).

[27] X. He, L. Yang, T. Yang, Opt. Express 19 (14), 12865 (2011).

[28] M. Sandtke, R. J. Engelen, H. Schoenmaker, I. Attema, H. Dekker et al., Rev. Sci. Instrum. 79, 013704 (2008).

[29] M. L. Jaun, M. Righini, R. Quidant, Nature Photonics 5 349 (2011).

[30] S. Chen, M. Svedendahl, M. Kall, L. Gunnarsson, A. Dimitriev, Nanotechnology 20, 434015 (2009).

Conclusions

Plasmonic nanostructures have been proved to allow light and electromagnetic field concentration in subwavelength regions, if the proper geometrical and physical conditions are fulfilled. The problem of designing and realizing these nanostructures has been studied and analyzed. A rigorous approach has been applied in this thesis work through each step of the process-chain: simulation - nanofabrication - characterization. The strength and validity of this approach is confirmed by the different results obtained, thanks to the interaction between two main processes: theoretical-numerical modeling and nanofabrication. The first allowed to understand the physical background underlying each plasmonic phenomena and consequently to tailor the optical response of the plasmonic structure trough an optimization process, while the latter by using the results coming from the first step has made possible the realization of the samples for experimental testing with the highest possible fidelity to the theoretical models. This is a not closed circle, since the different results obtained and problems encountered must be used and solved for a full interaction between each of the different steps. In this view we can say that the scientific paradigm of the Galilean approach described at the beginning of this work has been fulfilled.

The complete analysis of the transmission and resonance properties of 1D metallic gratings has allowed to elucidate the different physical mechanisms involved correlating near and far-field features both experimentally and numerically, highlighting a polarization symmetry properties of the system. The structure has been optimized for two main applications, consisting of SERS spectroscopy measures and the developing of an integrated plasmonic biosensing device. The results proved the reliability of plasmonic gratings for sensing purposes. Thanks to the simple geometry employed, the SERS signal of a benzenthiol monolayer of the realized nanostructures and its dependence on a generic hybrid polarization have been measured and compared with the theoretical calculated estimations. The integration of a plasmonic grating on a HEMT multilayer geometry represents a good example on how plasmonic can be successfully applied and integrated to other branch of physics towards the development of a complete and innovative electro-optical device.

The adiabatic theory for the description of the nanofocusing effect on conical tapered waveguide has been investigated with the help of analytical and numerical models, elucidating the mechanisms of plasmonic compression. The study on cone materials and geometry allowed to find the optimized configurations for maximum field enhancement at the tip's position and thus the nanofabrication of "nano rocket" tips. Near field optics characterizations by means of SNOM demonstrate the performances of the studied nanostructure, although in this experiment no polarization of the impinging light has been used. The problem of generating and coupling a SPP radial mode to a conical waveguide has be overcame by using as

excitation source a PVL which generates a Plasmonic Vortex. Due to the optimal polarization nature of the SPP mode and also due to the presence of the plasmonic lens, the observed focusing effect is greater by an order of magnitude than the one observed with a conventional SPP excitation scheme.

SPP propagation on planar metal waveguides has been also investigated, demonstrating that planar nanofocusing effect is possible if the correct mode is excited accordingly to the dielectric environment. We have also shown an original method to overcome the limitations in the focusing effect observed at metal/substrate interface. By using a bulk metallic substrate it is possible to excite a SPP bound mode which does not present cut-off during the propagation and hence produces a focusing effect at air/metal interface. A novel device, which combines the plasmonic planar nanofocusing with the exotic properties of light possessing Orbital Angular Momentum (OAM) has been modeled and fabricated. The new degree of freedom possessed by the SPP beam opens up to the possibility of charge control in nanometric volumes, besides granting an highest field enhancement at the tip respect to standard illumination allowing the possibility of light control at subwavelenght scales. Future works will be aimed to the characterization and testing of the plasmonic nanofocusing effect, especially the ones where the illumination with light carrying orbital angular momentum requires a non-trivial near-field detection scheme.

Further improvement of plasmonic structures is certainly needed both scientifically and technologically. Regarding the scientific aspect, the interaction and integration of plasmonic with other branches of physic, chemistry, biology, engineer and even medicine is still an open topic and it needs to be further optimized and developed for a general advantage of the entire nano science scientific community. From a technological point of view, plasmonic and light-based structures must evolve towards even more compact and integrated devices. Only in this way the limitations of standard microelectronics chips could be truly overcome, and thus opening the way for a branch of new electro-optical devices which exploit the advantages of both worlds.

Appendix A: SPP Dispersion Relation

SPP at Single Interface

The most simple geometry sustaining SPP (see Figure A.1) is that of a single flat interface between a dielectric with real dielectric constant ε_2 in $z>0$ and a metal described by an isotropic, frequency dependent, complex dielectric function $\varepsilon_1(\omega)=\varepsilon_1^{'}(\omega)+i\varepsilon_1^{''}(\omega)$ in $z<0$. We are looking for a solution of the wave equation that is bounded to the interface, i.e. with an evanescent decay in the z direction.

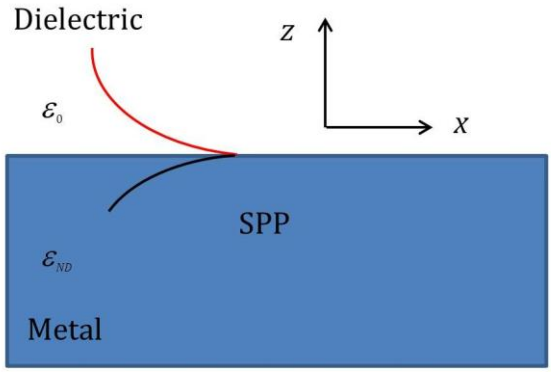

Figure A.1 Geometry of SPP propagation at a single interface between a metal and a dielectric.

Let's start with a p-polarized wave propagating along the x-direction (TM wave):

$$\begin{aligned}\mathbf{H}_2 &= (0,H_{y2},0)e^{i(k_{x2}x-k_{z2}z-\omega t)}\\ \mathbf{E}_2 &= (E_{x2},0,E_{z2})e^{i(k_{x2}x-k_{z2}z-\omega t)}\end{aligned} \tag{A.1}$$

for $z>0$ and:

$$\begin{aligned}\mathbf{H}_1 &= (0,H_{y1},0)e^{i(k_{x1}x+k_{z1}z-\omega t)}\\ \mathbf{E}_1 &= (E_{x1},0,E_{z1})e^{i(k_{x1}x+k_{z1}z-\omega t)}\end{aligned} \tag{A.2}$$

for $z<0$. k_{zi} is the component of the wave vector perpendicular to the interface between the two media. The electromagnetic field has also to obey to the boundary conditions at the interface:

$$\begin{aligned}\mathbf{n}\cdot(\mathbf{D}_1-\mathbf{D}_2)&=0\\ \mathbf{n}\times(\mathbf{E}_1-\mathbf{E}_2)&=0\\ \mathbf{n}\cdot(\mathbf{B}_1-\mathbf{B}_2)&=0\\ \mathbf{n}\times(\mathbf{H}_1-\mathbf{H}_2)&=0\end{aligned} \tag{A.3}$$

Conditions (A.3) can also be expressed as:

$$\begin{aligned} E_{x1} &= E_{x2} \\ \varepsilon_1 E_{z1} &= \varepsilon_2 E_{z2} \\ H_{y1} &= H_{y2} \end{aligned} \tag{A.4}$$

from which follows that:

$$k_{x1} = k_{x2} = k_x \tag{A.5}$$

Using the fields defined in (1.8) and (1.9) we have:

$$\begin{aligned} \nabla \times \mathbf{H}_j &= \begin{pmatrix} \mp H_{yj} i k_{zj} e^{i(k_{xj} x \pm k_{zj} z - \omega t)} \\ 0 \\ H_{yj} i k_{xj} e^{i(k_{xj} x \pm k_{zj} z - \omega t)} \end{pmatrix} \\ \varepsilon_j \frac{\partial \mathbf{E}_j}{\partial t} &= \begin{pmatrix} -i\varepsilon_j \omega E_{xj} e^{i(k_{xj} x \pm k_{zj} z - \omega t)} \\ 0 \\ -i\varepsilon_j \omega E_{zj} e^{i(k_{xj} x \pm k_{zj} z - \omega t)} \end{pmatrix} \end{aligned} \tag{A.6}$$

with $j = 1,2$. Taking the last equation in (A.6) and considering the x-component of (A.6) we get:

$$\begin{aligned} \frac{k_{z1}}{\varepsilon_1} H_{y1} &= \omega E_{x1} \\ -\frac{k_{z2}}{\varepsilon 2} H_{y2} &= \omega E_{x2} \end{aligned} \tag{A.7}$$

From (A.4) and (A.7) we get the system:

$$\begin{aligned} \frac{k_{z1}}{\varepsilon_1} H_{y1} + \frac{k_{z2}}{\varepsilon_2} H_{y2} &= 0 \\ H_{y1} - H_{y2} &= 0 \end{aligned} \tag{A.8}$$

This system admits solutions only if the coefficient's determinant vanishes, which yields to the relation:

$$\frac{k_{z1}}{\varepsilon_{z1}} + \frac{k_{z2}}{\varepsilon_{z2}} = 0 \tag{A.9}$$

By inserting the fields (1.8) and (1.9) into the wave equation (1.7), we obtain the relation:

$$k_{zj}{}^2 + k_x{}^2 = \varepsilon_j \left(\frac{\omega}{c} \right)^2 \tag{A.10}$$

From (A.9) and (A.10) we finally get the dispersion relation for a SPP:

$$k_x = \frac{\omega}{c}\left(\frac{\varepsilon_1\varepsilon_2}{\varepsilon_1+\varepsilon_2}\right)^{1/2} \tag{A.11}$$

If we now consider a p-polarized wave (TE wave):

$$\begin{aligned}\mathbf{E}_2 &= (0, E_{y2}, 0)e^{i(k_{x2}x - k_{z2}z - \omega t)} \\ \mathbf{H}_2 &= (H_{x2}, 0, H_{z2})e^{i(k_{x2}x - k_{z2}z - \omega t)}\end{aligned} \tag{A.12}$$

for $z > 0$ and:

$$\begin{aligned}\mathbf{E}_1 &= (0, E_{y1}, 0)e^{i(k_{x1}x + k_{z1}z - \omega t)} \\ \mathbf{H}1 &= (H_{x1}, 0, H_{z1})e^{i(k_{x1}x + k_{z1}z - \omega t)}\end{aligned} \tag{A.13}$$

for $z < 0$, we have from boundary conditions (A.3):

$$(k_{z1} + k_{z2})E = 0 \tag{A.14}$$

Since we are looking for a localized wave, the real part of k_{z1} and k_{z2} must be positive, so the only solution is $E = 0$. This means that a s-polarized SPP cannot propagate along the interface of a metal-dielectric system. Surface Plasmon Polaritons exist only for TM polarization.

SPP on Thin Metal Films

In this section we focus our attention to the dispersion relation of SPP in multilayers consisting of alternating conducting and dielectric thin films (IMI and MIM geometry, see Figure A.2) In order to not loose generality, the different domains are simply labeled with a number (I, II and III), The I layer is the core layer with thickness 2a, while the II and III layers are the claddings layers which can be metallic or dielectric depending on the IMI or MIM situation. For z>a the field components of the TM SPP fundamental mode are:

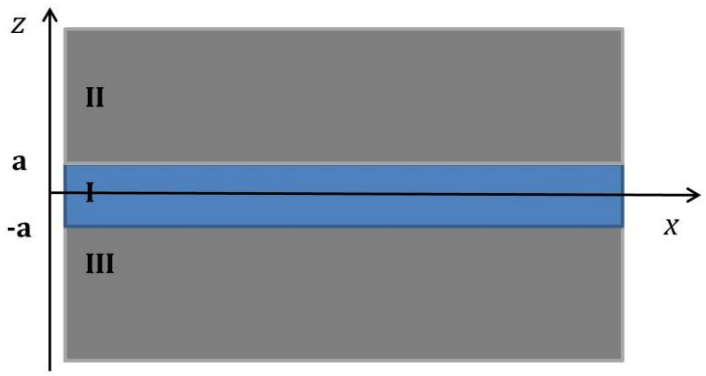

Figure A.2 Geometry of IMMI/MIM multilayer system sustaining SPP couple modes.

$$
\begin{aligned}
H_y &= Ae^{i\beta x}e^{-k_3 z} \\
E_x &= iA\frac{1}{\omega\varepsilon_0\varepsilon_3}k_3 e^{i\beta x}e^{-k_3 z} \\
E_z &= -A\frac{\beta}{\omega\varepsilon_0\varepsilon_3}e^{i\beta x}e^{-k_3 z}
\end{aligned}
\tag{A.15}
$$

While for z<-a we have:

$$
\begin{aligned}
H_y &= e^{i\beta x}e^{k_2 z} \\
E_x &= -iB\frac{1}{\omega\varepsilon_0\varepsilon_2}k_2 e^{i\beta x}e^{k_2 z} \\
E_z &= -B\frac{\beta}{\omega\varepsilon_0\varepsilon_2}ee^{i\beta x}e^{k_2 z}
\end{aligned}
\tag{A.16}
$$

Where for simplicity of notation $k_i \equiv k_{z,i}$. Equations (A.15) and (A.16) demand that the field decay exponentially in the claddings. In the core region –a<z<a, the modes localized at the bottom and top must couple if the core thickness is comparable with the skin depth of the metal, and the field can be expressed as:

$$
\begin{aligned}
H_y &= Ce^{i\beta x}e^{k_1 z} + De^{i\beta x}e^{-k_1 z} \\
E_x &= -iC\frac{1}{\omega\varepsilon_0\varepsilon_1}e^{i\beta x}e^{k_1 z} + iD\frac{1}{\omega\varepsilon_0\varepsilon_1}e^{i\beta x}e^{-k_1 z} \\
E_z &= C\frac{\beta}{\omega\varepsilon_0\varepsilon_1}e^{i\beta x}e^{k_1 z} + D\frac{\beta}{\omega\varepsilon_0\varepsilon_1}e^{i\beta x}e^{-k_1 z}
\end{aligned}
\tag{A.17}
$$

The continuity of the tangential components requires at z=a:

$$
\begin{aligned}
Ae^{-k_3 a} &= Ce^{k_1 a} + De^{-k_1 a} \\
\frac{A}{\varepsilon_3}k_3 e^{-k_3 a} &= -\frac{C}{\varepsilon_1}k_1 e^{k_1 a} + \frac{D}{\varepsilon_1}e^{-k_1 a}
\end{aligned}
\tag{A.18}
$$

And at z=-a:

$$
\begin{aligned}
Be^{-k_2 a} &= Ce^{-k_1 a} + De^{k_1 a} \\
-\frac{b}{\varepsilon_2}k_2 e^{-k_2 a} &= -\frac{C}{\varepsilon_1}k_1 e^{-k_1 a} + \frac{D}{\varepsilon_1}e^{k_1 a}
\end{aligned}
\tag{A.19}
$$

Moreover, the Helmholtz wave equation is valid in all three regions:

$$k_i^2 = \beta^2 - k_0^2 \varepsilon_i \tag{A.20}$$

For i = 1, 2, 3. This system of linear equations can be solved, leading to an implicit analytical expression for the dispersion relation for SPP on multilayer films. The expression is given by:

$$e^{-4k_1 a} = \frac{k_1/\varepsilon_1 + k_2/\varepsilon_2}{k_1/\varepsilon_1 - k_2/\varepsilon_2} \frac{k_1/\varepsilon_1 + k_3/\varepsilon_3}{k_1/\varepsilon_1 - k_3/\varepsilon_3} \tag{A.21}$$

It is worth noting that for infinite thickness of the core layer, this expression reduces to the dispersion relation of SPP on single metal/dielectric interface (see equation (1.10)). If we consider now the symmetric dielectric configuration in which the sub and super strates (II and III) are equal in terms of their dielectric constants, we have $k_2 = k_3$. In this case, the dispersion relation can be split into a pair of equations which describe modes of odd or even parity, depending on the IMI or MIM configuration:

$$\tanh k_1 a = -\frac{k_2 \varepsilon_1}{k_1 \varepsilon_2}$$
$$\tanh k_1 a = -\frac{k_1 \varepsilon_2}{k_2 \varepsilon_1} \tag{A.22}$$

This set of equations takes the form of equations (1.19) and (1.20) when the IMI and MIM dielectric environments are considered.

Appendix B: Analytical Model for EOT in 1D metallic gratings

In this section is provided the derivation for the analytical formula (3.7) which expresses the transmission trough a 1D grating, consisting of an array of one-dimensional metal slits, in subwavelength regime. This model was first proposed by M. Moreno and F. Garcia-Vidal in 2002 for a 2D hole array, and it was then simplified for the one-dimensional case. For the derivation of the various scattering coefficients, a different approach and formalism is used respect to the original model, making the notation simpler. Also for easy of reading the case presented here refers to the symmetric dielectric configuration, i.e. the one with super-strate and substrate fixed as vacuum. However, the final result is the same as the one proposed by Moreno and Vida and can be easily extended to any dielectric configuration.

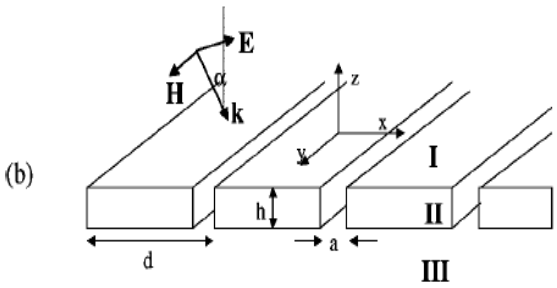

Figure B.1: Definition of the geometry for the transmission problem

Definition of the Model

Consider the transmission grating depicted in Figure B.1. The metal film has a thickness h, the grating period is denoted by d and the slits width is denoted by a. The grating is in the plane x-y. We denote by z the direction normal to the film, and take the metal-dielectric interface to be placed at $z=\pm h/2$. The array is illuminated by a plane wave with p-polarization and wave vector $\mathbf{k}_0$, impinging at an angle of incidence α. The structure can then be divided into three regions: the superstrate (from where the radiation is coming), the substrate (where radiation will be transmitted to) and the grating region. To simplify the problem, we will assume that the dielectric medium in the superstrate, substrate and into the interior of the slits, is all the same (symmetric configuration), and we take the dielectric constant to be equal to unity. The model is based on a modal exposition that foresees the computation of the EM field over the three space regions. In region I and III we have to take into account of the different diffraction

orders, while in region II we have to consider the waveguide eigenmodes inside each slit. The following approximations are used in this model:

- only the fundamental eigenmode in the modal expansion of the EM fileds inside each slit is considered, which is justified because in the sub-wavelength regime the fundamental mode is the only propagating one, and dominates the transmittance.
- Surface Impedance Boundary Conditions (SIBC) are imposed on the metal dielectric interfaces. This kind of approximation is applicable when the skin depth in the metal is much smaller than all other length scales in the system. Moreover, the vertical walls of the slits are assumed to be perfect metal surfaces.

Due to the symmetry of the array, only two components of the EM are needed to solve the problem. In particular, for p-polarization the y-component of the magnetic field and the x-component of the electric field are needed. To simplify the notation, the Dirac's notation is used: we denote by $\left|\mathbf{E}\right\rangle$ a bi-vector such that $\left\langle \mathbf{r}_{||}\middle|\mathbf{E}\right\rangle = \left(E_x\left(\mathbf{r}_{||}\right), E_y\left(\mathbf{r}_{||}\right)\right)^T$, where T stands for transposition and $\mathbf{r}_{||}$ is the in-plane (x-y) vector position. The z dependence is not included and must be explicitly stated in the definition of the EM field. With these notation the expression for the fields are more compact and the overlaps between waves can be written as:

$$\left\langle \mathbf{E}\middle|\mathbf{E}'\right\rangle = \int d\mathbf{r}_{||}\left\{E_x^*\left(\mathbf{r}_{||}\right)E_x'\left(\mathbf{r}_{||}\right) + E_y^*\left(\mathbf{r}_{||}\right)E_y'\left(\mathbf{r}_{||}\right)\right\} \tag{B.1}$$

The Gaussian system of unit is used, so that $c=1$ and $\omega = k_0$. Due to the symmetry of the problem, there is no y-dependence so that the bi-vector defined above has only x-component. The normalization for the magnetic field is chosen such that over a period the incoming magnetic field has unitary amplitude; the electric field is then obtained from the magnetic field through Maxwell's curl equation.

The EM field in the region of incidence $z < -h/2$ (region I) is given by:

$$\begin{aligned}\left|H_y(z)\right\rangle &= \left|k_0\right\rangle e^{ik_{z0}(z+h/2)} + \sum_n r_n \left|k_n\right\rangle e^{-ik_{zn}(z+h/2)} \\ \left|E_x(z)\right\rangle &= Y_{k_0}\left|k_0\right\rangle e^{ik_{z0}(z+h/2)} - \sum_n Y_{k_n} r_n \left|k_n\right\rangle e^{-ik_{zn}(z+h/2)}\end{aligned} \tag{B.2}$$

where $\left|k_n\right\rangle$ is given by:

$$\left|k_n\right\rangle = \frac{1}{\sqrt{d}} e^{ik_{xn}x} \tag{B.3}$$

The other coefficients appearing into equations (B.2) are defined by the following relations:

$$\begin{aligned} k_{xn} &= k_0 \sin(\alpha) + \frac{2\pi}{d} n \\ k_{zn} &= \sqrt{{k_0}^2 - k_{xn}^2} \\ Y_{kn} &= \frac{k_{zn}}{k_0} \end{aligned} \tag{B.4}$$

r_n is the reflection coefficient for the n-enth diffraction order.

The modes $|k_n\rangle$ form a complete orthonormal set when integrated over a unit cell (i.e. a period):

$$\langle k_m | k_n \rangle = \delta_{k_m, k_n} \tag{B.5}$$

The summations are all over the diffraction orders, which correspond to a summation over all $\mathbf{k} = \mathbf{k}_0 + \frac{2\pi}{d} n \mathbf{u}_x$, where $\mathbf{u}_x$ is a unitary vector in the x-direction. A single slit can be seen as rectangular waveguide with an infinite length. Using the standard waveguide theory and applying the appropriate boundary conditions it's easy to get the magnetic field inside the slit:

$$H_y(x,z) = \sum_{n \geq 0} \cos\left(\frac{n\pi x}{w}\right) \left\{ A_n \exp\left[i \sqrt{k_0^2 - \left(\frac{n\pi}{w}\right)^2}\, z \right] + B_n \exp\left[-i \sqrt{k_0^2 - \left(\frac{n\pi}{w}\right)^2}\, z \right] \right\}$$

The index n stands for the different modes inside the slit. The fundamental mode is the one labeled by n=0. With these definitions, the EM field in the grating region $-h/2 < z < h/2$ (region II) is given by:

$$\begin{aligned} |H_y(z)\rangle &= \sum_{\mathbf{R}} e^{i\mathbf{k}_0 \mathbf{R}} |0, \mathbf{R}\rangle \left\{ A e^{i k_z^{II} z} + B e^{-i k_z^{II} z} \right\} \\ |E_x(z)\rangle &= \sum_{\mathbf{R}} Y_k^{II} e^{i\mathbf{k}_0 \mathbf{R}} |0, \mathbf{R}\rangle \left\{ A e^{i k_z^{II} z} - B e^{-i k_z^{II} z} \right\} \end{aligned} \tag{B.6}$$

where the summation is made all over the slit's position in the 1D grating. *A* and *B* represents the amplitudes of the waveguide modes inside the slits propagating respectively in the positive and negative z-direction. The propagation constant for these modes is $k_z^{II} = k_0$ and $Y_k^{II} = k_z^{II} / k_0$. $|0, \mathbf{R}\rangle = \frac{1}{\sqrt{a}}$ is the normalization constant over the slit width for the fundamental waveguide mode. Given the symmetry of the problem, and according to Bloch's theorem, only one unit cell must be considered, and for simplicity we will take the one corresponding to the origin $\mathbf{R} = \mathbf{0}$ so that the notation simplify to $|0, \mathbf{R} = \mathbf{0}\rangle = |0\rangle$

In the transmission region $z > h/2$ (region III) the EM field is given by:

$$\left|H_y(z)\right\rangle = \sum_n t_n \left|k_n\right\rangle e^{ik_{zn}(z-h/2)}$$
$$\left|E_x(z)\right\rangle = \sum_n Y_{k_n} t_n \left|k_n\right\rangle e^{ik_{zn}(z-h/2)} \quad \text{(B.7)}$$

where t_n is the transmission coefficient for the scattered diffraction orders. The problem has four unknowns, namely the reflection and transmission coefficient and the amplitude of the waveguide modes. These unknowns will be determinate using a *multiple scattering* formalism and by matching the EM field at the different interfaces using the appropriate boundary conditions.

Surface Impedance Boundary Conditions

Surface impedance boundary conditions (SIBC) are an approximation of the standard Maxwell's boundary conditions that are applicable on a metal-dielectric interface. SIBC establish the following relation between the tangential components of the EM fields at the horizontal interfaces:

$$\mathbf{E}_{||} = Z_s \mathbf{u} \times \mathbf{H}_{||} \quad \text{(B.8)}$$

where $Z_s = \sqrt{\varepsilon_M}^{-1}$ is the metal impedance and $\mathbf{u}$ is a unit vector directed along the positive z axis (normal to the plane of the grating). Considering the case of p-polarization (H field directed along the y axis) and using Maxwell's curl equation and the identity $\nabla \simeq -\mathbf{u}\frac{\partial}{\partial z}$, the equation (B.8) can be expressed at the metal-dielectric interface (z=0) as:

$$Z_s H_y|_{z=surf} = \frac{i}{k_0}\frac{\partial H_y}{\partial z}|_{z=surf} \quad \text{(B.9)}$$

This conditions holds *only* at the interface, and H_y represents the *total* magnetic field at the interface. The physical meaning of SIBC can be explained as follows: the effect of the metal layer on the EM field is considered only on the surface through the surface impedance Z_s, while inside the layer no "metallic-ness" is considered at all. This approximation holds when the skin depth of the metal is very small compared to all other length of the system. We want now to apply the SIBC to the grating problem. Let's consider the interface between the incidence region and the upper part of the grating $(z=-h/2)$. Using the EM field defined in (B.2) and (B.6), the SIBC in the form (B.8) and projecting on the $\langle k_n|$ modes we get:

$$Y_{k_0}\delta_{k_n,k_0} - Y_{k_n} r_n - Y_k^{II}\langle k_n|0\rangle\left(Ae_h^{-1} - Be_h\right) = Z_s\left[\delta_{k_n,k_0} + r_n - \langle k_n|0\rangle\left(Ae_h^{-1} + Be_h\right)\right] \tag{B.10}$$

which can be solved for r_n :

$$r_n = -\frac{f_{k_n}^-}{f_{k_n}^+}\delta_{k_0,k_n} + \frac{\langle k_n|0\rangle}{f_{k_n}^+}\left[Ae_h^{-1} f_{II}^- + Be_h f_{II}^+\right] \tag{B.11}$$

where:

$$\begin{aligned} f_{k_n}^{\pm} &= Z_s \pm Y_{k_n} \\ f_{II}^{\pm} &= Z_s \pm Y_k^{II} \\ e_h &= e^{ik_z^{II}h/2} \end{aligned} \tag{B.12}$$

With a same reasoning applied to the lower interface $\left(z = h/2\right)$ we get:

$$t_n = \frac{\langle k_n|0\rangle}{f_{k_n}^+}\left[Ae_h f_{II}^+ + Be_h^{-1} f_{II}^-\right] \tag{B.13}$$

Multiple Scattering Formalism

The Multiple Scattering Formalism (MSF) is a technique that expresses the scattering coefficients of a stratified media in terms of scattering coefficients of isolated interfaces. This is particularly useful when surface modes, like SPP, are present, as they clearly show up in the two-media scattering coefficients. In the case in exam, we must divide the three-regions system in two-regions system, in which all regions are taken as semi-infinite (see Figure B.2). In this way, the scattering coefficients of the three region system can be obtained from the scattering coefficients of the two regions independent systems. This procedure can be divided into three steps:

- A plane wave coming from medium I with wave vector $\mathbf{k}_0$ impinges onto medium II which is now considered as a semi-infinite medium. The incoming field has unit amplitude at the interface $z = -h/2$, and can be reflected back into the different diffraction orders in medium I, with amplitude ρ^{11}, or can be scattered into the Bloch combination of waveguide modes in region II, with amplitude τ^{12}.

- The field coming from region II impinges onto medium I which is now considered as a semi-infinite medium. The incoming field is a Bloch combination of the fundamental waveguide mode inside the slit and has unit amplitude at the interface $z = -h/2$, and can be reflected back into a

waveguide mode with an amplitude ρ^L or be transmitted into the different plane waves in region I with amplitudes τ^{21}.

- For the II-III interface the situation is similar to the II-I interface. If a symmetric situation is considered (the I and III media have the same dielectric constant) then the scattering coefficients of the II-III interface are the same of the II-I interface.

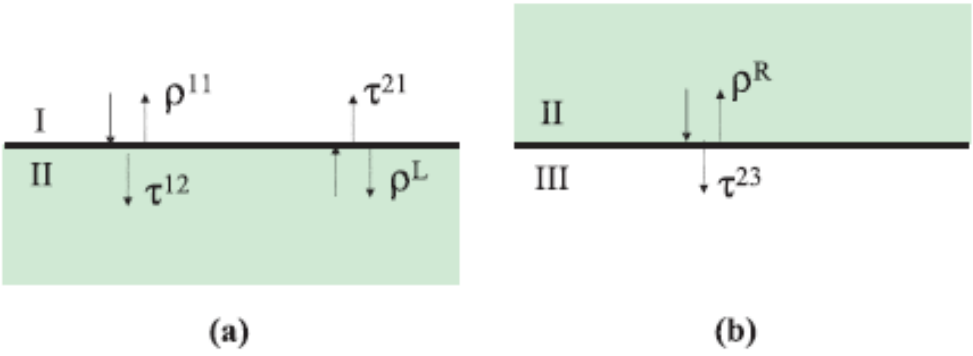

Figure B.2: Definition of the scattering coefficients for the two independent systems in which each medium is taken as semi-infinite.

Knowing all two region scattering coefficients, it's easy to calculate the total scattering coefficients. Actually, ρ^{11} and τ^{21} would be vectors, given the final state could be any of the diffraction orders. Since we are mainly interested in scattering properties for wavelengths larger than the grating period, only the zero diffraction order is propagating and thus the zero order will be the only one considered. For instance, in order to calculate the zero order transmission coefficient t_0 we have to sum up all the multiple scattering processes:

$$t_0 = \tau^{12} e_h^* \tau^{23} + \tau^{12} e_h^* \left(\rho^R e_h^* \rho^L e_h^*\right) \tau^{23} + \ldots \tag{B.14}$$

The origin of this expression is the following: the first term in the series represents the direct process of transmission through the slits (factor τ^{12}), propagation inside them (factor $e_h^* = e^{ik_0 h}$), and transmission through medium III (factor τ^{23}). The second term is similar but takes into account that, before propagating into medium III, the EM field can reflect at the exit and back into the holes (factor ρ^R), propagate inside the slits (factor $e_h = e^{ik_0 h}$), reflect back at the II-I interface (factor ρ^L), propagate again inside the slits (factor $e_h = e^{ik_0 h}$) and then exits to medium III (factor τ^{23}). This intermediate process

take places an infinite number of times, each time adding a partial amplitude for the process of transmission into medium III. Luckily, the infinite series is geometric and converges:

$$t_0 = \frac{\tau^{12} e^{ikh} \tau^{23}}{1 - \rho^L \rho^R e^{2ikh}} \tag{B.15}$$

As we can see, expression (B.15) is reminiscent of the expression of the Fresnel's transmission coefficient for a three-layer system. The other three-media scattering coefficients can be obtained with a similar reasoning, leading to:

$$r_0 = \rho^{11} + \frac{\tau^{12} e^{2ikh} \rho^R \tau^{21}}{1 - \rho^L \rho^R e^{2ikh}} \tag{B.16}$$

$$A = \frac{\tau^{12} e^{ikh/2}}{1 - \rho^L \rho^R e^{2ikh}} \tag{B.17}$$

$$B = \frac{\tau^{12} e^{ikh} \rho^R e^{ikh/2}}{1 - \rho^L \rho^R e^{2ikh}} = \rho^R e^{ikh} A \tag{B.18}$$

It's useful to note that for the symmetric configuration we have $\tau^{23} = \tau^{21}$ and $\rho^R = \rho^L$.

Scattering Coefficients

In order to calculate the scattering coefficients defined in the previous section, we have match the EM field at the different interfaces with proper boundary condition. For p-polarization, the EM field must satisfy the following boundary condition:

- The components of the electric field parallel to the surface must be continuous over the *whole* surface, i.e. over a period.
- The components of the magnetic field parallel over the surface must be continuous *only* over the slits. In fact, the magnetic field is discontinuous at the metal air interface, and the value of this discontinuity is not known a priori.

The various scattering coefficients can be calculated just by projecting each continuity equation onto the set of modes that span the spatial region over which the equation is defined. This projection, together with SIBC, provides as many equation as unknown scattering coefficients. Relations coming from continuity of electric field must be projected onto $\langle k_n |$ modes; this modes in fact form an orthonormal set in the spatial region defined by a period. Relations coming from magnetic field instead must be projected onto $\langle 0 |$ modes which are the waveguide modes defined in the slits region. It's worthwhile to remember that within region II only $\langle 0 |$ modes are possible. For the coefficients at the I-II interface, since in the

semi-infinite medium II there is no reflected wave, the only waveguide mode present is the one propagating along the positive z-direction. This implies $B=0$. So at $z=-h/2$ the continuity of the y component of the magnetic field can be expressed as:

$$|k_0\rangle+\sum_n \rho^{11}|k_n\rangle = Ae_h^{-1}|0\rangle \tag{B.19}$$

We identify $\tau^{12}=Ae_h^{-1}$, and for ρ^{11} we use the SIBC condition (B.11). Projection onto $\langle 0|$ gives:

$$\langle 0|k_0\rangle+\frac{f_{k_0}^-}{f_{k_0}^+}\langle 0|k_0\rangle+\sum_n \frac{|\langle 0|k_n\rangle|^2}{f_{k_n}^+}\tau^{12}f_{II}^- = \tau^{12} \tag{B.20}$$

which can be solved for τ^{12}:

$$\tau^{12}=\frac{2S_0\cos\alpha}{\cos\alpha+Z_s}\frac{1}{1+(1-Z_s)f} \tag{B.21}$$

where $\cos\alpha = k_{z0}/k_0$ and:

$$f=\sum_{n=-\infty}^{\infty}\frac{S_n{}^2}{\frac{k_{zn}}{k_0}+Z_s} \tag{B.22}$$

S_n represents the "overlap" between propagating modes and waveguide modes inside the slits, and it's given by the integral:

$$S_n=\langle 0|k_n\rangle=\frac{1}{\sqrt{ad}}\int_{-a/2}^{a/2}e^{ik_{xn}x}dx=\sqrt{\frac{a}{d}}\frac{\sin[k_{xn}a/2]}{k_{xn}a/2} \tag{B.23}$$

If we apply a similar reasoning at the II-III interface we have:

$$\langle 0|0\rangle\left(Ae_h+Be_h^{-1}\right)=\sum_n \tau^{23}\langle 0|k_n\rangle \tag{B.24}$$

The incoming wave must have unit amplitude at $z=h/2$, so $A=e_h^{-1}$. Identifying $\rho^R=Be_h^{-1}$ and using for τ^{23} the SIBC condition (B.13), we have:

$$1+\rho^R=\sum_n\frac{\langle k_n|0\rangle}{f_{k_n}^+}\left(f_{II}^+ +\rho^R f_{II}^-\right)\langle 0|k_n\rangle \tag{B.25}$$

which yields to:

$$\rho^R = -\frac{1-(1+Z_s)f}{1+(1-Z_s)f} \tag{B.26}$$

From (B.24) and (B.26) we have:

$$\frac{2f}{1+(1-Z_S)f} = \sum_n \tau^{23} S_n \tag{B.27}$$

Taking only the zero-order in equation (B.27) and using the expression (B.22) for f, we get:

$$\tau^{23} = \frac{2S_0}{\cos\alpha + Z_s}\frac{1}{1+(1-Z_s)f} \tag{B.28}$$

For completeness, the last scattering coefficient is reported:

$$\rho^{11} = \frac{\cos\alpha - Z_s}{\cos\alpha + Z_s} - \frac{2{S_0}^2(1-Z_s)\cos\alpha}{(\cos\alpha + Z_s)^2}\frac{1}{1+(1-Z_s)f} \tag{B.29}$$

The transmission spectrum as function of incident wavelength is obtained by taking the square modulus of the transmission coefficient:

$$T = |t_0|^2 = \left|\frac{\tau^{12} e^{ikh} \tau^{23}}{1-\rho^L \rho^R e^{2ikh}}\right|^2 \tag{B.30}$$

The spectrum is reported in Figure B.3 for a gold array with period of 500 nm, thickness of 375 nm and slits width of 250 nm, illuminated by a p-polarized radiation at normal incidence. As we can see, the spectrum presents a resonant peak around 545 nm, which is very near to the position predicted by the "standard" grating coupling formula, and also presents an almost perfect transmittance, thus confirming the EOT. Moreover, the spectrum is in a very good agreement with FEM simulations, as shown in Figure B.4. As noted before, the MSF is very useful when surface modes, like SPP, are presents, as their role in the transmission process is easily put in evidence.

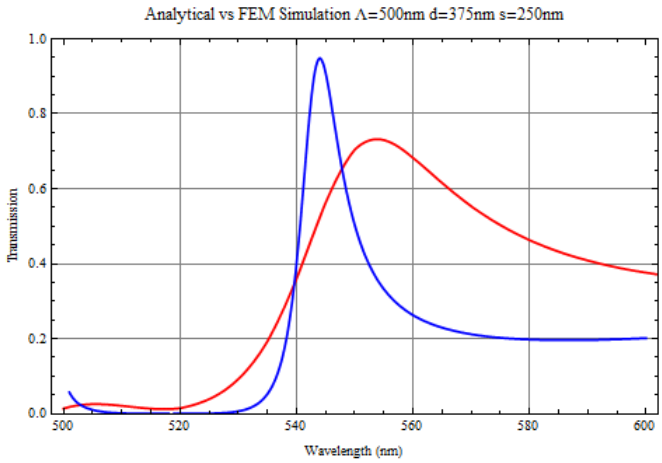

Figure B.3: Comparison between analytical model (red) and FEM simulation (blue). As we can see, the peak position differs only of 7 nm, while the transmission intensity is lightly smaller for the analytical model.

Looking at the expression for the different scattering coefficients, we see that function f plays a central role in the transmission process, as all scattering coefficients defined above diverges whenever $f \to \infty$. From equation (B.22) we see that f is singular when:

$$\frac{k_{zn}}{k_0} + Z_S = 0 \tag{B.31}$$

This relation takes the form for normal incidence:

$$\lambda_{SPP} = \frac{d}{n}\sqrt{\frac{\varepsilon_M - 1}{\varepsilon_M}} \tag{B.32}$$

which is just the condition of SPP excitation through grating coupling within SIBC approximation. From equation (B.21) we see that τ^{12} is singular when $f \to \infty$. In particular, τ^{12} is anti-resonant near the SPP condition (B.32) and τ^{21} presents also the same behavior (Figure B.4). From equation (B.26) we note instead that $\rho^R \approx 1$ when $f \to \infty$, and the same holds for ρ^L. Near the SPP condition ρ^R is resonant (Figure B.4).

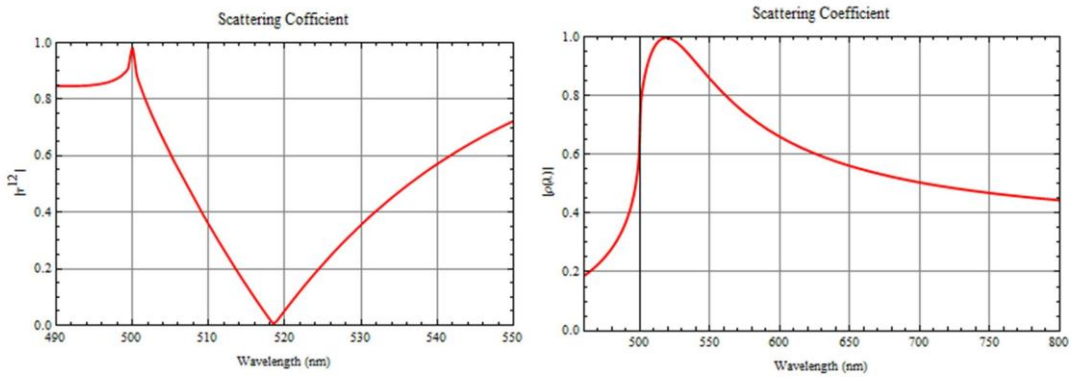

Figure B.4 Right: Modulus of τ^{12} as function of wavelength. Near the SPP location (518 nm), the scattering coefficient is anti resonant. Left: Modulus of ρ^{R} as function of wavelength. Near SPP location, the scattering coefficient is resonant.

Acknowledgements

Although the writing process of a PhD thesis is a solitary and somehow mystics experience, the work and related results presented in this work would not have been possible without the contribution and collaboration of different people which helped me in developing the necessary expertise required in a modern nanoscience environment. A special thanks to Denis Garoli for supporting my PhD activity with a lot of useful (and sometimes funny) discussions on plasmonic regarding nanofocusing effects and nanofabrication processes in particular on FIB and SEM, and most important for letting me use his office for a quiet and peaceful thesis writing experience. Thanks to Michele Massari and Marta Carli for the time we have shared together in learning and developing EBL processes and for general discussions on nanofabrication. Thanks also to Giuseppe Parisi and Pierfrancesco Zilio for the useful tips on FEM simulations, Elettra Mari for the help in learning the basic of OAM and Gianluca Ruffato for the help in collecting ellipsometric measures and for the very interesting and exciting discussion on optics and plasmonic in general. An acknowledgement to Roberto Pilot for the SERS measurements, to Valentina Giorgis for the electrolytic growth and to Marco Natali for metal evaporations. Thanks to Davide Sammito and Davide De Salvador for the developing and designing of the HEMT plasmonic biosensor.

I would like to thank my supervisor Filippo Romanato, for giving me the chance to grow up in the research group of LaNN in a young, challenging and exciting environment and to develop a strong sense of team's work and collaboration with different scientific fields, which are at the base of a successful research work.

A special thanks to my parents for always supporting me and to my brother for unconsciously stimulating me to give always the best I can. Finally thanks to my friends Cinese, Mancio, Maria and Mirko, and my trusty companions Les Paul, Tele, Alhambra and Taylor for the great time we had together and we will always have. Friendship, love and forgiveness is what life is really about.

List of Publications

This thesis is based on the following publications:

- **T.Ongarello**, F. Romanato, P. Zilio, M. Massari*, "Polarization independence of extraordinary transmission trough 1D metallic gratings",* OPTICS EXPRESS 19(10) 9426 (2011) (**Chapter 3**).
- F. Romanato, **T.Ongarello**, G. Zacco, D. Garoli, P. Zilio, M. Massari, *"Extraordinary optical transmission in one-dimensional gold gratings: near- and far-field analysis",* APPLIED OPTICS 50(22) 4529 (2011) (**Chapter 3**).
- F. Romanato, R.Pilot, M.Massari, **T.Ongarello**, G.Pirruccio, P.Zilio, G.Ruffato, M.Carli, D.Sammito, V.Giorgis , D.Garoli, R.Signorini, P.Schiavuta and R.Bozio *"Design, fabrication and characterization of Plasmonic Gratings for SERS",* MICROELECTRONIC ENGINEERING 88(8) 2717 (2011) (**Chapter 3**).
- D. Garoli, F. Romanato, P. Zilio, M. Natali, F. Marinello, **T. Ongarello**, D. Sammito, D. De Salvador, *"Fabrication of 'nano-rocket-tips' for plasmonic nanofocusing",* MICROELECTRONIC ENGINEERING 88(8) 2530 (2011) (**Chapter 4**).
- **T. Ongarello**, G. Parisi, D. Garoli, E. Mari, P. Zilio, and F. Romanato *"Focusing dynamics on circular distributed tapered metallic waveguides by means of Plasmonic Vortex Lenses",* OPTICS LETTER 37 (21) 4516 (2012) (**Chapter 5**).
- E. Mari, G. Parisi, **T. Ongarello**, D. Garoli P. Zilio, and F. Romanato "Resolving orbital angular momentum with nanostructures", submitted to Journal of Modern Optics (2012) (**Chapter 5**).

Other publications by the author during Phd years:

- M. Massari, F. Romanato, M. Carli, **T. Ongarello**, M. Prascioulu, E. Mari, F. Tamburini, A. Bianchini, A. Barbieri "Design, fabrication and characterization of phase masks for astronomical applications", MICROELECTRONIC ENGINEERING 88(8) 2675 (2011).
- D. Garoli, M. Natali, G. Parisi, **T. Ongarello**, E. Sovernigo, M. Massari, V. Giorgis, G. Ruffato, S. De Zuani, F. Romanato "Fabrication of metamaterials in the optical spectral range", MICROELECTRONIC ENGINEERING 88(8) 1951 (2011).
- D. Garoli, P. Zilio, M. Natali, M. Carli, **T. Ongarello**, F. Romanato "Plasmonic nanofocusing by means of metal coated dielectric nanowedges", Proceedings of SPIE - The International Society for Optical Engineering 8457 , art. no. 84572L (2012)

- D. Garoli, G. Ruffato, S. Cattarin, S. Barison, M. Perino, **T. Ongarello** and F. Romanato "Nanoporous Gold – Application to Extraordinary Optical Transmission of Light", J. Vac. Sci. Technol. B 31, 012601 (2013).